

© Copyright 2019

Steven F. Sholes

Geomorphic and Atmospheric Investigations on the Habitability of Past and
Present Mars

Steven F. Sholes

A dissertation

submitted in partial fulfillment of the
requirements for the degree of

Doctor of Philosophy

University of Washington

2019

Reading Committee:

David C. Catling, Chair

David R. Montgomery

Jonathan D. Toner

Program Authorized to Offer Degree:

Earth and Space Sciences

University of Washington

Abstract

Geomorphic and Atmospheric Investigations into the Habitability of Past and Present Mars

Steven F. Sholes

Chair of the Supervisory Committee:
David C. Catling, Ph.D.
Earth and Space Sciences

While the current surface of Mars is viewed to be inhospitable to life as we know it, past Mars may have harbored habitable environments though the extent and duration of such environment is still unclear. There are several requirements to make an environment habitable, which include a liquid solvent (e.g. liquid water), a source of energy (e.g. redox gradients), bioimportant major and trace elements (e.g. CHNOPS), and sustained clement conditions for necessary biochemical reactions to take place (e.g. temperature, pH). This dissertation focuses on better constraining these requirements through atmospheric modeling and quantitative surficial geomorphological investigations.

The first half of this dissertation explores the habitability of past and present Mars through the lens of atmospheric redox chemistry. The photochemically produced CO-O₂ redox

pair in the modern atmosphere produces the second largest atmospheric thermodynamic disequilibrium in the solar system (behind Earth's atmosphere-ocean system), which represents an untapped source of free energy for potential life to exploit. A rigorous upper limit on the possible extant biomass that can be sustained from this free energy is presented. Volcanic outgassing of reducing gases, e.g. CO and H₂, can shift the redox state of the atmosphere, changing the surface conditions towards being reducing and anoxic which are more favorable for the formation of prebiotic chemical compounds (e.g. amino acids). The required levels of volcanism needed to create reducing conditions and potential observables of such environments are also presented here.

The latter half of this dissertation focuses on assessing the current state of coastal evidence for past liquid water oceans on Mars. While nearly all aspects of these hypothesized oceans are vigorously debated, availability of large sustained bodies of liquid water would be a boon for constraining the past surface habitability. Presented here is a toolkit developed for quantitatively identifying paleoshorelines using topographic, morphological, and spectroscopic investigations. This toolkit is then applied to 40 individual sites across Mars that have been proposed as ancient ocean shorelines and evaluated along with the general mapped contacts on their consistency with such an origin. None of the putative paleoshoreline sites provided compelling evidence nor consistency with a coastal origin and can all be explained through more conservative geological processes.

Together, the chapters in this dissertation provide quantitative means of characterizing contributing aspects of potentially habitable environments on past and present Mars.

TABLE OF CONTENTS

List of Tables	viii
Chapter 1. Introduction	12
1.1 Motivation.....	12
1.2 Dissertation Outline	13
Chapter 2. Anoxic Atmospheres on Mars Driven by Volcanism	16
2.1 Abstract.....	16
2.2 Introduction.....	17
2.3 Methods.....	19
2.4 Results.....	27
2.5 Discussion.....	32
2.5.1 Consequences of Volcanism.....	32
2.5.2 Implications for Habitability.....	34
2.5.3 Potentially Observable Consequences of Anoxia.....	35
2.6 Conclusions.....	38
Chapter 3. A Maximum Subsurface Biomass on Mars From Untapped Free Energy.....	40
3.1 Abstract.....	40
3.2 Introduction.....	41
3.3 Methods.....	44
3.3.1 Fixed Parameter Model.....	46
3.3.2 Optimized Parameter Model.....	48
3.3.3 Atmospheric Diffusion Model	50
3.4 Results.....	53
3.5 Discussion.....	58
3.6 Conclusions.....	64
Chapter 4. Quantitative High-Resolution Re-Examination of a Hypothesized Ocean Shoreline on Mars	66
4.1 Abstract.....	66
4.2 Introduction.....	66
4.2.1 Background Information.....	66
4.2.2 Site Introduction.....	70
4.3 Methods.....	72
4.3.1 Photogeological Mapping	72
4.3.2 Topographic Analysis	74
4.3.3 Thermal Inertia.....	79

4.3.4	Spectroscopy	81
4.3.5	Classification.....	82
4.4	Results.....	83
4.4.1	Photogeology	83
4.4.2	Topography.....	87
4.4.3	Thermal Inertia and Spectroscopy	91
4.5	Discussion.....	93
4.5.1	Are These Shorelines?	93
4.5.2	Alternative Hypotheses.....	95
4.6	Conclusions.....	96
Chapter 5.	Mars' Ocean Shorelines: A High-Resolution Global Re-Examination	98
5.1	Abstract.....	98
5.2	Introduction.....	98
5.3	Methods.....	103
5.4	Observations	104
5.4.1	Mass Wasting Features	106
5.4.2	Collapse Features	107
5.4.3	Massif Ridges.....	110
5.4.4	Isolated and Trough Ridges	111
5.4.5	Lobate Flows.....	112
5.4.6	Miscellaneous Features.....	113
5.4.7	Uncertain Features	115
5.5	Discussion.....	115
5.5.1	Paleoshoreline Assessment.....	115
5.5.2	Elevation of the Mapped Shorelines	118
5.5.3	Other Lines of Evidence for Oceans.....	122
5.6	Conclusions.....	123
Chapter 6.	Conclusions	124
6.1	Chapter Summaries.....	124
6.2	Future Work	126
Appendix A:	Supplemental Material to Chapter 2	128
Appendix B:	Supplemental Material to Chapter 4.....	138
Appendix C:	Supplemental Material to Chapter 5.....	144
Bibliography	195

LIST OF FIGURES

- Figure 2.1. Schematic diagram showing the dominant sulfur photochemistry and pathways during volcanically-active Mars, ‘vol.’ indicates a volcano. Based on likely magma chemistry (see text) the most important volcanic sulfur gas is generally SO₂. Atmospheric oxidation reactions turn SO₂, H₂S, and S₂ into sulfuric acid aerosols, while photochemistry in reducing atmospheres also makes polysulfur aerosols (S₈). Additionally, there is direct deposition of SO₂ to the surface as another sink on S. H₂O and CO₂ concentrations are assumed to be buffered by large subsurface and surface reservoirs. Carbonyl sulfide (OCS) is able to build up through reactions with sulfur-bearing compounds and CO. 23
- Figure 2.2. Estimates of crustal production rates for Mars through time from various authors. Some models suggest that most volcanism should have occurred between the early Noachian and the early Amazonian. In the Breuer & Spohn model, different initial mantle temperatures give rise to different time histories. Schubert’s model varies χ , a crustal fractionation parameter (see text). 24
- Figure 2.3. Atmospheric response to steady-state volcanic outgassing from typical martian magmatic buffers. Symbols display the mixing ratios (mapped to left axes) and solid lines display species and aerosol (aer) surface deposition (dep) fluxes and atmospheric loss for H₂ (mapped to right axes). We used magma buffers to illustrate how a state of anoxia depends on the total amount of volcanic magma flux for each buffer. A vertical gray line shows the transition point between oxidizing and reducing conditions as dictated by Eqn. 2.5. Plots *a* through *d* show the cumulative effects of changing each melt parameter; *b* is a drier melt, *c* is more reduced, and *d* is outgassed under higher pressures. Melts that are drier, more reduced, and under greater pressure take the greatest amount of volcanism to reach reducing conditions ($\sim 4 \times 10^{-3} \text{ km}^3 \text{ yr}^{-1}$ for *a* versus $\sim 6 \times 10^{-2} \text{ km}^3 \text{ yr}^{-1}$ for *d*). 28
- Figure 2.4. Vertical mixing ratio profiles for modern and anoxic Mars. Temperature (T) is plotted as a dashed line. (a) C-O-H species for modeled modern Mars, (b) C-O-H species for anoxic Mars for the case of mantle buffer with FMQ-1.4, 0.4 wt% H₂O at 0.01 bar and magma flux of $0.15 \text{ km}^3 \text{ yr}^{-1}$ which is a good representation of typical modeled reducing and anoxic

conditions (See Fig. 2.3a), (c) S species for anoxic Mars under the same conditions as *b*.
..... 30

Figure 2.5. Deposition rates based on varying crustal production models (see Fig. 2.2, χ is a crustal fractionation parameter – see text). Total amounts of sulfate deposited are given in Table 2.1. Deposition rates for SO and S₂ are always less than 0.02 Tmol yr⁻¹..... 31

Figure 2.6. Plot showing crustal production flux (in km³ yr⁻¹) (associated with volcanic outgassing) needed to reach a reducing atmosphere (pOx < 0) as a function of magma water content (along x-axis), outgassing pressure (color), and redox state of the magma (symbols). Drier, more reducing magmas take the greatest amount of volcanic activity to switch the redox of the martian atmosphere. 34

Figure 3.1. Modeled atmospheres for Mets. 1-3 as biogenic sinks are incrementally ramped up. Left panels are for the fixed parameter model and the right panels for the optimized parameter version (see text). Shaded regions represent a 2 σ uncertainty for the mixing ratios of CO, O₂, H₂, CH₄, and CO₂. Vertical dotted lines indicate where the model diverges from observations (max biological sink). CO₂ concentrations do not vary for Met. 2 within or below this biogenic sink range. 54

Figure 3.2. Modeled atmosphere for Mets. 4 and 5, which produce the largest maximum biomass, as biogenic sinks are incrementally ramped up. Left panels are for the fixed parameter model and the right panels for the optimized parameter version (see text). Shaded regions represent a 2 σ uncertainty for the mixing ratios of CO, O₂, H₂, CH₄, and CO₂. Vertical dotted lines indicate where the model diverges from observations (max biological sink). CO₂ concentrations do not vary for Met. 5 within or below this biogenic sink range..... 55

Figure 3.3. Monte Carlo simulations calculating diffusive fluxes for CO and H₂ as a function of biotic layer depth. The resulting probability density is shown via colored bins. Solid black trendlines indicate median flux values while vertical lines show maximum allowable biogenic sinks for each metabolism from our photochemical model calculations. The interception of these vertical lines with the median diffusion flux shows the maximum depth to which subsurface life could be exploiting atmospheric free energy. Below these depths, microbes would be limited by the downward diffusion of atmospheric gases through the regolith rather than the supply of reactants from photochemical reactions 59

Figure 3.4. Potential sites for life on Mars. This study estimates the maximum number of actively metabolizing microbes that are in communication with the atmosphere (1). There could be actively metabolizing microbes in small communities that are sealed off from the atmosphere (2) or are neither taking advantage of the available atmospheric free energy nor producing detectable byproducts (3). The number of dormant microbes (e.g. endospores) (4) could be indefinitely large, but would not be evolutionarily advantageous for long-term survival on Mars. Downward arrows indicate fluxes of available free-energy reactants and upward arrows indicate flux of metabolized products into the atmosphere. All are assumed to be in contact with some form of liquid water (e.g. rare briny fluid pockets or a deep aquifer). 63

Figure 4.1. CTX mosaic of the three-crater system (centered three largest craters labeled A-C) to the NE of Cydonia Mensae showing the selected test site region. The center of the image is approximately 36.4°N, 350.2°E. White boxes indicate DEM footprints from HiRISE stereo pairs for the western and southern sites. The crater complex is open to the northern plains (and thus a potential ocean) on the NE of Crater A and NW of Crater C. *Inset* - MOLA colorized elevation showing the site (white box) in relation to the topographic dichotomy (which roughly follows the blue/green boundary on the globe). 71

Figure 4.2. Topographic expression of an idealized paleoshoreline terrace after Hare et al. (2001); Jewell (2016). *a*) Solid line shows the topography of an arbitrary example terrace showing the riser inflection (RI), riser crest (RC), benchtop (BT), and knickpoint (KP). Dotted line shows a polynomial-fit “idealized” slope. *b*) The residual topography taken from subtracting the “idealized” slope from the topographic data. *c*) Smoothed first derivative of the residual topography where the circles represent defining the characteristic of RI and BT. *d*) Smoothed second derivative of the residual topography where the circles denote the defining characteristic for RC and KP. 78

Figure 4.3. *a*) Our mapped lineaments that follow the putative shoreline contacts for the western site of Crater A. Topography for blue line A-A’ is shown in Fig. 5. Black lines map the lower contact of the smooth light-toned capping unit. Yellow rectangles show the locations of zoomed in areas displayed in *b-d*. HiRISE image: ESP_025650_2165. Arrows in *b* show sides of a bifurcation and the arrow in *d* show merging lineaments. 84

Figure 4.4. Mapped lineaments that follow the putative shoreline contacts for the southern site of Crater A. Solid white lines demark lineaments that we mapped in the visible imagery; dashed blue lines demark additional lineaments resolved only in the residual topography data (see Sec. 2.2.2); dotted green lines show mapped contacts by Clifford and Parker (2001). Yellow rectangles show the locations of zoomed-in areas displayed in b-e. Black rectangles show extents for Figs. 6 and 7. HiRISE image: PSP_001414_2165..... 86

Figure 4.5. Along-track elevation data for curvilinear line A-A' in Fig. 4.3 (solid blue line). Diamond markers indicate terraces found along profiles orthogonal to the lineament. Terraces appear to follow the topography rather than an equipotential surface. Ellipses outline clusters of terraces that appear to align with the topographic peaks of the promontory..... 88

Figure 4.6. Steps of the topographic expression analysis on a subsection of the southern site. *a)* Original HiRISE image, *b)* Our high-resolution digital elevation model, *c)* Surface polynomial fit surface representing an 'idealized' slope, *d)* Residual topography derived from subtracting the idealized surface from the topographic data. Potential paleoshoreline terraces appear as alternating dark/light bands in the residual topography. Further analysis of topographic transects is used to evaluate and eliminate false positives..... 90

Figure 4.7. Locations of potential terraces (bold white segments) found along a sample of transects (dashed lines) orthogonal to the lineaments found in the surface residual topography. *a)* HiRISE image, *b)* slope map, *c)* corresponding elevations. Higher elevations are to the south in *a-b* and all terraces map vertically to their corresponding points in *c*..... 92

Figure 5.1. Locations of the putative mapped shorelines and sites. The Deuteronilus Level is mapped with solid green lines (Ivanov et al., 2017). The Arabia Level is mapped in blue and white (Carr & Head, 2003), with blue showing the sections excluded from shoreline deformation models (N. H. Chan et al., 2018; Citron et al., 2018; Perron et al., 2007). Diamond markers show the different sites and are colored according to their data availability: yellow have HiRISE coverage, red only have CTX, and black have HiRISE coverage of adjacent or similar features not originally cited. MOLA hillshade, polar stereographic projection. 100

Figure 5.2. Examples of the contact used to describe the Arabia and Deuteronilus Levels. *a)* CTX mosaic showing the Arabia Level in Mamers Valles, in some places it follows a north-facing

escarpment, but is generally diffuse. *b*) THEMIS-IR day mosaic of the Arabia Level which is defined by the stark albedo contrast. *c*) CTX mosaic of the Deuteronilus Level (defined by the lobate flows overlapping the southern plains) in eastern Chryse Planitia. *d*) THEMIS-IR day mosaic of the Deuteronilus Level which is lighter-toned here than the surrounding plains.

..... 101

Figure 5.3. Examples of typical features associated with putative shorelines. *a*) Mass Wasting: Site S3 (GZ06-17a) showing discontinuous lineaments along a degraded crater rim. HiRISE image PSP_007648_1845 (0.5 m/px). *b*) Collapse Features: Site S6 (PC01-12) is an example of stepped massifs along the topographic dichotomy. MOLA shows that the platforms are angled in opposite directions with surfaces differing up to 100 m in elevation. CTX image G04_019756_2204 (6.1 m/px). *c*) Massif Ridges: Site S14 (GZ06-9a) exemplifies multiple ridges that are sinuous and cross-cut the massifs suggesting they are not tombolos, spits, or other coastal features. CTX image G19_025756_2132 (5.8 m/px). *d*) Isolated Ridges: Site S20 (P08-4) shows examples of curvilinear ridges within troughs. CTX image P21_009089_2081 (5.8 m/px). *e*) Lobate Flows: Site S23 (P89-9) shows multiple overlapping lobate flow deposits with different tones and textures (see unit map in Fig. S35). CTX mosaic. *f*) Uncertain: Site S40 (GZ06-15b) is a series of linear ridges in Isidis Planitia but are only a few kilometers in length, isolated from the “coastline,” are discontinuous with some bifurcations, and are too low in elevation to be from a global ocean. CTX image B21_017933_1943 (5.5 m/px). 109

Figure 5.4. Mapped shoreline disparities in western Deuteronilus Mensae. *Top*: Locations of the differently mapped Arabia and Deuteronilus Levels. Yellow lines (diamonds in *b*) and purple lines (squares in *b*) are the digitized locations by Carr and Head (2003) of the map in Clifford and Parker (2001). Black lines (points in *b*) show the detailed mapping by Ivanov et al. (2017). White lines (circles in *b*) show where the Arabia Level should be based on the original description in Parker et al. (1989) as mapped by us here. THEMIS-IR day mosaic with MOLA colorized elevation. *Bottom*: Elevations of the different levels (with corresponding colors) showing the >2.5 km spread in the de facto ‘standard’ mapping of the Carr and Head (2003) Arabia Level and 100s m elevation spread in the other putative shorelines. 121

LIST OF TABLES

Table 2.1. Modeled approximate total amounts of sulfate deposited over the 3.5-0 Gyr volcanic history of Mars for different crustal production rates and mantle buffers of oxygen fugacity: FMQ-0.5 (Fayalite-Magnetite-Quartz; with 0.4 wt% H₂O and 0.01 bar outgassing pressure) and IW (Iron-Wüstite; with 0.01 wt% H₂O and 1 bar outgassing pressure). S content of the magma is 3500 ppm. The total amount of each sulfur aerosol deposition is given in teramoles (10¹² mol). In Schubert’s models, χ is an assumed crustal fractionation parameter (see text).
 32

Table 3.1. Modern martian atmospheric composition and uncertainties for modeled fluxes. Here we use the slightly higher background value of Webster et al. (2015) rather than that from Webster et al. (2018) for a more conservative upper limit on biomass. 47

Table 3.2. Unknown tunable model parameters and their assumed ranges for Mars. Tuned values are for the fixed-parameter abiotic modern Mars model. Grid space refers to how many equally spaced values of the parameter were used in the optimization grid search within the plausible range for the optimized-parameter model. v_{dep} for CO, CO₂, H₂, and O₂ are set to 0 cm s⁻¹. The tuned v_{dep} parameter refers to that assumed for all reactive species including both O₃ and H₂O₂. 50

Table 3.3. Maximum allowable downward flux for each metabolism and the equivalent biomass. Biomass estimates are based on basal power requirements of 3×10⁻²³ kJ s⁻¹ cell⁻¹ (LaRowe & Amend, 2015; Lever et al., 2015) and an average cellular mass of 7×10⁻¹⁷ kg (Bratbak & Dundas, 1984; Hoehler & Jorgensen, 2013). The column headed ‘Break’ describes which atmospheric species deviates from observed abundance first and whether it is higher or lower than the 2 σ detection. The greatest biomass estimate model runs are highlighted in bold.
 57

Table 4.1. Necessarily abbreviated list of typical landforms and their associated characteristic features used for identifying the origin of contacts that may be shorelines in the case of coastal features or may mimic shorelines in the case of other landforms. While by no means exhaustive, the table provides a useful overview..... 73

Table 5.1. List of putative paleoshoreline sites and available high-resolution data. Resolutions (Res.) are provided in $m\ px^{-1}$. Candidacy designations are based on our own assessment, see text..... 105

ACKNOWLEDGEMENTS

First and foremost, I need to thank my advisor David Catling who took me on as a grad student and trained me as a planetary scientist. It is because of David's expertise (seemingly on everything), patience, commitment, and kindness that I was able to complete this dissertation. I am extremely grateful and fortunate for all of his guidance and support over the years. I would also like to thank Dave Montgomery, Jon Toner, Kevin Zahnle, Charlotte Schreiber, Amit Mushkin, Eric Agol, Steven Walters, and Roger Buick who have all aided and contributed to my research both within and beyond this dissertation.

I would also like to thank Victoria Meadows, Bruce Nelson, Ken Creager, and No  ll Bernard-Kingsley who all provided me with the much-needed support and opportunities to complete this dissertation during the birth of my son and my time working remotely in Arizona. The allowed flexibility with my schedule allowed me to watch and connect with my son Julian growing up these past two years which has been one of the most wonderful experiences of my life.

I also need to give thanks to the many teachers and professors I have had over the years who have provided encouragement to pursue planetary science. Joe Veverka, Martha Haynes, and Peter Thomas at Cornell all helped support and motivate me into pursuing a graduate degree. Special thanks go to Carol Burch, who in high school fueled my passion for science, mentored me, opened up many new opportunities, and allowed me to discover science as a career.

Thanks to all my family and friends for all their support: my parents Mary and David for providing unconditional love and support through everything; my brother Jayson who was there for my grandparents while I was on the other side of the country; my mother-in-law Beatriz Coachman who helped watch my son while I worked; my brother-in-law Chris Mendes for his enthusiasm and helping me get through my most stressful times; my grandfather Stuart Sholes who was my personal hero in life; my cat Glacier; and my many friends who got me through this all, especially Elena Amador, Chloe Hart, Paul Kintner, Matt Koehler, Joshua Krissansen-Totton, Owen Lehmer, John Meluso, Jill Schleicher, Meg Smith, Julia Weed, and Sarah and Mark Welch.

Finally, I need to provide a million thanks to my wife Louise. I know it has been incredibly difficult and stressful journey through grad school but words are not enough to express how much gratitude I have for everything she has done. The future holds many more adventures and good times to come with our little family!

DEDICATION

To Louise and Julian

Chapter 1. INTRODUCTION

This introductory chapter provides a brief framework for the motivation behind this research along with an outline for the material presented within. The original research chapters of this dissertation (**Chapters 2-5**) have all been written as standalone articles for publication. As such, they all contain detailed introductions with some overlapping material. A concluding chapter provides a summary of the main results of the research with some remarks on further research being conducted that expands on the work presented here. **Chapter 2** (Sholes et al., 2017b), **3** (Sholes et al., 2019a), and **4** (Sholes et al., 2019b) have already been published as standalone peer-reviewed articles. **Chapter 5** will be submitted in June 2019 following additional edits and revisions. Overall, one of the primary goals of this dissertation is to provide new or improved quantitative assessments on the general habitability conditions of Mars both past and present.

1.1 MOTIVATION

One of the main driving motivations for Mars exploration and research is the search for past or present life and the characterization of any habitable environments that could support such life (MEPAG, 2018). The four principal components required to build such habitable environments are: 1) presence and persistence of a liquid solvent (e.g. liquid water), 2) suitable energy sources (e.g. redox gradients), 3) availability of biologically useful elements to form useful macromolecules (e.g. CHNOPS), and 4) necessary clement conditions to provide biochemical stability (e.g. temperature, pH, salinity, radiation) (NASA Astrobiology Strategy 2015). Understanding the processes that influence these metrics, their evolution and availability over time, and the preservation of evidence of these past environments is of great importance.

While liquid water is known to have flowed on the surface of Mars in the past, the timing, magnitude, and duration of such surface waters is unknown. Climate models have difficulty producing realistic atmospheres that can sustain sufficient temperatures for liquid surface water, yet geological evidence has suggested that lakes, seas, and possibly oceans may have once covered the planet. This has led to the debate as to whether Mars was “warm and wet” (e.g. Ramirez & Craddock, 2018) or “cold and icy” with only ephemeral periods of liquid water (e.g. Wordsworth

et al., 2013). Geologic evidence for oceans is ambiguous with many unanswered assumptions and seeming paradoxes in where the water originated, where the vast amount of liquid water went, and the state it was in if it did pool as an ocean (Head et al., 2018; Turbet & Forget, 2019). Thus, by better assessing the validity of evidence for oceans, improved constraints on the availability and longevity of such large amounts of liquid surface water might be obtainable.

Atmospheric models of Mars are often used to model climate effects in an attempt to produce temperatures that are consistent with the observed geological evidence. However, the evolution of the redox chemistry of the martian atmosphere is also of considerable interest. The redox chemistry dictates the availability of atmospheric free energy and the surface conditions as reducing and anoxic atmospheres are much more favorable to the building of prebiotic compounds compared with oxidizing atmospheres (like present-day Mars). Assessing the factors that influence the current and prior atmospheric redox state provides useful metrics on the habitability of the planet and offers estimates on the possible geochemical deposits that could potentially serve as proxies for past redox state.

1.2 DISSERTATION OUTLINE

Modeling the redox chemistry of the martian atmosphere is the subject of the first half of this dissertation. **Chapter 2** investigates the effects of volcanic activity on the habitability of past Mars. Widespread volcanism throughout Mars' history would have outgassed large amounts of reducing gases, such as CO and H₂, which would likely have generated reducing atmospheres. While early Mars' atmospheres are generally assumed to have been reducing (e.g. Kasting, 1997), the magnitude of volcanism required to create such atmospheres (assuming from a current atmospheric composition and structure) has not yet been addressed.

The current oxidizing state of the martian atmosphere is generally unfavorable for producing habitable environments, as the oxidation reactions can inhibit the building of more complex bioimportant molecules. On the other hand, reducing and anoxic conditions allow for prebiotic organic chemical compounds to be more efficiently produced. The famous Miller-Urey experiments showed that highly reducing atmospheres can synthesize organic molecules such as

amino acids and nucleobase precursors, while subsequent studies showed that even weakly reducing atmospheres can build such molecules (e.g. Miller, 1953). Thus, it is important to understand the requirements to produce such atmospheres on past Mars and their potential longevity. Here, we use a one-dimensional photochemical model to test the atmospheric response to different magnitudes and compositions of volcanic outgassing. This in turn allows for quantification of the magnitude of volcanism required to shift the redox state of the atmosphere into reducing conditions along with quantifying potential observables that future missions can measure (e.g. sulfur deposits) and use as a proxy for past redox climate.

Chapter 3 examines the redox state of Mars' present-day atmosphere and its potential for sustaining a hypothetical extant biomass. Krissansen-Totton et al. (2016) quantified the available free energy in Mars' current atmosphere, driven by redox gradients, to be $\sim 136 \text{ J mole}^{-1}$, which is the largest thermodynamic disequilibrium in the solar system outside of the Earth). This raises the question as to why life has not evolved on Mars to take advantage of this "free lunch." B. P. Weiss et al. (2000) examined this problem and attempted to constrain the maximum biomass that could be sustained off this atmospheric free energy, however their methodology is potentially flawed. This is because there are inherently unknown variables used in photochemical codes, and while plausible value ranges exist for these variables, they are tuned so the model can reproduce the observed atmospheric composition, i.e. one assumed to be abiotic.

The work presented here vastly improves upon the maximum biomass estimates of B. P. Weiss et al. (2000) by tuning these unknown variables with the assumption of a hypothetical metabolizing biosphere. By ramping up the metabolic fluxes into and out of the atmosphere at the surface (assuming any microbes require a liquid groundwater table) and optimizing the model parameters to match present-day atmospheric compositions, we can determine the maximum allowable metabolic fluxes. Using conservative estimates for cellular power requirements and efficiencies, this maximum flux can then be converted into a maximum allowable biomass in contact with the atmosphere (under the assumption that any such life on Mars would evolve the simple metabolisms to take advantage of this free energy). Atmospheric chemical disequilibrium is often discussed as a life-detection model for planetary atmospheres and our results here provide robust constraints on the size limits of an extant subsurface martian biosphere.

The second half of this dissertation examines the evidence for ancient oceans on Mars, specifically paleoshorelines. Vast differences in opinion exist on whether Mars ever had oceans, and evidence in support of such bodies of waters is ambiguous at best. Observations of putative paleoshorelines have been touted as the most compelling evidence for ancient oceans, but these are most often qualitative photogeological observations leading to starkly contrasting interpretations of the same features, e.g. Malin and Edgett (1999) versus Clifford and Parker (2001). This is especially true given the orders of magnitude improvements in image resolution of Mars over the past 30 years. **Chapter 4** lays a framework for quantitatively testing the validity of hypothesized paleoshorelines and applies this methodology to an exemplar site with features strongly suggestive of wave-cut terraces and strandlines. One of the greatest additions to this paleoshoreline-identification toolkit is the inclusion of a terrestrially-validated quantitative identifier of wave-cut platforms, what we have termed topographic expression analysis (TEA). This method examines changes in the topographic residual between the actual topography and that of an ideal slope. Combined with traditional photogeological studies, use of high-resolution digital elevation maps, and spectroscopic analyses, putative shoreline features can be assessed on their consistency or inconsistency with a coastal origin.

Finally, **Chapter 5** takes the toolkit for identifying paleoshorelines and applies it to hypothesized ocean shoreline sites across Mars. This fulfills a much-needed critical quantitative and high-resolution investigation on the consistency of putative paleoshoreline features with an oceanic origin. A total of 40 individual sites are cataloged and examined using the latest available high-resolution topographic and photographic data. Furthermore, the globally mapped contacts are scrutinized and errors in their spatial and topographic are quantified

Chapter 2. ANOXIC ATMOSPHERES ON MARS DRIVEN BY VOLCANISM

This chapter was originally published in the journal Icarus:

Sholes, S.F., M.L. Smith, M.C. Claire, K.J. Zahnle, and D.C. Catling. (2017). “Anoxic Atmospheres on Mars Driven by Volcanism: Implications for Past Environments and Life.” *Icarus* 290: pgs. 46-62. doi:10.1016/j.icarus.2017.02.022

2.1 ABSTRACT

Mars today has no active volcanism and its atmosphere is oxidizing, dominated by the photochemistry of CO₂ and H₂O. Mars experienced widespread volcanism in the past and volcanic emissions should have included reducing gases, such as H₂ and CO, as well as sulfur-bearing gases. Using a one-dimensional photochemical model, we consider whether plausible volcanic gas fluxes could have switched the redox-state of the past martian atmosphere to reducing conditions. In our model, the total quantity and proportions of volcanic gases depend on the water content, outgassing pressure, and oxygen fugacity of the source melt. We find that, with reasonable melt parameters, the past martian atmosphere (~3.5 Gyr to present) could have easily reached reducing and anoxic conditions with modest levels of volcanism, >0.14 km³ yr⁻¹, which are well within the range of estimates from thermal evolution models or photogeological studies. Counter-intuitively we also find that more reducing melts with lower oxygen fugacity require greater amounts of volcanism to switch a paleo-atmosphere from oxidizing to reducing. The reason is that sulfur is more stable in such melts and lower absolute fluxes of sulfur-bearing gases more than compensate for increases in the proportions of H₂ and CO. These results imply that ancient Mars should have experienced periods with anoxic and reducing atmospheres even through the mid-Amazonian whenever volcanic outgassing was sustained at sufficient levels. Reducing anoxic conditions are potentially conducive to the synthesis of prebiotic organic compounds, such as amino acids, and are therefore relevant to the possibility of life on Mars. Also, anoxic reducing conditions should have influenced the type of minerals that were formed on the surface or deposited from the atmosphere. We suggest looking for elemental polysulfur (S₈) as a signature of past reducing atmospheres. Finally, our models allow us to estimate the amount of volcanically sourced atmospheric sulfate deposited over

Mars' history, approximately $\sim 10^6$ - 10^9 Tmol, with a spread depending on assumed outgassing rate history and magmatic source conditions.

2.2 INTRODUCTION

The modern martian atmosphere is oxidizing but the atmosphere on past Mars could have had significantly different chemistry and may have even been anoxic when there was a large input of volcanic gases (Catling & Moore, 2003; Zahnle et al., 2008). Today, there is no detectable volcanic input (Krasnopolsky, 2005) and the photochemistry of the atmosphere is dominated by CO₂, H₂O, and their photochemical byproducts (Krasnopolsky & Lefevre, 2013; Mahaffy et al., 2013; Zahnle et al., 2008). However, extinct volcanoes and volcanic terrains indicate that Mars experienced widespread volcanism in the past (Carr & Head, 2010; Greeley & Spudis, 1981) which would have injected reducing gases into the atmosphere, in addition to CO₂ and H₂O. The reducing volcanic gases, such as CO and H₂, would have reacted with oxidants and may have switched the redox chemistry of the atmosphere from oxidizing to reducing, depending on their proportions relative to CO₂ and H₂O in outgassing.

Planetary atmospheres can be categorized into two meaningful chemical endmembers: reducing and oxidizing. Reducing atmospheres are those in which oxidation is limited or prohibited and therefore elements like carbon and sulfur are more likely to be found in their hydrogenated reduced forms (e.g. CH₄, H₂S) than their oxidized forms (e.g. CO₂, SO₂). Oxidizing atmospheres are the reverse. Highly reducing atmospheres can become anoxic with non-zero but negligible oxygen levels.

The possibility that Mars had anoxic and reducing conditions is of considerable interest, not only for understanding the evolution of planetary atmospheres, but also in the creation of habitable environments. Reducing and anoxic atmospheres are much more favorable to prebiotic chemistry than oxidizing ones (e.g. Urey, 1952). These conditions enable photochemistry to create prebiotic organics (e.g. amino acids), which have been discussed in the context of the origin of life on Earth (e.g. Kasting, 1993). Very hydrogen-rich atmospheres can also provide greenhouse warming on early Mars through collision-induced absorption (Batalha et al., 2015; Ramirez et al., 2014; Sagan, 1977).

Terrestrial volcanic gases are weakly reducing, composed dominantly of oxidized gases (CO_2 , H_2O , and SO_2), minor amounts of reducing gases (H_2 , H_2S , and CO), and traces of other gases (S_2 , HCl , HF , OCS , and SO) (Symonds et al., 1994), whereas volcanic gases on ancient Mars are of uncertain redox state but were almost certainly more sulfur-rich (Wänke & Dreibus, 1994). The magnitude and proportions of volcanic gases on Mars would have depended on the chemical state of martian magmas: the redox state, water content, and abundance of other species such as sulfur and carbon (Gaillard et al., 2013; Gaillard & Scaillet, 2009).

Mars is sulfur rich compared to Earth, with upwards of 3-4 times as much sulfur in Mars's mantle than in Earth's (Gaillard & Scaillet, 2009; Gendrin et al., 2005; McSween, 1994; Yen et al., 2005). This has led to Mars having an active sulfur cycle that would have affected the surface environment (King & McLennan, 2010). Sulfate deposits are abundant on Mars, and sulfate in soils or rocks has been found at the sites of the Viking landers (Toulmin et al., 1977), Mars Exploration Rovers (Squyres et al., 2004), Phoenix (Kounaves et al., 2010), and Mars Science Laboratory (Mahaffy et al., 2013). These sulfur deposits could originate from the weathering of sulfides in surficial basalts (Burns & Fisher, 1993; King & McSween, 2005) or from volcanic gases (Settle, 1979; M. L. Smith et al., 2014). Sulfate in some martian meteorites shows mass independent isotope fractionations of sulfur which, although modest in magnitude compared to what is seen from the Archean Earth, suggest cycling of sulfur gases through the atmosphere (Farquhar et al., 2007). It is likely that a considerable amount of sulfur on the surface of Mars originated in volcanic outgassing (primarily in the form of SO_2), which was then oxidized and hydrated in the atmosphere to form sulfate aerosols (H_2SO_4) (McGouldrick et al., 2011; Settle, 1979).

The role sulfur plays in the atmospheric chemistry of Mars has been studied mainly for how it might have affected the climate. Some past work suggested that sulfur in the form of SO_2 could have acted as a prominent greenhouse gas in the past (Halevy et al., 2007; S. S. Johnson et al., 2008; Johnson et al., 2009; Postawko & Kuhn, 1986). However, such studies neglected the effect of sulfate aerosols. Models that include sulfate aerosols find that the increased planetary albedo more than offsets the increased greenhouse effect, so that the net effect of adding SO_2 is to cool Mars's surface (Tian et al., 2010). This latter result is consistent with expectations based on

what we know of Earth and Venus: volcanic sulfur aerosols cool the Earth (Robock, 2000) and contribute to the very large albedo of Venus (Toon et al., 1982). Others have found that it is possible to construct sulfate aerosols of dust coated with sulfate that can warm Mars (Halevy & Head, 2014), but whether such particles existed is unknown. Additionally, this study did not account for horizontal heat transport (Wordsworth et al., 2015) or elemental sulfur aerosols which would also contribute to cooling (Tian et al., 2010).

Volcanic S-containing gases have a reducing effect when injected into an oxidizing atmosphere because sulfur is removed from the atmosphere in its most oxidized form as sulfate. These sulfur-bearing gas species provide a source material for the sulfate deposits on the surface and also a sink for oxidizing species in the atmosphere when sulfate aerosols form. In reducing atmospheres sulfur can also be removed as elemental sulfur (S_8), or as a sulfide, both of which are more reduced than SO_2 (Pavlov & Kasting, 2002; Zahnle et al., 2006). Combined with other reducing gases from volcanic input (e.g. H_2 or CO), large amounts of sulfur gases on ancient Mars may have created anoxic conditions in the atmosphere.

In this paper, we model the martian atmosphere using an updated one-dimensional photochemical code (Catling et al., 2010; M. L. Smith et al., 2014; Zahnle et al., 2008) to determine whether past martian atmospheres could have been anoxic given plausible mantle buffers and outgassing rates. We simulate increasing extrusive volcanic activity to determine where the model reaches the tipping point from an oxidizing atmosphere (where the redox state is governed by H-escape) to a neutral or reduced atmosphere (where the redox state is governed by volcanoes). We then discuss the implications of the modeled environments in the context of possible future observables. Finally, we describe the implications for habitability of Mars.

2.3 METHODS

To investigate the effects of volcanic gases on atmospheric chemistry, we use a one-dimensional photochemical model originally developed by Kasting (1979) for the early Earth. The code has since been modified and validated with the known bulk composition of the modern martian atmosphere (Franz et al., 2015). It has been applied to past martian atmospheres with oxygen, carbon, and hydrogen (O-C-H) chemistry (Zahnle et al., 2008). Sulfur, chlorine, and

nitrogen chemistry were applied and validated against observations in a version of the code used for the modern Earth (Catling et al., 2010). Here we use a combined version that contains sulfur, oxygen, carbon, hydrogen, and nitrogen (C-H-O-N-S) chemistry developed for Mars, following M. L. Smith et al. (2014). We present a table of S reactions, which were omitted from the aforementioned studies, in Appendix A. This list has been updated to include 25 reactions to be consistent with other photochemical models (Domagal-Goldman et al., 2011; Zahnle et al., 2016). While chlorine is an important minor volcanic gas, and is outgassed in small amounts primarily as HCl on Earth, we chose to use a version of the model without chlorine species primarily because of their very minor role in overall atmospheric redox for modern Mars (M. L. Smith et al., 2014).

In our model, volcanic gases are assumed to flux into background atmospheric conditions similar to modern Mars so that we could assess the shift from a modern atmosphere to ancient atmospheres that may have occurred since the early Amazonian/late Hesperian boundary when Mars was volcanically active but the atmosphere was probably thin (Catling, 2009). Given the uncertainties in the chronostratigraphic epochs, we extend our model only to the past 3.5 Gyr, which is the earliest estimate for the start of the Amazonian (Hartmann, 2005; Werner & Tanaka, 2011).

CO₂ and H₂O vapor, while important volcanic gases on Earth, are held at constant mixing ratios for Mars (H₂O vapor is only held constant in the daytime convective zone). This is done primarily for ease and these gases are assumed to be replenished by and deposited into large surface and subsurface reservoirs. Atmospheric pressure is set to approximately present day levels of 6.5 mbar. The temperature profile follows Zahnle et al. (2008) with surface temperature, T₀, set to 211 K, which is close to a modern global mean value.

We impose a surface sink on all but the most abundant gas species in the form of a deposition velocity at the lower boundary layer. Unless otherwise stated, we follow Zahnle et al. (2008) and assign all chemically active species a deposition velocity (v_{dep}) of 0.02 cm s⁻¹ except for O₂ and H₂, which are given a $v_{\text{dep}}=0$. Unlike previous models, we also assume v_{dep} of OCS is 0 (see Appendix A). CO deposition is more complex. There is no known abiotic dry surface sink of CO, therefore $v_{\text{dep,CO}}$ has historically been set to 0. Modeled atmospheres with high-outgassing

rates of CO can readily reach instability via the well-known ‘CO-runaway’ effect (e.g. Zahnle et al., 2008), where the atmospheres are unstable against perturbations. A small deposition velocity on CO of $\sim 1 \times 10^{-8} \text{ cm s}^{-1}$ can be assumed if there were large bodies of water on the surface where hydration of dissolved CO forms formate and eventually acetate (Kharecha et al., 2005); and could be as high as $\sim 4 \times 10^{-6} \text{ cm s}^{-1}$ if CO reacts directly with dissolved O₂ (Harman et al., 2015). However, aqueous reactions may only apply during the Noachian-Hesperian when Mars may have experienced long lasting or episodic standing bodies of water, perhaps even as oceans (e.g. Parker et al., 1993). Because we are primarily looking at the Amazonian, we cannot assume large bodies of water. Instead, we consider the fact that the chemistry associated with continual hypervelocity impacts would remove CO.

Impacts have occurred throughout Mars’ history and have affected the atmospheric chemistry. We employ a depositional velocity on CO resulting from the catalytic conversion of CO to methane (CH₄) during hypervelocity impact blasts and one that does not require liquid water at the surface. M. E. Kress and McKay (2004) and Sekine et al. (2003) have argued that during large impact blasts from comets and high-iron content meteorites Fischer-Tropsch catalysis reactions provide a sink on atmospheric CO (H₂ can be supplied from dissociated impactor or surficial water). From cratering rates, impactor size distributions, and average impact compositions we estimate the average conversion rate of CO to CH₄, which is a sink on CO that can be expressed as a surface deposition velocity and associated stoichiometric release of CH₄. Appendix A contains details of our estimations for the deposition velocity of CO and flux of CH₄. From this, a suitable fixed v_{dep} is of order $10^{-7} \text{ cm s}^{-1}$ for CO, for high-outgassing regimes on Mars.

We implement a corresponding small input flux of CH₄, of $\sim 1 \times 10^7 \text{ molecules cm}^{-2} \text{ s}^{-1}$, from the Fisher-Tropsch reactions in hypervelocity impacts, which represents a maximum flux under a 1:1 conversion ratio from CO (Appendix A). However, even with this surface flux, p_{CH_4} is <3 ppb in all model runs. No volcanic source of methane is imposed, as under the assumed high-temperature volcanic regime CH₄ volcanic fluxes are negligible for all redox states, as in known from measurements from terrestrial volcanoes (Ryan et al., 2006).

The resulting model provides a fit to the modern martian abundances of the important redox-sensitive gases comparable to previous versions. The model is truncated at an altitude of 110 km, with ionospheric chemistry simplified to a downward flux of NO at a rate of 2×10^7 molecules $\text{cm}^{-2} \text{s}^{-1}$ and an equal flux of CO to preserve redox balance; atomic N also fluxes down at 2×10^6 molecules $\text{cm}^{-2} \text{s}^{-1}$. We allow hydrogen to escape out through the top of the model at the diffusion-limited rate (M. L. Smith et al., 2014; Zahnle et al., 2008).

The model allows for the formation of two sulfur aerosols which are able to precipitate and act as additional sinks on sulfur: elemental polysulfur, S_8 , and sulfate, H_2SO_4 . Fig. 2.1 is a diagram showing the predominant sulfur photochemistry and pathways. Sulfate aerosols form through the oxidation of the major volcanic gas SO_2 into SO_3 and the subsequent hydration into H_2SO_4 primarily through the following reactions:



In reducing atmospheres, S_8 forms. Sulfur polymerizes into long chains when disulfur (S_2), trisulfur (S_3), and tetrasulfur (S_4) react together, until S_8 is reached. The S_8 allotrope forms a molecular “ring” structure which is conducive to coagulation into aerosol particles. This reaction pathway is unfavorable in oxidizing atmospheres as any S_2 is more readily oxidized into SO and then further oxidized into SO_2 and H_2SO_4 . Additional sources of sulfur for aerosol formation, both S_8 and H_2SO_4 , come from the chemical reaction products involving the oxidation of volcanic H_2S gas.

Our flux of volcanic gases is scaled according to various estimates of past volcanic outgassing on Mars. Based on photogeologic data, the total magma production for Mars has been estimated as $6.54 \times 10^8 \text{ km}^3$, equivalent to an average of $0.17 \text{ km}^3 \text{ yr}^{-1}$ over the past 3.8 Ga (Greeley & Schneid, 1991). For comparison, the Earth’s magma flux is estimated to be around $26\text{-}34 \text{ km}^3 \text{ yr}^{-1}$ (Greeley & Schneid, 1991). More refined estimates for crustal production rates over time can be inferred using thermal evolution models (e.g. Breuer & Spohn, 2006; Schubert et al., 1992;

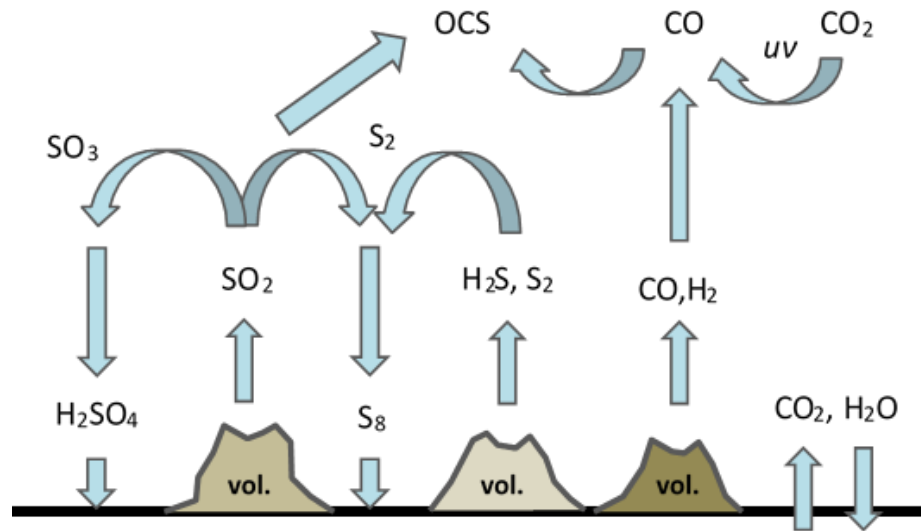


Figure 2.1. Schematic diagram showing the dominant sulfur photochemistry and pathways during volcanically-active Mars, ‘vol.’ indicates a volcano. Based on likely magma chemistry (see text) the most important volcanic sulfur gas is generally SO₂. Atmospheric oxidation reactions turn SO₂, H₂S, and S₂ into sulfuric acid aerosols, while photochemistry in reducing atmospheres also makes polysulfur aerosols (S₈). Additionally, there is direct deposition of SO₂ to the surface as another sink on S. H₂O and CO₂ concentrations are assumed to be buffered by large subsurface and surface reservoirs. Carbonyl sulfide (OCS) is able to build up through reactions with sulfur-bearing compounds and CO.

Xiao et al., 2012) as shown in Fig. 2.2. The rates range from $\sim 0\text{-}4 \text{ km}^3 \text{ yr}^{-1}$ since the Late Hesperian/Early Amazonian (3.5 Ga). Extrusive volcanic rates modeled by Breuer and Spohn (2006) and Xiao et al. (2012) typically have a peak in the mid-Hesperian to early Amazonian depending on the initial mantle temperature (1,800-2,000 K), while those modeled by Schubert et al. (1992) show a rapid decline of volcanism with a dependence on a crustal fractionation parameter. The crustal fractionation parameter, χ , used in those calculations is effectively a measure of the efficiency of magma generation in the crust (defined as the ratios of the characteristic mantle convection turnover time and the crustal fractionation time). We test the maximum crustal production rate model of Schubert et al. (1992) ($\chi=10^{-3}$) to provide an upper limit on their model over the past 3.5 Gyr. Over this time span, their lower rate model is essentially zero which is unlikely given observations. Many of these models show no volcanism in the past 1 Gyr, but volcanism is known to have occurred sporadically within the past 100 Ma on Mars

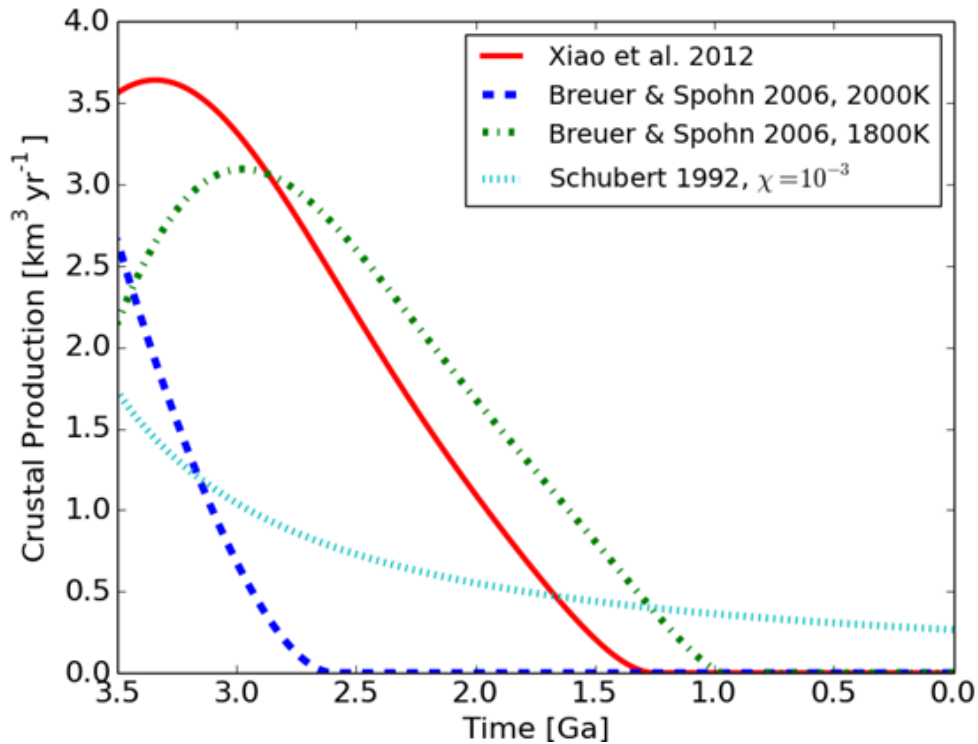


Figure 2.2. Estimates of crustal production rates for Mars through time from various authors. Some models suggest that most volcanism should have occurred between the early Noachian and the early Amazonian. In the Breuer & Spohn model, different initial mantle temperatures give rise to different time histories. Schubert’s model varies χ , a crustal fractionation parameter (see text).

(Werner, 2009). However, these models provide good estimates on average continuous volcanism over time rather than specifically accounting for intermittent periods of volcanism.

The flux of reducing gases depends on the volcanic source region. We cannot in a 1D model simultaneously impose a lower boundary condition that is both a sink (deposition velocity) and a source (a volcanic flux). Thus, as done in previous iterations of the model, we inject the volcanic gases directly into the atmosphere. The volcanic gases are distributed log-normally through the lower 20 km of the atmosphere (M. L. Smith et al., 2014; Zahnle et al., 2006; Zahnle et al., 2008). The ground-level mixing ratios are insensitive to the vertical distribution of the injected volcanic gases.

The composition of volcanic gases depends on the magmas that produce them, and thus varies according to the oxygen fugacity (fO_2), pressure at outgassing, and water content of the mantle. Gaillard et al. (2013) modeled martian magmas, varying the aforementioned parameters, to estimate volcanic gas compositions given in ppm wt%. These authors assume a melt temperature of 1300 °C, magmatic S content at 3500 ppm, and nominally 0.08 wt% CO₂ (0.02 wt% CO₂ for the most reduced mantles, i.e. IW). We calculate the outgassing rate of species A (mol_A) in moles s⁻¹ according to:

$$mol_A = \frac{s_A k_{dg} V \rho}{w_A} \quad 2.4$$

Here, s_A is the weight fraction of species A given by Gaillard et al. (2013), k_{dg} is the fraction of the species outgassed (here it is unity following Gaillard et al. (2013)), V is the volumetric rate of lava being extruded in km³ yr⁻¹, ρ is the density of the lava (assumed to be basalt of 2.9 g cm⁻³ after Wignall (2001)), and w_A is the molecular weight of species A (Leavitt, 1982). The fluxes for each species are converted into photochemical model units of molecules cm⁻² s⁻¹ and we vary V to simulate greater amounts of volcanism over time. We present the outgassing rates and ratios in Appendix A for the range of martian magma parameters.

The redox state and water content of martian magmas are uncertain. Consequently, we use the emitted volcanic volatile amounts over a range of fO_2 and water content from the outgassing model of Gaillard et al. (2013) to simulate the fluxes of volcanic species of erupted magmas. The redox state of the melt is defined by its fO_2 , which is represented by mantle mineral buffers. The fayalite-magnetite-quartz (FMQ) buffer is defined with an $fO_2=10^{-8.5}$ and is less reduced than the iron-wüstite (IW) buffer with $fO_2=10^{-11.9} \cong \text{FMQ-3.5}$. Estimates from martian meteorites suggest that the martian mantle has an fO_2 of FMQ-1 to FMQ-3 (Herd et al., 2002); to test this range, three buffers were used: FMQ-0.5, FMQ-1.4, and IW. Water content of the magmas is varied between dry melts with 0.01 wt% H₂O and wet melts with 0.4 wt% H₂O. The highest estimate of water content for Mars is an upper limit of 1.8 wt% from martian basaltic meteorites (McSween et al., 2001), but this may represent the effect of cumulate processes (e.g. assimilation of drier crustal material) and not the composition of the melt (Gaillard et al., 2013), and so is broadly consistent with our upper value of 0.4 wt% H₂O. However, others have argued for a drier mantle (Wänke & Dreibus, 1994), consistent with our lower value. The pressure at outgassing is varied between 0.01

bar and 1 bar. We vary the volumetric rate of lava from 0.001 to 1 km³ yr⁻¹ to simulate ranges around the time-average of 0.17 km³ yr⁻¹ over the past 3.5 Ga.

As a first-order test, we only examine the necessary conditions required to switch the current martian atmosphere into an anoxic reducing regime. We assume that the gases are being emitted at depth and the outgassing pressure represents the lithostatic pressure of the melt rather than the atmospheric surface pressure. This implementation gives a good representation of how much volcanism it takes to reach anoxic and reducing conditions. As a sensitivity test, we ran the model with atmospheric pressure matching the outgassing pressure and used the corresponding temperature profile as modeled by Ramirez et al. (2014). However, with greater temperatures the absolute humidity increases, as expected from the results of Zahnle et al. (2008), and the atmosphere is overall reducing even with no volcanic activity because much CO is produced. An additional sensitivity test was done to include the outgassing of H₂O based on the Gaillard et al. (2013) values. However, we found that no significant changes occurred.

In our photochemical model, we quantify the redox state due to the influx of volcanic gases as follows. We define the net redox balance (pOx) of the atmosphere as (Zahnle et al., 2008)

$$pOx \approx 2pO_2 - pCO - pH_2 \quad 2.5$$

where pO_2 , pCO , and pH_2 are the partial pressure of oxygen, carbon monoxide, and hydrogen respectively. Eqn. 2.5 is an approximation based on the dominant oxidants and reductants in the atmosphere. This equation can be expanded to include all non-redox neutral species, but only the three terms shown dominate. Even when OCS (carbonyl sulfide) concentrations reach ppm levels in anoxic atmospheres, pCO dominates. Modern Mars has an oxidizing atmosphere with a net redox state of $pOx \approx 15 \mu\text{bar}$, which is an imbalance caused by photodissociation of water vapor and subsequent rapid escape of hydrogen to space that leaves oxygen behind. As the atmosphere switches to a reducing regime, the redox state given by pOx will shift through zero and then become negative. Once pOx is negative, the atmospheric redox becomes dominated by the reducing gases CO and H₂, while O₂ becomes a trace gas. Thus, $pOx=0$ defines a tipping point.

2.4 RESULTS

We find that relatively small to moderate amounts of volcanic outgassing would have dramatically modified the past chemical composition and redox state of the martian atmosphere. Fig. 3 shows how modeled martian atmospheres respond to increasing amounts of volcanic outgassing with varying mantle parameters including redox state, water content, and pressure of outgassing. At low levels of volcanic magma flux (typically $<10^{-3} \text{ km}^3 \text{ yr}^{-1}$), the model atmosphere is largely unaffected, and remains oxidizing and similar to modern-day Mars. As the magma flux is ramped up, larger amounts of reducing gases flux into the atmosphere and the available free atmospheric oxygen declines as reactions produce oxidized species (e.g. CO_2 , H_2O , SO_2).

In our simulations, reducing gases can reach abundances on the order of a few percent under plausible volcanic outgassing levels. The abundance of hydrogen, and the escape of hydrogen to space, also increases as volcanic input is ramped up. In particular, carbon monoxide (CO) builds up to become a bulk constituent with a volume mixing ratio of $\sim 10\%$ or more. The main sink on CO is the hydroxyl radical, OH , which on Mars is derived from H_2O photolysis. These simulations assume a background atmosphere that is cold and dry, similar to the modern one, so CO does not have much of an OH sink and thus the volcanic gases build up, contributing to a highly reduced atmosphere. In a reduced state, there is negligible free oxygen and the atmosphere is anoxic.

Figures 2.3a-d show the effects of varying each melt parameter. Decreasing fO_2 of the magma, or decreasing the magma's water content, have the counter-intuitive effect of making it more difficult to reach reducing anoxic conditions (requiring greater amounts of volcanic magma fluxes) because more sulfur stays in the melt, as discussed below. Increases in the pressure of outgassing have a similar effect. Thus wet and more oxic melts at lower pressures allow the atmosphere to reach anoxia under lower volcanic fluxes than their reducing, dry, high-pressured counterparts.

The model also predicts that sulfur gases, such as SO_2 and the reduced form SO , would be likely to react directly with the surface, as the depositional fluxes of these gases build up to relatively high levels. As the atmospheres become anoxic, a shift occurs as more moles of S exit

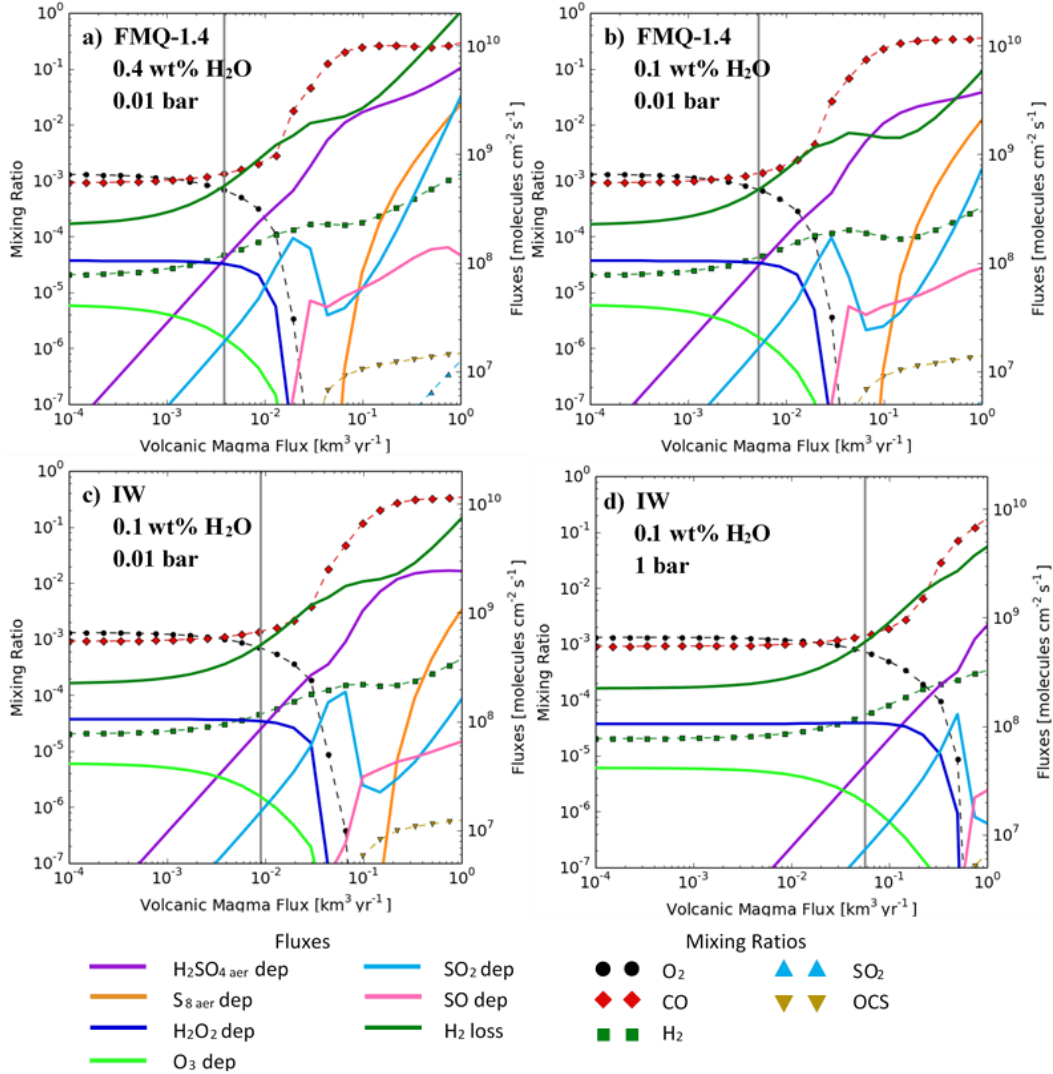


Figure 2.3. Atmospheric response to steady-state volcanic outgassing from typical martian magmatic buffers. Symbols display the mixing ratios (mapped to left axes) and solid lines display species and aerosol (aer) surface deposition (dep) fluxes and atmospheric loss for H_2 (mapped to right axes). We used magma buffers to illustrate how a state of anoxia depends on the total amount of volcanic magma flux for each buffer. A vertical gray line shows the transition point between oxidizing and reducing conditions as dictated by Eqn. 2.5. Plots *a* through *d* show the cumulative effects of changing each melt parameter; *b* is a drier melt, *c* is more reduced, and *d* is outgassed under higher pressures. Melts that are drier, more reduced, and under greater pressure take the greatest amount of volcanism to reach reducing conditions ($\sim 4 \times 10^{-3} \text{ km}^3 \text{ yr}^{-1}$ for *a* versus $\sim 6 \times 10^{-2} \text{ km}^3 \text{ yr}^{-1}$ for *d*).

the atmosphere as elemental polysulfur than as sulfate. As this happens, a small ramp up in the sulfate production limits available sulfur and decreases in SO₂ and SO deposition occur around or below a volcanic magma flux rate of ~0.1 km³ yr⁻¹ (Fig. 3a-c). In reducing atmospheres with high volcanic outgassing, SO₂ and OCS are able to build up levels approaching ~1 ppm.

We can quantify the shift to anoxic, reducing conditions using Eqn. 2.5. Reducing conditions occur when the pOx shifts from positive (oxidizing) to negative (reducing) values. The pOx can shift from modern-day values of ~15 μbar to less than -700 μbar in anoxic atmospheres (e.g. > 3×10⁻² km³ yr⁻¹ in Fig. 2.3a) primarily because of increased CO and lack of O₂ in the atmosphere. Regardless of the magma buffer used, all simulated atmospheres reached an anoxic reducing state within the modeled magmatic flux parameter space for magma production rates >0.14 km³ yr⁻¹.

Vertical mixing ratio profiles for various model atmospheres are plotted in Fig. 2.4. Even in highly reducing atmospheric conditions, the O₂ mixing ratio remains fairly large (~10 ppm) above the tropopause. The lower atmosphere is anoxic and reducing, while the upper atmosphere is less reducing, similar to models of a reducing atmosphere on the early Earth (Claire et al., 2014).

The chemistry of anoxic tropospheres produces elemental polysulfur, S₈, and sulfate, H₂SO₄ aerosols (see fluxes in Fig. 2.3). Sulfate aerosols readily form with even low volcanic fluxes and increase monotonically with volcanic flux. S₈ particles are only produced in large quantities once anoxic conditions are reached and elemental sulfur gases are no longer preferentially oxidized into sulfuric acid (see Fig. 2.1). Free elemental sulfur gases are also able to react with the abundant CO to form carbonyl sulfide (OCS), through the dominant net reactions:



This allows OCS to build up to the ppm level in reducing martian atmospheres.

It is instructive to integrate the deposition of sulfate over time for different volcanic outgassing histories because we can compare the integrated sulfate with estimates of the total sulfate inventory in martian soil and in light-toned layered deposits on Mars. The deposition rates of sulfate aerosols produced over Mars' history in model runs is shown in Fig. 2.5a, corresponding to the different crustal production rate models shown earlier in Fig. 2. Rates of SO₂, S₈, and H₂S

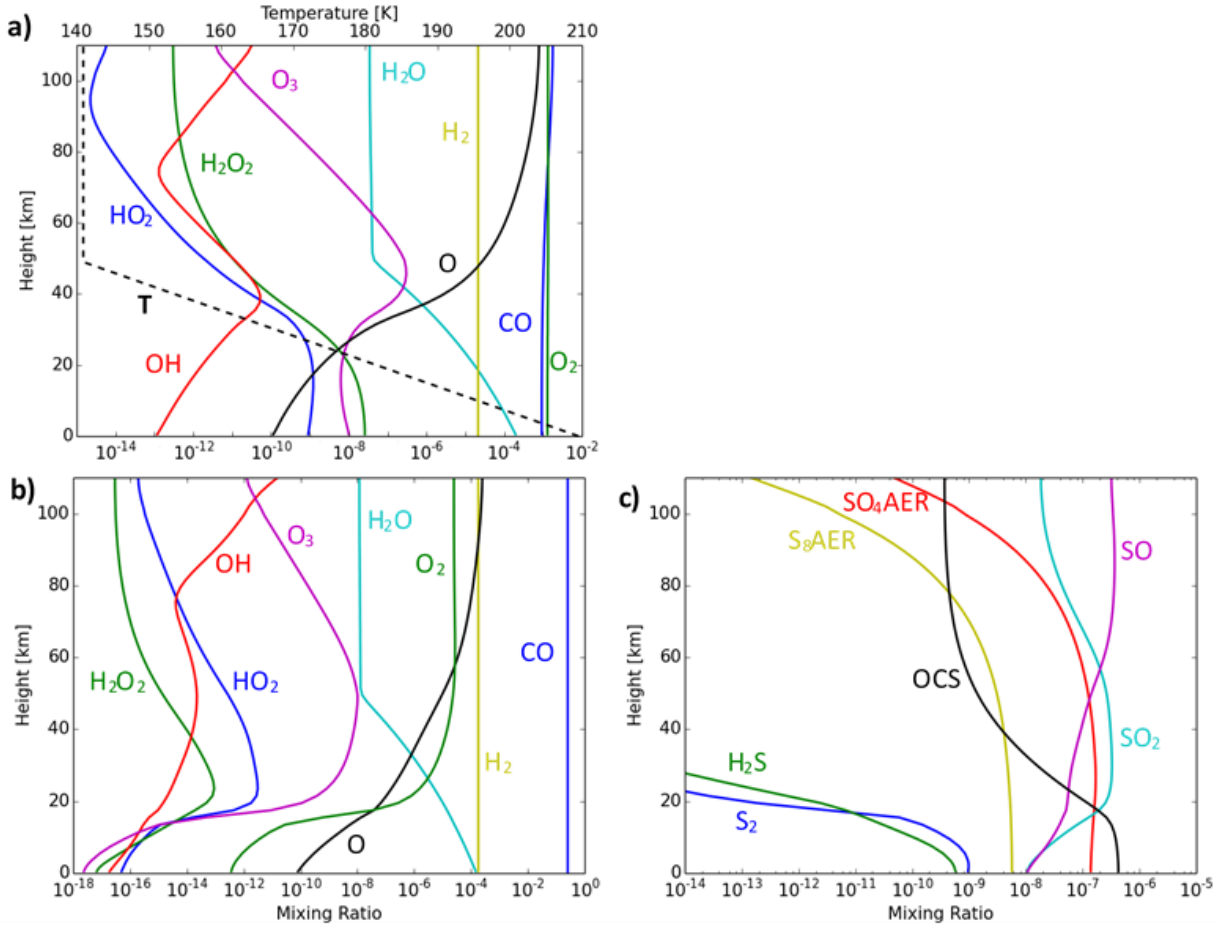


Figure 2.4. Vertical mixing ratio profiles for modern and anoxic Mars. Temperature (T) is plotted as a dashed line. (a) C-O-H species for modeled modern Mars, (b) C-O-H species for anoxic Mars for the case of mantle buffer with FMQ-1.4, 0.4 wt% H₂O at 0.01 bar and magma flux of 0.15 km³ yr⁻¹ which is a good representation of typical modeled reducing and anoxic conditions (See Fig. 2.3a), (c) S species for anoxic Mars under the same conditions as *b*.

deposition are also shown in Fig. 2.5. Deposition rates for SO and S₂ molecules are minor and always less than 0.02 Tmol yr⁻¹ (teramoles = 10¹² moles). Sulfate depositional fluxes were integrated over the entirety of the volcanic history for both an oxidizing wet magma buffer (FMQ-0.5, 0.4 wt% H₂O, 0.01 bar) and a reducing dry magma buffer (IW, 0.01 wt% H₂O, 1 bar) to cover the range of how much sulfate can be produced. These total integrated amounts of sulfate and elemental polysulfur deposition over the past 3.5 Gyr are given in Table 2.1. For most volcanic models, the total amount of sulfate ranges from ~5×10⁹ Tmol for sulfur-producing mantles and

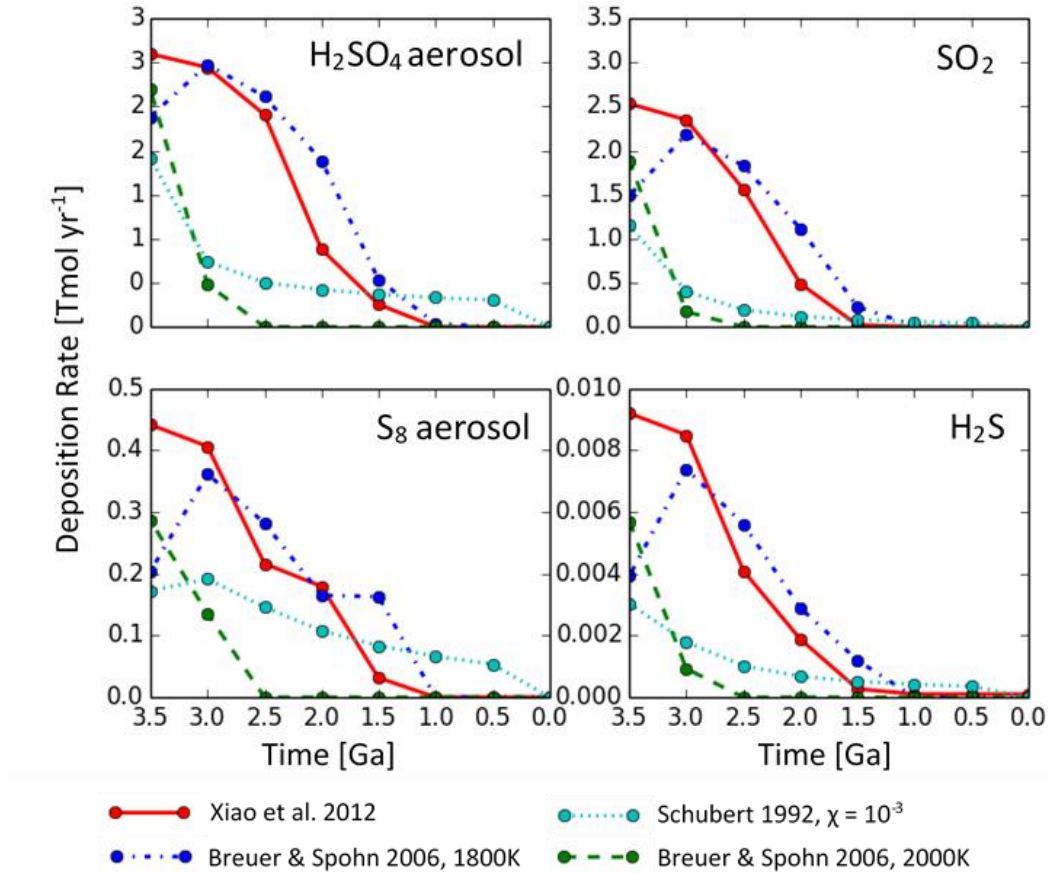


Figure 2.5. Deposition rates based on varying crustal production models (see Fig. 2.2, χ is a crustal fractionation parameter – see text). Total amounts of sulfate deposited are given in Table 2.1. Deposition rates for SO and S₂ are always less than 0.02 Tmol yr⁻¹.

high volcanism to $\sim 2 \times 10^6$ Tmol for sulfur-retaining mantles and low total volcanism. For comparison, estimates of the total amount of sulfur in the sulfate sedimentary rock reserves on Mars is of order 10^6 Tmol (Catling, 2014; Michalski & Niles, 2012).

In low volcanism models with reduced dry melts, there is no S₈ deposition but in high total volcanism models with oxidized wet melts total S₈ deposition ranges up to $\sim 5 \times 10^8$ Tmol of S₈. The difference is discussed below. Additionally, because volcanic activity is not continuous, the majority of the sulfur aerosol production and precipitation will occur during discrete highly volcanic epochs. There will be a bias for S to exit as S₈ during the intense episodes of volcanism compared to the average conditions modeled here.

Table 2.1. Modeled approximate total amounts of sulfate deposited over the 3.5-0 Gyr volcanic history of Mars for different crustal production rates and mantle buffers of oxygen fugacity: FMQ-0.5 (Fayalite-Magnetite-Quartz; with 0.4 wt% H₂O and 0.01 bar outgassing pressure) and IW (Iron-Wüstite; with 0.01 wt% H₂O and 1 bar outgassing pressure). S content of the magma is 3500 ppm. The total amount of each sulfur aerosol deposition is given in teramoles (10¹² mol). In Schubert's models, χ is an assumed crustal fractionation parameter (see text).

Reference for Crustal Production Model	Key Crustal Production Model Parameter	Sulfate Dep. FMQ-0.5 (Tmol)	Sulfate Dep. IW (Tmol)	S ₈ Dep. FMQ-0.5 (Tmol)	S ₈ Dep. IW (Tmol)
Xiao et al. (2012)	Initial mantle temp. = 1900 K	4.0×10 ⁹	9.8×10 ⁶	5.2×10 ⁸	2.3×10 ⁻⁸
Breuer and Spohn (2006)	Initial mantle temp. = 1800K	4.6×10 ⁹	1.1×10 ⁷	5.3×10 ⁸	1.4×10 ⁻⁸
Breuer and Spohn (2006)	Initial mantle temp. = 2000 K with primordial crust	9.1×10 ⁸	2.3×10 ⁶	1.4×10 ⁸	2.1×10 ⁻⁹
Schubert et al. (1992)	$\chi = 10^{-3}$	1.7×10 ⁹	4.7×10 ⁶	3.5×10 ⁸	negligible

2.5 DISCUSSION

2.5.1 *Consequences of Volcanism*

The range of mantle buffers from Gaillard et al. (2013) (depending on magma water content, pressure of outgassing, and oxygen fugacity (fO_2)) all predict volcanic outgassing where the redox state of the atmosphere switches from oxidizing to reducing for crustal production rates $> 0.14 \text{ km}^3 \text{ yr}^{-1}$. Such rates of volcanic activity are relatively low compared to typical estimates for past Mars (Fig. 2.2). Water content and mantle fO_2 have the greatest impact on the amount of volcanic flux needed for an anoxic atmosphere. As mentioned earlier, we obtain the counterintuitive result that the more reducing conditions of the IW melts require greater total volcanic flux to produce a reducing atmosphere. These effects are predominantly at higher outgassing pressures and in drier melts. While the volcanic emissions from reducing magmas are composed of a higher percentage of reducing gases than the more oxic buffers, they can require up to an order of magnitude greater amount of volcanic production to reach the redox switch. This

is because sulfur is more stable in the melt at lower fO_2 (Fincham & Richardson, 1954; O'Neill & Mavrogenes, 2002). The following equilibrium controls sulfur in the melt:



Following Le Châtelier's Principle, decreasing fO_2 (on the right side of Eqn. 2.8) causes an increase in melt sulfide while simultaneously decreasing the emitted sulfur dioxide. Higher pressures act to make the sulfur more siderophile (iron-loving) in the melt, thus the sulfur prefers to be in the form of metal sulfides than as a gas (Li & Agee, 1996). The effect of high water content on outgassed sulfur is predominantly the result of dilution effects – the gas-phase species are dominated by water and thus yield relatively sulfur-poor gases (Gaillard & Scaillet, 2009), given the fixed outgassing pressure. Dry melts retain more sulfur in the melt, caused by partitioning the sulfur in the melt, but produce more sulfur-rich gases. With less sulfur outgassed in the low fO_2 regimes, a major sink for atmospheric oxygen is lost. In sulfur-rich systems, outgassed sulfur readily reacts with oxidizing species, first forming intermediate products, e.g. SO_3 , and eventually forming sulfate aerosols (H_2SO_4). The sulfate falls out of the atmosphere.

Over a large parameter space, only moderate amounts of volcanism are required to switch the atmosphere's redox state from oxidizing to reducing. Given plausible fO_2 and water-content constraints on martian melts, magmatism on the order of $0.01\text{-}0.14 \text{ km}^3 \text{ yr}^{-1}$ (Fig. 2.6) is enough to eliminate free oxygen from a past martian atmosphere that is similar to today's. These values are well within the range of estimated volcanic activity on Mars in the past. Photogeological studies estimate an average magma extrusion rate of $0.17 \text{ km}^3 \text{ yr}^{-1}$ over the past 3.8 Gyr, and crustal production models estimate the rate to be between $0\text{-}4 \text{ km}^3 \text{ yr}^{-1}$ over the past 3.5 Gyr (Fig. 2.2). Given that the moderate amount of volcanism required is well within estimated values from the Late Hesperian to Middle Amazonian, our results suggest that the past martian atmosphere should have had episodes of mildly to strongly reducing atmospheres throughout most of Mars' early Amazonian history, $\sim 3.5\text{-}1.0 \text{ Ga}$. However, volcanic eruptions are well known for being episodic, so activity was not continuous. Consequently, the atmosphere should have had periods of oxidizing atmospheres during volcanic quiescence, and today's atmosphere is such a state.

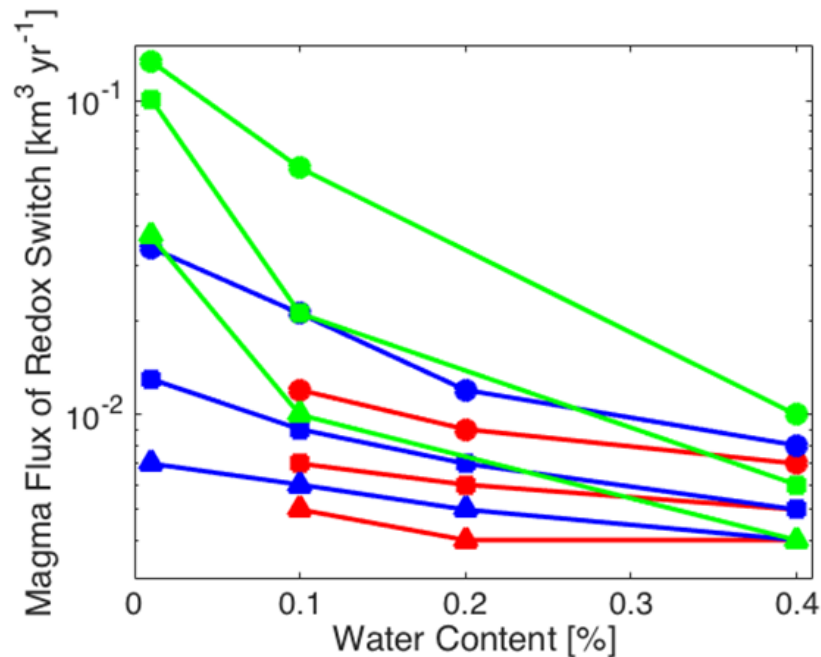


Figure 2.6. Plot showing crustal production flux (in $\text{km}^3 \text{yr}^{-1}$) (associated with volcanic outgassing) needed to reach a reducing atmosphere ($p\text{Ox} < 0$) as a function of magma water content (along x-axis), outgassing pressure (color), and redox state of the magma (symbols).

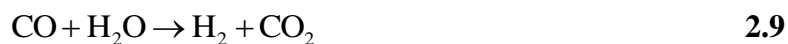
Drier, more reducing magmas take the greatest amount of volcanic activity to switch the redox of the martian atmosphere.

2.5.2 Implications for Habitability

The origin of life requires the presence of prebiotic organic chemical compounds, which are most efficiently produced in reducing conditions (Orgel, 1998). Highly reducing atmospheres, such as those with high concentrations of CH_4 or ammonia (NH_3), can synthesize organic molecules, such as amino acids (Miller, 1953, 1955) or precursors of nucleobases (i.e. hydrogen cyanide (HCN) for purines and cyanoacetylene and urea for pyrimidines) (Miller, 1986). Even weakly reducing atmospheres can build such compounds (Abelson, 1966; Pinto et al., 1980; Tian et al., 2005; Zahnle, 1986). The high abundance of OCS in anoxic atmospheres could also have polymerized accumulated amino acids to form peptides (A. P. Johnson et al., 2008; Leman et al., 2004).

The most reducing of our model atmospheres are CO-dominated, and these are well documented to efficiently produce organic prebiotic compounds via the photolysis of H₂O and CO. Carbon monoxide can also be used directly as a substrate for prebiotic chemistry (Huber & Wächtershäuser, 1998). Acetic and formic acids, along with a variety of alcohols, aldehydes, and acetone can easily be built in these atmospheres with relatively high quantum yields (Bar-Nun & Chang, 1983; Bar-Nun & Hartman, 1978; Hubbard et al., 1973; Miyakawa et al., 2002). All of our modeled atmospheres eventually became weakly to highly reducing with realistic amounts of volcanism. Consequently, past, volcanically active Mars may have been more suitable to the genesis of prebiotic chemistry.

Abundant CO in the atmosphere also provides a source of free energy for potential life to utilize. A dominant pathway for CO metabolisms is as follows:



This pathway occurs in organisms on Earth and is an efficient way of extracting energy from the atmosphere if liquid water is present (Kharecha et al., 2005; Ragsdale, 2004).

Abundant CO also enables significant quantities of OCS to form. OCS is a greenhouse gas which has been hypothesized in warming scenarios for the early Earth (Byrne & Goldblatt, 2014; Ueno et al., 2009), but the lack of CO combined with more vigorous photolysis by the young Sun prevents OCS concentrations from growing large in plausible early Earth scenarios (Domagal-Goldman et al., 2011). The primary sink of OCS is in sulfate aerosols, so it is likely to have a similar net radiative effect as SO₂, where cooling from aerosols is important. On the modern Earth, the negative forcing from stratospheric sulfate aerosols derived from OCS photochemistry approximately cancels the positive radiate forcing from OCS acting as a greenhouse gas (Brühl et al., 2012).

2.5.3 *Potentially Observable Consequences of Anoxia*

Given past volcanic activity and expected reducing anoxic conditions, there should be geologic features associated with such atmospheric conditions, particularly the deposition of sulfur to the surface. The most obvious observable is the large amount of sulfur-bearing aerosols deposited directly on the surface as both H₂SO₄ and S₈ during high volcanism. Sulfate minerals

have readily been observed both *in situ* and remotely largely in the form of jarosite ($\text{KFe}^{3+}(\text{SO}_4)_2(\text{OH})_6$), kieserite ($\text{MgSO}_4 \cdot \text{H}_2\text{O}$), and gypsum ($\text{CaSO}_4 \cdot 2\text{H}_2\text{O}$) (Murchie et al., 2009; Squyres et al., 2004). Elemental polysulfur has yet to be discovered in any martian rocks. Possibly, S_8 is subject to post-depositional oxidation or burial. *In situ* detection from landers would need to account for S_8 breaking up into reactive fragments during pyrolysis experiments. If found, S_8 would indicate periods when volcanism was relatively high and conditions were almost certainly reducing and anoxic.

Detection of S_8 could be done using the instruments on the Mars Science Laboratory (MSL) or the future Mars 2020 rover mission. When heated, vapor phase S_8 dominates but will also break into smaller chains at higher temperatures – typically S_2 but also S, S_4 , and S_6 . From the mass to charge ratios, S_2 and S could be confused for more common species (e.g. SO_2 and O_2 respectively) whereas S_4 and S_6 would have fewer interferences. During pyrolysis, vapor S may react with released H_2O to form SO_2 and other sulfides. Elemental sulfur has not yet been found on Mars, but SO_2 and H_2S have, which are interpreted to be the thermal decomposition of iron sulfates or calcium sulfites but are consistent with sulfur-bearing amorphous phases (McAdam et al., 2014). The lower negligible estimate for total S_8 production comes from dry reduced melts in a low total volcanism model. These atmospheres are not able to reach anoxic conditions and therefore unable to initiate S_8 aerosol production. However, these models all represent continuous average volcanism and there may be brief periods where enough volcanism occurred to shift the atmosphere anoxic and some non-negligible S_8 could be deposited.

Martian elemental sulfur and sulfate produced in an anoxic troposphere should produce mass-independent fractionation (MIF) sulfur isotopes, although direct interrogation of this record would likely require sample return. The magnitude and sign of MIF sulfur depend on the incident radiation field, the concentration of sulfur gases, their respective depositional fluxes, as well as on the concentrations of absorbing gases (such as OCS) in the atmosphere above the region of SO_2 photolysis (Claire et al., 2014). These elements would combine to produce sulfur MIF signatures distinct to those seen on Earth.

The total amount of sulfate estimated to be on the surface of Mars today, $\sim 10^6$ Tmol (Catling, 2014; Michalski & Niles, 2012), is about an order of magnitude less than the model-predicted amount for even the most sulfur-retaining melts. However, data from sulfur isotope MIF in martian meteorites suggests that some of the sulfur assimilates into magmatic processes and some sulfate is reduced to sulfide (Franz et al., 2014). This converted sulfur provides a subsurface reservoir of sulfur that may explain the discrepancy. Alternatively, this discrepancy may mean that the martian magmas produced even less sulfur than estimated, suggesting either a more reduced mantle, lower water content, or an increase of outgassing pressure. More realistically, Mars probably either experienced intermittent periods of volcanism (producing less sulfates) or there are greater unseen reserves of sulfates buried. Sulfate may also be hidden in cements of sandstones, which may not have been fully accounted for in published inventories.

Anoxic reducing conditions could also have affected the minerals formed on the surface of Mars in the past. One possible indicator volatile is carbonyl, derived from CO. The two most commonly found carbonyls, iron pentacarbonyl ($\text{Fe}(\text{CO})_5$) and nickel tetracarbonyl ($\text{Ni}(\text{CO})_4$), readily form in reducing CO-rich environments – such as those in the end state of our models. While iron pentacarbonyl should exist in the Earth's mantle (Wetzel et al., 2013), and presumably Mars' as well, areas of enrichment relative to the mantle may indicate more reducing conditions. Additionally, siderite (FeCO_3) is a good tracer for anoxia (Catling, 1999) and reducing conditions (Hausrath & Olsen, 2013). Siderite generally forms from acidic waters which allows soluble ferrous iron (Fe^{2+}) to exist in solution. Acidic waters are common in CO_2 -rich environments, as expected on early Mars. In oxic atmospheric conditions, O_2 dissolved in the water would rapidly oxidize the ferrous iron into minerals that can end up as hematite (Fe_2O_3). In anoxic atmospheres, the ferrous iron can form siderite. Due to lowest solubility amongst the carbonates, siderite will be the first to precipitate out, followed by magnesium carbonate. Siderite has been found on Mars at the Comanche site in Gusev Crater (Morris et al., 2010; Ruff et al., 2014) and possible ancient layered carbonates excavated in impact craters (Michalski & Niles, 2010). These siderite deposits may be evidence of such anoxic conditions, although they could also be representative of local hydrothermal activity (Ehlmann et al., 2008).

Clay minerals, especially phyllosilicates, have been mapped on Mars from orbital spectrometers (Bibring et al., 2005; Ehlmann et al., 2013; Poulet et al., 2005) and the predicted anoxic reducing conditions should have affected the types of clays forming on early Mars (Chemtob et al., 2015; Peretyazhko et al., 2016). The highly reducing conditions at the surface would, by definition, create an environment with negative Eh, which allows Fe^{2+} to be soluble. In Eh-pH conditions that favor ferrous iron, trioctahedral clays will form, such as saponites and talc (Velde, 1992). The most common clay to form with abundant Fe^{2+} and low Eh is berthiérine, a trioctahedral Fe-rich clay mineral of the kaolinite-serpentine group with the general formula $(\text{Fe}^{2+}, \text{Fe}^{3+}, \text{Al}, \text{Mg})_{2-3}(\text{Si}, \text{Al})_2\text{O}_5(\text{OH})_4$. However, berthiérine can form in both oxidizing and reducing conditions (positive and negative Eh respectively) and therefore cannot be a sole indicator mineral of reducing anoxic conditions (Chevrier et al., 2007).

In addition to the presence of berthiérine, indicating acidic and/or reducing conditions, the absence of nontronite, an Fe^{3+} -rich smectite that requires highly oxidizing conditions to form (Chevrier et al., 2007), may provide evidence of reducing conditions. Levels of pH are similarly important in the formation of both nontronite and berthiérine: the former is favored by neutral to weakly alkaline conditions and the latter by alkaline solutions. While paleo-pH levels are unknown for early Mars, the high partial pressures of CO_2 (and to a lesser extent SO_2) may have led to more acidic conditions, which would lead to aqueous Fe^{2+} and the formation of minerals such as pyrite (FeS_2). However, some aqueous environments would be buffered by basaltic minerals to higher pH. Overall, the reducing and anoxic conditions of early Mars should have favored Fe-rich clays (Harder, 1978) and Fe/Mg smectite secondary minerals (Dehouck et al., 2016).

2.6 CONCLUSIONS

We used a 1-dimensional photochemical model to calculate the composition and redox state for past martian atmospheres (~3.5 Gyr to present) for plausible levels and compositions of volcanic outgassing. The results suggest the following conclusions:

- The atmospheric redox state can rapidly shift from oxidizing to reducing conditions at levels of extrusive volcanism $>0.14 \text{ km}^3 \text{ yr}^{-1}$ under a range of reasonable melt parameters and magmatic

oxygen fugacity, water content, and outgassing pressure constraints. This shift is driven primarily by the release of large quantities of reducing gases (e.g. CO and H₂) and the formation of sulfate aerosols which act as a large sink of oxygen.

- When Mars was volcanically active, it should have produced a considerable flux of sulfur-bearing aerosols. In oxidizing and transitional-to-anoxic atmospheres, sulfate aerosols are the most important aerosols with $\sim 10^6$ - 10^9 Tmol of sulfate being deposited over the volcanic outgassing history since 3.5 Ga. Reducing conditions also allow the deposition of elemental polysulfur aerosols ranging from $\sim 10^{-8}$ Tmol S₈ to $\sim 10^8$ Tmol S₈, when rates are non-negligible. S₈ deposition onto the surface increases in more reducing atmospheres. The smallest deposition occurs at IW oxygen fugacity when S stays in the melt. Detection of elemental polysulfur or a distinct sulfur MIF isotopic signature would indicate past reducing atmospheres.

- Reducing anoxic environments should lead to the formation of minerals that are favored by low-Eh and/or contain ferrous iron (Fe²⁺). Trioctahedral Fe-rich clays, such as berthiérine, should be favored, and the absence of clays that only form under high Eh (e.g. nontronite) can indicate reducing conditions. The formation of minerals such as siderite, nickel carbonyl, and pyrite may also be indicative of anoxia, especially if found in bedded deposits that were subaerial.

- The formation of prebiotic chemical compounds is possible in anoxic and reducing atmospheres expected from a volcanically active early Mars. The atmospheric formation of organics, such as amino acids, may have created conditions making a martian de novo origin of life possible.

Chapter 3. A MAXIMUM SUBSURFACE BIOMASS ON MARS FROM UNTAPPED FREE ENERGY

This chapter was originally published in the journal Astrobiology:

Sholes, S.F., J. Krissansen-Totton, and D.C. Catling. (2019). “A Maximum Subsurface Biomass on Mars from Untapped Free Energy: CO and H₂ as Potential Antibiosignatures.” *Astrobiology* 19(5): pgs. 655-668. doi:10.1089/ast.2018.1835

3.1 ABSTRACT

Whether extant life exists in the martian subsurface is an open question. High concentrations of photochemically produced CO and H₂ in the otherwise oxidizing martian atmosphere represent untapped sources of biologically useful free energy. These out-of-equilibrium species diffuse into the regolith, so subsurface microbes could use them as a source of energy and carbon. Indeed, CO oxidation and methanogenesis are relatively simple and evolutionarily ancient metabolisms on Earth. Consequently, assuming CO- or H₂- consuming metabolisms would evolve on Mars, the persistence of CO and H₂ in the martian atmosphere set limits on subsurface metabolic activity. Here, we constrain such maximum subsurface metabolic activity on Mars using a 1-D photochemical model with a hypothetical global biological sink on atmospheric CO and H₂. We increase the biological sink until the model atmospheric composition diverges from observed abundances. We find maximum biological downward subsurface sinks of 1.5×10^8 molecules cm⁻² s⁻¹ for CO and 1.9×10^8 molecules cm⁻² s⁻¹ for H₂. These convert to a maximum metabolizing biomass of $\lesssim 10^{27}$ cells or $\leq 2 \times 10^{11}$ kg, equivalent to $\leq 10^{-4}$ - 10^{-5} of Earth's biomass, depending on the terrestrial estimate. Diffusion calculations suggest this upper biomass limit applies to the top few kilometers of the martian crust in communication with the atmosphere at low to mid latitudes. This biomass limit is more robust than previous estimates because we test multiple possible chemoautotrophic ecosystems over a broad parameter space of tunable model variables using an updated photochemical model with precise atmospheric concentrations and uncertainties from *Curiosity*. Our results of sparse or absent life in the martian subsurface also demonstrate how the atmospheric redox pairs of CO-O₂ and H₂-O₂ may constitute antibiosignatures, which may be relevant to excluding life on exoplanets.

3.2 INTRODUCTION

An open question about Mars is whether it currently hosts life in its subsurface. The *Viking* landers of the 1970s have been the only direct life detection missions on Mars and the consensus is that their results were negative (Klein, 1978, 1998). This is consistent with the poor habitability of the surface environment. Aside from plausible ephemeral briny solutions (Martín-Torres et al., 2015; Ojha et al., 2015; Rennó et al., 2009; Toner et al., 2014), the surface is cold and lacks lasting liquid water (Rummel et al., 2014) to provide a solvent for life. Also, bombardment from harsh galactic cosmic ray (GCR), solar ultraviolet (UV), and solar energetic proton (SEP) radiation in the upper few meters is enough to deactivate cells over timescales of 1,000-200,000 years depending on radioresistance and regolith materials (Cockell et al., 2000; Dartnell et al., 2007; Pavlov et al., 2012; Teodoro et al., 2018). Furthermore, highly-oxidizing perchlorate in the soil can become microbicidal under martian conditions (Wadsworth & Cockell, 2017).

However, the possibility of extant martian life remains. Reported detections of transient methane (Formisano et al., 2004; Krasnopolsky et al., 2004; Mumma et al., 2009; Webster et al., 2015; Webster et al., 2018) have resulted in a surge of interest in the possibility of biological methanogenesis on Mars (Mickol & Kral, 2016; Yung et al., 2018); although see Zahnle (2015; *et al.* 2011) for a dissenting view on the detections. Terrestrial microbes have also been found to use perchlorate oxidation-based metabolisms (Myers & King, 2017). Subsurface life could also use deep subsurface H₂ gas sourced through cataclastic (McMahon et al., 2016), serpentinizing (Ehlmann et al., 2010), or radiolytic (Onstott et al., 2006) reactions as a potential energy source before reaching the surface but there is generally no way to constrain the extent of such life based on observables.

Instead, one way to constrain extant subsurface martian life is to assume that it is in contact with the atmosphere through the porous regolith and to consider atmospheric disequilibrium. Atmospheric chemical disequilibrium is often discussed as a life-detection method for planetary atmospheres. For example, the co-existence of oxygen and methane in Earth's atmosphere is a biosignature because this out-of-equilibrium redox pair would not persist without replenishing fluxes of methane and oxygen (Hitchcock & Lovelock, 1967; Krissansen-Totton et al., 2016;

Lovelock, 1965). If abiotic sources of O₂ and CH₄ can be ruled out, then the O₂-CH₄ pair is a disequilibrium biosignature. However, when the source of atmospheric disequilibrium is known to be abiotic, such as from photochemical or geological fluxes, and the predicted abiotic concentrations of the disequilibrium pair match that observed, then it suggests that life is not exploiting the atmospheric free energy.

Historically, it was argued that the martian atmosphere is essentially at equilibrium and therefore Mars is unlikely to support life (Lovelock, 1975, 1979, 1988). However, with modern observations, it is understood that Mars' atmosphere has the largest thermodynamic disequilibrium in the Solar System aside from Earth, with an available free energy of ~136 J per mole of atmosphere (Krissansen-Totton et al., 2016). This free energy is predominantly attributable to the CO-O₂ redox pair produced abiotically by the photolysis of CO₂ and H₂O in a thin, dry atmosphere.

There are compelling reasons to believe that martian life – even if it possesses radically different biochemistry to Earth life – would evolve to exploit the disequilibrium available from the redox pairs in Mars' atmosphere. The net reaction for the anaerobic CO metabolism is $\text{CO} + \text{H}_2\text{O} \rightarrow \text{CO}_2 + \text{H}_2$ (Techtmann et al., 2009) and is a relatively simple metabolism that only requires water, given a source of CO. The enzymes that catalyze this reaction on Earth, carbon monoxide dehydrogenases (CODHs), possess a variety of simple Ni-Fe or Mo active sites suggesting that they have evolved independently multiple times (Ragsdale, 2004; Techtmann et al., 2009). Additionally, the genes encoding CODH are prolific with some 6% of sequenced microbial genomes having one or more copies of the Ni-Fe CODH. This has led some to argue that CO oxidation to be an evolutionarily ancient process, serving as both an energy and carbon source for the earliest forms of life in volcanic settings (Ferry & House, 2005; Huber & Wächtershäuser, 1997; Lessner et al., 2006; Ragsdale, 2004). Indeed, genomic evidence suggests the last universal common ancestor (LUCA) possessed genes encoding CODH (M. C. Weiss et al., 2016). Additionally, there are modern methanogenic archaea that use CO for their entire metabolisms (Rother & Metcalf, 2004).

Aerobic CO-metabolisms also exist, which oxidize CO through the net reaction $2\text{CO} + \text{O}_2 \rightarrow 2\text{CO}_2$ (Meyer & Schlegel, 1983; Ragsdale, 2004). These aerobic carboxydrotrophs

also use CODH enzymes that possess a variety of Mo-, Fe-, and Cu- activation sites (Jeoung & Dobbek, 2007). Given the diversity of transition metal catalysts and the abundance of CO in the martian atmosphere, it is reasonable to expect that microbial life in contact in the atmosphere would evolve to exploit this available free energy.

A much smaller portion of Mars' atmospheric thermodynamic disequilibrium, due to the small concentration of H₂, is attributable to the H₂-O₂ redox pair. Microbial methanogenesis, oxidizing H₂ with CO₂, may be one of the most primitive metabolisms on Earth (Ueno et al., 2006; M. C. Weiss et al., 2016; Wolfe & Fournier, 2018). Thus H₂-oxidation could also be a source of free energy for martian life, although it should be noted that CO provides >98% of the available atmospheric free energy.

All life as we know it, without exception, uses redox chemical reactions to generate energy (e.g. Falkowski et al., 2008). Given abundant free energy in the martian atmosphere, microbial life – if it exists – ought to take advantage of this ‘free lunch’ (Zahnle et al., 2011). The thermodynamic drive to equilibrium by chemosynthetic life suggests that certain molecules in abundance, such as the CO-O₂ and H₂-CO₂ redox pairs, constitute antibiosignatures (Catling et al., 2018; Wang et al., 2016) - evidence that actively metabolizing life is absent or sufficiently meager that it does little to perturb the atmosphere beyond its abiotic photochemical state. The persistence of this photochemically induced disequilibrium and the reasonable assumption that martian life would evolve a simple CO- or H₂-metabolism to take advantage of such a disequilibrium, suggests that any microbial life in communication with the atmosphere has not exploited this free lunch and thus it represents an antibiosignature.

Disequilibrium in Mars' atmosphere has previously been used to constrain a maximum extant biomass in the subsurface using a modified photochemical model to include biogenic sinks on CO and H₂ (B. P. Weiss et al., 2000). However, this study was potentially inaccurate because it used fixed values for photochemical model parameters tuned to modern abiotic martian conditions whereas one should use values that account for their large uncertainties. Instead, given the uncertainties on these parameters (described in Sec. 2.2), they could be tuned differently, but

within allowable error bars, to an assumed Mars with biogenic sinks on CO or H₂. This procedure could potentially alter the outcome for calculated subsurface biomass.

Here we consider how much biomass could exist in the current subsurface and be feeding off atmospheric redox couples. A subsurface environment is assumed because persistent liquid water on Mars today can only exist in the subsurface where the geothermal gradient allows an aquifer (e.g. Dundas et al., 2014; Feldman et al., 2004; Grimm & Painter, 2009; Mellon et al., 1997).

We use a novel approach by optimizing the photochemical model over a broad range of tunable parameter space that assumes a biosphere for calculating unknown variables. In addition to the significance of the optimization procedure, we additionally improve and expand upon the work done by B. P. Weiss et al. (2000) in four major ways: 1) We include sources and sinks for all metabolic reactants and products as opposed to only sinks on CO and H₂. 2) We use updated, more precise present day atmospheric compositions collected by the *Curiosity* rover with an improved photochemical model. 3) We account for multiple combinations of the plausible chemoautotrophic ecosystems that use different net metabolic pathways and use improved estimates for cellular maintenance energy. 4) Because the delivery of substrate gases to subsurface life (and hence its biomass) might be restricted by downward diffusion through the regolith, we develop an improved gas diffusion model and test over a broad range of surface properties and crustal gradients. Thus, our comprehensive results provide rigorous constraints on the maximum biomass that could exist on Mars today that is in communication with the atmosphere.

3.3 METHODS

To investigate the effects of biological sinks on the martian atmosphere, we use a one-dimensional photochemical code originally developed for modeling the early Earth by Kasting (1979) but our nominal model has since been modified and validated for the modern martian atmosphere (Sholes et al., 2017b; M. L. Smith et al., 2014; Zahnle et al., 2008). This model is built to include C-H-O-N-S (carbon, hydrogen, oxygen, nitrogen, and sulfur) chemistry and improves upon the Nair et al. (1994) model used by B. P. Weiss et al. (2000) in three major ways: 1) for redox conservation, hydrogen-escape is balanced via an abiotic tunable deposition velocity (v_{dep})

of reactive oxidizing species to the surface rather than arbitrary O escape at the top of the model (Lammer et al., 2003; Lillis et al., 2017; Zahnle et al., 2008); 2) the implementation of diffusion-limited hydrogen escape, both of which are justified by Zahnle et al. (2008) with reference to data and models and by measurements by the *Mars Atmosphere and Volatile Evolution* (MAVEN) mission (Jakosky et al., 2018) where the measured H escape rate of $0.8-7.6 \times 10^8$ atoms $\text{cm}^{-2} \text{s}^{-1}$ encompasses the estimated diffusion-limited escape rate of $(3.3 \pm 1.1) \times 10^8$ H atoms $\text{cm}^{-2} \text{s}^{-1}$ within uncertainties (Catling and Kasting 2017, pg. 148); and 3) implementing a lower boundary condition where the CO_2 concentration is no longer fixed.

With the exception of the CO_2 treatment (described in more detail below), we follow the same parameters as the aforementioned models. Atmospheric surface pressure is set to 6.5 mbar, close to present day global-average levels (Haberle et al., 2008). The model uses uniformly spaced 1 km resolution grids up to 110 km. Ionospheric chemistry is not directly modeled, but downward fluxes at the top of the model of key photolytically produced ionospheric species are included, namely NO, N, and CO. Oxygen escapes out the top of the model at a rate of 10^7 O atoms $\text{cm}^{-2} \text{s}^{-1}$ following (Zahnle et al., 2008) and is of the same order as measurements made by MAVEN ($\sim 3 \times 10^7$ O atoms $\text{cm}^{-2} \text{s}^{-1}$ Jakosky et al. (2018)). Vertical transport of species is dominated by eddy diffusion. The temperature profile is approximated by $T = T_s - 1.4h$ for the lower 50 km and isothermal above; T_s is the surface temperature (detailed below) and h is the height above the surface (in km). Water vapor is kept at a constant relative humidity in the lower atmosphere to produce the observed 9.5 μm (Zahnle et al., 2008)

Previous versions of the photochemical model held CO_2 at a constant mixing ratio, assuming it to be replenished by indefinitely large surface (e.g. polar caps) and subsurface reservoirs (e.g. Zahnle et al., 2008). Here, we allow the CO_2 mixing ratio to vary, rather than be fixed at a set concentration. This allows for more accurate behavior when biology is included because some metabolisms release or draw down CO_2 . In particular, CO and O_2 are replenished through the photolysis of CO_2 , so even though they would be drawn down as sinks in different metabolisms, they are being artificially replenished by an unrealistic injection of CO_2 (up to the set value) at all grids and time steps if CO_2 were fixed numerically in the model.

Validation tests were successfully performed to ensure that the updated model, where the CO₂ concentrations can vary, matches the previously validated models in their atmospheric structure and composition. Additional tests were done to compare each modeled metabolism with and without a fixed CO₂ mixing ratio (for both the “fixed parameter” and “optimized parameter” models described below). No significant differences were found other than a decrease in the maximum allowable sink for the net aerobic carboxydrophy metabolism. When CO₂ concentrations are fixed, the maximum allowable biogenic sink for the net aerobic carboxydrophy metabolism is unrealistic as it approaches the column-integrated production limit of CO due to the artificial replenishment of CO and O₂ in the atmosphere. All work presented here reflects the improved model with CO₂ concentrations no longer fixed, thus more accurately modeling the effect of each metabolism.

The influence of possible subsurface biological metabolic activity is modeled by ground-level fluxes in the model. For each of the metabolic ecosystems simulated, the model is run with that metabolism’s substrate gases removed directly from the atmosphere via a fixed downward surface flux while we simultaneously inject its metabolic products directly into the atmosphere at the lower boundary. The model is then run to steady state and ground-level mixing ratios are compared with the observed abundances measured for the modern martian atmosphere (see Table 3.1) (Franz et al., 2017; Krasnopolsky & Feldman, 2001; Webster et al., 2015; Webster et al., 2018). This process is repeated as the surface fluxes are incrementally increased until the modeled atmosphere diverges from the current atmospheric compositions within a 2 σ (95%) uncertainty. We assume that this divergence then sets the limit on the extent of a metabolizing subsurface biomass because its activity would not violate the known atmospheric composition.

3.3.1 *Fixed Parameter Model*

We use the aforementioned nominal Mars model, which has been tuned and validated against the modern martian atmosphere (Sholes et al., 2017b; M. L. Smith et al., 2014; Zahnle et al., 2008). There are five possible net chemoautotrophic metabolisms that could feasibly

Table 3.1. Modern martian atmospheric composition and uncertainties for modeled fluxes. Here we use the slightly higher background value of Webster et al. (2015) rather than that from Webster et al. (2018) for a more conservative upper limit on biomass.

Species	Observed Mixing Ratio	Uncertainty (1 σ)	Reference
O ₂	1.74×10^{-3}	6×10^{-5}	Franz et al. (2017)
CO	7.47×10^{-4}	2.6×10^{-6}	Franz et al. (2017)
H ₂	1.5×10^{-5}	5×10^{-6}	Krasnopolsky and Feldman (2001)
CH ₄	6.9×10^{-10}	1.3×10^{-10}	Webster et al. (2015) ^a
CO ₂	0.96	7×10^{-3}	Mahaffy et al. (2013)

^aThese measurements are of a mean atmospheric level of 0.69 ppb and are controversial (see Zahnle et al., 2011), thus we place an upper bound of 9.4×10^{-10} representing a 2σ detection

be living off atmospheric energy. We express these metabolisms as both individual metabolic pathways and as combined metabolic ecosystems as the Gibbs free energy produced through either net reaction are identical. The metabolisms (Mets.) are:

- Met. 1: Anaerobic CO metabolism only:



- Met. 2: Methanogenesis only:



- Met. 3: Anaerobic CO metabolism and methanogenesis (i.e., $4 \times \text{Met.1} + \text{Met. 2}$):



- Met. 4: Aerobic carboxydrotrophy or an equivalent net CO metabolism, methanogenesis, and methanotrophy ecosystem (i.e., $4 \times \text{Met.1} + 2 \times \text{Met.2} + \text{methanotrophy}$ ($\text{CH}_4 + 2\text{O}_2 \rightarrow 2\text{H}_2\text{O} + \text{CO}_2$)):



- Met. 5: Aerobic hydrogenotrophy or an equivalent net methanogenesis and methanotrophy ecosystem (i.e., $\text{Met.2} + \text{methanotrophy}$):



These end-member cases represent the full range of possible martian ecosystems subsisting off atmospheric free energy. B. P. Weiss et al. (2000) only modeled Met. 4 and Met. 5 as they believed the most energetic reactions would likely use O₂ as an oxidant. We do not consider a methanotrophy-only metabolic system (or combinations of ecosystems that include methanotrophs without methanogens) because it is infeasible given that the concentration of background methane is <1 ppb (Webster et al., 2015; Webster et al., 2018) and thus will produce a much smaller maximum biomass than other metabolisms. Reported transients of methane >10 ppb are localized and controversial in nature (Zahnle et al., 2011). Notably, in the *Curiosity* tunable diode laser results of Webster et al. (2018), such transients are only found sometimes in a direct measurement protocol but never found in a more sensitive enrichment protocol. Thus, these results demand skepticism as the transients appear to be more of a function of measurement protocol than of Mars. Similarly, we do not test metabolisms that produce species not observed in the current martian atmosphere (e.g. sulfate reducers producing H₂S).

3.3.2 *Optimized Parameter Model*

The methodology for what we call the “fixed parameter” model (Section 3.3.1) may not provide a rigorous maximum biogenic sink because it is tuned to a modern abiotic Mars with fixed unknown parameters (described below) that have been tuned in the model. If life is actively metabolizing on Mars, then the tuned parameter values could be different to what is commonly assumed, and their incorrect tuning could mask biogenic sources/sinks. Thus, the “fixed parameter” model underestimates the maximum biogenic sink.

We have identified three main tunable variables in the nominal model where the value has significant impact on the atmospheric composition and is either unknown or not agreed upon in the literature: surface temperature, ionospheric flux, and deposition velocity. Of these, mean surface temperature is the most constrained based on observed measurements, but *global* mean surface temperature is dependent on factors such as global circulation model integrations and atmospheric dust content (Haberle, 2013). Ionospheric fluxes of the odd nitrogen species (NO and N) are dependent on their concentrations and ratio, which are not entirely known. Krasnopolsky (1993) considers cases where the upper boundary flux of NO into the neutral atmosphere is both

nonexistent and appreciable (10^7 molecules $\text{cm}^{-2} \text{s}^{-1}$), so we consider the range 10^1 - 10^8 molecules $\text{cm}^{-2} \text{s}^{-1}$ consistent with sensitivity testing by M. L. Smith et al. (2014). A flux of CO into the upper atmosphere is set to be equal to that of NO to conserve redox balance while N is set to 10% that of NO (Sholes et al., 2017b; Zahnle et al., 2008).

Deposition velocity of reactant species is the dominant free parameter of the model. It is a constant used to simulate mixing, molecular diffusion, adsorption, and reactions of species with the surface regolith in a single variable. Higher v_{dep} indicates a more chemically reactive species (Catling & Kasting, 2017; Seinfeld & Pandis, 2016). In a physical system, the deposition velocity for each species would be different, but these variations would be small so a single v_{dep} is assumed for all reactive species. This is considered a good approximation (Zahnle et al., 2008) as H_2O_2 and O_3 are the primary reactants that must have the v_{dep} tuned for each model run to produce the modern abundances for the primary atmospheric constituents and computational restrictions prevent optimization of v_{dep} over 30+ species. CO_2 , CO, O_2 , and H_2 are considered non-reactive with the surface and their $v_{dep}=0 \text{ cm s}^{-1}$ (See Zahnle *et al.* 2008 for more on O_2 dry deposition and Sholes *et al.* 2017 for a review on CO deposition). For each species, v_{dep} is a fixed value, but is used to compute a variable surface flux (Φ) for each chemically reactive species, which depends on species abundance as $\Phi = -v_{dep} n_{i,surf}$, where $n_{i,surf}$ is the surface number density for species i (Catling & Kasting, 2017; Seinfeld & Pandis, 2016). This net oxidant sink balances the atmospheric redox budget by countering hydrogen escape to space, which oxidizes the atmosphere (Lammer et al., 2003; Seinfeld & Pandis, 2016; Zahnle et al., 2008). The biological consumptions of CO, O_2 , and H_2 are included using a separate fixed flux term.

To test whether optimizing the tunable parameters affects the maximum biological sink in the modern martian atmosphere, we perform a grid search and optimization procedure through the parameter space for the five net ecosystems described in Section 3.3.1. We incrementally increase the net metabolic source/sink fluxes as described for the nominal model, but at each increment we perform a grid search of model parameter space to find whether any possible sets of parameters (for temperature, ionospheric flux, and deposition velocity) can reproduce the observed martian atmosphere while incorporating the biogenic fluxes; what we describe as our “optimized parameter” model. At every grid point in parameter space we perform an optimization procedure

(`scipy.optimize.minimize` in Python) to ensure that all regions in parameter space were explored and not missed by the coarse grid search. Table 3.2 summarizes the plausible parameter ranges, bounds, and number of grid points for each parameter in addition to the tuned values that produce the modern atmospheric concentrations.

The optimization procedure minimized the Chi-Squared (χ^2) value comparing the modeled atmospheric composition with the measured atmospheric composition and uncertainties in Table 3.1. This procedure was continued until the modeled atmospheric compositions diverged from the observed composition, regardless of parameter values.

Table 3.2. Unknown tunable model parameters and their assumed ranges for Mars. Tuned values are for the fixed-parameter abiotic modern Mars model. Grid space refers to how many equally spaced values of the parameter were used in the optimization grid search within the plausible range for the optimized-parameter model. v_{dep} for CO, CO₂, H₂, and O₂ are set to 0 cm s⁻¹. The tuned v_{dep} parameter refers to that assumed for all reactive species including both O₃ and H₂O₂.

Parameter	Plausible Range	Grid Space	Tuned Value	Reference(s)
Mean surface temperature, T_s (K)	199 – 215	5	210	Haberle (2013)
Surface deposition velocity, v_{dep} (cm s ⁻¹)	0.001 – 0.1	3	0.012	Zahnle et al. (2008)
Ionospheric flux, $\phi_{NO,CO}$ (molecules cm ⁻² s ⁻¹)	10 ¹ - 10 ⁸	5	7.3 × 10 ²	Krasnopolsky (1993); M. L. Smith et al. (2014)

3.3.3 Atmospheric Diffusion Model

Once maximum permissible biogenic sinks are found in both the “fixed parameter” and “optimized parameter” versions of the model, we consider how these fluxes compare with passive atmospheric diffusion into the crust. This is because the dry, harshly irradiated, and constantly oxidized martian surface is ostensibly uninhabitable (see Sec. 3.2) so any extant life would need to take advantage of aquifers in the subsurface. There may be small pockets of briny fluids in the

upper few kilometers (Orosei et al., 2018), but a deep water-saturated layer should exist within 10 km of the surface as a consequence of the geothermal gradient (Clifford, 1993; Clifford et al., 2010; Michalski et al., 2013). Here, we calculate to what depth microbes could plausibly exploit the atmospheric free energy and thereby assign a maximum crustal depth to our upper biomass limit (i.e. the biomass of microbes living below this depth would be limited by diffusion of substrate gases and would therefore have smaller surface sinks than the calculated maximum fluxes that ignore a diffusion restriction).

To calculate the diffusion flux of CO and H₂ at depth (the potential flux), we use a modified form of Fick's laws which assume mean free paths of diffusing gases are greater than the typical pore size such that Knudsen diffusion dominates. In one dimension, the general form of Fick's second law states:

$$\frac{\partial n_i}{\partial t} = \frac{\partial}{\partial z} \left(D_i(z) \frac{\partial n_i}{\partial z} \right) \quad 3.6$$

where n_i is the number density for species i (molecules cm⁻³), z is the depth (cm), t is time (s), and D_i is the diffusion coefficient (diffusivity, cm² s⁻¹). In steady state, the concentrations will not change with time, so the left-hand side of this equation is set to 0. The solution for the concentration gradient, $\frac{\partial n_i}{\partial z}$, can then be used to find the potential flux, F_i , via Fick's first law:

$$F_i = -D_i(z) \frac{\partial n_i}{\partial z} \quad 3.7$$

The physical environment over which the gas diffuses changes greatly through the upper ~10 km of martian regolith. This means that the diffusivity, the controlling factor, changes drastically with increasing depth due to increasing pressure and temperature and can be written as:

$$D_i = \frac{\varepsilon(z) r(z)}{3 \tau(z)} \sqrt{\frac{8 R T(z)}{\pi m_i}} \quad 3.8$$

where $\varepsilon(z)$, $r(z)$, $\tau(z)$, $T(z)$ are the porosity, pore size (cm), tortuosity (path twistiness), and temperature (K) at a given depth. R is the gas constant and m_i is the molar mass of the species. We follow Stevens et al. (2015); (2017) in assuming that porosity and tortuosity decrease exponentially with depth with $\varepsilon(z) = \varepsilon_0 e^{\frac{-z}{k}}$ and $\tau(z) = \tau_0 e^{\frac{-z}{3k}}$ where ε_0 and τ_0 are the surface porosity and tortuosity respectively and k is a scaling factor set by the pore closure depth (Clifford, 1993).

Temperature is modeled as a linear geothermal gradient, $T(z) = a_T z + T_0$ where T_0 is the modeled surface temperature and a_T is the gradient (Michalski et al., 2013). We assume pore size follows a constant pressure gradient (Stevens et al., 2015), $r(z) = a_r z + r_0$ where a_r is the gradient defined as $\frac{r_0}{-k}$ such that pore size is 0 at the pore closure depth and r_0 is the average surface pore size. We perform these calculations over a range of plausible gradients and surface parameter values (detailed below).

If we consider a layer of biota sustaining off atmospheric energy, living at a depth z_b , and metabolizing all available reactants (CO or H₂), Eqn. 3.6 can be numerically solved as a boundary value problem. Using observed surface number densities, $n_i(0)$, and setting $n_i(z_b)=0$ we numerically solve for $n(z)$ (scipy.integrate.solve_bvp in Python) in steady state. We can then use Eqn. 3.7 to solve for potential flux as a function of biotic layer depth (z_b). In practice, microbes cannot metabolize with substrate conditions of zero within the biologically active layer, but observations of Antarctic soils have found that microbes can metabolize with CO concentrations of 20 ppb (Ji et al., 2017). Setting $n_i(z_b)$ to the equivalent of 20 ppb for CO under Antarctic conditions (approximated as 1 bar and 255 K) results in nearly identical potential fluxes as the $n_i(z_b)=0$ case demonstrating that a zero-concentration lower boundary condition is a reasonable assumption.

Given the uncertainties of the physical surface conditions and gradients, we employ a Monte Carlo simulation to test the potential flux under both a range of z_b and physical parameter values (for porosity, tortuosity, average pore size, pore closure depth, and temperature). For each possible z_b , spaced every 10 m between 0-10 km, we perform 10,000 diffusion calculations where we assume each parameter has a uniform distribution bounded by the parameter ranges described above and sample these distributions randomly. From these outputs, we obtain a likelihood distribution for the diffusion flux as a function of biological layer depth.

Surface porosity ranges from $\epsilon_0=0.2-0.6$, with low values characteristic of lunar estimates and high values approximating *Viking* lander observations (Clark et al., 1976; Clifford, 1993; Sizemore & Mellon, 2008). Estimated surface tortuosity ranges from $\tau_0=1.5-2.5$ as measured in Mars-regolith simulant soil (Sizemore & Mellon, 2008). We take an average surface pore size

range of $r_0=10^{-3}$ - 10^{-4} cm based around the typically cited value of 6×10^{-4} cm (B. P. Weiss et al., 2000) and experimental pore size distributions using glass beads (Sizemore & Mellon, 2008). The pore closure depth due to compaction ranges from $k=6$ - 26 km depending on how saturated the crust is with water. The extremes are most likely over/under estimates and a value of 10 km is typically assumed (Hanna & Phillips, 2005). We test temperature gradients of 10 - 30 K km^{-1} (Michalski et al., 2013).

3.4 RESULTS

Figure 3.1 shows the effects of increasing the subsurface biological sinks for Mets. 1-3 while Figure 3.2 shows the results for Mets. 4 and 5. In all cases, as the sink is ramped up, the resulting modeled atmospheric composition eventually diverges from the 2σ uncertainty of the measured modern atmospheric composition. For example, in the fixed-parameter model Met. 1 case, the CO abundance falls below the observed 2σ abundance of 744 ppm at a downward biologic flux of 8.4×10^5 CO molecules $\text{cm}^2 \text{s}^{-1}$. In this case, CO is considered the “break species” as CO diverges from the observed concentrations at a lower biological sink than the other measured constituents (O_2 , H_2 , CH_4 , CO_2). The flux at which this divergence occurs is the maximum permissible flux where the modeled metabolism can still replicate observed abundances and is listed in Table 3.3 for the fixed-parameter model Met. 1 case.

In this example (Met. 1, anaerobic CO metabolism, fixed-parameter model), as the biological sink on CO is ramped up, CO concentrations decline, O_2 abundances steadily rise, and CO_2 abundances eventually decline as well. These behaviors are the result of the simulated biological draw-down on CO. CO_2 is readily converted into CO and O_2 through photolysis, thus removal of CO through high biological sinks inhibits the recombination reactions back into CO_2 and the injection of CO_2 as a product of the metabolism eventually becomes insufficient to counteract the removal of CO. This leads to low CO, excess O_2 and eventually low concentrations of CO_2 (Catling & Kasting, 2017, pp. 338-340 pgs. 338-340).

Except for metabolisms that produce CH_4 , in all other metabolisms in the fixed-parameter model runs, CO concentrations deviate from observations at the lowest flux levels (CH_4 deviates

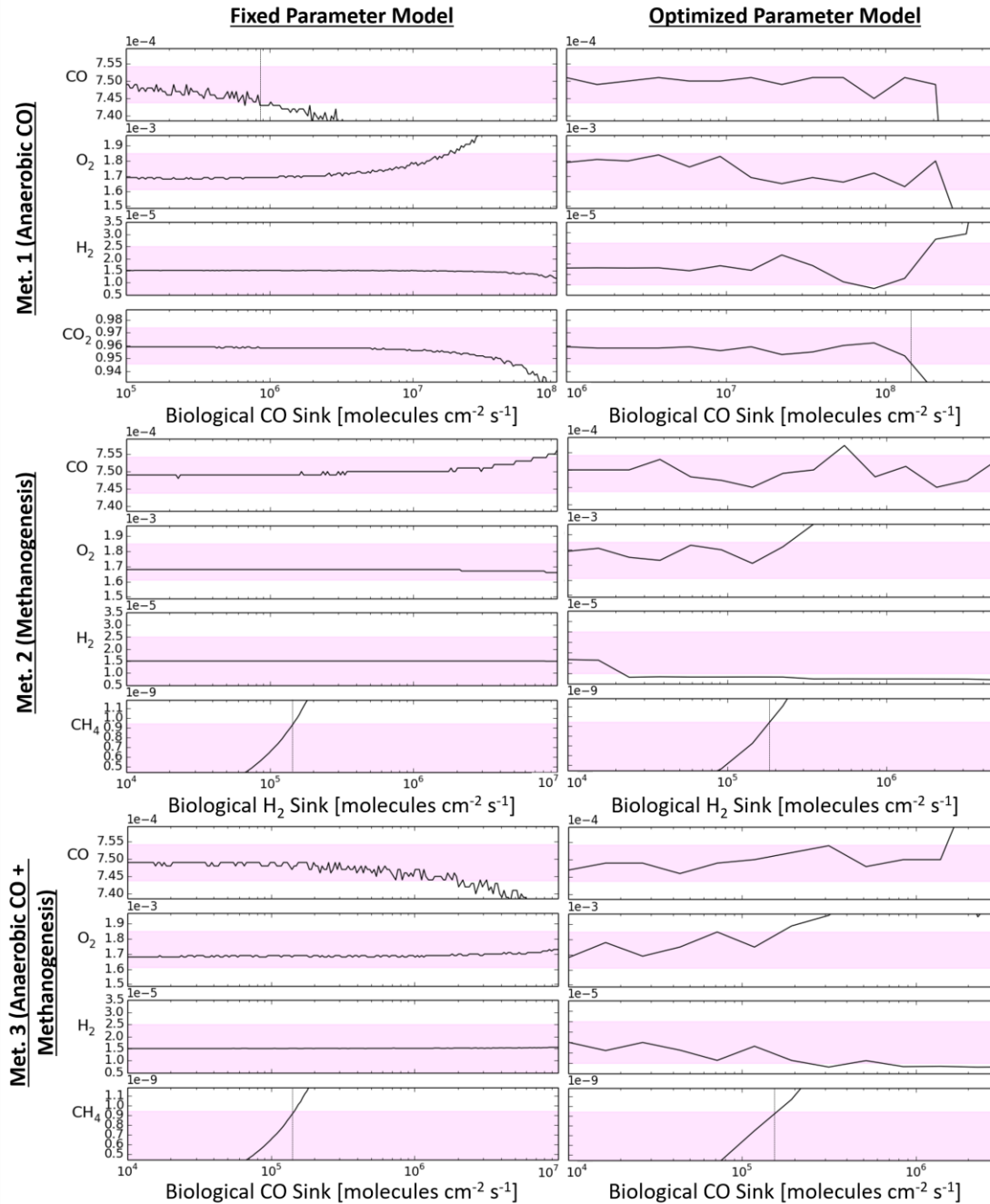


Figure 3.1. Modeled atmospheres for Mets. 1-3 as biogenic sinks are incrementally ramped up. Left panels are for the fixed parameter model and the right panels for the optimized parameter version (see text). Shaded regions represent a 2σ uncertainty for the mixing ratios of CO, O₂, H₂, CH₄, and CO₂. Vertical dotted lines indicate where the model diverges from observations (max biological sink). CO₂ concentrations do not vary for Met. 2 within or below this biogenic sink range.

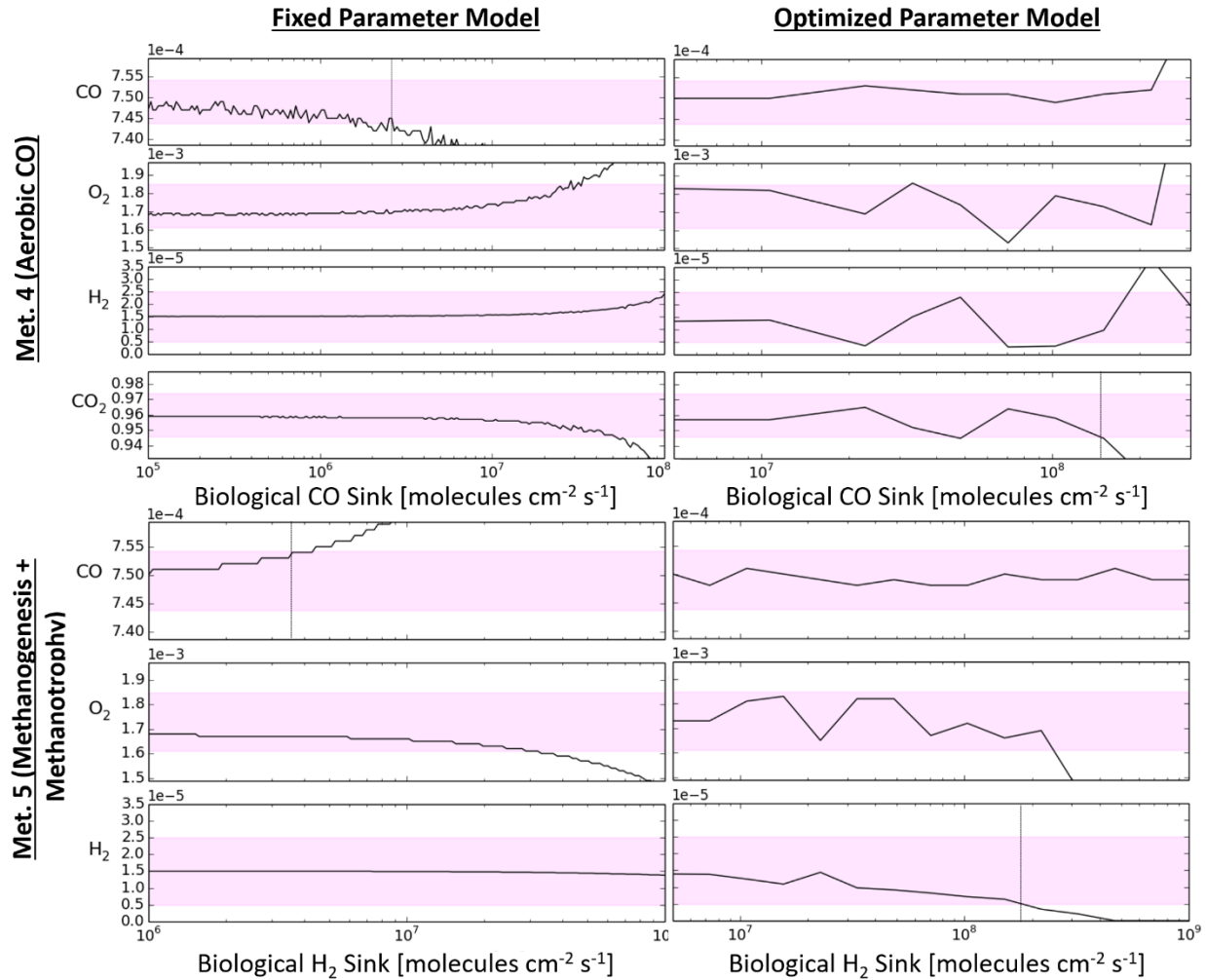


Figure 3.2. Modeled atmosphere for Mets. 4 and 5, which produce the largest maximum biomass, as biogenic sinks are incrementally ramped up. Left panels are for the fixed parameter model and the right panels for the optimized parameter version (see text). Shaded regions represent a 2σ uncertainty for the mixing ratios of CO, O₂, H₂, CH₄, and CO₂. Vertical dotted lines indicate where the model diverges from observations (max biological sink). CO₂ concentrations do not vary for Met. 5 within or below this biogenic sink range.

at lower fluxes in metabolisms that produce it). This is due to either the direct biogenic sink on CO or the removal of O₂ (a byproduct of CO₂ photodissociation), which throttles the recombination of CO₂ and leads to excess CO. Because CO has the smallest observational uncertainty, the nature of the χ^2 -calculation in the optimized-parameter model will end up attempting to constrain CO more precisely than the other species. Thus, the optimized-parameter model runs generally have

CO₂ concentrations that deviate at lower fluxes except for CH₄-producing metabolisms and the aerobic H₂-metabolism (where O₂ and H₂ are drawn down and eventually diverge from observations).

The maximum biogenic sink fluxes for each of the net ecosystems with both the fixed- and optimized-parameter models are summarized in Table 3.3. We find that the maximum downward flux on CO or H₂ ranges from 10⁵-10⁸ molecules cm² s⁻¹. As expected, the optimized version of the model produced maximum fluxes that were consistently higher than their fixed-parameter model counterparts. The exceptions are Mets. 2 and 3 which had comparable maxima due to CH₄ building up too high and the tunable parameters unable to effectively remove CH₄. The anaerobic H₂-metabolism (Met. 5) allowed for the greatest downward biogenic sink of 1.9×10⁸ H₂ molecules cm² s⁻¹ in the optimized-parameter model with the aerobic CO-metabolism (Met. 4) having a similar maximum of 1.5×10⁸ CO molecules cm² s⁻¹.

Our fixed-parameter model results show a maximum downward sink of 2×10⁶ CO molecules cm² s⁻¹ for Met. 4 and 4×10⁷ H₂ molecules cm² s⁻¹ for Met. 5, which are, respectively, 30 times smaller and 2 times greater than the maximum sinks from B. P. Weiss et al. (2000) (which tested only these two metabolisms). While it is expected, given our model improvements, that we find an improved result for Met. 4, it may seem counterintuitive that we find a slightly greater sink for Met. 5 (methanogenesis and methanotrophs) compared with B. P. Weiss et al. (2000). This stems from our use of 2σ uncertainties on atmospheric abundances rather than an arbitrary 25% of the observations (the ratio of the measured uncertainty to the value) they used (at 1σ we find a maximum sink of ~2×10⁶ H₂ molecules cm² s⁻¹ for the fixed model Met. 5).

Maximum biogenic fluxes can be used to estimate maximum extant biomass. The conversion from flux to biomass is done using:

$$M_{\max} = \frac{\Phi_{\max} A_{\text{Mars}} \Delta G}{q_{\text{BPR}} N_A} \quad 3.9$$

Here, the maximum metabolizing biomass (M_{\max}) is equal to the maximum biogenic sink in model units (Φ_{\max} ; molecules cm⁻² s⁻¹) times the surface area of Mars (A_{Mars} ; cm²) over the ratio of the basal power requirement (BPR) for life (q_{BPR} ; kJ s⁻¹ cell⁻¹) to the specified reaction free energy (ΔG ; kJ mol⁻¹) for each metabolism times Avogadro's number (N_A ; molecules mol⁻¹). The

Table 3.3. Maximum allowable downward flux for each metabolism and the equivalent biomass. Biomass estimates are based on basal power requirements of 3×10^{-23} kJ s⁻¹ cell⁻¹ (LaRowe & Amend, 2015; Lever et al., 2015) and an average cellular mass of 7×10^{-17} kg (Bratbak & Dundas, 1984; Hoehler & Jorgensen, 2013). The column headed 'Break' describes which atmospheric species deviates from observed abundance first and whether it is higher or lower than the 2σ detection. The greatest biomass estimate model runs are highlighted in bold.

#	Metabolism	Net Reaction	Fixed				Optimized			
			Max Flux [mol. cm ⁻² s ⁻¹]	Break	Biomass [cells]	Biomass [kg]	Max Flux [mol. cm ⁻² s ⁻¹]	Break	Biomass [cells]	Biomass [kg]
1	Anaerobic CO-only	CO + H ₂ O → CO ₂ + H ₂	8.4 × 10 ⁵	CO ↓	1.6 × 10 ²⁴	1.1 × 10 ⁸	1.4 × 10 ⁸	CO ₂ ↓	2.6 × 10 ²⁶	1.8 × 10 ¹⁰
2	Methanogenesis	CO ₂ + 4H ₂ → CH ₄ + 2H ₂ O	1.4 × 10 ⁵	CH ₄ ↑	2.6 × 10 ²³	1.8 × 10 ⁷	1.9 × 10 ⁵	CH ₄ ↑	3.5 × 10 ²³	2.5 × 10 ⁷
3	Anaerobic CO and methanogenesis	4CO + 2H ₂ O → 3CO ₂ + CH ₄	1.4 × 10 ⁵	CH ₄ ↑	5.2 × 10 ²³	3.7 × 10 ⁷	1.6 × 10 ⁵	CH ₄ ↑	5.9 × 10 ²³	4.2 × 10 ⁷
4	Aerobic CO-only	2CO + O ₂ → 2CO ₂	2.6 × 10 ⁶	CO ↓	5.3 × 10 ²⁵	3.7 × 10 ⁹	1.5 × 10⁸	CO₂ ↓	3.1 × 10²⁷	2.2 × 10¹¹
5	Methanogenesis and methanotrophy	O ₂ + 2H ₂ → 2H ₂ O	4.4 × 10 ⁶	CO ↑	7.3 × 10 ²⁵	5.1 × 10 ⁹	1.9 × 10⁸	H₂ ↓	3.2 × 10²⁷	2.2 × 10¹¹

Gibbs free energies for each equation are -24 kJ mol⁻¹ CO, -24 kJ mol⁻¹ H₂, -48 kJ mol⁻¹ CO, -264 kJ mol⁻¹ CO, and -215 kJ mol⁻¹ H₂ for Equations 1-5 respectively (calculated with the freely available database model of Krissansen-Totton et al., 2016 and using the nominal surface conditions and gas concentrations for Mars).

Quantifying the minimal basal power requirement (BPR) of organisms is currently the subject of much debate because all the contributing factors are not well characterized (see Discussion) (Bradley et al., 2018; Hoehler & Jorgensen, 2013; Kempes et al., 2017; LaRowe & Amend, 2015; Lever et al., 2015). Many estimates have been made, but we elect to use the value of 3×10^{-23} kJ s⁻¹ cell⁻¹ from Lever et al. (2015) and LaRowe and Amend (2015). This value is the smallest measured BPR from measurements of sulfate-reducing bacteria in anoxic marine sediments (Lever et al., 2015). However, the BPR could potentially be as low as 1×10^{-24} kJ s⁻¹ cell⁻¹ which is a theoretical limit to prevent racemization of amino acids. BPRs less than this value may be able to sustain individual cells, but are

characterized by population decay and thus not appropriate for characterizing a robust minimum biomass (one that is neither growing nor decaying).

Using this minimum BPR value, we find an upper limit of $\sim 10^{27}$ cells that could be supported of the available free energy of the martian atmosphere. This corresponds to the maximum biogenic sink for both the optimized-parameter Met. 4 (aerobic carboxydrotrophs) and Met. 5 (aerobic hydrogenotrophs) models. These provide similar maximum biomass values as their slightly varying max fluxes and free energy converge on a similar maximum biomass based on Eqn. 6. Additional conversions from this estimated cellular biomass into a metric biomass are provided in the Discussion.

The likelihood functions for our Monte Carlo simulation on diffusion of CO and H₂ into the subsurface are plotted in Fig. 3.3. The depths at which these potential fluxes equate to our calculated maximum downward biogenic sinks (2.1×10^8 molecules cm⁻² s⁻¹ for CO-sink metabolisms and 1.3×10^8 molecules cm⁻² s⁻¹ for H₂) represent the maximum plausible depth of any microbes subsisting off atmospheric free energy. The intercept depths for the CO-sink and H₂-sink metabolisms with the median flux distribution are ~ 6.5 km and ~ 1 km respectively. Below these depths, the limiting factor for determining the maximum extant biomass is the flux of reactants rather than the photochemistry.

3.5 DISCUSSION

Our calculated maximum extant metabolizing martian biomass of $\sim 10^{27}$ cells is difficult to interpret in isolation and so we compare it to Earth's total biomass. Typical estimates for Earth's biomass are classically given in terms of petagrams of carbon mass (Pg C = 10^{15} g C) and range from 550 Pg C (Bar-On et al., 2018) to 720 Pg C (Kallmeyer et al., 2012). Converting these values into an estimated number of cells requires an assumption on the average cellular carbon weight. Average cellular carbon mass ranges from 5-85 fg C cell⁻¹ for microbial cells (Bakken, 1985; Kallmeyer et al., 2012), so an estimated total number of cells on Earth ranges from $\sim 6.5 \times 10^{30}$ to

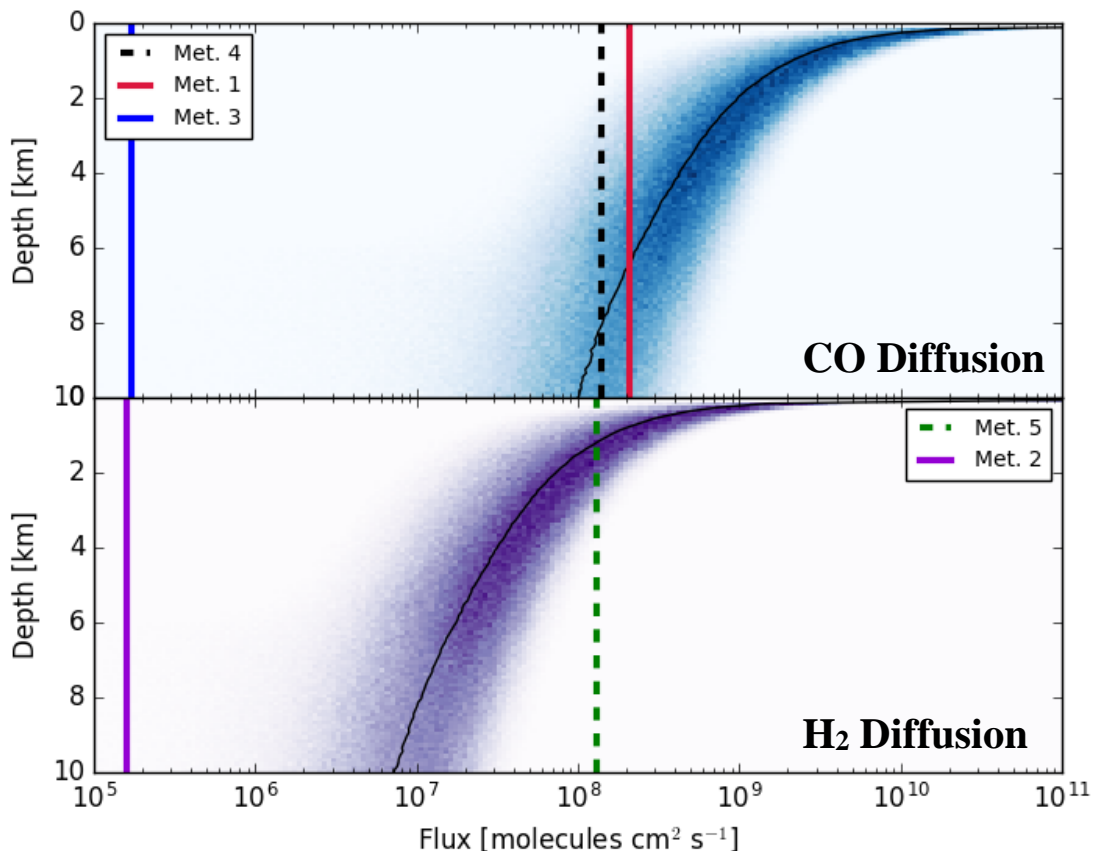


Figure 3.3. Monte Carlo simulations calculating diffusive fluxes for CO and H₂ as a function of biotic layer depth. The resulting probability density is shown via colored bins.

Solid black trendlines indicate median flux values while vertical lines show maximum allowable biogenic sinks for each metabolism from our photochemical model calculations. The interception of these vertical lines with the median diffusion flux shows the maximum depth to which subsurface life could be exploiting atmospheric free energy. Below these depths, microbes would be limited by the downward diffusion of atmospheric gases through the regolith rather than the supply of reactants from photochemical reactions

$\sim 1.4 \times 10^{32}$ cells. Thus, our calculated maximum cellular biomass estimate of 10^{27} cells is $2\text{-}40 \times 10^{-5}$ of the Earth's biomass or roughly one hundred thousandth of the estimated total of Earth's biomass.

Converting this maximum cellular biomass for Mars into a metric biomass (in kg) requires an average microbial mass. Assuming an average dry mass of 14 fg cell^{-1} (Hoehler & Jorgensen, 2013; Kallmeyer et al., 2012), this amounts to $\sim 10^{11}$ kg total mass, assuming dry cell mass

constitutes 20% of total cellular mass (Bratbak & Dundas, 1984). In more tangible terms, this total mass is the equivalent to approximately 1 million blue whales (taking the average mass of a blue whale as 1.85×10^5 kg). While this amount of blue whales worth of microbial life on Mars appears large, it is vanishingly small compared to the total biomass on Earth today and is an upper limit based on generous assumptions that give the largest biomass.

As a comparison to the previous estimate, B. P. Weiss et al. (2000)'s work produced maximum biomass of $\sim 10^{10}$ kg or $\sim 120,000$ blue whale masses. However, this value uses their calculated energy flux at 10 m depth, assumes only 10% metabolic efficiency, and use a “typical maintenance energy” value of $\sim 10^{-4}$ kJ g⁻¹ s⁻¹ ($\sim 10^{-18}$ kJ cell⁻¹ s⁻¹ using our assumed average cell mass). While it may be reasonable to assume such a power requirement and biological efficiency, this does not place an upper limit on the maximum possible biomass as microbes have been discovered subsisting off smaller energy fluxes. Indeed, if we take the maximum flux values used in their biomass calculations and apply our updated values for basal power requirement, full metabolic efficiency, and updated Gibbs free energy then their maximum biomass would be $\sim 10^{29}$ cells equivalent to $\sim 10^{13}$ kg or approximately 70 million blue whale masses.

The maximum biomass we calculate is likely an overestimate. Other considerations that we have not included in this methodology would lower the upper bound on biomass. It is assumed here that the metabolisms work at 100% efficiency - which is unlikely as energy is wasted in ‘spillover’ reactions and Darwinian evolution favors survival over efficiency (B. P. Weiss et al. (2000) assume the biological oxidation process works at $\sim 10\%$). We also use basal power requirements to estimate biomass, but this is the minimum energy required to keep cells alive and does not account for additional energy costs such as reproduction. Abiological oxidation reactions with the regolith should contribute a small portion of our calculated maximum reactant sinks, thus the maximum biological sinks would be smaller than reported here.

There is also a great uncertainty in the minimum power requirements necessary to sustain actively metabolizing life. Older literature typically used the term “minimum maintenance energy” (including Weiss et al. 2000), which is defined as the minimum energy flux required to sustain a steady-state population without growth. However, recent work has contested this term as it

includes both energy that is useful for the cells, e.g. motility and synthesis of bioimportant macromolecular compounds, along with energy that is wasted in “spill-over” reactions and thus does not accurately represent the actual minimal energy required for life to survive. Following Hoehler and Jorgensen (2013), we elected to use the basal power requirement, which is the energy flux required for the minimal amount of cellular functions to maintain a metabolically active cell.

Both the minimum maintenance energy and basal power requirement are notoriously difficult to measure. Lab studies have yielded maintenance energies of order 10^{-5} kJ g⁻¹ s⁻¹ (Tijhuis et al., 1993) to downwards of 10^{-7} kJ g⁻¹ s⁻¹ (Scholten & Conrad, 2000). The upper end of these values are especially problematic as it is ~26 times greater than the maintenance energy of a human body, which is not operating near its limits (Hoehler, 2004), and because it is temperature dependent. Minimum power requirements are especially difficult to characterize in natural settings (Kempes et al., 2017; Onstott et al., 2014; Van Bodegom, 2007), and recent work has shown that the BPR is a function of cellular volume (Kempes et al., 2016). Measurements of sulfate-reducing bacteria in anoxic marine sediments show BPRs as low as 3×10^{-23} kJ s⁻¹ cell⁻¹ (Lever et al., 2015). This lower value agrees well with other recorded lower bounds on BPR of $\sim 5 \times 10^{-23}$ kJ s⁻¹ cell⁻¹ (LaRowe & Amend, 2015; Marschall et al., 2010). A back-of-the-envelope attempt by LaRowe and Amend (2015) at arriving to a theoretical lower limit provides a BPR of $\sim 1 \times 10^{-24}$ kJ s⁻¹ cell⁻¹ to prevent racemization of amino-acids and thus population decay. However, the authors do note that this may not be a true limit and could be off by orders of magnitude. Additionally, a BPR of $\sim 2 \times 10^{-22}$ kJ s⁻¹ cell⁻¹ is more characteristic of microbes in these ultra-low energy environments rather than the lowest cell-specific BPR of $\sim 3 \times 10^{-23}$ kJ s⁻¹ cell⁻¹. We have also been assuming in our calculations that the microbes are living at their lower limits with no population growth with very long turnover rates, which may very well be not the case.

It is also important to note that this is a rigorous biomass estimate for *actively* metabolizing microbes in communication with the atmosphere. There are other possible scenarios for extant life on Mars (see Fig. 3.4). For example, there could be an indefinitely large community of dormant microbes. Bacterial endospore states are highly durable to withstanding inclement environmental conditions and very low energy fluxes. Cellular turnover times of $\sim 10^3$ years have been found in deep biospheres on Earth (Lomstein et al., 2012), but the energy costs required of these dormant

cells is unclear (Hoehler & Jorgensen, 2013). Nevertheless, it is unlikely that spore-formation is evolutionarily advantageous for long-term survival in environments subject to harsh and degrading conditions, such as on Mars, due to the deterioration of DNA over time if molecular repair does not meet or exceed molecular damage (Cockell et al., 2016; Johnson et al., 2007; McKay, 1997; Teodoro et al., 2018).

Additional biomass could also be concentrated in self-sustaining isolated pocket communities that are closed-off from the atmosphere via impermeable lithological units (e.g. terrestrial microbes in Lin et al., 2006). However, these smaller isolated pockets would be harder to detect even with advanced drilling. One could also conceive of rarer unusual metabolisms that are in communication with the atmosphere but live off the regolith without excreting detectable products into the atmosphere. But these ecosystems seem unlikely, given the abundance of free energy available in the atmosphere and the simplicity and primitive nature of the CO₂-reaction genes in terrestrial microbes.

Finally, the results from our diffusion calculations place additional restrictions on the abundance and distribution of life. We find that CO and H₂ can diffuse into the subsurface at much higher rates than our maximum calculated biological sinks in the upper 500 m. This suggests that life is not taking full advantage of this available free energy in the upper regolith as the photochemical energy far outweighs alternative subsurface sources (Jakosky & Shock, 1998). Therefore, any life in the upper crust is not limited by the available free energy but by some other factors (e.g. lack of liquid water or temperature dependency). Of course, this is consistent with the calculated instability of liquid water in the upper regolith, likely making it uninhabitable (Clifford et al. 2010). Future missions could also measure the CO and H₂ fluxes at the surface of Mars to place tighter constraints on the availability of reactants into the subsurface.

It should also be noted that we consider these diffusion calculations to apply to the low to mid-latitudes as the high latitudes will have an ice-saturated cryosphere, which is not considered here. The lower latitudes will be desiccated due to the instability of ground ice with respect to the water vapor content of the atmosphere (Clifford et al., 2010; Dundas et al., 2014; Feldman et al., 2004). Our calculations are relevant to the low to mid-latitudes because subsurface

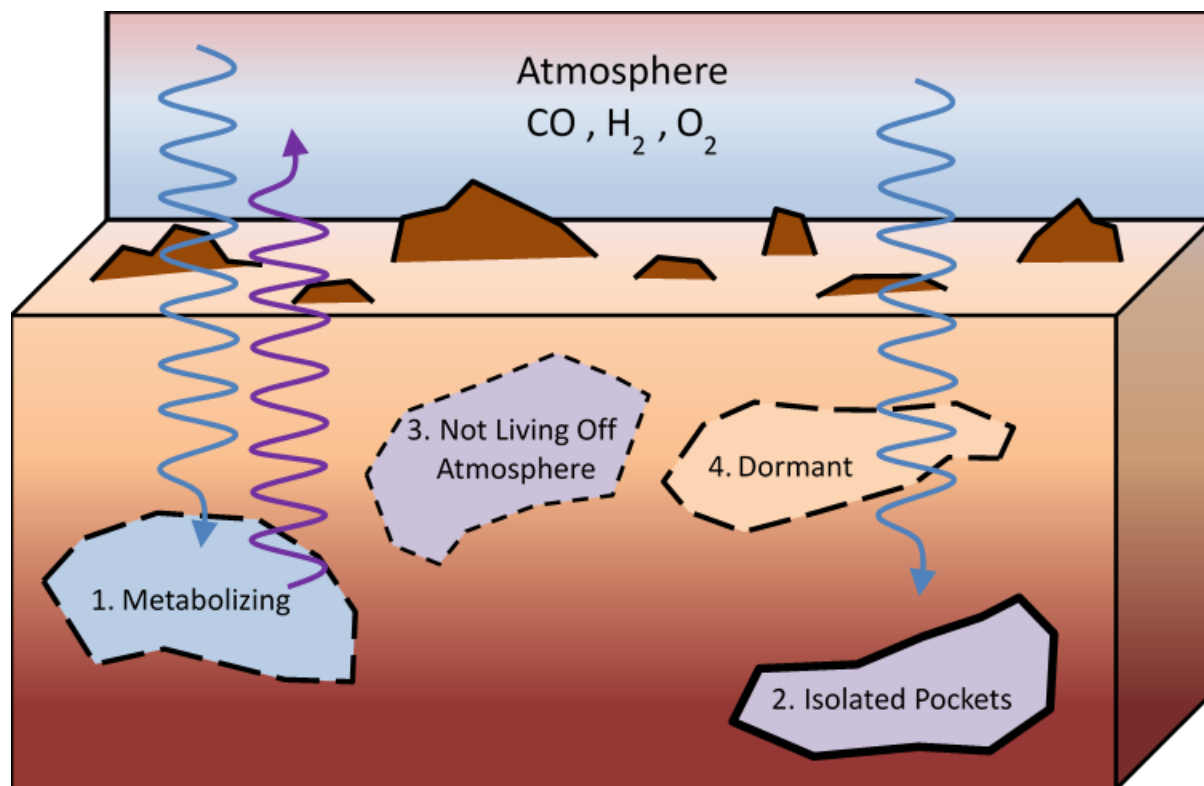


Figure 3.4. Potential sites for life on Mars. This study estimates the maximum number of actively metabolizing microbes that are in communication with the atmosphere (1). There could be actively metabolizing microbes in small communities that are sealed off from the atmosphere (2) or are neither taking advantage of the available atmospheric free energy nor producing detectable byproducts (3). The number of dormant microbes (e.g. endospores) (4) could be indefinitely large, but would not be evolutionarily advantageous for long-term survival on Mars. Downward arrows indicate fluxes of available free-energy reactants and upward arrows indicate flux of metabolized products into the atmosphere. All are assumed to be in contact with some form of liquid water (e.g. rare briny fluid pockets or a deep aquifer).

aquifers could be stable there over geological timescales (Grimm et al., 2017; Grimm & Painter, 2009). As subsurface life presumably requires a liquid groundwater table, which is typically estimated around ≥ 5 km depth (Clifford et al., 2010), the potential diffusive flux may be smaller than our calculated maximum biogenic surface sinks at these depths and further limit the maximum allowable biomass unless a minimum water activity level for life is maintained by a minimum H_2O layer thickness in the pore space somehow. Additionally, we note our use of a 1D photochemical

model assumes a globally-distributed biosphere, but if life exists it could be more spatially limited, so the biomass estimate would presumably be even lower.

3.6 CONCLUSIONS

The martian atmosphere has an untapped free energy source of $\sim 136 \text{ J mol}^{-1}$ predominantly contributed by the CO-O_2 ($\sim 133 \text{ J mol}^{-1}$) and $\text{H}_2\text{-O}_2$ ($\sim 3 \text{ J mol}^{-1}$) redox pairs (Krissansen-Totton et al., 2016). This constant photochemically-produced disequilibrium is far larger than any other energy sources known to exist on Mars, such as internal heat. Given life's tendency to exploit chemical free energy, we show how these relatively high concentrations of CO and H_2 coexisting with high concentrations of O_2 can represent antibiosignatures and that any extant life on Mars is severely limited.

We quantify how much life could be taking advantage of this 'free lunch' by using a 1-D photochemical code and modeling biological activity as a downward surface flux of CO and ramping it up until the modeled atmosphere diverges from observations. We find maximum feasible downward biogenic sinks of $1.5 \times 10^8 \text{ molecules cm}^{-2} \text{ s}^{-1}$ and $1.9 \times 10^8 \text{ molecules cm}^{-2} \text{ s}^{-1}$ for CO and H_2 respectively that are robust to uncertainties in observations and tunable model parameters. Using very conservative estimates on the minimal power requirements for microbial life and metabolic efficiencies, this equates to an upper limit of approximately 10^{27} cells or 1 million blue whales worth of metabolizing biomass that could be living off this atmospheric energy. This biomass estimate is highly dependent upon choice of cellular basal power requirements and typical microbes have higher requirements, thus any life is likely to be much smaller in extent. Diffusion calculations also imply that this biomass limit applies to life actively metabolizing within a few kilometers of the surface with the overall desiccation of the upper crust further limiting the possible biomass.

These results imply that any extant life on Mars is extremely limited in scope. CO and H_2 metabolisms are simple and phylogenetically widespread on Earth so that any microbial-like life on Mars should evolve to exploit this energy. Additionally, more plausible assumptions on metabolic efficiencies, combined with recognizing the maximum gas diffusion limit into the crust

realistically only reach small pockets of liquid water, imply that any biomass may be orders of magnitude smaller than presented here. Thus, what we present here is a robust upper limit on extant actively metabolizing martian life in contact with the atmosphere.

Additionally, the concept of using sufficient atmospheric CO and H₂ concentrations as an antibiosignature could be applied to future research in exoplanet characterization. While the possibility for biogenic gases in exoplanet atmospheres as possible biosignatures has garnered much attention (e.g. Schwieterman et al., 2017; Seager & Bains, 2015), the possibility of anti-biosignatures has received less (Catling et al., 2018; Wang et al., 2016). Where sufficient knowledge is known on the atmospheric composition, the presence of high concentrations of CO or H₂ in thermodynamic disequilibrium would allow for a deduction of an absence of a productive biosphere.

Chapter 4. QUANTITATIVE HIGH-RESOLUTION RE- EXAMINATION OF A HYPOTHESIZED OCEAN SHORELINE ON MARS

This chapter was originally published in JGR: Planets:

Sholes, S.F., D.R. Montgomery, and D.C. Catling. (2019). “Quantitative High-Resolution Re-Examination of a Hypothesized Ocean Shoreline in Cydonia Mensae on Mars.” *Journal of Geophysical Research: Planets* 124: pgs. 316-336. doi:10.1029/2018JE005837

4.1 ABSTRACT

Primary support for ancient Martian oceans has relied on qualitative interpretations of hypothesized shorelines on relatively low-resolution images and data. We present a toolkit for quantitatively identifying paleoshorelines using topographic, morphological, and spectroscopic evaluations. In particular, we apply the validated topographic expression analysis (TEA) of Hare et al. (2001) for the first time beyond Earth, focusing on a test case of putative shoreline features along the Arabia level in northeast Cydonia Mensae, as first described by Clifford and Parker (2001). Our results show these curvilinear features are inconsistent with a wave-generated shoreline interpretation. The TEA identifies a few potential shoreline terraces along the historically-proposed contacts, but these tilt in different directions, do not follow an equipotential surface (even accounting for regional tilting), and are not laterally continuous. Lineaments appear blocky in nature at small scales and they bifurcate, truncate, and merge along track, which is more consistent with material boundaries for lithological units exposed along a degraded crater wall. These results do not preclude the existence of an ancient hemispheric ocean, but the geophysical and high-resolution topographic data at this site do not support such an interpretation.

4.2 INTRODUCTION

4.2.1 *Background Information*

The extent and duration of large open reservoirs of liquid water on the surface of Mars is one of the most intriguing questions about the planet’s past. Support for vanished oceans

historically stems from the recognition that large outflow channels and valley networks empty into the northern plains, suggesting these lowlands served as a basin where water pooled (V. R. Baker et al., 1991; Jöns, 1985; Lucchitta et al., 1986). These observations, coupled with hand-mapped contacts along the edges of the northern plains on comparatively low-resolution images led to the interpretation of these contacts as paleoshorelines (Parker et al., 1993; Parker et al., 1989). The question of whether or not such an ocean (or oceans) existed, has profound implications for the past climate of Mars (e.g. Banfield et al., 2015; Jakosky & Phillips, 2001; Lammer et al., 2018; Ramirez & Craddock, 2018), the possibility of the planet harboring ancient life (e.g. Beaty et al., 2005), and the evolution and role of liquid water in its surficial geology (e.g. Carr & Head, 2010, 2015).

Two distinct contacts identified by Parker *et al.* (1989; 1993) were described roughly following the topographic dichotomy along the northern plains boundary and interpreted as corresponding to different hypothesized ocean highstands. The Arabia level (“Contact 1”) roughly follows the dichotomy transition region and represents a hypothesized larger and older ocean stand. The Deuteronilus level (“Contact 2”) is an inner contact almost entirely within the northern plains thought to represent a smaller and younger ocean stand (Parker et al., 1993; Parker et al., 1989). Additional possible discontinuous shorelines have been proposed, along with the “Meridiani Contact” that extends beyond the dichotomy boundary into the southern highlands and would represent a much larger and earlier ocean stand (Edgett & Parker, 1997).

Initial identification of these hypothesized shorelines was based on the best available high-resolution *Viking* images ($\sim 10 \text{ m px}^{-1}$) with most of the contacts mapped at comparatively lower resolutions ($\sim 50\text{-}200 \text{ m px}^{-1}$) (Clifford & Parker, 2001; Parker et al., 1993; Parker et al., 1989). Later interpolation of these contacts onto Mars Orbiter Laser Altimeter (MOLA) topographic data (D. E. Smith et al., 2001) show vast ranges in elevations of $\sim 2.5 \text{ km}$ for the Arabia contact (Carr & Head, 2003) and $\sim 0.6 \text{ km}$ for the Deuteronilus contact (Carr & Head, 2003; Ivanov et al., 2017). Such wide ranges in elevation for suspected equipotential surfaces cast doubt on a paleoshoreline interpretation. Misidentification along parts of the Arabia contact with the low-resolution *Viking* data may contribute up to $\sim 2 \text{ km}$ of the discrepancy (Parker & Calef, 2012), while some have invoked true polar wander and/or Tharsis-induced long-wavelength flexure as a means of

deforming the shorelines to their present levels (N. H. Chan et al., 2018; Citron et al., 2018; Perron et al., 2007).

Since these contacts were first proposed, many studies have used them as evidence of past oceans on Mars despite near complete ambiguity in other lines of evidence relevant to assessing their existence. Studies have found that past Mars water inventories are both consistent with (Villanueva et al., 2015) and incompatible with (Carr & Head, 2015) an early ocean. Similarly, radar investigations into the underlying deposits under the northern plains show permittivity values argued to be in agreement with both vesicular lavas (Boisson et al., 2011) and sedimentary ocean remnants (Mouginot et al., 2012). Further investigations of these geomorphological contacts have similarly both supported and challenged a coastal origin for segments along both the Arabia and Deuteronilus contacts (e.g. Carr & Head, 2003; Parker et al., 2010). Many putative paleoshoreline locations exhibit landforms that more closely resemble features formed by other processes, such as lava flows and mass wasting events (Carr & Head, 2003; Ghatan & Zimbelman, 2006; Sholes et al., 2014).

Much of the recent focus on geomorphological evidence of shorelines has been placed on reconciling the discrepancies in the absolute elevations along the contacts with regional equipotential surfaces (e.g. N. H. Chan et al., 2018; Di Achille & Hynek, 2010; Parker & Calef, 2012; Parker et al., 2010). Apart from the occasional paper (e.g. studies of south Isidis by Erkeling et al. (2014); Erkeling et al. (2012)), little research has been done to re-examine individual proposed shorelines using the latest available high-resolution data products. As the amount of data grows, it is important to reassess these regional contacts at the local level. This reassessment can test if broad-scale mechanistic interpretations are supported by the fine-scale geomorphological evidence.

Understanding the role and extent of past liquid water is especially crucial in determining the habitability of past Mars. Life, as we know it, requires liquid water, which cannot persist on the current surface of Mars under the cold, dry, and thin atmosphere. Analysis of closed-basin crater lakes suggests that they represent past transient bodies of liquid water (Goudge et al., 2015; Grotzinger et al., 2015) and there is evidence of a $>10^6$ km² liquid-water Eridania sea (Irwin et al.,

2004; 2002). However, positive identification of wave-generated paleoshorelines could aid in constraining the paleobarometry of Mars' atmosphere (Banfield et al., 2015; Kraal et al., 2006) and indicate whether the climate was stable enough to prevent the geologically rapid dissipation of any oceans to create such landforms (Jakosky & Phillips, 2001). Long-lived periods of clement conditions and hydrologic cycling in the presence of an ocean have been proposed (Hynek et al., 2010). Oceans have also been proposed as aiding in the production of prebiotic chemistry (e.g. Stüeken et al., 2013). Thus, the presence, longevity, and magnitude of any putative ocean(s) are important habitable conditions on early Mars.

Here, we present and apply a quantitative toolkit for resolving and characterizing landforms on Mars that are hypothesized to be paleoshorelines. We include classical tools such as spectral analysis, thermal inertia, and qualitative photogeologic mapping. But in addition, for the first time, we apply the topographic expression analysis (TEA) methodology used for quantitatively identifying and comparing wave-generated paleoshorelines on Earth (Hare et al., 2001; Jewell, 2016), to their suspected Martian counterparts. With the success of this methodology in identifying subtle intermittent paleoshorelines on Earth, we propose using TEA as a useful additional criterion for identifying extraterrestrial wave-generated paleoshoreline candidates. While the TEA method is unable to positively identify the genetic origin of the landforms due to the potential for false positives, recognizable and coherent terrace features should meet the criteria described below in their topographic signal (when they exist in the geomorphology). Thus, the combined approach using all the available tools presented here can aid in determining a probable origin.

Any Martian shorezones should be laterally continuous across the basin and general opinion suggests that preserved wave-generated erosional shorelines should exhibit a bench or platform shape (M. A. Chan et al., 2016). Given the climatic uncertainty for past Mars, perennially ice-covered, or even completely frozen, oceans have been hypothesized (Carr & Head, 2019; Clifford & Parker, 2001), potentially limiting wave-generated coastal landforms. However, the amount of time for a convecting sea to freeze (Banfield et al., 2015; Carr, 1996), depends on the salinity, water depth, and climate, and some parameter combinations allow sufficient time to erode shoreline features (Clifford & Parker, 2001; Kreslavsky & Head, 2002). Even once frozen, potential seasonal breakup of thin shoreline ice may allow for wind-generated waves (Parker &

Currey, 2001) under suitable climatic regimes and with sufficient wave energy (Banfield et al., 2015; Kraal et al., 2006). Otherwise, coastal processes along a permanently ice-capped sea would likely be subject to currents formed by stream input, ice-cover oscillations due to winds (creating standing-wave like currents), and heat transfer (Castendyk et al., 2015; Malm, 1999; Wharton et al., 1995).

Despite an abundance of newer high-resolution data, many of the proposed wave-generated shoreline “bench” features have been identified primarily upon a qualitative assessment in orbital imagery that has much lower spatial resolution (e.g. Viking, Thermal Emission Imaging Spectrometer (THEMIS), and Mars Orbiter Camera (MOC) wide angle) than currently available and quantitatively with limited low-resolution elevation data (i.e. MOLA). Little research has been done to reinvestigate these features with the new data. Thus, there is a growing need for both a reanalysis with higher resolution data and better quantitative methods for defining and measuring these potential terrace features.

Ultimately, our approach provides a framework for testing the validity of hypothesized extraterrestrial wave-generated paleoshoreline contacts. Here we apply these methods to a proposed Martian paleoshoreline first described at depth in Clifford and Parker (2001) (their Fig. 4) at a site multiple sources have cited as having contacts strongly reminiscent of terrestrial strandlines (erosional features demarking equipotential water levels) (Cabrol & Grin, 1999; Clifford & Parker, 2001; El Maarry et al., 2010; Parker, 2004; Parker et al., 2002; Parker et al., 2010; Sholes et al., 2014; Świąder, 2014; Webb, 2004).

4.2.2 *Site Introduction*

The site itself lies to the northeast of the Cydonia Mensae region along the topographic dichotomy and is centered at approximately 36.4°N, 350.2°E. It straddles the early Hesperian transition unit and the middle Noachian highland unit (Tanaka et al., 2014) along the older Arabia level with the Deuteronilus level only ~100 km north. Most studies have focused on the eastern-most crater (Crater A) in a complex of three adjacent remnant craters ~50 km in diameter (see Fig. 4.1). Though, hypothesized paleoshorelines have also been identified locally along Crater B’s

western rim (Parker et al., 2010). Parts of the crater rim septa separating the craters have been eroded away and the northeast section of Crater A and the northwest section of Crater C are also opened, exposing the craters' interiors to the northern plains. Thus, depending on the timing of these breaches, these hypothesized paleoshorelines potentially could be the result of either a crater lake or a northern ocean. We focus primarily on Crater A (the easternmost crater) given multiple targeted high-resolution stereo pair imagery available for that area (white boxes in Fig. 4.1).

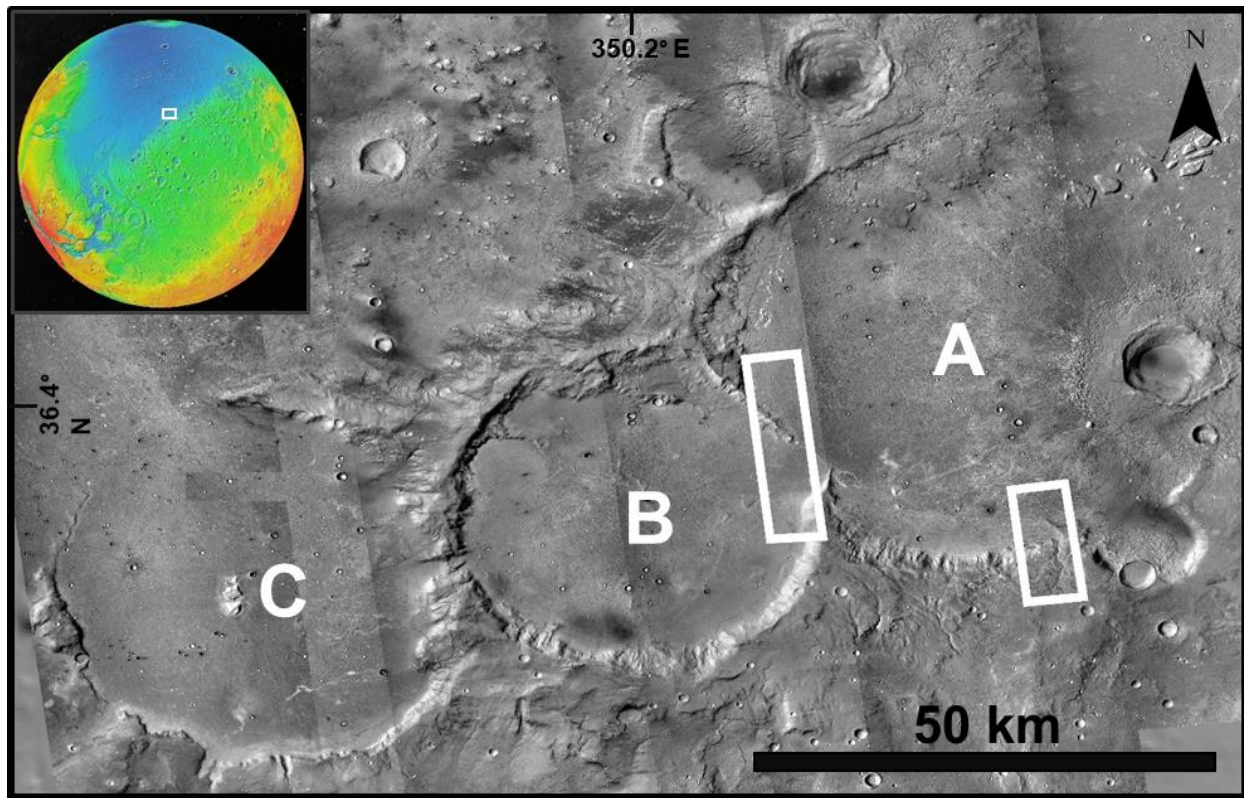


Figure 4.1. CTX mosaic of the three-crater system (centered three largest craters labeled A-C) to the NE of Cydonia Mensae showing the selected test site region. The center of the image is approximately 36.4°N, 350.2°E. White boxes indicate DEM footprints from HiRISE stereo pairs for the western and southern sites. The crater complex is open to the northern plains (and thus a potential ocean) on the NE of Crater A and NW of Crater C. *Inset* - MOLA colored elevation showing the site (white box) in relation to the topographic dichotomy (which roughly follows the blue/green boundary on the globe).

Interpretation of these features as paleoshorelines largely hinged on numerous visually identified subtle arcuate ridges that follow the dissected margin of the highlands. These ridges were interpreted by Clifford and Parker (2001) as constructional coastal barrier ridges while other visible arcuate lineaments were interpreted as possible strandlines. Later assessments by Ghatan and Zimbelman (2006) claimed that these ridges were more likely created by interstitial-ice-creep deformation (Squyres, 1979; Squyres & Carr, 1986), aeolian processes, or debris-covered glaciers (Levy et al., 2010) based on similar features found in a nearby enclosed crater (i.e., one not open to the northern plains). However, since then, the *Mars Reconnaissance Orbiter* has acquired a wealth of high-resolution data and allowed production of sub-meter elevation data. These data products allow for a more complete and thorough analysis of the site than was otherwise possible, especially given the typically narrow extent of both constructional and erosional coastal landforms. Crater floor polygons have also been identified within the base of Crater A and used in support for a paleolake interpretation (Cabrol & Grin, 1999; El Maarry et al., 2010). These polygons typically occur in crater infill material and are usually interpreted as the result of thermal stress and periglacial processes; though water ice is expected to be unstable at these lower latitudes (Clifford et al., 2010; Mellon et al., 1997). Modeling suggests they can instead be ancient crater lake desiccation polygons. However, both past climatic variations, caused by changes in obliquity, and desiccation of crater lake sediments can account for the observed ~40 m diameter polygons (El Maarry et al., 2010) leaving an ambiguous interpretation as to their origin.

4.3 METHODS

4.3.1 *Photogeological Mapping*

We map geomorphic features using ArcGIS (www.esri.com) for the sites of interest (where paleoshoreline features have been proposed) identifying key landforms and units to determine a likely formational mechanism. We focus on using available High Resolution Imaging Science Experiment (HiRISE) images as they provide the greatest detail at ~30-50 cm px⁻¹ (McEwen et al., 2007). However, HiRISE data have small surface footprints and limited global coverage so Context Camera (CTX) images (~6 m px⁻¹, nearly global coverage) are used for regional mapping and supplementing local HiRISE coverage (Malin et al., 2007). Since many of the putative contacts have previously been investigated with resolutions comparable to CTX images (e.g. Clifford &

Parker, 2001; Ghatan & Zimbelman, 2006; Parker et al., 2010), much more emphasis here is placed on characterizing the lineaments with available HiRISE data. This includes testing for lateral continuity.

Contacts previously published in the literature are mapped, as are any additional contacts that arise in examining the higher resolution data. After locating the candidate paleoshoreline contacts, we mapped and described characteristic landforms that are locally adjacent or congruent with the contacts. Table 4.1 provides a necessarily incomplete list of possible characteristic landforms and their associated formational processes which we have lumped into five broad formational categories, including coastal landforms that define true shorelines (both from open and ice-covered seas), and four categories that can mimic shoreline-like contacts: volcanic, glacial, impact, and “other” (e.g., diffuse albedo contacts and mass-wasting features).

Table 4.1. Necessarily abbreviated list of typical landforms and their associated characteristic features used for identifying the origin of contacts that may be shorelines in the case of coastal features or may mimic shorelines in the case of other landforms. While by no means exhaustive, the table provides a useful overview.

Volcanic	Glacial	Coastal	Impact	Other
overlapping lobate flows	lobate flows	coastal bluffs/cliffs	craters	fault escarpments
destroyed craters	contact scouring	strandlines	ejecta blankets	albedo contacts
lava tubes	debris aprons	marine terraces	melt flows	lithological contacts
pressure ridges (perpendicular to flow direction)	flow lineaments (in direction of flow)	beaches, berms, arcuate beach ridges	concentric lineaments	colluvium, mass wasting features
rocky terrain	moraines	deltas		
dark color (basaltic?)	drumlins, erratics, eskers	barrier islands, spits, tombolos		
resistant cap rocks	U-shaped valleys	sea-stacks		
terminus slopes downward	terminus slopes downward	ocean slopes upward to shore		
high lava marks (from lava drainage)	pressure ridges (perp. to flow)	pillow basalt transitions		

The difficulty in qualitative photogeological mapping lies in the 1) overlap between landforms formed through vastly different processes and 2) their unknown preservation potential over billions of years. This difficulty often forces a subjective interpretation (e.g. barrier ridges, ice-shoved ridges, volcanic and glacial pressure ridges). Arguably some of the best features to identify paleoshorelines would be exposed subaerial lava flows that progress into pillow basalts such as subaerial-to-subaqueous transitions found in terrestrial geology even as far back as in Archean rocks (e.g. Som et al., 2016). Pillows, however, are unlikely to be observable even with modern high-resolution images but could be identified with future missions. While mega-pillows would be easier to observe and have been identified on Earth, they are much rarer than typical pillow basalts and not as densely packed (Bear & Cas, 2007; Walker, 1992).

4.3.2 *Topographic Analysis*

4.3.2.1 Digital Elevation Models

Many common landforms have distinct topographic expressions that aid in their identification. MOLA data has typically been used in the past as it had nearly global coverage, but at $\sim 400\text{-}500\text{ m px}^{-1}$ binned lateral resolution (and $\sim 300\text{ m}$ N-S along-track altimetry shot spacing) it is too coarse for studying narrow features but is useful for studying regional trends. Digital elevation models (DEMs) have been made available for many of the High Resolution Stereo Camera (HRSC) stereo pair images (Jaumann et al., 2007). These HRSC DEMs have better spatial resolution at $\sim 75\text{ m px}^{-1}$ but at the expense of vertical resolution.

Typical terrestrial non-tidal shorezone topographic features (e.g. lacustrine wave-cut terraces not subject to terrestrial oceanic-scale tides, modulated by fetch, wind-speed, atmospheric pressure, and local shore geometry) are on the order of tens of meters wide (or less), thus, MOLA and HRSC DEMs are ill-equipped to accurately identify them. To get submeter resolution DEMs we use the open source NASA Ames Stereo Pipeline (ASP) (Moratto et al., 2010; Öhman, 2013; Shean et al., 2016) to perform automated photogrammetry on HiRISE stereo pair images located at each site. This produces DEMs with typically $1\text{-}2\text{ m px}^{-1}$ spatial resolution and $\sim 1\text{ m}$ vertical resolution. Where HiRISE stereo pair images are unavailable, CTX and MOC narrow angle stereo pairs (and some overlapping CTX images, given sufficient illumination angles and viewing

geometries) can also be used with ASP to create DEMs with resolutions as good as $\sim 6 \text{ m px}^{-1}$ (Öhman, 2013; Tao et al., 2018). In the absence of images suitable for photogrammetry, MOLA PEDR (Precision Experiment Data Record) data products offer individual altimetry shot readings. The resulting DEM is checked for artifacts using ASP-outputted masks. Some areas, typically places that are featureless or with steep slopes, fail the correlation process and appear as no-data pixels. We patch these small discontinuous areas with the mean value of their surrounding pixels (using the FocalStatistics command in ArcMap) while larger collections of missing pixels are cropped out entirely. Other possible DEM artifacts usually manifest as seams in the data caused by slight differences across the CCDs (charged coupled device) or as a “block” pattern caused by problems with the parameters set in the ASP algorithm (Kirk et al., 2008). These features can be difficult to remove (if reprocessing with different parameters is unable to create fewer errors). So, to avoid incongruous topographic analyses (e.g. sharp vertical jumps in elevation along artifact boundaries), we evaluate transects bounded within any artifacts.

To compare the resulting ASP elevation data with the traditionally cited shoreline levels (and across separately-derived ASP built DEMs), we attempt to correct for absolute elevations. HiRISE data products are map projected and bundle adjusted in ISIS3 (Integrated Software for Imagers and Spectrometers) before DEM creation and then subsequently referenced to the MOLA spheroid. Since ASP-derived stereo photogrammetry measurements yield MOLA ellipsoidal-referenced raster data rather than orthometric rasters, a correction must be applied for the deviation from the areoid (Mars geoid). MOLA PEDR points are overlaid onto a resampled (to the median value) DEM that matches the 300 m point shot resolution. Points where the resampled slope is greater than 15° are discarded. The elevation difference between the resampled topography and the MOLA PEDR points is then calculated and outliers (> 2 sigma) are also removed. An IDW (Inverse Distance Weighted) interpolation function (3rd order polynomial) is performed on the elevation difference points in ArcMap to create a surface raster that characterizes any cross-track “tilt” in the MOLA data. This resulting raster is then added to the areoid-subtracted DEM to form absolute elevations that are tied to MOLA elevation data. Total error on the absolute elevations is estimated at ± 3.2 m based on an areoid error of at least ± 3 m (Lemoine et al., 2001), individual shot point errors of ± 1 m (Neumann et al., 2001), and an estimated ASP-derived DEM vertical precision of 0.3 m.

4.3.2.2 Topographic Expression Analysis (TEA)

We employ the topographic signal processing techniques of Hare et al. (2001) which have been used successfully for identifying subtle, degraded, and topographically “noisy” (due in part to surface roughness) shoreline terraces on Earth (Hare et al., 2001; Jewell, 2016; Schide et al., 2018). Many of these subtle terrestrial paleoshorelines are difficult to discern with remote imagery, lidar, and field observations but can be clearly followed using this topographic expression analysis (TEA) on a high-resolution DEM (See Figs. 2 and 13 of Jewell (2016) for examples of identifying subtle shoreline features). Given the age of these hypothesized Martian paleoshorelines it is expected that any preserved features would be subtle in their topographic signature expressions. While the TEA signal is not unique to paleoshorelines, it should be expressed by all erosional wave-generated paleoshoreline terraces when they exist in the geomorphology. Thus, we employ TEA as a key tool for testing whether putative wave-generated terrace features meet the topographic criteria necessary for paleoshoreline identification.

Given the challenges associated with recognizing and characterizing degraded wave-generated terrace features, analysis is done on the residual topography rather than the raw elevation data (Becerra et al., 2016; Hare et al., 2001; Head et al., 2002). The residual topography is the difference between the high-resolution DEM elevation data and an “idealized” local hillslope (one without terraces), highlighting where landforms deviate significantly from the overall slope and enhancing their morphological signal locally. By evaluating changes in the slope of the residual topography, subtle yet coherent geomorphic properties are illuminated. ArcMap’s Trend tool is used to approximate the overall hillslope using a surface polynomial of varying degree (given the high-number of potential shore/strand-line features in each area, we elect for a high polynomial degree of 6). The approximated hillslope is then subtracted from the high-resolution DEM to create the residual topography raster.

In the residual topography raster, terraces appear as alternating light/dark bands of high and low residual topography making this process a quick litmus test as to whether the DEM shows evidence of laterally-continuous features for additional investigation. Interpolated equally-spaced residual-topographic profiles are created orthogonal to the strike of the follow-up hypothesized terraces. The first derivative (the slope of the residual) and the second derivative (changes in the

slope) are also calculated to find the necessary inflection points of terraces. To reduce any “topographic noise” (e.g., from differential erosion or surface debris), a Savitsky-Golay filter is applied, via a MatLab script, to the residual topography profiles and their derivatives, which behaves similar to a moving-average filter. Choosing a window size and polynomial degree for the filter requires some experimentation to find a smoothing balance between data resolution and stability. Decreasing polynomial degree or increasing filter increases the amount of smoothing. We opt for similar parameters used by Jewell (2016) as default, given the similar resolution between their lidar DEM and our stereo-derived DEM (i.e. a window size of ~11 m and a 4th degree polynomial).

Terraces are identified by four components in the smoothed residual topography derivative products (Figure 4.2): the riser inflection (RI), marked by a maximum in the first derivative (max. slope) but only if there is a lower terrace, the riser crest (RC), marked by a minimum in the second derivative (max. concavity), the benchtop (BT), marked by minimum in the first derivative (flattest part of the terrace), and the knickpoint (KP), marked by a maximum in the second derivative (max. convexity and break in the basal slope to the hillslope). The bench width (BW) is defined as the distance between the RC and the KP. Figure 4.2 summarizes the process for an arbitrary terrace feature and shows the characteristic behaviors of each residual derivative that define the terrace components.

If there are any paleoterrace landforms present in the profile they will display these consecutive components (RI, RC, BT, and KP) even if they are degraded or subtle. Our MatLab script parses through the entire profile and outputs segments that fit the necessary criteria within a small epsilon value tailored to ignore insignificantly small maximum and minimum derivative values that correspond to any remaining “topographic noise”. While terrace features will exhibit this topographic behavior, there are other landforms that can appear as false positives. Thus, we manually inspected each identified segment for false positives (we also inspected for any terraces that were not identified by the TEA, but found none).

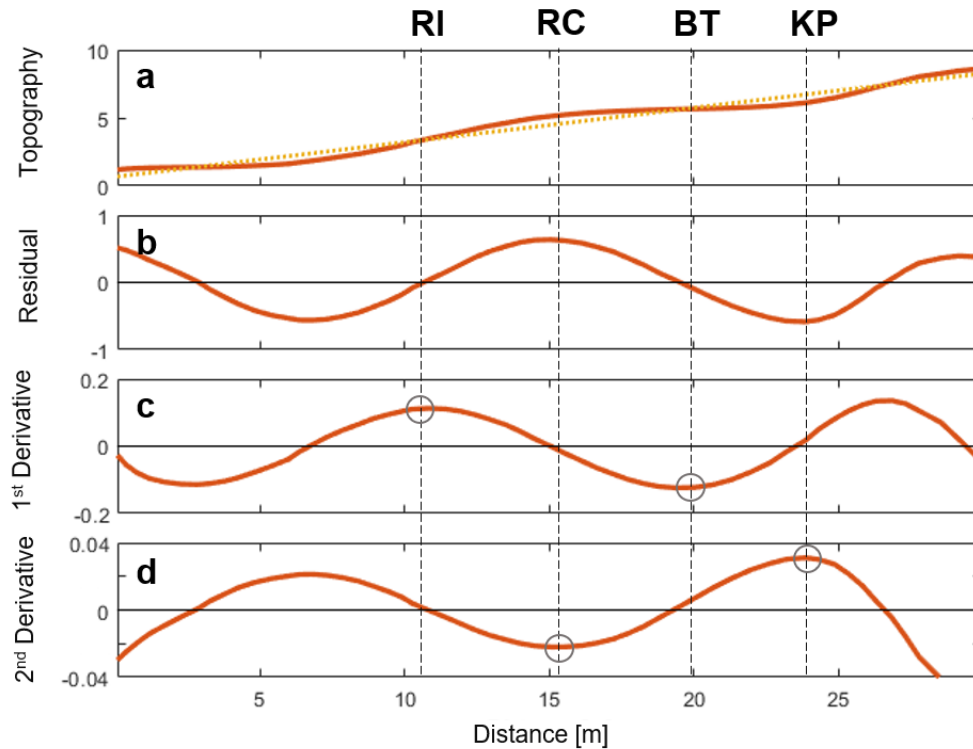


Figure 4.2. Topographic expression of an idealized paleoshoreline terrace after Hare et al. (2001); Jewell (2016). *a*) Solid line shows the topography of an arbitrary example terrace showing the riser inflection (RI), riser crest (RC), benchtop (BT), and knickpoint (KP). Dotted line shows a polynomial-fit “idealized” slope. *b*) The residual topography taken from subtracting the “idealized” slope from the topographic data. *c*) Smoothed first derivative of the residual topography where the circles represent defining the characteristic of RI and BT. *d*) Smoothed second derivative of the residual topography where the circles denote the defining characteristic for RC and KP.

Running this TEA for multiple (~20-30) transects along the hypothesized paleoshorelines allows for correlation of all quantitatively identified terrace features across the basin. Not only does this highlight whether the possible terraces follow the mapped contacts but creates standard reference points for comparing elevation data. We compared the calculated absolute elevation data of all found RC, BT, and KP to evaluate whether the identified terrace features follow an equipotential surface. Terrestrial shorelines can vary regionally in elevation by a few meters due to the local shorezone geometry (Atwood, 2006). Therefore, barring any significant geological activity (e.g. tectonic uplift or isostatic rebound) since their formation, shoreline contacts should

appear within a narrow band of elevations approximating an equipotential surface. Non-coastal-origin terrace features (e.g. lithological units undergoing differential erosion) could also exist but would be expected to have a trend across the basin following any coherent dip in the lithology. Additionally, the topographic profiles can be used in simple tests for typical shoreline geometries, such as the directionality of the slope. For example, lobate escarpments that face towards areas of high relief would be the opposite of what is expected in coastal zones (Malin & Edgett, 1999). Indeed, onlap of a deposit of some material up the marginal slope from the northern plains has been noted previously (Parker et al., 2010).

4.3.3 *Thermal Inertia*

Thermal inertia is a representation of a surface material's resistance to changes in temperature and its ability to conduct and store heat and thus provides important information about the bulk physical properties of the surface geology that cannot be acquired purely from images. Thermal inertia, I [$\text{J m}^{-2} \text{K}^{-1} \text{s}^{-1/2}$ or tiu (thermal inertia units) from now on], is defined as $I \equiv \sqrt{\kappa \rho c}$ where κ is the thermal conductivity [$\text{W m}^{-1} \text{K}^{-1}$], ρ is the density [kg m^{-3}], and c is the heat capacity [$\text{J kg}^{-1} \text{K}^{-1}$] (e.g. Putzig & Mellon, 2007a).

Variations in thermal inertia on Mars are dominated by changes to κ , which are affected by the porosity, grain size, and induration (degree of cementation) of the surface material (κ can vary by up to a factor of 1,000 while ρc only varies by a factor of ~ 5 for Martian surface materials (Catling et al., 2006; Wood, 2011)). Compositional differences due to changes in mineralogy have smaller effects on thermal inertia values. Given the range of factors that influence thermal inertia it should be viewed as an approximate guide to a qualitative physical designation: generally low values indicate mantling of loose fines (e.g., dust or very fine sand), intermediate values indicate cemented surfaces composed of sand-sized grains, and high values indicate rocky surfaces and bedrock. Uncemented dust-sized particles ($< 20 \mu\text{m}$) coating the Martian surface could have thermal inertias up to ~ 170 tiu (Catling et al., 2006; Presley & Christensen, 1997) while values > 1200 tiu have been interpreted as bedrock (C. S. Edwards et al., 2009).

Thermal inertia maps can be used in identifying gradational grain-size boundaries that would be expected along shorezone contacts. The largest transportable sediments are generally located where wave energy is the highest, therefore if the coastal sediments are preserved and exposed, thermal inertia maps could show evidence of sediment sorting with grain size. Generally, the average grain size decreases land-ward (from the inshore to foreshore to backshore subzones) (A. C. Edwards, 2001; Komar, 1998) and this may manifest itself as an increase in thermal inertia towards the highlands. These maps can also be used to analyze and identify potential constructional landforms versus underlying bedrock material and other heterogeneities that are useful for placing a genetic origin for uncertain morphological features (e.g., moraines or lava flows).

Global thermal inertia maps are available (e.g. Putzig & Mellon, 2007a), but we elect to create more finely tuned maps that better take into account local topography given the strong effects local slope and azimuthal orientation of the surface has on diurnal and seasonal surface temperature variations (Colwell & Jakosky, 2002; Putzig & Mellon, 2007b). We derive best-fit thermal inertia maps following the procedure of Sefton-Nash et al. (2012) and Catling et al. (2006) which use infrared (IR) images from the THEMIS (Christensen et al., 2004) and HRSC topography for each region.

The numerical thermal model generates lookup tables for spatially coincident THEMIS IR day and night images. These lookup tables provide synthetic diurnal surface temperatures as a function of topographic orientation (slope and azimuth angles), albedo, and thermal inertia for the THEMIS day-night images' latitude, solar longitude (season), and local time of day. Thermal inertia values are then determined by a best-fit least-squares analysis (Catling et al., 2006). Topographic data are primarily obtained from HRSC DEMs as opposed to the even higher-resolution HiRISE DEMs due to the small HiRISE footprint and incompatible fine resolution given THEMIS IR image resolution of $\sim 100 \text{ m px}^{-1}$. MOLA topographic data ($\sim 400 \text{ m px}^{-1}$) is used where HRSC DEMs are unavailable or of poor quality. Full details of surface temperature retrieval methods are found in Sefton-Nash et al. (2012). THEMIS images are chosen to reduce possible attenuating effects (e.g., seasonal aerosols).

4.3.4 Spectroscopy

Differences in aqueous activity across potential paleocoastlines on Mars could be preserved in the surface mineralogical record as hydrous or aqueous alteration minerals. To investigate surface mineral composition, we use near-infrared spectroscopic data obtained by the Compact Reconnaissance Imaging Spectrometer for Mars (CRISM) which operates at 0.36-3.92 μm sampled at 6.55 nm spectral resolution (Murchie et al., 2007). CRISM has multiple observation modes and, where available, we use the full resolution targeted (FRT) or the half-resolution targeted (HRL/HRS) hyperspectral data at 18 m px^{-1} and 36 m px^{-1} respectively. However, in places where high-resolution spectral data is limited or non-existent we rely on the multispectral survey data (MSP) which has nearly global coverage at lower spatial and spectral resolutions (72 spectral bands at 200 m px^{-1} sampling).

Processing of CRISM spectral data is performed in a manner similar to Amador and Bandfield (2016) and Bandfield et al. (2013) using ENVI software (www.harris.com) and the CRISM Analysis Toolkit (CAT; available on the Planetary Data System (PDS)). Atmospheric gas absorptions are corrected for using the scaled volcano-scan method described in McGuire et al. (2009). Existing spectral index maps (as described in Pelkey et al. (2007) and Viviano-Beck et al. (2014)) are used to rapidly assess evidence for key phase groups over an entire CRISM image. Follow up on regions of interest in the spectral index maps is done by evaluating I/F values (CRISM incident radiance over the solar radiance at Mars distance divided by π) and spectral ratios of individual pixels. Spectral ratios are used to confirm the presence of spectral features by eliminating any systematic instrument error in the image. These spectral ratios are produced by dividing a pixel of interest's I/F value by the I/F value of a pixel considered spectrally neutral within the same image column.

Hydrated minerals display diagnostic absorption features between 1.1-2.65 μm (Carter et al., 2013). A variety of indices diagnostic of particular mineral features have been developed for CRISM data based on the band depth at a particular wavelength. For example, the D2300 index is sensitive to a negative drop in slope at 2.3 μm , characteristic of hydroxylated Fe/Mg-silicates while the OLINDEX is sensitive to the broad Fe^{2+} absorption feature centered near 1.0 μm and is characteristic of olivine (possibly indicating unweathered basaltic minerals) (Pelkey et al., 2007;

Viviano-Beck et al., 2014). Additionally, we combine multiple indices to further constrain mineralogy such as how strong parameter values from both the BD1900 index (an indicator for bound H₂O) and the BD2210 index (which indicates Al-OH minerals) to determine the presence of Al-phyllsilicates.

Much of the surface of Mars is covered in a layer of fine dust, which has the potential to limit and interfere with spectral results. General circulation model (GCM) results suggest that much of the northern plains represent a net erosive regime where fines have the potential to be removed (Haberle et al., 2003). However, dust coverage maps, based on observed surface properties, suggest a moderate level of dust along the topographic dichotomy with higher dust content in the northern lowlands (Ruff & Christensen, 2002). Therefore, spectral analysis of regions of interest may be impractical in many cases as the result of masking from fines or lack of adequate observations.

4.3.5 *Classification*

To assess the genetic origin of putative wave-generated paleoshoreline features with all available high-resolution images, we use the multi-faceted approach outlined above. Given the data, each site can be classified as either 1) consistent with a paleoshoreline, 2) consistent with another origin (e.g., volcanic, glacial, impact, mass wasting) and inconsistent with a paleoshoreline at a local and/or regional scale, or 3) indistinguishable with current data. While many formational processes produce similar features (e.g., lobate flows found in both volcanic and glacial settings), multiple lines of evidence are needed to classify a site to a specific genetic origin. Table 2 presents a list of the different data products used for the two sites in this study.

Given the wide range of possible morphologies, spectral properties, and unknown geologic history, there is no definitive list of expected features for paleoshorelines. So we evaluate all available evidence to assess whether suspected paleoshorelines show consistency regarding: *photogeologic* evidence of erosional and/or depositional coastal landforms; *topographic* evidence in the form of TEA-defined terraces (if wave-generated landforms exist), lateral continuity of landforms across the basin, an equipotential surface (or following the regional trend if deformation

occurred), shorezone slope; *mineralogic* evidence of some hydrous and aqueous alteration minerals, carbonates (McKay & Nedell, 1988) (or possibly hydrous sulfates (Fairen et al., 2004)); and *physical properties* such as grain-size sorting.

4.4 RESULTS

4.4.1 Photogeology

4.4.1.1 Western Site Photogeology

The western site is dominated primarily by a degraded promontory that makes up the northern end of the breach between Craters A and B (Figure 4.1). Figure 4.3a presents our mapped lineaments around the southern tip of this promontory that correspond to the putative shoreline contacts within the extent of the DEM elevation-corrected footprint. Clifford and Parker (2001) did not map lineaments here, but it represents a western continuation of their inferred shoreline with similar curvilinear features at the ~100 m spatial scale. The promontory is capped by a light-toned layer which was mapped and defined by Parker et al. (2010) as the Arabia level. There also appears to be a darker unit that mantled over the topography that has been stripped back.

Most of the curvilinear features in the visible imagery data were challenging to accurately map. Despite clear correlative features visible at the kilometer-scale (Fig. 4.3a), the spatial integrity of the features disappears at finer resolutions. Multiple lineaments bifurcate into additional features and/or truncate and grade into the surrounding material. This behavior makes it difficult to map the lineaments at the large scale for more than a few 100 m before they become convoluted with other lineaments or the surrounding mottled terrain.

Figures 4.3b-d show sections of these putative shorelines at finer scales without the aid of the mapped lineament shapefiles. Here it becomes apparent that the individual lineaments lack any landform cohesion (recognizable as a single continuous distinct landform). The terrain these features are found in is predominantly composed of mottled terrain with some large boulders and blocks that tend to cluster around the mapped lineaments. As such, the lineaments appear as a

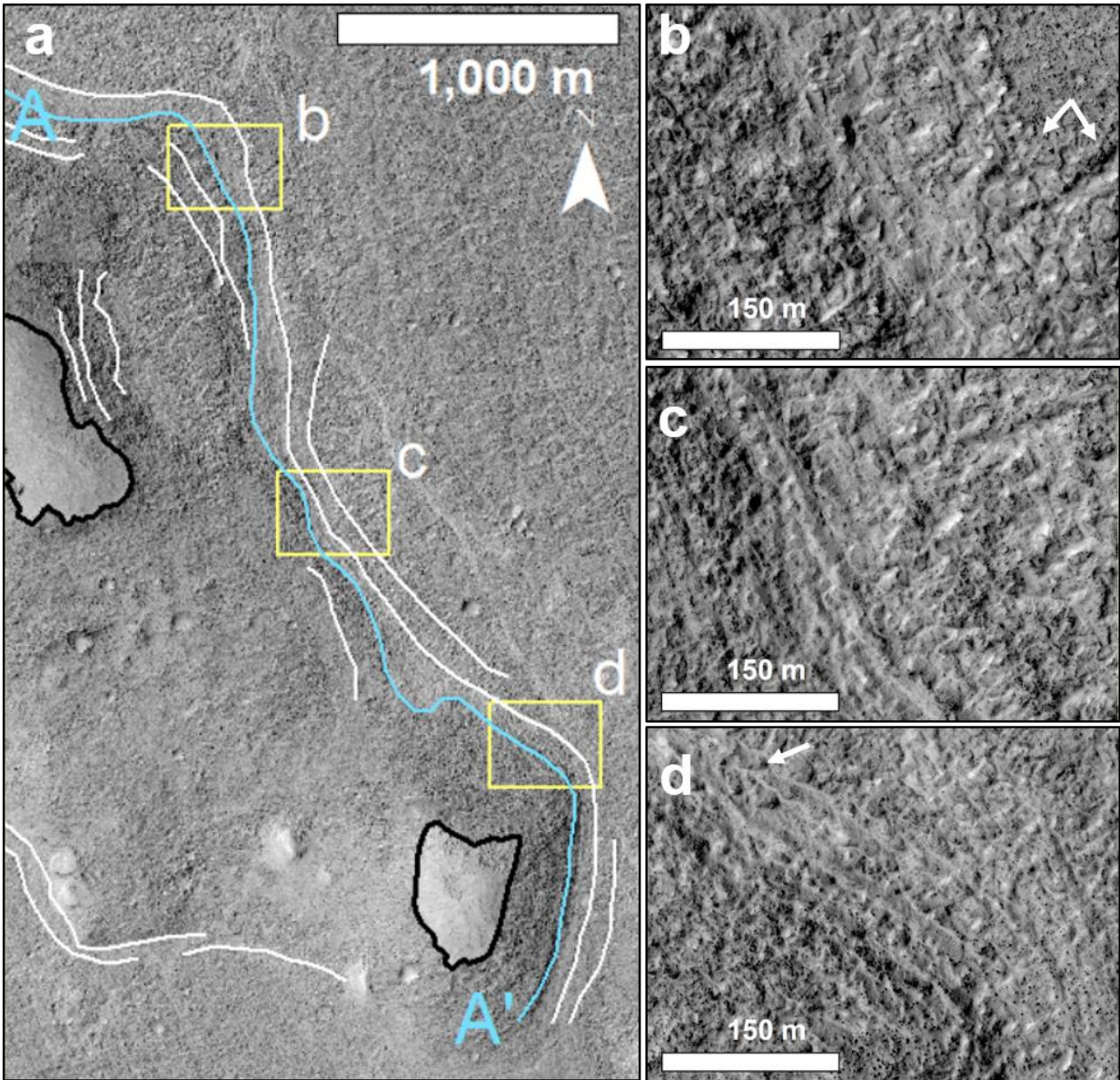


Figure 4.3. *a)* Our mapped lineaments that follow the putative shoreline contacts for the western site of Crater A. Topography for blue line A-A' is shown in Fig. 5. Black lines map the lower contact of the smooth light-toned capping unit. Yellow rectangles show the locations of zoomed in areas displayed in *b-d*. HiRISE image: ESP_025650_2165. Arrows in *b* show sides of a bifurcation and the arrow in *d* show merging lineaments.

roughened surface made up of disjointed blocky features with troughs cross-cutting the lineaments with no dominant preferred orientation and a lack of a coherent organization expected of drainage

features. In many places, lighter toned material is interposed between lineaments suggesting in some cases that these features are tonal lineaments with some lateral continuity representing material properties rather than landforms.

Lineaments are no longer visibly identifiable at the finer resolutions of Fig. 4.3b. Instead it appears there is a faint lighter toned unit running through the center that loosely runs between the mapped lineaments. Note also the bifurcation on the east side of the image. Fig. 4.3c shows a single clear identifiable lineament running NW-SE with additional smaller and fainter lineaments merging into it. The majority of features identified through the residual topography do not appear to map to any visible features in the visible image here. More arcuate lineaments are found in Fig. 4.3d, though two merge in the NW corner and subsequently terminate. As seen at coarser scales, the southernmost lineament follows a shallow cliff. No constructional coastal terrain landforms or other erosional landforms are identifiable in the image.

4.4.1.2 Southern Site Photogeology

The southern site is characterized by a small embayment in the crater wall at the terminus of multiple valley networks (Figure 4.1). Figure 4.4 shows the historical mapped lineaments of Clifford and Parker (2001) with dotted lines, our mapped lineaments with solid thin lines, and lineaments observed only in the residual topography (see Sec. 4.3.2.2) with dashed lines. Additional more pronounced lineaments are found in the CTX images to the west of the site, but we focus on the available high-resolution data. Parts of the dissected highland margin at the peak of the crater rim have eroded away into multiple alcoves (Świąder, 2014), some of which have short discontinuous lineaments corresponding to features mapped by Clifford and Parker (2001).

At coarse scales, the lineaments within the embayment are visible as shorter segments and difficult to trace as continuous features across the image. More pronounced lineaments are found to the east of the short promontory and are traceable for multiple kilometers. Unlike at the western site, bifurcation of the lineaments is not seen at these scales. However, most of the lineaments

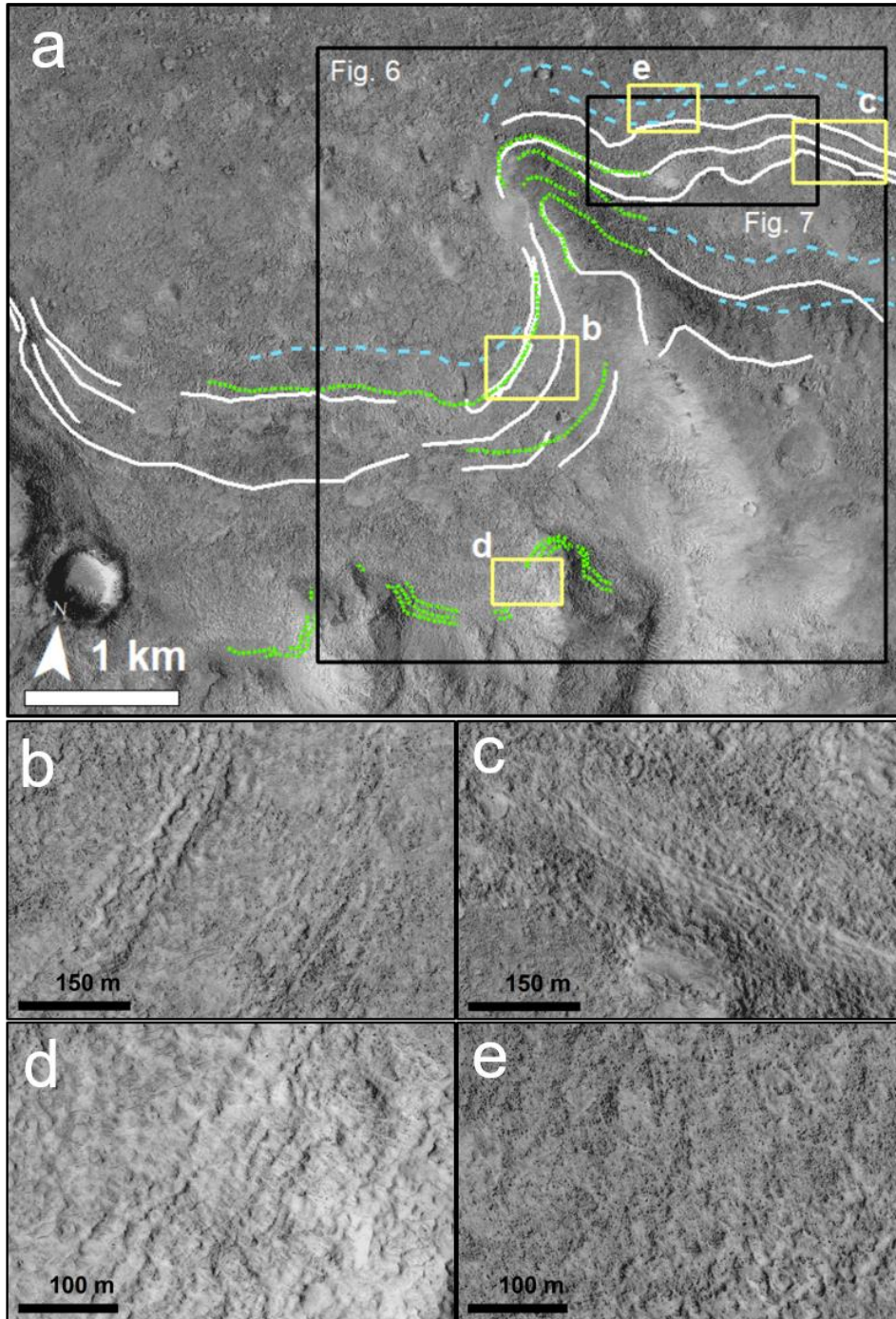


Figure 4.4. Mapped lineaments that follow the putative shoreline contacts for the southern site of Crater A. Solid white lines demark lineaments that we mapped in the visible imagery; dashed blue lines demark additional lineaments resolved only in the residual topography data (see Sec. 2.2.2); dotted green lines show mapped contacts by Clifford and Parker (2001). Yellow rectangles show the locations of zoomed-in areas displayed in b-e. Black rectangles show extents for Figs. 6 and 7. HiRISE image:

PSP_001414_2165.

visually dissolve into the surrounding terrain at some point along trend. Mapping them thus involved some estimation.

The lineaments at finer scales behave similarly to those at the western site. Figure 4b exemplifies the lineaments as observed at the 100 m-scale wherein clear visible linear trends in the terrain lack any clear landform continuity. The blocky nature of the lineaments at these scales make it difficult to discern any continuity of the features and show bifurcations and gradation into the surrounding terrain. Similar features displayed in Figure 4.4c also include bifurcations and merging of lineaments.

Analysis of the short discontinuous lineaments mapped by Clifford and Parker (2001) in the small alcove to the south (Fig. 4.4d) show highly disjointed segments that roughly follow short arcuate paths. Figure 4.4e shows a section of the terrain where the residual topographic data (see Sec. 4.3.2.2.) indicated a possible terrace landform. The terrain shows no visual lineaments and is dominated by the mottled terrain and boulders that appear as black specks at the scale of Figure 4.4e. At fine resolutions, lineaments that are apparent at coarse resolutions completely dissolve into the surrounding terrain and show no evidence for erosional or constructional landforms.

4.4.2 *Topography*

4.4.2.1 Western Site Topography

The residual topography map for the western site shows only two curvilinear bands for follow up TEA. The upslope lineament shows long-scale continuity across the DEM footprint, while the other band is truncated to only ~500 m. The primary long-scale band follows the mapped lineament in Fig. 4.3 and is also identifiable in the slope map as a sharp incline. TEA was applied to over 30 equally-spaced 100 m topographic profiles (50 m to either side of the curvilinear line A-A') and all but a quarter of them showed terrace expressions. The profiles that showed no terrace structures were primarily found in the central part of the mapped lineament creating two separate populations of terrace features. However, these terraces are widely varied in their morphologies

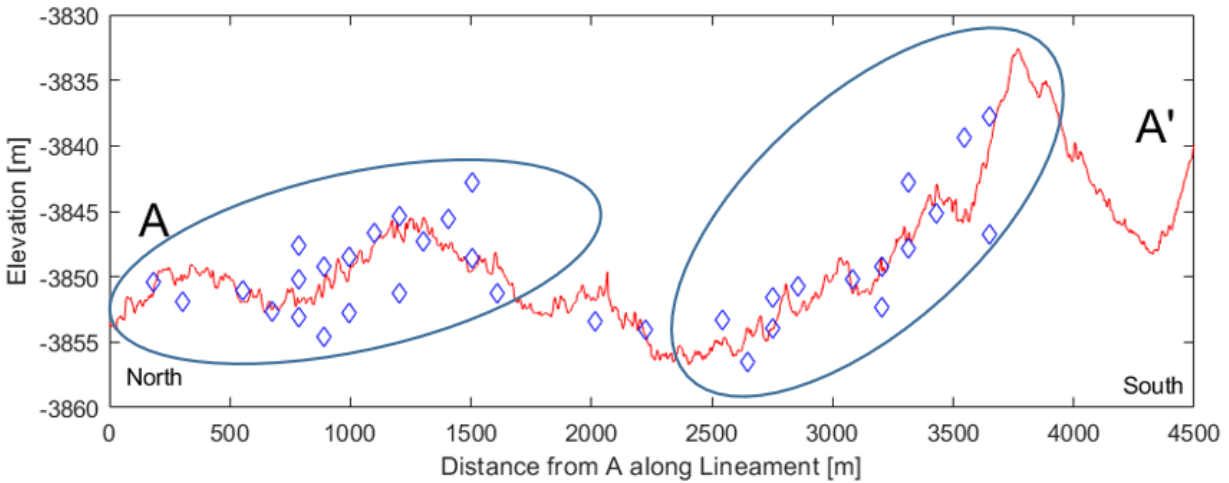


Figure 4.5. Along-track elevation data for curvilinear line A-A' in Fig. 4.3 (solid blue line). Diamond markers indicate terraces found along profiles orthogonal to the lineament. Terraces appear to follow the topography rather than an equipotential surface. Ellipses outline clusters of terraces that appear to align with the topographic peaks of the promontory.

(e.g., the shape and the width of the bench) with a handful of profiles showing multiple terraces at different elevations.

Plotting the elevation of the riser crests and knickpoints (the start and end of the benches) as a function of latitude shows that both populations of terraces show a distinct downward tilt to the north (diamond markers in Fig. 4.5). The southern population of terrace features show an elevation difference of ~ 20 m over ~ 1.25 km while the northern population tilts ~ 10 m over ~ 1 km, but there is substantial variance in the distributions, with almost a 20 m range in elevations across all sites and up to about 10 m among proximal sites. The solid line in Fig. 4.5 shows the elevations of the mapped lineament laterally. Mapping of the lineaments onto the CTX stereo pair show a similar northern downward tilt of ~ 10 m km^{-1} . In contrast, we also mapped out the exposed contact of the light-toned capping unit of the promontory peaks. Fitting these elevations to a planar surface shows an approximate tilt of ~ 45 m km^{-1} to the south and ~ 30 m km^{-1} to the west.

The terraces appear to align with the topography rather than following an equipotential surface. Furthermore, the two populations of terraces tilt northward at different angles while the unit stratigraphy appears to be tilting in the opposite direction (southward which itself is opposite

than the general trend of the putative Arabia contact (Parker et al., 2010)). Hence, the two terrace populations are likely manifestations resulting from the degradation of the promontory, which has created two peaks (corresponding to the smooth light-toned layer capping the promontory to the SE and WNW in Fig. 4.3). Mapping the locations of the terraces with respect to their profiles along the lineaments highlights their discontinuous nature.

TEA was also performed for profiles along shorter truncated lineaments around the promontory. Some terraces were present in individual profiles, but the terraces could not be correlated along the lineaments and showed a highly discontinuous nature. The terraces that were identified only appeared when the topographic profiles were drawn across the blocks that make up the lineaments as was described with the HiRISE images. Analysis of the cliff at the southern tip of the promontory shows it is actually a series of shallow cliffs, ~2 m in height, that act as knickpoints in the slope with no terraces.

4.4.2.2 Southern Site Topography

At the southern site (Fig. 4.4), topographic profiles across the putative shorelines in our high-resolution DEM show what appear to be multiple terrace features that visually resemble terrestrial wave-cut paleoshorelines. This is consistent with the findings of previous studies that have used the same stereo pair HiRISE images to conclude that the presence of terraces along these few profiles is consistent with a coastal origin (Sholes et al., 2014; Świąder, 2014). Figure 4.6 visually presents the process of our topographic expression analysis for the southern site which allows for a more thorough investigation into the extent of these terraces. This residual topography map identifies multiple possible terrace locations (appearing as alternating dark/light bands), including many that are too subtle to identify in the visible image.

The TEA code was performed along regularly-spaced topographic profiles drawn orthogonal to the candidate terrace contacts found in the residual topography map. Fig. 4.7a shows the locations of the terraces found that meet the necessary criteria for being a shoreline (i.e. having a recognizable RI, RC, BT, and KP in the residual derivatives) for five profiles on the east side of the southern site where the residual data was most pronounced. Manual inspection was performed across all profiles, as were sensitivity tests to explore the parameter space regarding the smoothing

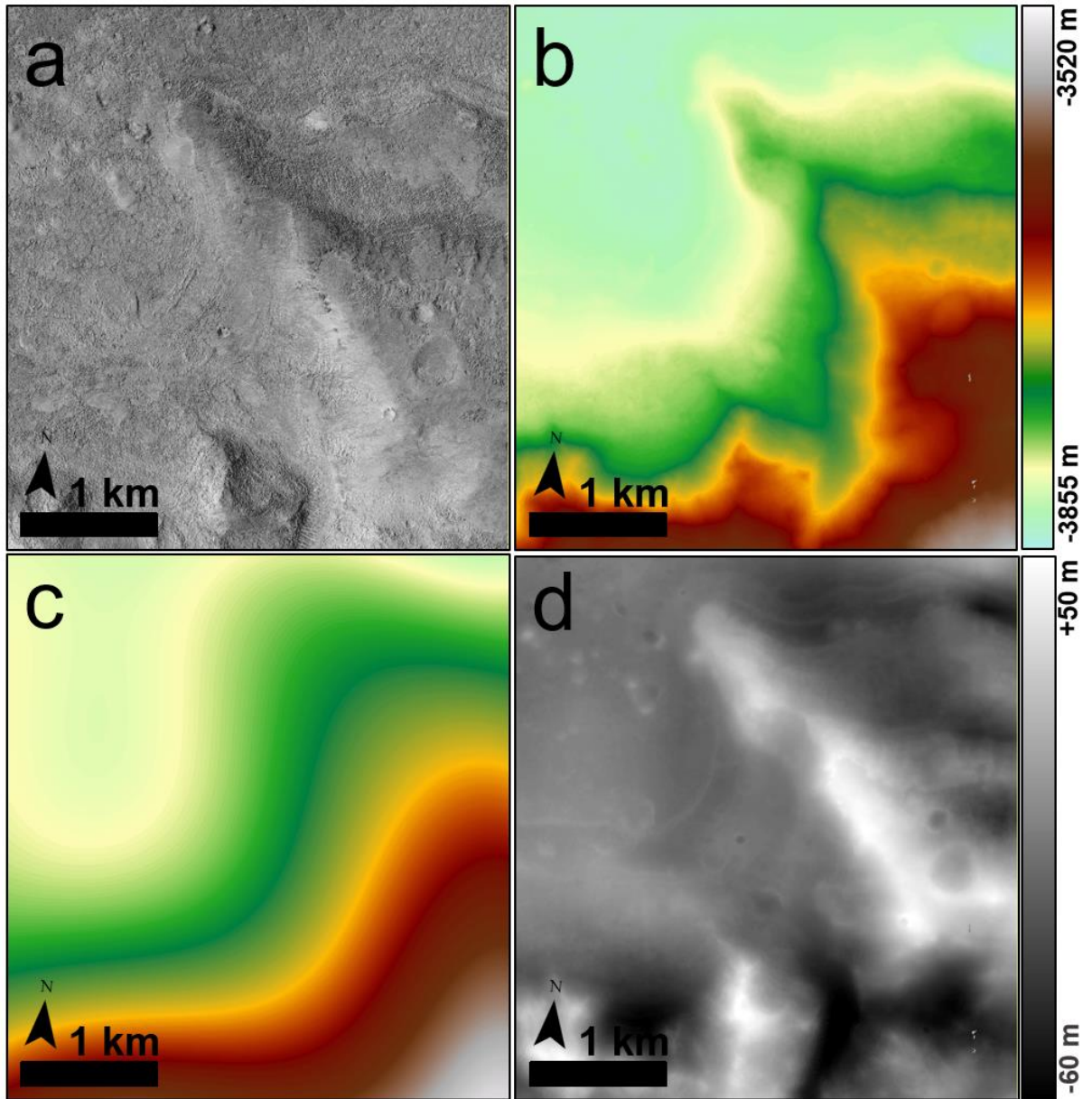


Figure 4.6. Steps of the topographic expression analysis on a subsection of the southern site. *a)* Original HiRISE image, *b)* Our high-resolution digital elevation model, *c)* Surface polynomial fit surface representing an ‘idealized’ slope, *d)* Residual topography derived from subtracting the idealized surface from the topographic data. Potential paleoshoreline terraces appear as alternating dark/light bands in the residual topography. Further analysis of topographic transects is used to evaluate and eliminate false positives.

function (window size and polynomial degree) and the idealized slope (polynomial degree). These efforts found no convincing evidence for additional terrace features along the contact that were not found by the TEA code. The terraces found along the profiles range from -3,819 to -3,792 m in elevation (27 m of relief), using the MOLA-corrected absolute elevations. Half of them do not map to any lineaments found in the visible imagery and most have a subdued expression with little to no lateral continuity.

Along these profiles, a collection of terraces (~7) were found clustered in a small region midway up the slope (shown in the lower part of Fig. 4.7a), but do not appear spatially coherent as they do not map continuously along any visual lineament (either in the visual or residual data). Analysis of the local slope (Fig. 4.7b) shows that these clustered terraces do not follow any continuous approximation of a flat surface bounded by sharp changes in slope that are normally associated with terraces. Rather, the slope map shows that the terraces are bounded within individual small disjointed arcuate steep slopes. Elevation data (Fig. 4.7c) agrees, showing no consistent lateral trend across the terrace sites and >10 m range in topography.

The residual topography does highlight a pronounced subtle lineament that is not visible in the HiRISE imagery located (see Fig. 4.4e) at the base of the crater wall slope. TEA analysis on the five profiles orthogonal to this feature confirm terraces along the lineament. An additional 30 transects were taken across this lower lineament to test for topographic continuity. Of these transects 9 did not show the necessary criteria for a terrace and the others showed a wide diversity in benchwidth and morphology. Evaluation of the elevations for the riser crests and knickpoints finds that the along-strike trend of the terraces laterally is ~11 m downward to the east across the 2.5 km mapped stretch. Note that these terraces do not appear to follow any continuous landform and are not continuous in the slope map.

4.4.3 *Thermal Inertia and Spectroscopy*

There appears to be no consistent trend with the thermal inertia data across the contacts. The crater floor is relatively homogenous and characterized by thermal inertia values of ~400-550 tiu which we interpret as bedrock covered by a layer of sand or dust (Catling et al., 2006). The

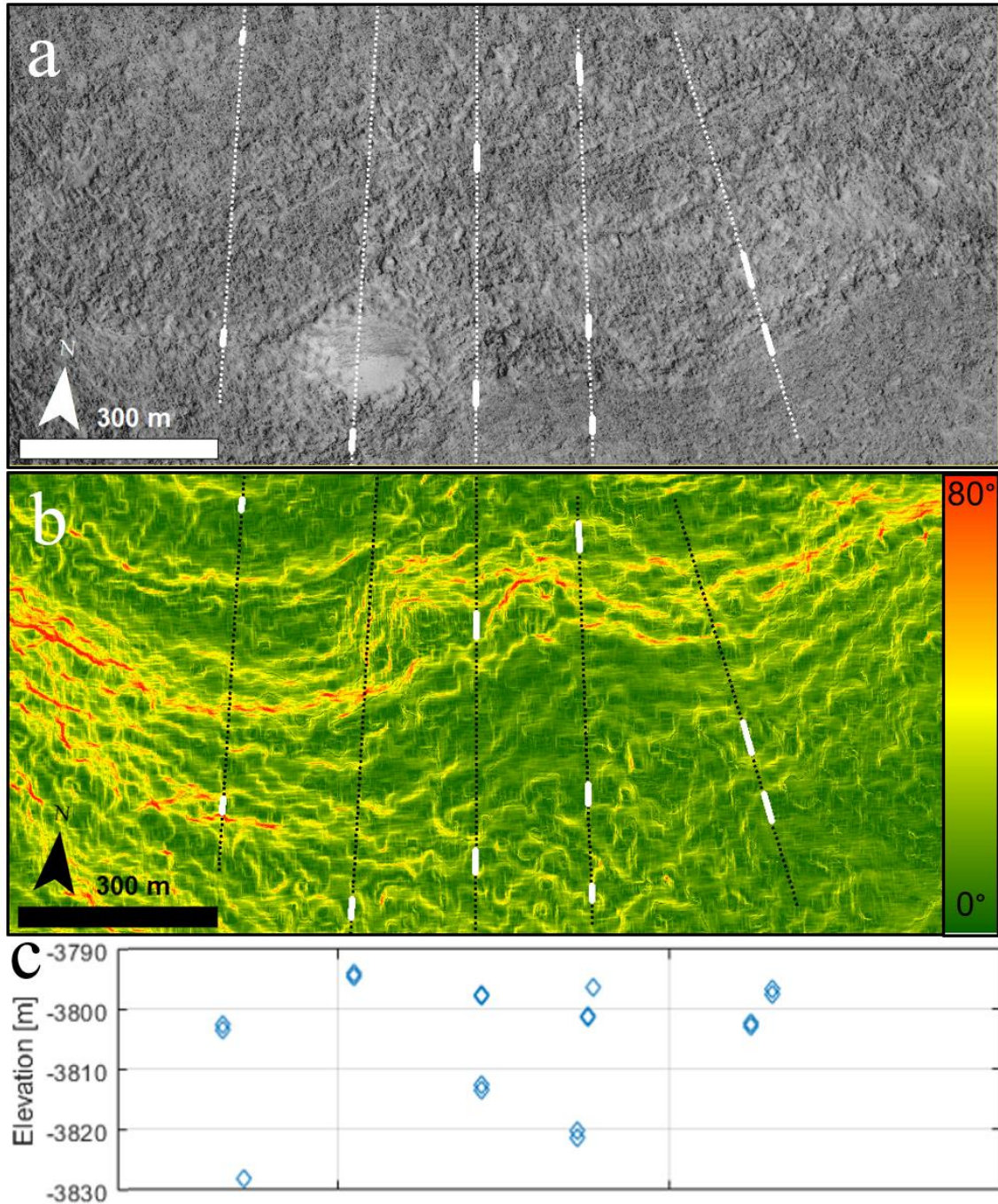


Figure 4.7. Locations of potential terraces (bold white segments) found along a sample of transects (dashed lines) orthogonal to the lineaments found in the surface residual topography. *a*) HiRISE image, *b*) slope map, *c*) corresponding elevations. Higher elevations are to the south in *a*-*b* and all terraces map vertically to their corresponding points in *c*.

crater wall and highlands have thermal inertia values of ~300-350 tiu with some patches upwards of ~450 tiu. These values are consistent with bedrock covered by a thin layer of poorly consolidated fines. Thermal inertia values of ~600-700 tiu are typically smaller craters and their associated ejecta with the exception of a lighter-toned boulder-free capping unit on the eastern site, which is interpreted as bedrock with a thin layer of dust. TI maps can be found in the supplemental materials.

High-resolution spectral/spatial CRISM data is only available for the western site. However, the site appears spectrally bland with a lack of mineralogical diversity. The derived visible and IR data products available on the PDS show stronger values in the VNIR_FEM (very near infrared Fe-minerals), with homogenous and bland in other relevant products (e.g. IR_HYD, infrared hydrated mineralogy) suggesting the area is coated in dust (Viviano-Beck et al., 2014). Follow up spectral ratios of individual pixels along transects orthogonal to the mapped contacts confirm the lack of non-dust related spectroscopic signals.

4.5 DISCUSSION

4.5.1 *Are These Shorelines?*

Along with the lack of clarity from the spectroscopic and thermal inertia maps, both the geomorphic and topographic data build a case that these lineaments at both sites are unlikely to be paleoshorelines or other ancient coastal features. At broad scales the lineaments superficially resemble coastal ridges and strandlines, but at finer resolutions identification of contacts is lost as they lack landform continuity in both the high-resolution visual and topographic data.

Degradation of paleoshorelines over geologic time (such as via periglacial or aeolian destruction) can produce roughened texture and discontinuity at fine scales. However, at these fine scales, and often in coarse scales, it becomes apparent that these features bifurcate, terminate, and merge. Identifiable terraces also do not line up with the lineaments, have no elevation or lateral coherence, and are limited in extent. These observations are incompatible with a preserved shoreline interpretation for the lineaments. Instead, the terrain appears to loosely follow material

continuity along the degraded crater walls, as evidenced by multiple lighter-toned units interposed between the lineaments and clustering of boulders around the putative shorelines.

Topographic data agrees with the visual geomorphic analysis. While terraces are found along certain topographic profiles (in agreement with previous studies), these are highly dependent upon the position and choice of such profiles. As the visual imagery suggests, the lineaments are made up of blocky material and the terraces typically only appear when the profile crosses the blocks rather than the surrounding troughs. The TEA method we employ verifies that terrace features do exist, but when applied to multiple profiles along a proposed contact confirms their lateral discontinuity. Many of the terraces are bounded by small disjointed arcuate steep slopes which we interpret to be slumped parts of the mottled terrain of the crater wall.

TEA was able to identify a single lineament at the southern site that had some topographically continuous terrace features. However, the morphology of the terraces varied widely and nearly a third of the profiles did not have terraces that met the necessary criteria for interpretation as a shoreline. The terraces that were found along the lineament showed a consistent downward tilt of ~11 m (over ~2.5 km) to the east which is also inconsistent with unmodified shorelines. While the discrepancy of the westward ~60 m (over ~35 km) downward tilt between the eastern and southern site follows the long-wavelength topographic trends proposed as a result of true polar wander and/or flexure (Citron et al., 2018; Perron et al., 2007), the local trends of the putative shorelines tend in the opposite direction. Thus, at both scales these features do not form an expected equipotential surface and likely represent separate features.

There is also no compelling evidence for constructional or erosional landforms at either site, a finding in agreement with the results of Ghatan and Zimbelman (2006), who used MOC narrow angle image data before HiRISE imagery was available. Given that these lineaments are found along the hypothesized Noachian-aged Arabia shoreline, it is expected that constructional landforms, typically composed of sand/pebble sized grains, would have eroded away, especially given the enhanced erosive rates of the Noachian (Carr & Head, 2010). The lack of any deltas or alluvial fans at the termini of the valley networks (located above the lineaments) suggests the reworking of the material and subsequent formation of the lineaments. Bedrock erosional

landforms are expected to be better preserved, but impact gardening is expected to obscure any Noachian-aged shoreline features (erosional or otherwise) of $\lesssim 20$ m (Hartmann et al., 2001).

4.5.2 *Alternative Hypotheses*

The lack of supporting geomorphic and topographic evidence does not necessarily preclude a paleoshoreline interpretation, as these lineaments could be highly-degraded remnants of ancient coastal landforms that have undergone additional post-formational modification processes (to account for local tilting opposite the western Arabia level trend and the lack of an equipotential surface). However, there is no geomorphological evidence to suggest such a scenario and compelling additional data would be required to accept such an interpretation.

An ocean on Mars is an extraordinary hypothesis that requires extraordinary evidence (because an ocean hypothesis raises questions of where the large volumes of water came from, where the water went, compatibility with geochemical tracers, consistency with past climates, and so on (e.g. Head et al., 2018)). It has been said that “the most compelling evidence that Mars once had oceans is the presence of potential shorelines” (Zuber, 2018), so their reexamination is important. We propose that a much less speculative, conservative, and parsimonious explanation is that the lineaments that we have examined are likely the result of erosional degradation working on lithological differences in crater wall units. The blocky nature of the lineaments may be caused by differential erosion from thermophysical differences in inter- and intra-rock units. This interpretation is in general agreement with the unit characteristics described by Tanaka et al. (2014) in which Noachian-aged material is commonly layered in crater walls.

These lineaments could also be the vestigial remnants of concentric crater fill (CCF) (Ghatan & Zimelman, 2006) caused by ice-creep, aeolian erosion, or debris-covered glaciers typically found at these mid-latitudes (Fastook & Head, 2014). The bifurcations, terminations, troughs, and overall mottled terrain closely resemble the CCF “brain terrain” morphology of Levy et al. (2009; 2010 and references therein). These morphologies are common at the western site with the ridge and through structures and associated polygonal terrain at the crater base. Identification of the brain terrain morphologies also suffers from disagreements between scales,

with contacts within the brain terrain (“open-cell” vs. “closed-cell”) appearing as lineaments at large scales (Levy et al., 2010). However, this interpretation would also require invoking significant post-formational modification due to the lack of large areal debris aprons associated with CCF.

The long-scale tilting nature of the terrace features also supports a non-coastal interpretation. At these scales it is unlikely that post-formational modification processes could account for the >60 m elevation displacements. Isostatic rebound is a proposed mechanism. However, the putative shoreline is circumferentially-oriented (as opposed to radially) with respect to the basin center and only represents a small fraction of the Arabia contact both of which lessen the effect on the elevation variation (Currey, 1980; Webb, 2004). A simpler explanation is a shallow dip in the underlying rock layers.

4.6 CONCLUSIONS

We apply terrestrially validated topographic expression analysis (Hare et al., 2001; Jewell, 2016) to Mars for the first time as a more detailed quantitative approach to characterizing putative paleoshoreline features. We focused on an area in Cydonia Mensae that had been promoted as one of the better candidates for shorelines in the literature. Results from this analysis show neither elevational nor lateral coherence in identified terrace features. Additional high-resolution geomorphological analysis identifies inconsistencies between broad and fine scales with the lineaments, along with bifurcating along-trend behavior. Thus, we find that the lineaments identified within this crater complex are inconsistent with a wave-generated paleoshoreline interpretation. Rather, these lineaments appear to follow subtle discontinuous material-property boundaries.

Given both the highly localized nature of these features and their age, the lack of evidence for coastal landforms at this site does not preclude the existence of past oceans. Post-formational modification of any coastal landforms compounded over billions of years may erase any such geomorphic evidence. Additional work is required to apply the toolkit presented here to additional hypothesized shoreline contacts to assess their validity as coastal landforms and test the

geomorphological evidence at a global scale. Furthermore, this toolkit can be applied elsewhere to characterize potential subtle paleoshorelines, such as on Titan given adequate topographic information.

Chapter 5. MARS' OCEAN SHORELINES: A HIGH-RESOLUTION GLOBAL RE-EXAMINATION

5.1 ABSTRACT

The possibility of liquid water ocean(s) occupying Mars' northern plains is a subject of contentious, long-standing debate. Putative ancient shorelines have been argued to be the most compelling evidence to support such an ocean hypothesis despite controversy over their interpretation. To date, no global-scale compilation and re-investigation of these features using the available high-resolution data products from the *Mars Reconnaissance Orbiter* has been presented. Here, we catalog and reexamine 40 sites that have been proposed as possible candidate shoreline features and apply the methodology of Sholes et al. (2019b). We find that the features can be grouped into six broad categories of features: mass wasting features, highland collapse features, ridges attached to massifs, isolated ridges within curvilinear depressions, lobate flow fronts, and miscellaneous features with specific alternative interpretations. With the exception of the lobate flow front deposits that characterize the southern boundary of the Vastitas Borealis Formation (VBF), none of these sites provides supportive, let alone compelling, evidence for a coastal origin. The margins of the VBF, however, are often highland-facing escarpments which is the opposite slope normally expected for a shoreline. All features (including the VBF and stacked ridges) can be explained through more conservative processes that do not require invoking an ocean. Additionally, we quantify how portions of the mapped putative paleoshoreline levels have been grossly misidentified and misplaced within Deuteronilus Mensae.

5.2 INTRODUCTION

It has long been hypothesized that oceans or seas may have once occupied the northern plains on Mars. Large outflow channels and valley networks, believed to have been formed by liquid water in catastrophic outflow events, empty into the northern lowlands where the high-volumes of water presumably pooled (V. R. Baker et al., 1991; Jöns, 1985; Lucchitta et al., 1986; Parker et al., 1993; Parker et al., 1989; Scott et al., 1992). While past bodies of liquid water on Mars are well known to have existed in the form of lakes (Goudge et al., 2015; Grotzinger et al.,

2015) or possible seas (Irwin et al., 2004; Irwin et al., 2002), evidence in support of extensive liquid oceans has been ambiguous at best, leading to a long-standing contentious debate.

Historically, evidence in support of ancient oceans has largely been based on the identification of putative paleoshorelines that encircle much of the northern plains as first formally documented by Parker et al. (1989; 1993). These features were originally analyzed using a few rare high-resolution Viking images (~10 m/px) in west Deuteronilus Mensae and Cydonia Mensae while the global contacts were mapped at much lower resolutions (~50-200 m/px). They identified both possible wave-cut erosional landforms (e.g. cliffs, terraces, and stepped massifs) along with albedo variations, onlap/embayment relationships, and “thumbprint terrain” (patterned ground of whorled ridges) which were interpreted as sediments deposited by standing water.

Two primary distinct hypothesized paleoshorelines were described by Parker et al. (1989): the Arabia Level (“Contact 1”) that roughly follows the topographic dichotomy and would represent an older larger ocean stand; and the Deuteronilus Level (“Contact 2”) which largely follows the southern boundary of the Hesperian-aged Vastitas Borealis Formation (VBF) in the northern plains. Fig. 5.1 shows the mapped extent of both contacts and Fig. 5.2 shows the typical contacts used to describe the shorelines. While other paleoshoreline levels have been proposed representing either smaller localized transitional stages of an ocean (e.g. the Ismenius and Acidalia Levels) or older more expansive ocean stands (e.g. the Meridiani Level approximately following the 0 m elevation datum) (Clifford & Parker, 2001), these have received much less attention in the literature.

However, interpreting the Arabia and Deuteronilus Levels as paleoshorelines faces two critical issues: 1) both levels display wide variance in their elevations, >4 km along the Arabia Level (Carr & Head, 2003; Head et al., 1999; 1998), which is at odds with an expected equipotential surface for a coastline; and 2) reinvestigations of features along the suspected shoreline levels using contemporaneous high-resolution imagery (typically Mars Orbiter Camera narrow angle, MOC NA (Malin et al., 1992), at ~4 m/px and Thermal Emission Imaging Spectrometer visible, THEMIS VIS (Christensen et al., 2004), at ~18 m/px) have consistently

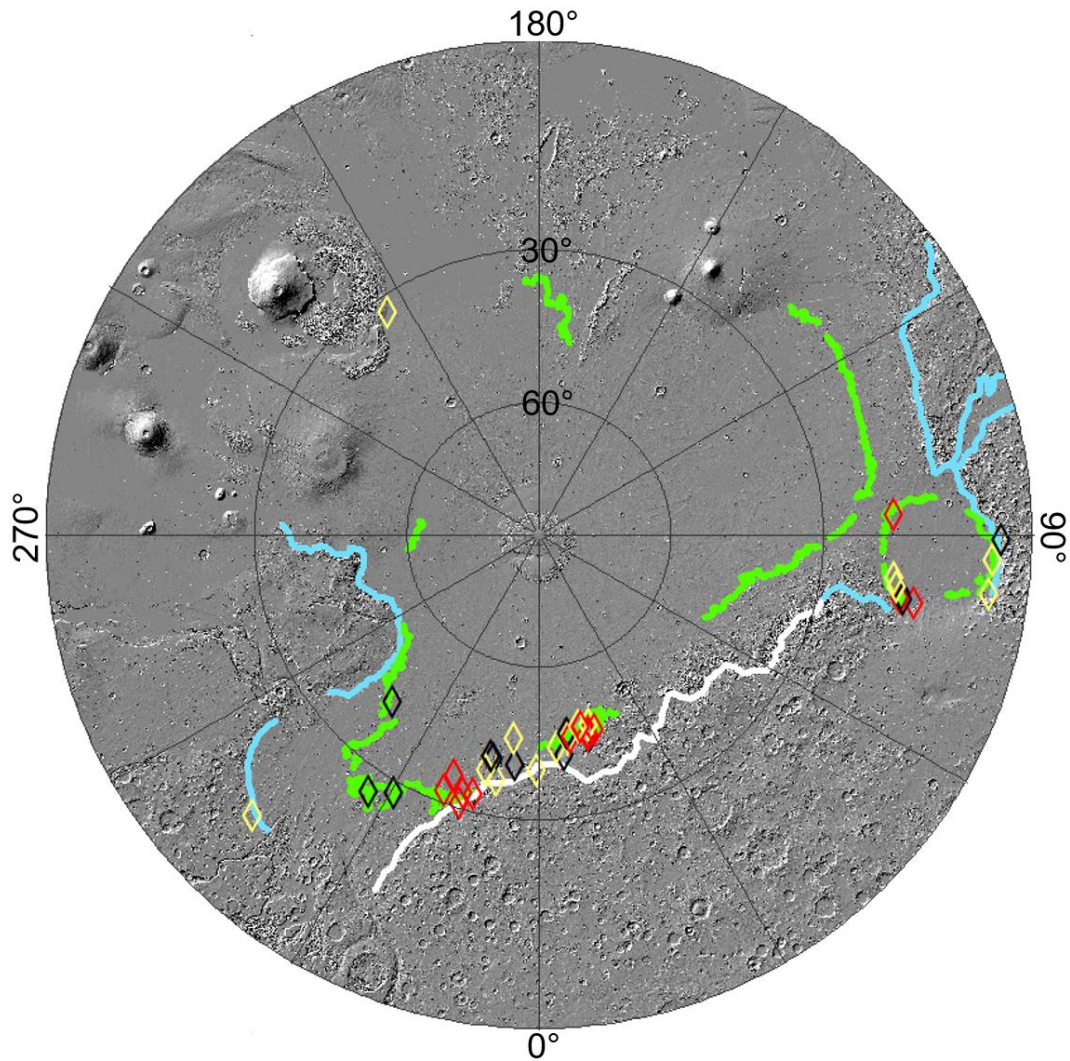


Figure 5.1. Locations of the putative mapped shorelines and sites. The Deuteronilus Level is mapped with solid green lines (Ivanov et al., 2017). The Arabia Level is mapped in blue and white (Carr & Head, 2003), with blue showing the sections excluded from shoreline deformation models (N. H. Chan et al., 2018; Citron et al., 2018; Perron et al., 2007). Diamond markers show the different sites and are colored according to their data availability: yellow have HiRISE coverage, red only have CTX, and black have HiRISE coverage of adjacent or similar features not originally cited. MOLA hillshade, polar stereographic projection.

found no obvious or unambiguous supporting evidence for a coastal origin (Carr & Head, 2003; Ghatan & Zimbelman, 2006; Malin & Edgett, 1999, 2001; Sholes et al., 2014; 2019b).

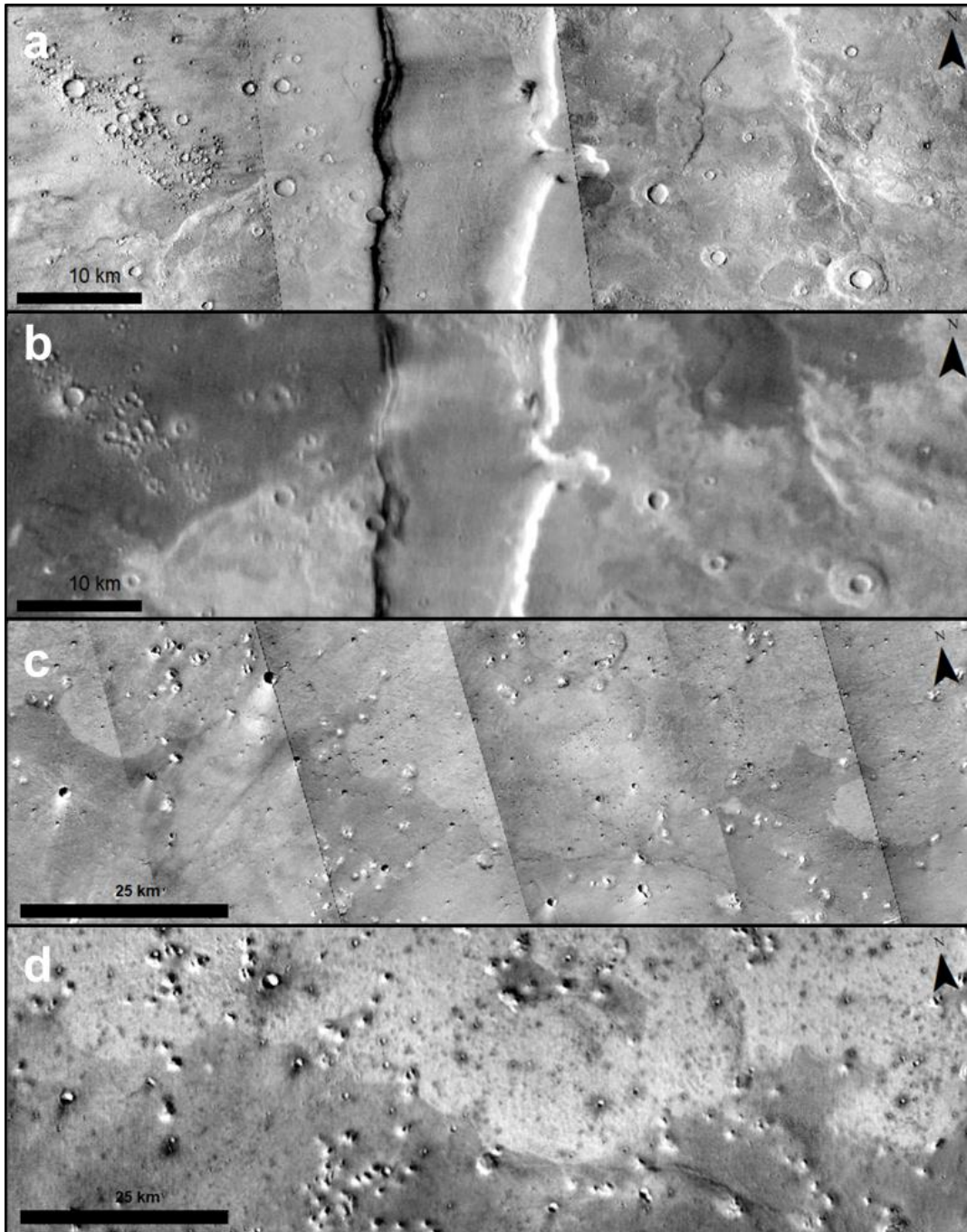


Figure 5.2. Examples of the contact used to describe the Arabia and Deuteronilus Levels. *a)* CTX mosaic showing the Arabia Level in Mamers Valles, in some places it follows a north-facing escarpment, but is generally diffuse. *b)* THEMIS-IR day mosaic of the Arabia Level which is defined by the stark albedo contrast. *c)* CTX mosaic of the Deuteronilus Level (defined by the lobate flows onlapping the southern plains) in eastern Chryse Planitia. *d)* THEMIS-IR day mosaic of the Deuteronilus Level which is lighter-toned here than the surrounding plains.

Counterarguments have been proposed to explain these problematic observations. True polar wander (Perron et al., 2007), Tharsis-induced long-wavelength crustal flexure (Citron et al., 2018), a combination of the two (N. H. Chan et al., 2018), or thermal isostasy (Ruiz et al., 2004) have all been invoked to explain the topographic deformation of the levels. Objections to the high-resolution images have also been made, suggesting that some of the features are more exotic forms of coastal features, such as seen in large terrestrial paleolakes, or that the shorelines have been misidentified and/or extremely degraded (M. A. Chan et al., 2016; Clifford & Parker, 2001; Parker et al., 2010).

Despite the disparate conclusions on the validity of a paleoshoreline interpretation, it is believed by many that “the most compelling evidence that Mars once had oceans is the presence of potential shorelines” (Zuber, 2018). Yet, very little work has been done to assess the state of these features with the now available high-resolution data from the *Mars Reconnaissance Orbiter* with High Resolution Imaging Science Experiment, HiRISE (McEwen et al., 2007), images at 0.25-0.5 m/px and nearly global coverage with Context Camera, CTX (Malin et al., 2007) at 6-10 m/px.

Whether Mars ever had oceans has profound implications for understanding Mars’ past climate, planetary evolution, and potential for life (e.g. Beaty et al., 2005). Understanding the timing, duration, magnitude of water, and ice-cover of any such oceans is important for constraining past temperatures (e.g. Banfield et al., 2015; Haberle et al., 2017; Jakosky & Phillips, 2001; Lammer et al., 2018; Ramirez & Craddock, 2018). Yet, climate models have difficulty producing sustained early surface temperatures >273 K for a long-lived past ocean, suggesting that a martian ocean would quickly freeze, producing an ocean sized-body of ice rather than liquid water (Carr & Head, 2019; Clifford & Parker, 2001; Kreslavsky & Head, 2002).

The purpose of this study is to compile and evaluate features that have been proposed as possible martian paleoshorelines, reinvestigating them using the latest high-resolution data available and assess their consistency with a coastal origin. We also examine the history and problems that arise from differences in prior mappings of the levels.

5.3 METHODS

We identified 40 sites that have been previously investigated or featured in the peer-reviewed literature as hypothesized paleoshorelines of a martian ocean (Clifford & Parker, 2001; Ghatan & Zimbelman, 2006; Malin & Edgett, 1999; Parker, 2008; Parker & Currey, 2001; Parker et al., 1993; 2010; 1989; Webb, 2004). While we attempted to find all previously studied sites, some may have inadvertently been missed, the sites we compiled exhibit the representative landforms, features, or contacts that researchers have considered candidate coastal evidence. Thus, we do not investigate the entire mapped levels but focus on sites along with available high-resolution imagery and topographic data products.

The methodology toolkit established in Sholes et al. (2019b) is largely used here for analyzing and classifying whether a site was (1) consistent with a paleoshoreline, (2) consistent with a non-coastal origin (e.g., volcanic, glacial, tectonic) while inconsistent with a paleoshoreline, or (3) of inconclusive origin based off current data. A few sites showed no improvements in the spatial resolution of imagery directly over the site (typically sites previously investigated with MOC NA footprints at ~4-6 m/px), but now near-global CTX data provides the necessary contextual regional imagery at comparable resolutions to aid in their classification. Roughly half of the sites had some HiRISE coverage and all sites had CTX coverage at ≤ 6 m/px.

Where possible, we use the topographic expression analysis (TEA) method of Sholes et al. (2019b) to determine consistency with wave-eroded terraces using derivatives in the residual topography with an ideal slope (Hare et al., 2001; Jewell, 2016). This method examines the observed high-resolution topographic data and compares it with an “idealized” slope represented by a polynomial trend surface to create a residual topographic map. Wave-eroded terraces will exhibit a specific set of identifiable inflection points within the first and second derivatives of this residual topography (Sholes et al., 2019b). For most sites, however, TEA is largely unhelpful due to the lack of either adequate high-resolution topographic data or identifiable wave-eroded platforms (e.g. they are depositional landforms and TEA can only test for specific erosional landforms). HiRISE stereo-derived digital elevation maps (DEMs) are preferred for TEA, as many suspected terraces are narrow (<10 m), but available stereo imagery is limited. CTX stereo-derived

DEMs can be used, but would only be useful for terraces many 10s of meters wide while Mars Orbiter Laser Altimeter, MOLA (D. E. Smith et al., 2001), and High Resolution Stereo Camera, HRSC (Jaumann et al., 2007), topography are inadequate for TEA.

Much of the northern plains of Mars is covered in a layer of fine dust, which obscures the surface and limits the usefulness of thermal inertia and spectral results (e.g. Ruff & Christensen, 2002). We have found that when available, these maps provide ambiguous results that add little to aiding in identifying the origin of the features (Sholes et al., 2019b). This is consistent with previous studies that have failed to find mineralogical evidence for oceans (e.g. evaporites and carbonates) along the boundary of the northern plains (e.g., Bibring et al., 2006). Thus, we do not present thermal inertia or spectroscopic results here. Rather, we focus on the improved high-resolution topographic and photogeologic evidence now available.

For full transparency, we provide detailed figures of both the contextual and high-resolution zoomed images in the Supplemental Material (Appendix C) for all sites and present a brief summary of the sites below.

5.4 OBSERVATIONS

Our interpretations of all sites can be divided into six plausible broad categories based on the observed features at the regional and local scales: 1) mass wasting features, 2) general collapse features, 3) ridges branching off from massifs, 4) ridges within linear depressions and/or isolated from massifs/highlands, 5) lobate flows, 6) miscellaneous other features (e.g. deltaic, albedo contacts, tectonic, glacial). One site was considered “uncertain.” Table 5.1 groups the sites by this classification scheme. Here, we briefly present our observations and analysis for each of the sites as to whether they are consistent with a coastal origin.

Herein each site will be referred to by an abbreviated descriptor based on the citing reference (initials of citing author(s) and a two-digit abbreviation of the year) and figure of the site within the reference. For example, Site GZ06-9a designates the site found in Fig. 9a of Ghatan and Zimbelman (2006).

Table 5.1. List of putative paleoshoreline sites and available high-resolution data. Resolutions (Res.) are provided in m px^{-1} . Candidacy designations are based on our own assessment, see text.

#	Citation	Lat	Lon	HiRISE	Res.	CTX	Res.	Topographic	Res.
<i>Candidacy: Mass Wasting</i>									
1	Parker et al. (1989), Fig. 13a	44.3	14.1	PSP_006556_2245 ESP_044506_2245	0.25 0.25	P13_006200_2228	6.0	h1289_0000_dt4	100
2	Parker et al. (1989), Fig. 13b	44.7	14.0	--	--	B18_016643_2264* P15_006912_2263*	6.1 5.3	CTX stereo*	7.4
3	Parker et al. (1989), Fig. 13c	45.1	14.0	--	--	B18_016643_2264* P15_006912_2263*	6.1 5.3	CTX stereo*	7.4
4	Ghatan and Zimbelman (2006), Fig. 17a	4.7	82.4	PSP_007648_1845	0.5	F02_036697_1849	5.4	h2206_0002_dt4	75
5	Ghatan and Zimbelman (2006), Fig. 17b	3.6	89.3	PSP_009032_1835	0.25	P14_006593_1827	5.3	MOLA PEDR	300
6	Clifford and Parker (2001), Fig. 4	36.4	350.2	PSP_001414_2165* PSP_001968_2165*	0.5 0.5	B18_016789_2162	5.8	HiRISE stereo*	0.7
<i>Candidacy: Collapse</i>									
7	Parker and Currey (2001), Fig. 11	38.0	347.4	ESP_016011_2185* ESP_016499_2185*	0.25 0.25	P05_003155_2184	5.9	HiRISE stereo* h1260_0000_dt4	75
8	Parker and Currey (2001), Fig. 12	40.7	348.0	ESP_055069_2210 ^c	0.5	G04_019756_2204* P03_002166_2204*	6.5 5.9	CTX stereo* h1249_0000_dt4	75
9	Ghatan and Zimbelman (2006), Fig. 12b	40.2	348.7	--	--	P17_007704_2223 ^b	5.9	h1238_0000_dt4	75
10	Ghatan and Zimbelman (2006), Fig. 12d	39.0	359.6	ESP_034656_2195	0.5	D19_034656_2193	5.9	h1410_0009_dt4	100
11	Ghatan and Zimbelman (2006), Fig. 12f	41.6	318.8	--	--	G18_025282_2210 ^b	5.9	MOLA PEDR	300
<i>Candidacy: Massif Ridges</i>									
12	Parker et al. (1993), Fig. 3	31.0	343.6	--	--	P22_009761_2113 P13_006188_2123	5.7 5.8	h1542_0009_dt4	115
13	Ghatan and Zimbelman (2006), Fig. 8b	33.0	345.9	--	--	D01_027536_2083	5.7	h2938_0000_dt4	150
14	Ghatan and Zimbelman (2006), Fig. 8c	32.7	343.7	--	--	P13_006188_2123 B03_010684_2117	5.8 5.8	h1542_0009_dt4	125
15	Ghatan and Zimbelman (2006), Fig. 9a	32.2	339.7	--	--	B16_016051_2121 G19_025756_2132	5.8 5.8	h1326_0000_dt4	75
16	Ghatan and Zimbelman (2006), Fig. 12c	35.3	340.7	--	--	D22_035672_2152	5.8	h1326_0000_dt4	75
17	Ghatan and Zimbelman (2006), Fig. 15c	16.6	80.1	--	--	G14_023814_1955	5.5	h5234_0000_dt4	75
<i>Candidacy: Isolated Ridges and Ridges within Troughs</i>									
18	Ghatan and Zimbelman (2006), Fig. 17c	17.5	81.8	ESP_037620_1980 ESP_053602_1975	0.5 0.5	F05_037620_1978	5.6	h2948_0000_dt4	75
19	Ghatan and Zimbelman (2006), Fig. 17d	18.4	93.2	--	--	B20_017471_1977 ^b G06_020517_1976 ^b	5.6 5.6	MOLA PEDR	300
20	Ghatan and Zimbelman (2006), Fig. 17e	18.1	83.0	ESP_025449_1985	0.25	P18_008228_1981	5.6	h2948_0000_dt4	75
21	Ghatan and Zimbelman (2006), Fig. 12e	25.9	326.5	ESP_026284_2060* ESP_027339_2060*	0.25 0.25	B20_017291_2046	5.7	HiRISE stereo* h1619_0000_dt4	200
22	Parker (2008), Fig. 4	28.1	330.7	PSP_009089_2080* PSP_008878_2080*	0.25 0.25	P20_008878_2081* P21_009089_2081*	5.8 5.8	HiRISE stereo* CTX stereo*	
23	Ghatan and Zimbelman (2006), Fig. 16b	4.6	86.8	ESP_055237_1845	0.5	B20_017379_1871	5.4	MOLA PEDR	300
<i>Candidacy: Lobate Flows</i>									
24	Malin and Edgett (1999), Fig. 1c	39.8	354.0	--	--	K03_054660_2181	5.9	h5314_0000_dt4	100
25	Malin and Edgett (1999), Fig. 1e	44.9	353.0	ESP_046498_2250* ESP_046788_2250*	0.5 0.5	B19_016868_2250* B22_018081_2250*	5.9 6.6	HiRISE stereo* CTX stereo*	0.8

								h1194_0000_dt4 h1465_0009_dt4	75 100
26	Parker et al. (1989), Fig. 9	43.3	4.7	ESP_045878_2235	0.5	F23_044691_2235	6.0	h1626_0000_dt4	75
27	Parker et al. (1989), Fig. 11	44.7	8.2	ESP_057561_2250	0.25	F22_044480_2251* P18_008112_2251*	7.2 6.1	CTX stereo*	
28	Ghatan and Zimbelman (2006), Fig. 15a	16.6	80.7	--	--	P06_003244_1975 B19_017155_1969	5.6 5.6	h5216_0000_dt4	75
29	Ghatan and Zimbelman (2006), Fig. 15f	16.2	80.0	--	--	G06_020412_1953 ^b	5.5	h5234_0000_dt4	75
30	Parker (2008), Fig. 3	46.5	14.5	ESP_016498_2265 PSP_006912_2270* PSP_005989_2270*	0.5 0.25 0.25	B18_016643_2264* P15_006912_2263*	6.1 5.3	HiRISE stereo* CTX stereo*	7.4
31	Parker et al. (2010), Fig. 12	45.6	7.9	ESP_016129_2260	0.25	F22_044480_2251* P18_008112_2251*	7.2 6.1	CTX stereo*	
32	Parker et al. (2010), Fig. 13	44.9	9.1	--	--	P18_008046_2253	6.0	MOLA PEDR	300
33	Parker et al. (2010), Fig. 15	46.8	11.7	ESP_028801_2270	0.5	D04_028801_2268	6.1	h5339_0000_dt4	75
34	Parker et al. (2010), Fig. 16	46.6	12.2	--	--	B01_010195_2277	6.0	h5339_0000_dt4	75
<i>Candidacy: Miscellaneous – Volcanic, Deltas/Alluvial Fans, Tectonic, Outflow Channel Deposits, Glacial</i>									
35	Malin and Edgett (1999), Fig. 1a	32.9	214.2	PSP_007498_2130	0.5	F04_037470_2129	5.8	h1525_0001_dt4	75
36	Ghatan and Zimbelman (2006), Fig. 12a	11.7	314.5	ESP_022434_1920	0.25	F19_043282_1919 F21_044060_1919	5.5 5.5	HiRISE stereo ^a	1
37	Parker et al. (1989), Fig. 6	41.7	6.5	PSP_006464_2220	0.25	P14_006464_2214	5.9	h1604_0000_dt4	125
38	Parker et al. (2010), Fig. 9	45.3	16.0	--	--	P17_007492_2261 B19_016999_2240	6.1 5.9	h3304_0000_dt4	100
39	Webb (2004), Fig. 9e	39.8	350.9	ESP_017145_2200	0.25	F21_044019_2185* F21_044164_2185*	5.9 6.0	CTX stereo*	
<i>Candidacy: Uncertain</i>									
40	Ghatan and Zimbelman (2006), Fig. 15b	14.5	79.7	--	--	B21_017933_1943 ^b	5.5	h5234_0000_dt4 MOLA PEDR	75 300

Note: Sites are referenced in text by an abbreviated version of the citation (initial(s) of the author(s) listed, last two digits of the year, and the figure number). For example: Site P89-13a refers to Site #1 here.

^aPDS-derived stereo (DTEEC_022434_1920_021577_1920_L01).

^bNo higher-resolution imagery exists than was used by the citation (e.g. the MOC NA used in the initial analysis is higher resolution than the CTX and no HiRISE coverage currently exists).

^cData does not cover the exact ridge investigated by the citing article but does cover a locally adjacent feature.

5.4.1 Mass Wasting Features

Multiple sites appear to have curvilinear ridges or lineaments that have previously been interpreted to be strandlines, “ridge-and-swale” terrain (typical of migrating beaches), small wave-cut benches, or coastal ridges exemplified in Fig. 5.3a (Site GZ06-17a). At coarse resolutions, these features appear as continuous ridges, but at high-resolution the lineaments lack landform continuity and dissolve into the surrounding terrain. The lineaments are highly discontinuous, bifurcate, terminate, and merge along track. Site CP01-4 shows similar lineament features, and a

detailed quantitative high-resolution assessment by Sholes et al. (2019b) found them to be inconsistent with a shoreline hypothesis. We interpret these features as the result of mass wasting of material along a steep surface (degraded crater rims).

In Mamers Valles, Sites P89-13a, P89-13b, and P89-13c were some of the original sites used in support of a paleoshoreline interpretation with changes in slope and “ridge-and-swale” structures along the canyon wall. However, at higher-resolutions these appear to be colluvium deposits along the canyon wall with modification from Amazonian glacial processes. The lobate debris flows and lineated valley fill within Mamers Valles (and adjacent to these sites) are well documented and largely believed to be the remnants of late Amazonian glaciation (D. M. Baker & Head, 2015; D. M. Baker et al., 2010; Head et al., 2006a; Head et al., 2006b; Levy et al., 2007; Morgan et al., 2009; Plaut et al., 2009; Van Gasselt et al., 2010). Ridges at Site P89-13a are revealed to be escarpments that face towards the canyon wall, opposite what would be expected for a shoreline. Lineaments at Sites P89-13b and P89-13c are discontinuous and sinuous within the colluvium deposits and topographic data show no sign of related benches.

Site GZ06-17b is a series of ridges located in southern Isidis Planitia following the margin at the base of the dissected Libya Montes highlands. In HiRISE, the ridges are shown to be more sinuous than previously identified and exposed beds are observed with different dips. We interpret this as an unconformity between the inclined north-dipping bedding of the lower unit and the less inclined overlain bedding. Weathering and mass wasting processes have eroded back some of the units, manifesting as a ridge at the base of the slope.

5.4.2 *Collapse Features*

A specific subset of the mass wasting features are the stepped massifs that Parker et al. (1993) and subsequent papers used as a major point in support for a paleoshoreline interpretation. These sites are massifs or mounds that are encircled by smooth and near-flat aprons that appear to locally approximate an equipotential surface (Carr & Head, 2003) and have been interpreted as wave-cut island terraces. Alternatively, the features may be the result of progressive degradation and collapse of the highland material along the topographic dichotomy (Tanaka, 1997). Previous

work has generally found that the platforms surrounding the massifs vary in height, have rounded shoulders, and are often fractured which is less consistent with a wave-cut origin. Subsequent topographic data from MOLA showed that many of these stepped massifs/knobs are located in topographic depressions, further supporting a collapse origin (Tanaka et al., 2003).

Fig. 5.3b (Site PC01-12) shows an example of two adjacent stepped massifs at high-resolution. The western massif's platform itself can be seen weathering into smaller knobs/massifs and both show uneven surfaces. Fitting planes to the individual MOLA shot points over each platform show that they tilt in opposite N-S directions with the western massif ~100 m lower in elevation compared to the eastern massif. Both this site and the nearby Site PC01-11 are located within or along the margin of local topographic depressions and fractured terrain (with Site PC01-11 having little to no platform present and dominated by colluvium). This contradicts the original assessment that these aprons could be used as a "marker bench" across the region and supports a general collapse origin.

Clusters of stepped massifs can be found at Sites GZ06-12f, GZ06-8c, GZ06-9a, and GZ06-12c (the latter three sites are described in more detail in Section 3.3 below). It is apparent that the massif platforms overlap each other throughout the larger complex of massifs, thus do not form a paleo-equipotential surface. At other sites (GZ06-12b) the massif platforms are uneven, vary in elevation, and onlap not only adjacent platforms but also fractures and escarpments on the plains floor. There are also extensive talus piles forming from the massifs both above and below the aprons. This all suggests these aprons were not carved as the result of an ocean stand, but rather individually degraded into the observed morphologies.

Other types of collapse features include Site GZ06-12d which are a series of ridges on the floor of Oxus Patera along the topographic dichotomy. These ridges are angled at various orientations to each other and the patera rim shows signs of partial collapse. The site is not open to the northern plains and has been proposed as an ancient supervolcano caldera (Michalski & Bleacher, 2013).

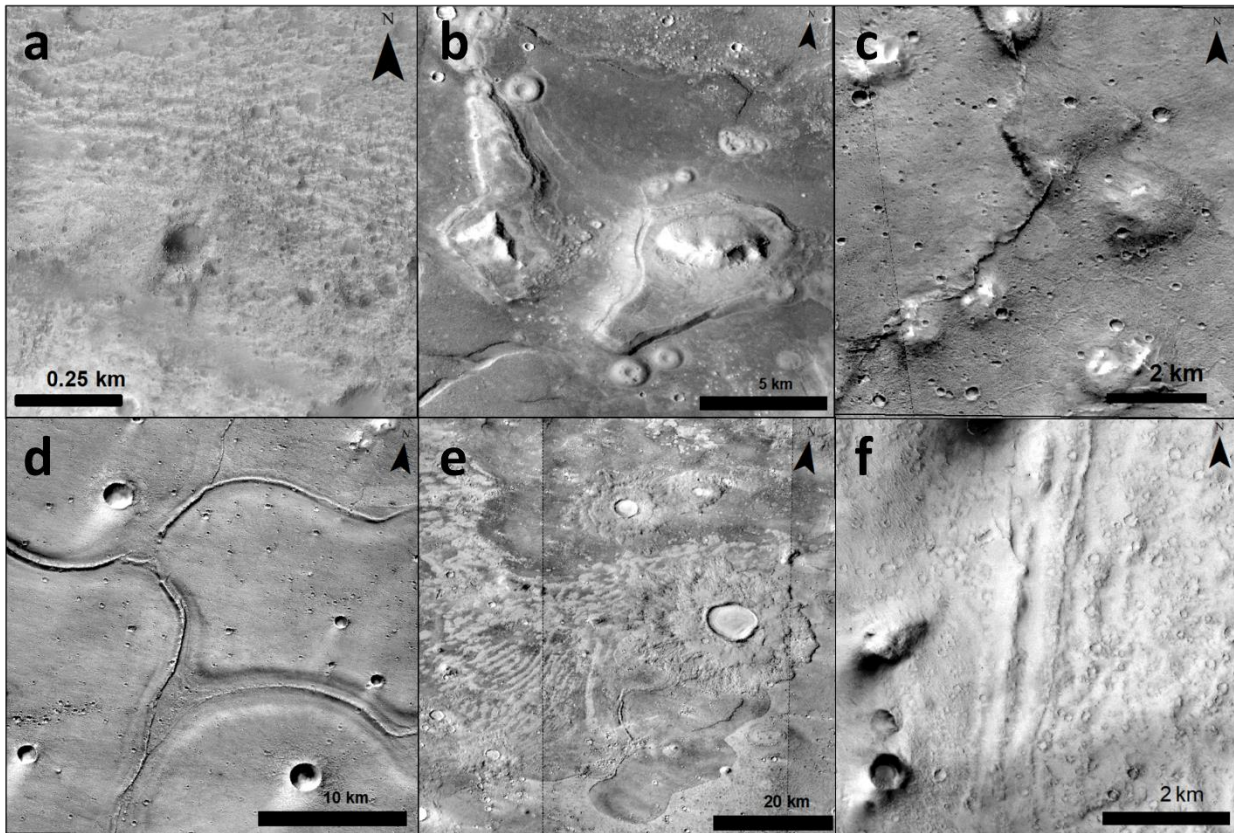


Figure 5.3. Examples of typical features associated with putative shorelines. a) Mass Wasting: Site S3 (GZ06-17a) showing discontinuous lineaments along a degraded crater rim. HiRISE image PSP_007648_1845 (0.5 m/px). b) Collapse Features: Site S6 (PC01-12) is an example of stepped massifs along the topographic dichotomy. MOLA shows that the platforms are angled in opposite directions with surfaces differing up to 100 m in elevation. CTX image G04_019756_2204 (6.1 m/px). c) Massif Ridges: Site S14 (GZ06-9a) exemplifies multiple ridges that are sinuous and cross-cut the massifs suggesting they are not tombolos, spits, or other coastal features. CTX image G19_025756_2132 (5.8 m/px). d) Isolated Ridges: Site S20 (P08-4) shows examples of curvilinear ridges within troughs. CTX image P21_009089_2081 (5.8 m/px). e) Lobate Flows: Site S23 (P89-9) shows multiple overlapping lobate flow deposits with different tones and textures (see unit map in Fig. S35). CTX mosaic. f) Uncertain: Site S40 (GZ06-15b) is a series of linear ridges in Isidis Planitia but are only a few kilometers in length, isolated from the “coastline,” are discontinuous with some bifurcations, and are too low in elevation to be from a global ocean. CTX image B21_017933_1943 (5.5 m/px).

5.4.3 *Massif Ridges*

Many of the massifs are also observed with curvilinear ridges branching off or connecting the massifs from one another. These were interpreted to be the remnants of constructional coastal landforms (e.g. spits and tombolos) attached to islands in the early literature (Parker et al., 1993). None of these putative massif ridge sites had HiRISE coverage, though CTX provided sufficiently higher resolutions than the Viking and THEMIS imagery previously used.

Highlighted in Fig. 5.3c, Site GZ06-9a displays several massifs within a more concentrated massif-unit. Here, we observe that the massif ridges crosscut the massifs and their associated debris aprons, which we infer to mean that the ridges are chronostratigraphically younger than the massif platforms and not the result of depositional coastal processes. Additional ridges here and elsewhere (e.g. Site P93-3) in the massif units change morphology along track with some appearing to be escarpments, cross-cutting debris aprons, bifurcating, and simply demarking the boundary between the VBF and the massif-units. These are more consistent with glacial eskers rather than coastal tombolos.

A variety of other massif ridge morphologies and orientations are found. The presence of highly sinuous ridges that terminate abruptly at the margin of the massifs and mesas within plains material that locally is dense with wrinkle ridges suggest that Sites GZ06-8b and GZ06-12c are larger wrinkle ridges. The crests of the ridge in Site GZ06-8c is covered in shallow pits with larger oblong pits along the southern side and resemble the topographic ridge pit chains seen elsewhere in the northern plains. Additional isolated ridge pit chains are seen elsewhere in the region not associated with the massifs, suggesting these features have high amounts of volatiles (Orgel et al., 2019). Located within Isidis Planitia's VBF-like material, Site GZ06-15c shows two ridges that form an arcuate layout, but rather than joining they curve away from each other at their ends. The orientation of the arcuate nature of the ridges follows that of the local lobate flows of the Deuteronilus Level and the arcuate thumbprint terrain of the VBF nearby. This suggests it may be related to the flows associated with the Deuteronilus Level.

Our analysis of these massif-ridges further support the assessment by Ghatan and Zimbelman (2006) that the ridges are more consistent with the “leveed margins of a lava flow or

the edges of debris flows associated with the massifs” rather than coastal deposition. The cross-cutting relationships in particular suggest these are geologically younger than the massif terrain and not coastal in origin. Other ridges may be larger wrinkle ridges that happen to contact massifs within the dense massif terrain or associated with the viscous flow behavior of the VBF.

5.4.4 *Isolated Ridges and Ridges within Troughs*

Some of the features suggested as possible coastal ridges along the putative shoreline levels include isolated ridges and medial ridges within curvilinear depressions (which we will refer to as “trough ridges”) found predominantly within Isidis Planitia. These latter trough ridges are curvilinear ridges that have linear depressions paralleling both sides of the ridge. Others have also investigated some of these features and interpreted them to be the eskers overlaying tunnel valleys from mass glaciation over Isidis Planitia (e.g. Guidat et al., 2015; Kargel et al., 1995).

All of these sites are located within the VBF or VBF-like material (Ivanov et al., 2017 found that the "VBF" within Isidis Planitia is distinctly younger than the rest of the northern plains) and are unlikely to be coastal ridge candidates. They are either isolated and located far from the “coastline” (e.g. the highlands or Deuteronilus Level) and/or have orientations inconsistent with a shoreline (e.g. orthogonal to the Deuteronilus Level or bifurcating and overlapping with other ridges).

Trough ridges found within Chryse Planitia (Sites P08-4 and GZ06-12e), such as those within the terminus of Tiu Valles (Fig. 5.3d, Site P08-4), are typically arcuate in shape with overlapping and merging ridges between streamlined islands. Their arcuate orientations are both convex and concave to the northern plains. In comparison, the trough ridges within Isidis Planitia (Sites GZ06-17c, GZ06-17d, and GZ06-17e) generally have linear to splined geometries and are oriented perpendicular to the regional Deuteronilus Level. The ridge crests display varied morphologies along-track as well, including pitted, discontinuous, sharp, and trough. At the southern end of Site GZ06-17c is a more complex geometry where a trio of ridges form a triangle shape, though it appears that the main ridge overlies one of the smaller ridges, perhaps indicating

multi-stage formational process. Small bifurcations and lateral displacements can also be seen within these trough ridges.

Site GZ06-16b in southern Isidis Planitia is characterized by multiple crosscutting, sinuous, and curvilinear ridges. These features are found within the surface veneer unit and superimpose a larger sinuous topographic ridge interpreted to be from buried volcanic wrinkle ridges within the basin (Head et al., 2002; Ivanov & Head, 2003). The orientation, crosscutting relationships, and sinuous morphologies suggest that these are wrinkle ridges within the plains material.

5.4.5 *Lobate Flows*

Nearly a third of the sites are typical examples of the lobate flow fronts that predominantly defines the Deuteronilus Level and makes up large swaths of the southern boundary of the VBF (Fig. 5.2c). These deposits onlap the surrounding terrain and often have curvilinear ridges that parallel their margins. The edges of the VBF themselves are most often highland-facing escarpments, which is the opposite from what would be typically expected for a shoreline.

Sites P89-9, -11, P08-3, P10-12, -13, -15, and -16 are all clustered in western Deuteronilus Mensae where the VBF has filled in the topographic lows in the fretted terrain while Sites GZ06-15a and GZ06-15f are located in western Isidis Planitia. For all of these sites, we find no specific coastal landforms. Topographic data confirms the previous assessments that these flow fronts either occupy topographic lows or onlap the surrounding terrain (and in some places up regional slopes, e.g. Site P08-3 in Mamers Valles). HiIRSE imagery along the margins of the VBF show an irregular contact that appears sharp at larger scales. Site ME99-1c is an outlier to the typical broad lobate flow boundaries associated with the Deuteronilus Level, but still drapes over the adjacent knobby terrain with no coastal landforms present.

The VBF has a range of different textural and tonal units though is commonly defined as a single unit (Tanaka et al., 2005). Fig. 5.3e (Site P89-9) shows examples of where these different terrains flow over one another with a lighter-toned unit with the “thumbprint terrain” appears to flow over a smooth dark-toned flow. The thumbprint terrain flow unit here also appears to be two possibly distinct units as viewed with THEMIS-IR day imagery where Ivanov et al. (2017) mapped

the Deuteronilus Level through the thumbprint terrain (see mapped image in Sec. C.2.25). Site P10-15 also shows what appears to be a small lobate tongue that underlies the dominant flow contacts suggesting a previous flow event. Elsewhere (Sites P10-12 and P10-13), the VBF material appears to have filled in irregular fractures.

One of the most diverse sites investigated is Site ME99-1e where the lobate flow front morphology associated with the Deuteronilus Level appears on top of a mesa ~200 m above the surrounding plains. The mesa has a relatively flat top, with MOLA shot points having a mean elevation of $-4,200 \pm 10$ m (1σ). This occurs ~200 m below the low-end of the decile range for the mapped Deuteronilus Contact in the region (Tempe-Chryse-Acidalia-Cydonia-Deuteronilus-Phlegra in Ivanov et al. (2017)). The unit making up the Deuteronilus Level has fractured, with visible collapse structures along the southern margin of the mesa with light-toned pitted mounds erupting from these collapse fractures (and elsewhere in the plains unit). These mounds have been interpreted to be possible mud volcanoes (e.g. Oehler & Allen, 2010). The eastern flank of the mesa has features that superficially resemble possible terraces, but visual inspection and TEA show no continuous terraces, likely related to mass wasting events.

5.4.6 *Miscellaneous Features*

A few of the sites have since been featured in detailed studies that suggest they are not shorelines. The Olympus Mons aureole was originally mapped as the shoreline contact (Parker et al., 1993; 1989), however lava flows emanating from under the aureole deposits have since been observed, showing that the aureole deposits were emplaced or thrust over the northern plains and thus that the contact is not a primary shoreline (Carr & Head, 2003; Fuller & Head, 2002). While it has been proposed that the western flank of the aureole were deposited subaqueously (De Blasio, 2018), coastal landforms have not been observed on or above the aureole. High-resolution imaging of Site ME99-1a along the aureole shows that this contact is also unlikely to be a secondary shoreline contact as the transition is scalloped with no coastal features.

Another site (GZ06-12a) exhibits a series of stepped benches near the terminus of Hypanis Valles. TEA was unable to provide useful information as the benches are tightly packed both laterally and vertically, causing even the HiRISE DEM to have an inadequate resolution. However,

these features appear to be layering within a branch of a larger fan deposit. Detailed work by Fawdon et al. (2018) and Adler et al. (2019) showed that the observed stacked benches and ridges are most likely exposed stratigraphic sets of either a delta or an alluvial fan. If this site is indeed a delta, it may lend some support for the delta as a whole being a coastal feature, but the authors cannot preclude an alluvial fan origin and additional coastal landforms are not observed.

The Arabia Level in Deuteronilus Mensae (Fig. 2a and Site P10-9) appears to simply be a unit boundary between a dark-toned northern plains unit and the lighter toned highlands (in THEMIS-IR [infrared] day imagery). Some places along the contact follow a cliff face, but elsewhere the contact is diffuse and difficult to identify with a much shallower slope. Parker et al. (2010) described the rim of the canyon associated with Site P10-9 as more rounded to the south (topographically lower) and sharper to the north (topographically higher). We do not observe any such discernible difference. Indeed, the eastern side of the fret canyon appears to be softened (compared to the western side) to the south of the Arabia Level on that side (topographically higher), the opposite of what would be expected for a coastal-derived contact. This tonal contact is more readily explained as a geologic unit that has been exposed (sometimes sharply) as part of the general collapse of the highlands during the formation of the fretted terrain in Deuteronilus Mensae.

Site P89-6 was one of the original “type” localities to define the Arabia Level, located in western Deuteronilus Mensae. Unlike other sections of the Arabia Level that are defined by diffuse tonal contacts in the visible range (and more distinct in THEMIS-IR Day), the contact here is clearly a dark-toned deposit overlapping the highlands terrain. The material is also associated with the adjacent channels both from the nearby Semeykin Crater and the highlands themselves. HRSC topography shows that the material flows northward out of Semeykin Crater, which is the opposite of what Parker et al. (1989) interpreted as oceanic deposits flowing into the crater. Indeed, our investigations support the work of Mangold and Howard (2013) that these are the end ponding zones of a Hesperian-aged outburst flood or floods from a crater further south in Ismenius Lacus region. Neither we nor them find evidence that these zones were occupied by a lake or ocean when deposited as the contact is somewhat diffuse and bouldery with no observed coastal landforms in HiRISE. Thus, we have categorized the site as “outflow channel” related features in origin.

Both the Arabia and Deuteronilus Levels were mapped along massifs in Site W04-9e. However, now-available HiRISE imagery shows that the Arabia Level is the exposure of a different lithological unit along a steep slope of a massif. Here, the Deuteronilus Level is incorrectly identified as the plains-facing escarpment along a massif debris apron. Additionally, the floor material between the massifs has lineated ridges, suggesting modification by more recent glacial activity.

5.4.7 *Uncertain Feature*

A single site, Site GZ06-15b, is classified as uncertain as some observed features are consistent with a paleoshoreline interpretation and there has been no increase in spatial data resolution since the assessment with MOC NA by Ghatan and Zimbelman (2006). The site, shown in Fig. 5.3f, is a series of stacked ridges located in western Isidis Planitia ~30 km from the highlands. This would be an ideal location to apply TEA, but the best topographic data is from HRSC (75 m/px). However, MOLA shotpoints indicate that the ridges lie approximately 200 m below the topographic divide between the Isidis basin and the Utopia basin of the northern plains. Thus, even if these were indeed wave-cut terraces or coastal ridges, they would be of an Isidis sea and not a northern ocean. Furthermore, there appears to be some bifurcations associated with some of the narrower ridges.

5.5 DISCUSSION

5.5.1 *Paleoshoreline Assessment*

Overall, we find no supporting, let alone convincing, evidence for paleoshorelines among the proposed sites. Of the 40 sites investigated, only Site GZ06-15b (Fig. 5.3f) was a reasonable candidate for coastal features, but its location in Isidis Planitia, well below the topographic divide separating Isidis from the northern plains, shows that even if the features were shorelines, they were not from a hemispheric ocean. The remaining sites all exhibited features that could be more readily explained from other known and conservative martian surface processes without needing to invoke an oceanic origin.

Mass wasting along steep slopes can create the observed discontinuous lineaments, especially if mediated by ice (e.g. Levy et al., 2009; Squyres, 1979). Collapse of the highlands along a smooth plain can account for the relatively equipotential surface of the stepped massifs (e.g. Carr & Head, 2003; Tanaka et al., 2003). The massif ridges may be eskers, wrinkle ridges, volcanic ridges, contractional deformation, or erosional features associated with the degradation of the massifs (e.g. Ghatan & Zimbelman, 2006; Tanaka et al., 2003). Isolated and trough ridges may be related to glacial tunnel valley and esker complexes (e.g. Guidat et al., 2015; Kargel et al., 1995) or soft-sediment deformation (e.g. Tanaka, 1997; Tanaka et al., 2003). Furthermore, neither the Arabia nor Deuteronilus Levels as a whole show any unambiguous characteristics of a coastal origin in the high-resolution data.

The Arabia Level has two different morphological expressions: it appears most prominently as a sharp albedo contrast between the darker-toned plainsward material and the lighter-toned highlands but also manifests as putative terraces along steeper slopes. However, despite claims that the contact can be mapped to near complete closure around the plains, the dominant investigations have focused only on a handful of sites within northern Arabia Terra between Cydonia and Deuteronilus Mensae (Fig. 5.1). Our high-resolution investigation of these sites has found no convincing evidence for a paleoshoreline interpretation. The putative terraces in Cydonia Mensae have been found to be discontinuous both spatially and topographically (Sholes et al., 2019b). The tonal contact near and within Semeykin Crater has been found to be the likely ponding zone of outflow channels originating from the highlands with no indication of prior occupation by water (Mangold & Howard, 2013).

In Mamers Valles and Deuteronilus Mensae the tonal contact is easily recognizable in THEMIS-IR Day, but is more subtle and gradational in visible CTX. Thus, it may simply be a contrast between underlying geological units with differing thermophysical properties exposed as part of the breakup of the highlands in the fretted terrain. Stepped massifs throughout the region have also been used to support an erosional shoreline interpretation, but these platforms overlap and may be simply mass wasting landforms from the massifs onto the flat plains associated with the collapse of the highlands (Carr & Head, 2003; Tanaka, 1997; Tanaka et al., 2003).

Unlike the somewhat tenuous expressions of the Arabia Level, the Deuteronilus Level has been extensively mapped across the northern plains and is easily recognizable as a series of lobate flow fronts (Ivanov et al., 2017). Several different modes of emplacement have been hypothesized for the origin of the VBF, whose margins make up most of the Deuteronilus Level, including volcanic, glacial, and fluvial. Investigations of the VBF itself have found consistency with both volcanic and sedimentary origins. Shallow Radar (SHARAD) measurements of Amazonia Planitia find the permittivity of the VBF to better match low-loss basaltic lava terrain rather than ice-rich terrain (Boisson et al., 2011). On the other hand, Mars Advanced Radar for Subsurface and Ionosphere Sounding (MARSIS) data find that the dielectric constant of the VBF is consistent with oceanic sediments and inconsistent with basalt (Mouginot et al., 2012). However, such a dielectric constant can also be explained by 35% porosity of volcanics, noting that vesicular lavas have primary porosities ranging from 5-50% (Weight & Sonderegger, 2001). The low latitude shallow regolith was also ice-filled during obliquity cycles (Haberle et al., 2003) and is probably very porous. Similarly, the pitted mounds found within the VBF and in association with the thumbprint terrain have been suggested to be forms of mud volcanism (e.g. Oehler & Allen, 2010; Salvatore & Christensen, 2014), though a volcanic origin (e.g. tuff cones or pseudocraters) cannot be ruled out (Farrand et al., 2005).

The margins of the VBF that make up the Deuteronilus Level are equally as ambiguous in their genetic origin as the deposits themselves. Glacial lobes and lava flows have been proposed as possible mechanisms, though a catastrophic fluvial emplacement is largely considered the primary mechanism. In many places the VBF is observed to flow upslope (e.g. in Mamers Valles, Site P08-3), which has been seen to be at odds with dominantly gravity-driven lava and glacial flows. Deposits from more recent glacial flows have been observed trending upslope along the dichotomy boundary (Dickson et al., 2008) and the paleotopography during deposition may have been different (N. H. Chan et al., 2018; Citron et al., 2018; Perron et al., 2007; Ruiz et al., 2004).

Hypotheses regarding emplacement of the VBF vary in their reliance on an ocean during formation. These include: subaerial debris flows associated with the mobilization of sediment from the outflow channels (Jöns, 1985), sediment-laden water effluents from the ponding (into an ocean)

of the outflow channels and rapid freezing (Carr & Head, 2019; Kreslavsky & Head, 2002), extrusion of mud onto the surface (Salvatore & Christensen, 2014), tsunami deposits or ice-surges (Rodriguez et al., 2016), CO₂-H₂O charged fluidization (Tanaka et al., 2001) or near-surface groundwater activity (Tanaka et al., 2003) of sediments from the degradation of the highlands, or shoving of sediments under an ice and debris covered ocean (Parker et al., 2010).

The formation and margins of the VBF would have obscured or possibly obliterated marine sediments from an earlier ocean (Tanaka et al., 2003). Small crater morphology (Catling et al., 2012) and detection of basaltic mineralogy in the shallow subsurface of the northern plains (Salvatore et al., 2010) may suggest an igneous origin or at least an igneous component. The timing of the VBF formation is also questionable as Tanaka et al. (2003) find that it postdates the Hesperian-aged outflow channels while Ivanov et al. (2017) suggests they formed contemporaneously.

Our observations and analysis of the Deuteronilus Level lead us to categorize it as inconclusive with current data. While we find no obvious coastal features, many of the hypothesized emplacement methods are rather unique to Mars in scale with limited to no terrestrial analogs for comparison. Many of the landforms we observe are consistent with multiple different origins and thus can lead to disparate interpretations. The different overlapping lobate flow units we mapped may be attributed to discharge of sediment laden water as a result of near-surface groundwater interacting with highland and outflow channel sediments (Tanaka et al., 2003).

5.5.2 *Elevation of the Mapped Shorelines*

Furthermore, there is the question of whether the mapped putative shoreline levels at these sites, invoked as evidence of coastal features (e.g. Ghatan & Zimbelman, 2006; Malin & Edgett, 1999) form an expected equipotential surface (e.g. Carr & Head, 2003; Head et al., 1998). While many of the geomorphological and stratigraphic relationships first used to describe the contacts were done on extremely limited high-resolution *Viking* images (at ~10 m/px) (Parker et al., 1989), most of the putative global contacts were drawn free-hand on printed out lower resolution *Viking* images (at ~200-400 m/px) (Parker et al., 1993; Parker et al., 1989, T. Parker, personal

communication, 2013). Thus, at these resolutions, the contacts were at the limits of detectability and therefore prone to misidentification and misplacement (Clifford & Parker, 2001).

To test whether the putative shorelines form an equipotential surface, Head et al. (1999; 1998) digitized the mapped levels of Parker et al. (1989) and, with the limited number of MOLA tracks at the time, found that the Deuteronilus Level approximated an equipotential surface while the Arabia Level varied by many kilometers. Later, the levels were again digitized by Carr and Head (2003) from an updated map presented in Clifford and Parker (2001, their Fig. 6) which was still largely based on the Viking data with some regional improvements from the MOC. Since then, Ivanov et al. (2107) presented a new detailed mapping of the Deuteronilus Level using THEMIS-IR day images. Yet with the exception of a segment of the Arabia Level mapped by Webb (2004), which was largely based on elevation data to circumvent the Bamberg Crater ejecta blanket, the Arabia Level has not received a published detailed mapping based on morphological characteristics.

However, this history of the mapped levels shows how misidentification of the shorelines has compounded over time. Uncertainties in the exact location stem not only from resolution limitations, but also from errors in the digitization process (e.g. line widths, number of points, projection issues). This progressive datamining process based on older low-resolution data has led to an unclear understanding as to whether the levels truly show considerable range in their elevations or whether they are not truly continuous features or shorelines (Carr & Head, 2019).

Fig. 5.4 shows a snapshot of the extent of misplacement of the mapped shorelines within Deuteronilus Mensae as compiled and reprojected into the same data frame using ArcMap 10.6 (www.esri.com). The Arabia and Deuteronilus Levels digitized by Carr and Head (2003) (as used in Perron et al., 2007) are compared directly against the detailed mapping of the Deuteronilus Level by Ivanov et al. (2017) and our own remapping of the Arabia Level (based off the original designation as a tonal contact in Parker et al. (1989) using CTX imagery and the THEMIS-IR Day global mosaic at 100 m/px). Here, it is obvious how much the mapped levels differ both spatially and topographically. Laterally, the Arabia Level is offset by more than 500 km and the Deuteronilus Level by up to 300 km. Of course, some of this offset was caused by generalization

of the contact during the digitization process as the mapped levels were complex in nature due to the numerous mesas, massifs, and valleys in the region.

Topographically, our remapping found the Arabia Level forms a local mean elevation of -3,560 m with an interdecile range of 200 m (over a ~750 km spatial distance). Compare this with the local mean elevation of -2,430 m and an interdecile range of 1,300 m from the datamined version (and a range of >4 km globally). Elsewhere, unpublished remapping efforts have found up to ~2 km of elevation discrepancy within the Arabia Level east of Isidis Planitia due to misidentification in the Viking data (Parker & Calef, 2012).

While the Deuteronilus Level has been mapped in detail, it is also not without error. We found because it was mapped using the THEMIS-IR day mosaic (Ivanov et al., 2017) parts of the Deuteronilus Level were excluded or erroneously placed within the VBF rather than entirely along the margin (see Sec. C.2.25). While the boundary is often readily identifiable in visible imagery, the tonal and textural variations lead to apparent misidentification in the infrared data. However, unlike the Arabia level, the variations in elevation appear to be minor.

Despite these extremely large variations in the Arabia Level, its digitized location and elevation data have permeated throughout the literature (e.g. N. H. Chan et al., 2018; Citron et al., 2018; Perron et al., 2007). The Deuteronilus Level is still found at two distinct regional levels (with decile elevation differences of ~180m and ~270 m) which can be explained by accounting for subsequent true polar wander (Ivanov et al., 2017). Yet we find that the Arabia Level more closely approximates an equipotential surface than previously thought. This ought to change the modeled magnitude and timing of the deformation of the contacts (Zuber, 2018). Additionally, it is worth noting that the deformation models exclude large portions of the mapped Arabia Level (blue lines in Fig. 1) without any justification. Thus, we urge extreme caution when examining or evaluating the poorly mapped Arabia Level.

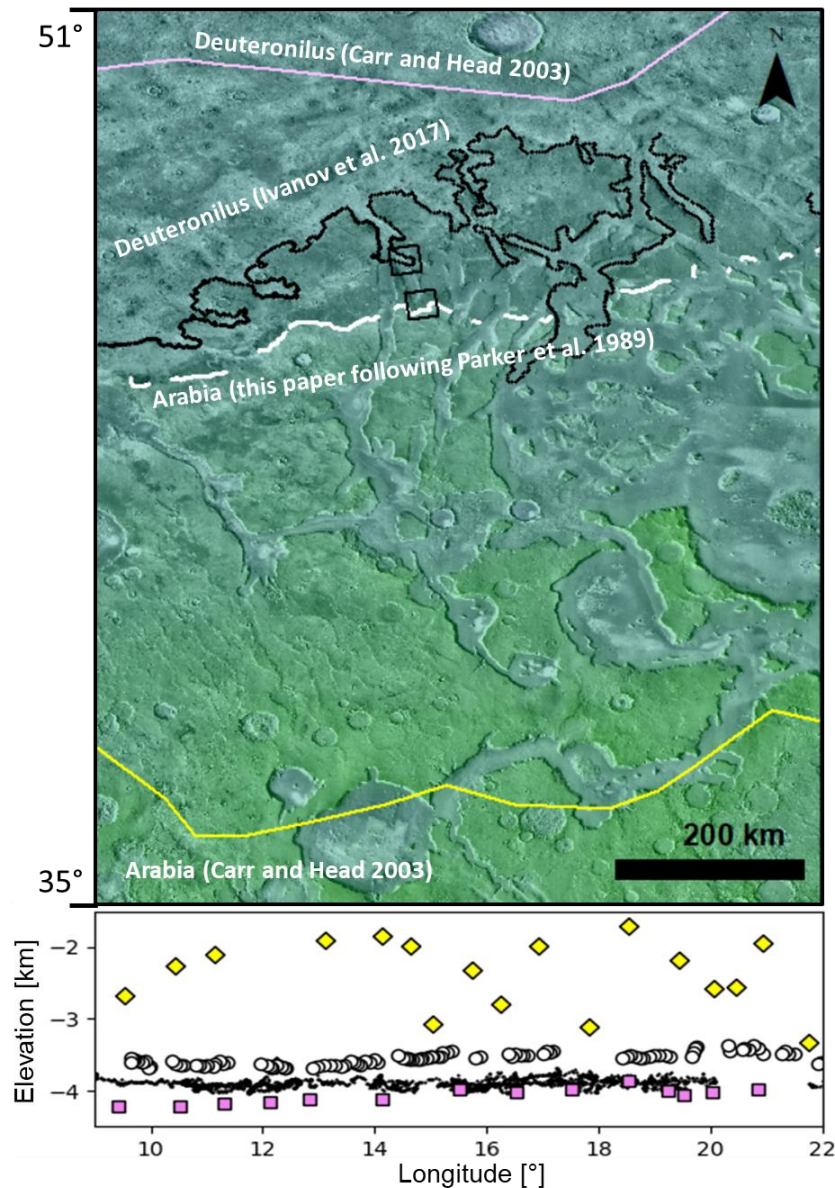


Figure 5.4. Mapped shoreline disparities in western Deuteronilus Mensae. *Top*: Locations of the differently mapped Arabia and Deuteronilus Levels. Yellow lines (diamonds in *b*) and purple lines (squares in *b*) are the digitized locations by Carr and Head (2003) of the map in Clifford and Parker (2001). Black lines (points in *b*) show the detailed mapping by Ivanov et al. (2017). White lines (circles in *b*) show where the Arabia Level should be based on the original description in Parker et al. (1989) as mapped by us here. THEMIS-IR day mosaic with MOLA colorized elevation. *Bottom*: Elevations of the different levels (with corresponding colors) showing the >2.5 km spread in the de facto ‘standard’ mapping of the Carr and Head (2003) Arabia Level and 100s m elevation spread in the other putative shorelines.

5.5.3 *Other Lines of Evidence for Oceans*

While we find no convincing paleoshoreline evidence *for* oceans, this does not preclude the existence of such oceans or their coastal features. Alternative explanations concerning the state of the levels include: 1) billions of years of erosion and modification by surface processes that may make any coastal features unrecognizable, 2) the potential inability for such an ocean to produce long-lasting morphologies either from the difficulty in generating sufficient wave-energy (Banfield et al., 2015; Kraal et al., 2006) or being ice-covered or fully frozen (Carr & Head, 2019), 3) or having been geologically very short-lived (e.g. Clifford & Parker, 2001).

The lack of unambiguous or obvious coastal features along the putative shorelines and the 100s m of elevation range presented here echo the conclusions of Carr and Head (2003) in that the putative paleoshorelines along the margins of the northern plains offer little to no support for an ocean. Thus, other lines of support are required to invoke such an extraordinary hypothesis as oceans. This is especially true given the many questions and paradoxes associated with the hypothesis (such as to where the large volumes of water came from and where they went, compatibility with past climates and current geochemical tracers, etc.) (Head et al., 2018; Turbet & Forget, 2019).

Other lines of support for an ocean include the presence of putative tsunami deposits (Costard et al., 2017; Rodriguez et al., 2016) and the distribution of open-basin deltas (Di Achille & Hynek, 2010; DiBiase et al., 2013; Fawdon et al., 2018; Hughes et al., 2019) or valley networks (N. H. Chan et al., 2018; Hynek et al., 2010) along the topographic dichotomy. Of these, the distribution of deltaic fans has been proposed as one of the stronger lines of support (Fawdon et al., 2018), but recent detailed topographic analysis of the hypothesized deltas along the topographic dichotomy suggest they are in topographic lows recording large lakes rather than an ocean (Rivera-Hernandez & Palucis, 2018). While investigating and evaluating these features is beyond the scope of this paper, the evidence in support of oceans is contested.

5.6 CONCLUSIONS

Here we cataloged and examined 40 sites previously investigated as possible candidate coastal landforms on Mars. Using the latest available high-resolution imagery and topographic data, we find that the features, contacts, and landforms that have been used to define the putative paleoshorelines are either inconsistent with such an interpretation or can be more readily explained through more conservative and known surface processes. The majority of sites appear to be the result of mass wasting, glacial action, or general terrain collapse along the topographic dichotomy associated with the fretted terrain.

Of the putative features, the lobate morphology characterizing the Deuteronilus Level may provide the strongest support for a paleoshoreline interpretation. However, there are many other plausible and consistent explanations that do not necessitate an ocean. Observations and investigations of the VBF unit interior of the contact have provided ambiguous and sometimes contradictory data on whether the unit represents marine, glacial, volcanic, or fluvial sediments. Thus, the available data do not provide sufficient evidence to conclude that the VBF is the remnants of a Hesperian-aged ocean.

We also remapped a small portion of the Arabia Level in western Deuteronilus Mensae (based on the original contact definition) to assess the inaccuracy of maps of this level both laterally and topographically. The majority of this global contact has also received little attention in defining the exact position and characteristic landforms, with most sites located within Deuteronilus and Cydonia Mensae. Hence, we urge caution when using this contact as a reference for the putative shoreline as, unlike the Deuteronilus Level, a robust mapping effort has not been published and the mapped version fails to capture the contact even where it has been most heavily investigated.

Our results and observations here do not preclude the existence of a past Mars oceans but rather show that the putative paleoshoreline features provide little to no support for such a hypothesis.

Chapter 6. CONCLUSIONS

This dissertation advances our understanding on the habitability potential of past and present Mars by: 1) demonstrating that only moderate amounts of volcanism (in line with estimates and models of past volcanic activity) are required to produce anoxic and reducing atmospheric conditions in the past; 2) determining the maximum biomass that currently can be supported on Mars based on the available free energy in the atmosphere; 3) developing a comprehensive toolkit for determining whether landforms are ancient coastal environments; and 4) applying said toolkit to the hypothesized martian shorelines and finding that none provide any convincing or unambiguous evidence for paleoshorelines.

Furthermore, direct consequences of the work for this dissertation have resulted in: 1) the advancement of the 1D photochemical code to no longer require a fixed concentration of CO₂, thus allowing more accurate modeling in future endeavors; 2) a reasonable and justified deposition velocity on CO for Mars that does not necessitate the assumption of large bodies of liquid water (see Appendix A) which helps mitigate the “CO-runaway” effect (Zahnle et al., 2008); 3) an improved subsurface atmospheric diffusion model (see Section 3.3.3); and 4) a catalog of published candidate paleoshoreline features on Mars and their locations in relation to the putative mapped shoreline levels (see Table 5.1 and Figure 5.1).

6.1 CHAPTER SUMMARIES

Chapter 2 uses a 1D photochemical model to find that extrusive volcanism levels $>0.14 \text{ km}^3 \text{ yr}^{-1}$ (under a range of plausible magmatic parameters) are sufficient to produce anoxic and reducing conditions. These atmospheres may have allowed for the formation of organics such as amino acids, thus aiding in the production of habitable environments on past Mars. We also find the counter-intuitive result that the more reducing magmas require greater amounts of volcanism to create reducing atmospheres. This is due to combined effects where sulfur prefers to remain in the melt rather than be outgassed as SO₂, thus limiting a major pathway to remove oxygen from the atmosphere (as sulfate aerosols). Our results also place estimates on the total amount of sulfate and elemental sulfur (S₈) that would be deposited over Mars’ volcanically active history. In

particular, future detection of S₈ on Mars ought to aid in identifying past reducing atmospheric conditions.

We quantify a robust upper limit on the size of any extant biomass on Mars in communication with the atmosphere in **Chapter 3**. Using conservative estimates on the minimal power requirements for microbial life and assuming ideal efficiencies, this upper limit equates to $\sim 10^{27}$ cells or the equivalent of ~ 1 million blue whales. This is miniscule compared to estimates of the total life on Earth ($\sim 10^{32}$ cells) and assumes any such microbes are small, perfectly efficient, and metabolizing at the lower limits of power requirements without population growth. Thus, any such extant biomass would likely be much smaller given more typical cellular power requirements and efficiencies. Diffusion calculations also show that these biomass limits apply to within the few kilometers of the surface. As subsurface life presumably requires a liquid groundwater table (typically estimated around >5 km deep), the availability of these redox pairs at these depths is limited, thus further lowering the maximum allowable biomass. Overall, these results suggest that any extant life on Mars is extremely limited or entirely absent.

Both **Chapter 4** and **Chapter 5** provide compelling evidence that most hypothesized ancient martian ocean shorelines are unlikely to be coastal in origin and can be explained through more conservative surface processes. Using terrestrially-validated mathematical tests for wave-generated terraces, the latest high-resolution images at up to 0.25 m px^{-1} resolutions, and stereo-derived digital elevation models, we find no obvious or unambiguous evidence to support the paleoshoreline hypothesis. This is in line with previous assessments (Carr & Head, 2003; Ghatan & Zimbelman, 2006; Malin & Edgett, 1999) and provides the first published compilation of candidate paleoshorelines with their available high-resolution data products. Many features appear as sharp continuous contacts at large scales, but become highly discontinuous and degraded at small scales. As such, most features are more readily explained and consistent with mass wasting along steep slopes, differential erosion of lithological units with varying thermophysical properties, more recent volcanic, glacial, or tectonic surface processes, or debris flows. Not only do we show that these landforms are unlikely to be paleoshorelines, but our investigations and remapping of parts of the Arabia Level quantitatively address the inaccuracy of the maps both laterally and topographically. However, while we show that the paleoshorelines provide little to

no support for ancient martian oceans, we cannot preclude the existence of such large bodies as their geological fingerprints may have been buried or obliterated.

It is also worth noting that the conclusions of these chapters have broader implications for research on the habitability of worlds outside of Mars. The modeling of the thermodynamic equilibrium in **Chapter 3** shows that any actively metabolizing life on Mars (in communication with the atmosphere) is extremely limited in extent. This suggests that the persistence and abundance of the CO-O₂ and H₂-CO₂ redox pairs constitute antibiosignatures, under the reasonable assumption that microbial life would evolve the simple metabolisms to take advantage of the “free lunch.” Thus, future analysis of exoplanetary atmospheres may be able to deduce the likely absence of a productive biosphere where sufficient knowledge of the atmospheric concentration is known. Indeed, while consideration of CO as an antibiosignature has recently been reconsidered, atmospheres with high CO with stoichiometric ratios of O consistent with CO₂ photolysis (such as on Mars) likely still suggest that any life would be sparse or absent (Schwieterman et al., 2019). Furthermore, our paleoshoreline toolkit described in **Chapter 4** can be used for evaluating candidate sites elsewhere, such as the liquid hydrocarbon seas on Titan with adequate topographic information in the future.

6.2 FUTURE WORK

While the work presented in this dissertation provides a solid framework for better understanding the redox chemistry and classification of paleoshorelines, there are still many outstanding questions to be explored further. We are currently completing a follow-up paper to **Chapter 2** that examines the time-dependent response of the atmosphere to individual volcanic eruption events. Chapter 2 presents the steady state solutions for variable volcanic fluxes and compositions, but does not provide information on how the atmosphere evolves over a variety of timescales. This is an important distinction as gas concentrations and fluxes can be misrepresentative in steady state. For example, due to the different time constants for particular species, the assumed average depositional flux over the timescale needed to reach steady state ($\sim 10^7$ years) may vary drastically from the temporal changes during the initial eruption event ($\sim 10^0$ - 10^2 years). Future missions (such as a proposed polar drilling mission (Hecht, 2006)) may

be able to use these resulting calculations as a valuable theoretical basis to compare sampled measurements with and use as a proxy for transient volcanic events. Such comparisons will allow for possible estimates of the degree, duration, and magnitude of these potentially habitable reducing/anoxic conditions. This would also greatly improve our estimates of the expected observable consequences of anoxia and the gas-phase production component of salts in the martian atmosphere.

Currently, we are also working on applying the paleoshoreline toolkit laid out in **Chapter 4** to putative lacustrine shorelines (as opposed to the hypothesized marine features examined in Chapters 4 and 5). There are many candidate open- and closed-basin paleolakes on Mars (Goudge et al., 2015; Goudge et al., 2012) including the future landing site for the *Mars 2020* rover (Jezero Crater), so applying this quantitative methodology to find any potential wave-generated terraces could provide valuable information on past water volumes and possibly better constrain the longevity of such bodies (Kraal et al., 2006). Furthermore, while we did not explicitly address the evidence for putative tsunami deposits in the northern plains, we are currently analyzing the boulder size-frequency distribution patterns across the northern plains both manually (Sholes et al., 2017a) and with automated software (Hood et al., 2019). Tsunamis should produce fining of sediments (including boulders) inland (towards the southern highlands on Mars) (Bourgeois, 2009), thus allowing us a metric to test the tsunami hypothesis.

APPENDIX A: SUPPLEMENTAL MATERIAL TO CHAPTER 2

Appendix A1: Photochemical Reactions Involving Sulfur Species

Table A.1. List of sulfur reactions used in the photochemical model in Chapters 2 and 3.

#	Reactants	Products	Rate [$\text{cm}^3 \text{s}^{-1}$] or [$\text{cm}^6 \text{s}^{-1}$]	Reference
1	SO + O ₂	→ O + SO ₂	$2.4 \times 10^{-13} e^{-2370/T}$	Sander et al. (2006)
2	SO + O	→ SO ₂	$6.0 \times 10^{-31} \times den$	Sander et al. (2006)
3	SO + OH	→ SO ₂ + H	8.6×10^{-11}	Sander et al. (2006)
4	SO + NO ₂	→ SO ₂ + NO	1.4×10^{-11}	Sander et al. (2006)
5	SO + O ₃	→ SO ₂ + O ₂	$4.5 \times 10^{-12} e^{-1170/T}$	Atkinson et al. (2004)
6	SO + SO	→ SO ₂ + S	3.5×10^{-15}	Martinez and Herron (1983)
7	SO + HCO	→ HSO + CO	$5.6 \times 10^{-12} (T/298)^{-0.4}$	Kasting (1990)
8	SO + H + M	→ HSO + M	$k_0 = 5.7 \times 10^{-32} (T/300)^{-1.6}$ $k_\infty = 7.5 \times 10^{-11}$	Kasting (1990)
9	SO + HO ₂	→ SO ₂ + OH	2.8×10^{-11}	Kasting (1990) ¹
10	SO ₂ + OH + M	→ HSO ₃ + M	$k_0 = 3.0 \times 10^{-31} (T/300)^{3.3}$ $k_\infty = 1.5 \times 10^{-12}$	Sander et al. (2006)
11	SO ₂ + O + M	→ SO ₃ + M	$k_0 = 1.3 \times 10^{-33} (T/300)^{-3.6}$ $k_\infty = 1.5 \times 10^{-11}$	Sander et al. (2006)
12	SO ₂ + HO ₂	→ SO ₃ + OH	8.6×10^{-16}	Lloyd (1974) ¹
13	SO ₃ + H ₂ O	→ H ₂ SO ₄	1.2×10^{-15}	Sander et al. (2006)
14	SO ₃ + SO	→ SO ₂ + SO ₂	2.0×10^{-15}	Chung et al. (1975)
15	HSO + OH	→ H ₂ O + SO	5.2×10^{-12}	Sander et al. (2006)
16	HSO + H	→ HS + OH	7.3×10^{-11}	Sander et al. (2006)
17	HSO + H	→ H ₂ + SO	6.5×10^{-12}	Sander et al. (2006)
18	HSO + HS	→ H ₂ S + SO	1.0×10^{-12}	Kasting (1990)
19	HSO + O	→ OH + SO	$3.0 \times 10^{-11} e^{-200/T}$	Kasting (1990)
20	HSO + S	→ HS + SO	1.0×10^{-11}	Kasting (1990)
21	HSO + NO	→ HNO + SO	1.0×10^{-15}	Atkinson et al. (2004) ¹
22	HSO ₃ + O ₂	→ HO ₂ + SO ₃	$1.3 \times 10^{-12} e^{-330/T}$	Sander et al. (2006)
23	HSO ₃ + H	→ H ₂ + SO ₃	1.0×10^{-11}	Kasting (1990) ¹
24	HSO ₃ + O	→ OH + SO ₃	1.0×10^{-11}	Kasting (1990) ¹
25	HSO ₃ + OH	→ H ₂ O + SO ₃	1.0×10^{-11}	Kasting (1990) ¹
26	H ₂ S + OH	→ H ₂ O + HS	$6.1 \times 10^{-12} e^{-81/T}$	Atkinson et al. (2004)
27	H ₂ S + H	→ H ₂ + HS	$1.5 \times 10^{-11} e^{-855/T}$	Schofield (1973)
28	H ₂ S + O	→ OH + HS	$9.2 \times 10^{-12} e^{-1800/T}$	DeMore et al. (1997)
29	H ₂ S + S	→ HS + HS	$1.4 \times 10^{-10} e^{-3720/T}$	Shiina et al. (1996) ¹
30	H ₂ S + CH ₃	→ HS + CH ₄	$2.1 \times 10^{-13} e^{-1160/T}$	Perrin et al. (1988) ¹
31	HS + O	→ H + SO	1.6×10^{-10}	Sander et al. (2006)
32	HS + OH	→ S + H ₂ O	$4.0 \times 10^{-12} e^{-240/T}$	Zahnle et al. (2016) ¹
33	HS + HO ₂	→ H ₂ S + O ₂	1.0×10^{-11}	Stachnik and Molina (1987)
34	HS + HS	→ H ₂ S + S	1.5×10^{-11}	Schofield (1973)
35	HS + HS	→ S ₂ + H ₂	$1.3 \times 10^{-11} e^{-20600/T}$	Zahnle et al. (2016) ¹
36	HS + HCO	→ H ₂ S + CO	5.0×10^{-11}	Kasting (1990)
37	HS + H	→ H ₂ + S	3.0×10^{-11}	Schofield (1973)

38	HS + H + M	→	H ₂ S + M	$1.4 \times 10^{-31} (T/298)^{-2.5} e^{500/T}$	Zahnle et al. (2016) ¹
39	HS + S	→	H + S ₂	4.0×10^{-11}	Schofield (1973)
40	HS + O	→	S + OH	$1.7 \times 10^{-11} (T/298)^{0.67} e^{-956/T}$	Schofield (1973) ¹
41	HS + O ₂	→	SO + OH	4.0×10^{-19}	Sander et al. (2006) ¹
42	HS + O ₃	→	HSO + O ₂	$9.0 \times 10^{-12} e^{-280/T}$	Sander et al. (2006)
43	HS + NO ₂	→	HSO + NO	$2.9 \times 10^{-11} e^{240/T}$	Sander et al. (2006)
44	HS + CO	→	OCS + H	$4.2 \times 10^{-14} e^{-7660/T}$	Kurbanov and Mamedov (1995)
45	HS + CH ₃	→	S + CH ₄	$4.0 \times 10^{-11} e^{-500/T}$	Shum and Benson (1985) ¹
46	HS + CH ₄	→	CH ₃ + H ₂ S	3.0×10^{-31}	Kerr and Trotman-Dickenson (1957) ¹
47	S + O ₂	→	SO + O	2.3×10^{-12}	Sander et al. (2006)
48	S + OH	→	SO + H	6.6×10^{-11}	DeMore et al. (1997)
49	S + HCO	→	HS + CO	6.0×10^{-11}	Moses et al. (1995)
50	S + HO ₂	→	HS + O ₂	1.5×10^{-11}	Kasting (1990)
51	S + HO ₂	→	SO + OH	1.5×10^{-11}	Kasting (1990)
52	S + CO ₂	→	SO + CO	1.0×10^{-20}	Yung and Demore (1982) ¹
53	S + H ₂	→	H ₂ S	$1.4 \times 10^{-31} (T/298)^{-1.9} e^{-8140/T}$	Zahnle et al. (2016) ¹
54	S + S	→	S ₂	$2.0 \times 10^{-33} e^{206/T} \times den$	Du et al. (2008) ²
55	S + S ₂	→	S ₃	$2.8 \times 10^{-32} \times den$	Kasting (1990) ²
56	S + S ₃	→	S ₄	$2.8 \times 10^{-31} \times den$	Kasting (1990) ²
57	S + O ₃	→	SO + O ₂	1.2×10^{-11}	Sander et al. (2006)
58	S + CO	→	OCS	$6.5 \times 10^{-33} e^{-2180/T} \times den$	Domagal-Goldman et al. (2011) ¹
59	S + HCO	→	OCS + H	6.0×10^{-11}	Moses et al. (1995) ¹
60	S + S ₃	→	S ₂ + S ₂	4.0×10^{-11}	Zahnle et al. (2016)
61	S ₂ + O	→	S + SO	1.1×10^{-11}	Hills et al. (1987)
62	S ₂ + S ₂	→	S ₄	$2.8 \times 10^{-31} \times den$	Baulch et al. (1976) ²
63	S ₃ + H	→	HS + S ₂	$5.0 \times 10^{-11} e^{-500/T}$	Zahnle et al. (2016) ¹
64	S ₃ + O	→	S ₂ + SO	$2.0 \times 10^{-11} e^{-500/T}$	Moses et al. (1995) ¹
65	S ₃ + CO	→	S ₂ + OCS	$1.0 \times 10^{-11} e^{-10000/T}$	Zahnle et al. (2016) ¹
66	S ₄ + S ₄	→	S ₈	$7.0 \times 10^{-30} (T/298)^{-2.0} \times den$	Zahnle et al. (2016) ²
67	S ₄ + H	→	S ₃ + HS	$5.0 \times 10^{-11} e^{-500/T}$	Zahnle et al. (2016) ¹
68	S ₄ + O	→	S ₃ + SO	$2.0 \times 10^{-11} e^{-500/T}$	Moses et al. (1995) ¹
69	¹ SO ₂ + O ₂	→	SO ₃ + O	1.0×10^{-16}	Turco et al. (1982)
70	¹ SO ₂ + SO ₂	→	SO ₃ + SO	4.0×10^{-12}	Turco et al. (1982)
71	³ SO ₂ + SO ₂	→	SO ₃ + SO	7.0×10^{-14}	Turco et al. (1982)
72	OCS + O	→	CO + SO	$7.8 \times 10^{-11} e^{-2620/T}$	Singleton and Cvetanovic (1988)
73	OCS + O	→	S + CO ₂	$8.3 \times 10^{-11} e^{-5530/T}$	Singleton and Cvetanovic (1988)
74	OCS + H	→	CO + HS	$9.1 \times 10^{-12} e^{-1940/T}$	Lee et al. (1977) ¹
75	OCS + OH	→	CO ₂ + HS	$1.1 \times 10^{-13} e^{-1200/T}$	Atkinson et al. (2004)
76	OCS + S	→	OCS ₂	$8.3 \times 10^{-33} \times den$	Basco and Pearson (1967)
77	OCS + S	→	CO + S ₂	$1.5 \times 10^{-10} e^{-1830/T}$	Schofield (1973) ¹
78	OCS ₂ + S	→	OCS + S ₂	2.0×10^{-11}	Zahnle et al. (2006)
79	OCS ₂ + CO	→	2 OCS	3.0×10^{-12}	Zahnle et al. (2006)

*Photolysis Reactions*³

80	SO + hv	→	S + O	1.32×10^{-4}	
81	H ₂ S + hv	→	HS + H	7.89×10^{-5}	
82	S ₂ + hv	→	S + S	3.18×10^{-4}	
83	S ₃ + hv	→	S ₂ + S	3.18×10^{-4}	
84	S ₄ + hv	→	S ₂ + S ₂	3.18×10^{-4}	
85	S ₈ + hv	→	S ₄ + S ₄	1.93×10^{-5}	
86	SO ₃ + hv	→	SO ₂ + O	1.20×10^{-5}	
87	SO ₂ + hv	→	SO + O	4.94×10^{-5}	
88	SO ₂ + hv	→	¹ SO ₂	5.17×10^{-4}	
89	SO ₂ + hv	→	³ SO ₂	3.11×10^{-7}	
90	HSO + hv	→	HS + O	1.76×10^{-4}	
91	OCS + hv	→	CO + S	6.89×10^{-6}	
92	¹ SO ₂ + hv	→	³ SO ₂	1.0×10^{-12}	Turco et al. (1982) ⁴
93	¹ SO ₂ + hv	→	SO ₂	1.0×10^{-11}	Turco et al. (1982) ⁴
94	¹ SO ₂ + hv	→	³ SO ₂ + hv	$1.5 \times 10^{+3}$	Turco et al. (1982) ⁴
95	¹ SO ₂ + hv	→	SO ₂ + hv	$2.2 \times 10^{+4}$	Turco et al. (1982) ⁴
96	³ SO ₂ + hv	→	SO ₂	1.5×10^{-13}	Turco et al. (1982) ⁴
97	³ SO ₂ + hv	→	SO ₂ + hv	$1.1 \times 10^{+3}$	Turco et al. (1982) ⁴

¹ Added reactions that were not included in the previous versions of this model, Catling et al. (2010) and Smith et al. (2014).

² These reactions have a minimum reaction rate of $5.0 \times 10^{-11} \text{ cm}^3 \text{ s}^{-1}$, which are generally consistent with those of Moses et al. (2002) and Yung et al. (2009).

³ Photolysis rates [s^{-1}] are evaluated at the top of the atmosphere subject for a 50° slant path, and reduced by a factor of 2 to account for the diurnal cycle. Absorption cross sections were obtained from JPL-11 (Sander et al. 2011).

⁴ These reaction rate constants [$\text{cm}^3 \text{ s}^{-1}$] are for the photolysis reactions modeled as two-body reactions.

Appendix A2: Surface Sink on CO

Previous versions of this one-dimensional photochemical code have used a depositional velocity of 0 cm s^{-1} on CO and 0.02 cm s^{-1} on carbonyl sulfide (OCS) (Catling et al., 2010; Smith et al., 2014; Zahnle et al., 2008). However, in our high-outgassing rate atmospheres, volcanically sourced CO readily builds up in anoxic atmospheres. This is due in part to the assumptions of a cold, dry atmosphere similar to modern day Mars, where few OH radicals react with CO to produce redox neutral CO₂. Consequently, CO accumulates.

With the previous v_{dep} for CO and OCS, most of the carbon in the model (that was not removed as redox-neutral CO₂) deposits to the surface as OCS. This v_{dep} on OCS presents a couple

of problems, as a) large amounts of OCS do not generally deposit on planetary surfaces and b) OCS begins to compete with S₈ for the available atmospheric sulfur in anoxic reducing conditions. While this did not matter in previous model versions, since OCS was a minor constituent, we reexamine the assumption here. On Earth, OCS sinks include vegetation (Brown and Bell, 1986) and soil microbes (Kesselmeier et al., 1999), which are irrelevant for an assumed abiotic Mars. A minor sink occurs from the reaction of OCS and OH at the surface; but this process is very slow on Earth (Khalil and Rasmussen, 1984), and would only be slower on Mars with even less OH available, especially in anoxic reducing conditions. Thus, it is more appropriate to use zero deposition velocity for OCS.

However, once the surface sink for OCS is removed, CO can build up at a rate that may not be reasonable given possible CO sinks. OCS is mostly formed through the net reactions:



When the sink for OCS is removed, atmospheric OCS photolyzes back into its products, CO and S, which leads to a greater amount of atmosphere CO.

There are possible surface sinks for CO. Gas-phase reactions involving CO are kinetically inhibited at low temperatures ($T < 1000\text{K}$) due to the high activation energy barrier required to break the CO bond. Therefore, conversion of CO to other forms of carbon (e.g. CO₂ and CH₄) requires a catalyst and/or high temperatures in the absence of abundant OH. Hypervelocity impact events from large space debris (e.g. chondrites, iron-meteorites, and comets) create temporary conditions of high temperature and pressure in a vapor plume. In this plume, CO can adsorb onto iron and nickel particles from the impactor and participate in Fischer-Tropsch catalysis reactions that convert CO into CO₂ or CH₄:



Iron and nickel show a selectivity in their catalytic properties towards producing CH₄ over CO₂ (Eqn. A.3) (Kress and McKay, 2004). Such reactions are a sink on CO for early and modern Mars.

Kress and McKay (2004) describe the process of converting CO to CH₄ via the aforementioned process with comets. They show that comets of diameter (L) > 1 km produce ~10¹³ g of CH₄ per impact, and furthermore impactors with L > 10 km produce ~10¹⁵ g of CH₄. Thus, the total production of CH₄ from an impactor approximately depends on the square of the impactor radius. We use this dependency to approximate the distribution of fluxes from variously sized impactors and convert into photochemical model units of molecules of CH₄ produced per impact event. Also given that the conversion of CO to CH₄ is 1:1 (See Eqn. B3), the same number of moles of CO will be removed via reaction A.3 as moles of CH₄ are produced.

The number of impactors of diameter L impacting Mars can be estimated from the cratering record and scaling from crater diameter (D) to impactor diameter (L). From integrating the Hartmann and Neukum (2001) cratering rate over the past 4.1 Ga the average rate is ~6.79×10⁻¹¹ impact events per second, or equivalently ~2.5 impacts every thousand years. This rate provides a first-order average approximation to the CO sink, although the sink is obviously higher in the Noachian than the late Amazonian, as discussed below.

The amount of CH₄ released is a function of impactor size. A relationship from Yen et al. (2006), derived from Melosh (1989), scales from crater diameter to impactor diameter, as follows:

$$D_{crater} = 1.8 \rho_{proj}^{0.11} \rho_{target}^{-1/3} g^{-0.22} L_{impactor}^{0.13} W^{0.22} \quad \mathbf{A.6}$$

Here, D_{crater} is the diameter of the crater, ρ_{proj} and ρ_{target} are the densities of the projectile and the target respectively, g is the gravitational acceleration of the target, $L_{impactor}$ is the diameter of the impactor, and W is the impact kinetic energy (a function of the impact velocity, V). To first order $\rho_{proj} \sim \rho_{target}$ and the equation simplifies to the following:

$$L_{impactor} = 0.58 D_{crater}^{1.27} g^{0.28} V^{-0.56} \quad \mathbf{A.7}$$

Typical comet and asteroid impacts have mean speeds of around $V = 10 \text{ km s}^{-1}$ (Bottke et al., 1994; Carr, 2006; Zahnle, 1998; Zahnle, 1990).

Robbins and Hynek (2012) provide a global database of craters on Mars greater than 1 km diameter as shown in Fig. A.1 which is used to determine impactor size distribution. This provides a first order estimate as degradation of larger craters could be a factor.

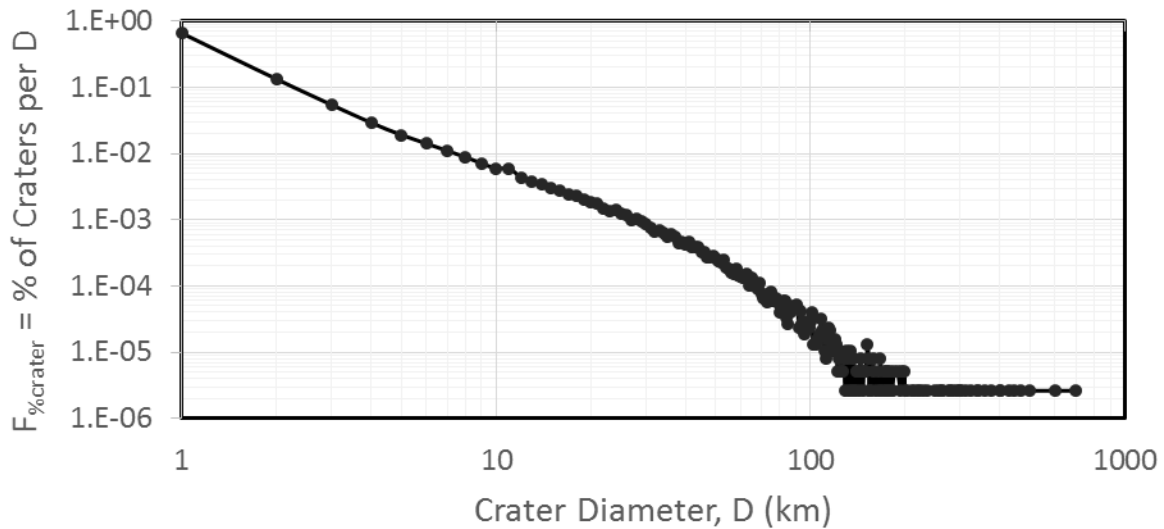


Figure A.1. Distribution of craters, as a percentage of total craters, as a function of crater diameter for craters with diameters > 1 km. Each point represents a 1 km crater size bin which can be converted into impactor size using Eqn. A.7. Craters with $D > \sim 200$ km have a frequency of only 1.

Finally, we must consider the efficiency of the impact chemistry. Kress and McKay (2004) present CH_4 production values for cometary bodies, which are a small fraction of the total impactor population. The majority of the impactors are stony ordinary chondrites. The smaller amount of iron and nickel present in ordinary chondrites makes them less efficient at catalytically converting CO to CH_4 . We take the percentage of iron and nickel in the meteorite to be a good estimate of the efficiency based on the work of Sekine et al. (2003); ordinary chondrites have 3-20% iron/nickel present and are 5-20% as efficient as purely iron and nickel meteorites in removing CO . Table A.2 provides a list of meteorite types (stony, stony/iron, and iron) and their percentage of impacts on the Earth (Hutchison, 2004). We also provide an efficiency of each meteorite type based on the iron/nickel content and an effective efficiency for each type. Stony/iron meteorites, e.g. pallasites, contain iron contents ranging from 20-90% but we take 50% to represent a typical stony/iron meteorite. The total effective efficiencies of all three meteorite groups is 25%.

Table A.2. Types of meteorites and the percentage of impacts on Earth. Efficiency correlates strongly with percentage of iron/nickel in the meteorite. Effective efficiency is the percentage of impacts (% of falls) multiplied by the efficiency of that body.

Meteorite Type	% of Falls	Efficiency	Effective Efficiency, ϵ_i
Stony (chondrites)	93.8 %	20 % (max.)	18.8 %
Stony/Iron	1.2 %	50 % (typical)	0.6 %
Iron	5.0 %	100 %	5.0 %
Total Effective Efficiency, ϵ			24.4 %

The total flux of CH₄, F_{CH_4} (molecules cm⁻² s⁻¹) into the atmosphere is then calculated using:

$$F_{CH_4} = \int_{0km}^{136km} \frac{f_{flux}(L) \times f_{\%craters}(L) \times \epsilon \times F_{impacts}}{A_{Mars}} dL \quad \mathbf{A.8}$$

Here, f_{flux} is the calculated CH₄ flux (in molecules/impact event) and is a function of impactor diameter as given in Kress and McKay (2004), $f_{\%craters}$ is the percentage of craters per impactor size as given in Fig. A.1, ϵ is the efficiency of the impactor as found in Table A.2, $F_{impacts}$ is the average flux of impactors over 4.1 Ga (6.79×10^{-11} impactors per second), and A_{Mars} is the surface area of Mars (in cm²). This is shown graphically in Fig. A.2.

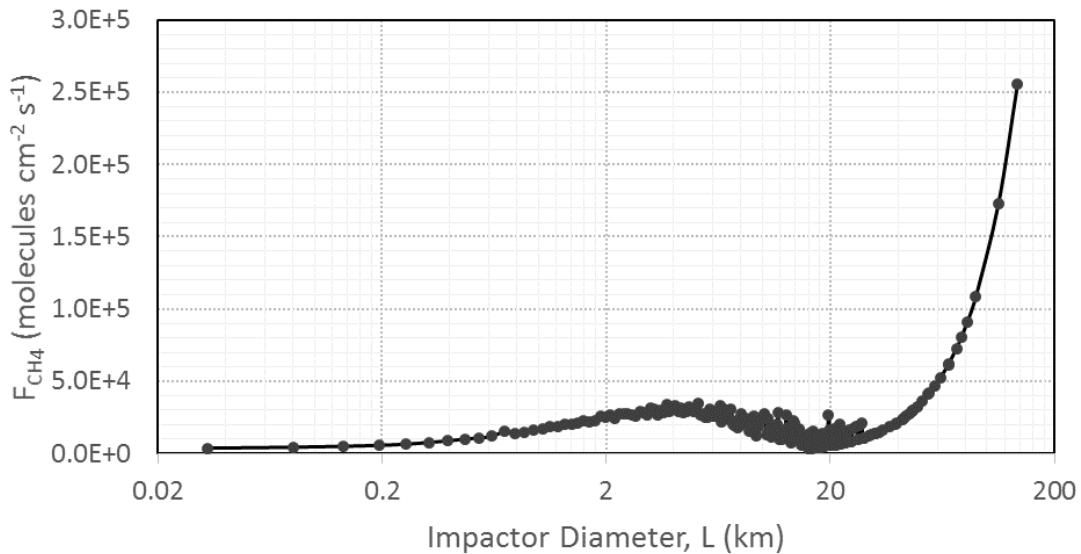


Figure A.2. Flux of methane, F_{CH_4} , as a function of impactor diameter, L . For small impactors, $L < 18$ km, despite not producing much methane in each impact there are significantly more impacts occurring. Larger impacts are more infrequent but produce more methane.

Integrating over the range of impactor sizes in Fig. A.1 provides a total flux of CH₄ that is used as a lower boundary condition. The maximum crater size from the Robbins and Hynek (2012) database has a ~470 km diameter (Schiaparelli Crater), which corresponds to an impactor size of ~85 km. However, their database does not include the larger buried craters in the northern plains. Thus we use the crater distribution from Frey et al. (2002) to include craters up to 700 km in diameter, corresponding to an impactor size of ~136 km. The authors find a quasi-circular depression (QCD), interpreted to be a large buried crater, of diameter 1075 km but we do not include this along with the other largest craters greater than Schiaparelli (Isidis, Argyre, and Hellas). These craters formed around the pre-Noachian/Noachian boundary (Werner, 2008) and represent very large impacts that appear to have only happened before ~3.9-4.1 Ga (Robbins et al., 2013). Given that surfaces are rarely older than this on Mars and that we wish to estimate the time-integrated average from Noachian surfaces and onwards, we ignore these anomalously large craters. To obtain the equivalent depositional velocity on CO, we use the number density of CO at the surface (for present day Mars) to calculate the downward flux of CO, $\Phi = v_{\text{dep}} n$. Here, v_{dep} is the deposition velocity, and n is the number density.

Meteoritic impact events can account for a time-average flux of CH₄ at the surface of $\sim 1 \times 10^7$ molecules cm⁻² s⁻¹ and a corresponding deposition velocity on CO of $\sim 7.5 \times 10^{-8}$ cm s⁻¹. This is of the same order as the deposition velocity derived by Kharecha et al. (2005) for an abiotic ocean planet via the conversion of dissolved CO to formate and eventually acetate.

The change in cratering rate for each martian geologic period would cause the average CO sink to vary over time (Table A.3). Today, the rate is virtually negligible at only $\sim 3 \times 10^{-9}$ cm s⁻¹, while during the early Noachian the rate was nearly 20 times faster than the average.

The availability of atmospheric H₂ or water-dissociated H₂ also plays a large factor in the efficiency of impact conversion of CO. We assume here that the impacts will happen either with sufficiently water-enriched bodies or impact on surface or subsurface reservoirs of water.

Table A.3. Comparison of CO deposition velocity, which depend on the cratering rate, over the geologic periods of Mars.

Era	Time	Cratering Rate (impacts s ⁻¹)	$v_{\text{dep,CO}}$ (cm s ⁻¹)
<i>Early Noachian</i>	4.1 Ga	1.47×10^{-9}	1.39×10^{-6}
<i>Early Hesperian</i>	3.7 Ga	1.54×10^{-10}	1.46×10^{-7}
<i>Early Amazonian</i>	3.0 Ga	2.45×10^{-12}	2.32×10^{-9}
<i>Mid Amazonian</i>	1.0 Ga	2.33×10^{-12}	2.21×10^{-9}
<i>Present</i>	1 Ma	3.52×10^{-12}	3.33×10^{-9}
Average	--	6.79×10^{-11}	7.51×10^{-8}

We performed multiple sensitivity tests to determine how much the deposition velocity on CO affects the overall chemistry and evolution of the modeled atmospheres. We find that deposition velocities of $0\text{-}10^{-7}$ cm s⁻¹ still produce modern martian conditions with no volcanic sources. They also show little change in the overall atmospheric evolution with increasing volcanic magma flux. Mixing ratios and depositional fluxes of all major constituents remain fairly uniform in magnitude. The only major difference is in the transitional atmospheres between oxidizing and reducing atmospheres where the steepness of the rise of CO with increasing volcanic flux becomes less sharp around $v_{\text{dep,CO}}=10^{-7}$ cm s⁻¹. This, however does not change how much volcanism is required to produce the redox switch between the oxidizing and reducing atmospheres (see Eqn. 2.5 in the main text). When the depositional velocity of CO becomes very large, on the order of 10^{-6} cm s⁻¹, the redox switch shifts towards requiring greater amounts of volcanism and the model is unable to adequately simulate present-day Mars. If the deposition velocity is too small, we encounter the CO-runaway numerical problem described at the beginning of this appendix.

Finally, other processes may have also contributed to a surface sink on CO. CO could very slowly adsorb onto surface iron and nickel (Kishi and Roberts, 1975; Rabo et al., 1978), dissolved CO could react directly with dissolved O₂ in surface waters (Harman et al., 2015), and CO may photodissociate into atomic C and O at a small rate and deposit on the surface or escape to space (Hu et al., 2015; Lu et al., 2014). Detailed consideration of all such processes is beyond the scope of this paper, but effectively, they could allow for the value of $v_{\text{dep,CO}}$ we have adopted.

Appendix A3: Volcanic Outgassing Rates and Ratios

For convenience, here we present a table showing the nominal volcanic outgassing rates calculated using Eqn. 2.4 and sourced from Gaillard et al. 2013 (Table A.4). These rates are given for a very small amount of volcanism, $1 \times 10^{-4} \text{ km}^3 \text{ s}^{-1}$, which represents the lowest values in Fig. 2.3. We only include fluxes for the maximum and minimum values of water content and outgassing pressure. As was described in Appendix A2, we also include a static flux of $1 \times 10^7 \text{ molecules cm}^{-2} \text{ s}^{-1}$ for CH_4 but this is negligible.

Table A.4. Nominal volcanic outgassing rates and speciation under varying magmatic conditions (water content, oxygen fugacity, and outgassing pressure) for a small amount of volcanism, $1 \times 10^{-4} \text{ km}^3 \text{ s}^{-1}$.

Magma Conditions	Volcanic Species Flux [$\text{molecules cm}^{-2} \text{ s}^{-1}$]				
	SO_2	S_2	H_2S	CO	H_2
IW					
<u>0.01 wt% H_2O</u>					
0.01 bar	1.2×10^5	1.0×10^6	4.7×10^4	2.5×10^6	6.0×10^5
1 bar	--	1.2×10^4	1.2×10^4	2.4×10^6	--
<u>0.4 wt% H_2O</u>					
0.01 bar	6.4×10^6	9.9×10^6	1.5×10^6	2.0×10^6	2.3×10^7
1 bar	1.5×10^6	2.1×10^6	3.9×10^6	1.3×10^6	1.2×10^7
FMQ-1.4					
<u>0.01 wt% H_2O</u>					
0.01 bar	2.5×10^6	6.7×10^6	4.7×10^4	5.2×10^6	4.0×10^5
1 bar	1.0×10^6	1.1×10^6	2.3×10^4	2.6×10^6	--
<u>0.4 wt% H_2O</u>					
0.01 bar	1.2×10^7	9.7×10^6	1.2×10^6	4.6×10^6	1.9×10^7
1 bar	4.9×10^6	3.7×10^6	3.5×10^6	2.6×10^6	8.4×10^6
FMQ-0.5					
<u>0.1 wt% H_2O</u>					
0.01 bar	8.2×10^6	9.5×10^6	4.2×10^5	4.9×10^6	4.6×10^6
1 bar	4.9×10^6	3.1×10^6	7.4×10^5	2.3×10^6	1.2×10^6
<u>0.4 wt% H_2O</u>					
0.01 bar	1.7×10^7	8.8×10^6	1.0×10^6	4.5×10^6	1.7×10^7
1 bar	8.5×10^6	4.4×10^6	3.1×10^6	2.4×10^6	7.2×10^6

APPENDIX B: SUPPLEMENTAL MATERIAL TO CHAPTER 4

Here we present alternate versions of the figures found in the main text with their topographic information and the results of the spectral and radiative data analysis (which were inconclusive). Details on the topographic processing are described at length in Sec. 4.2.2 of the main text.

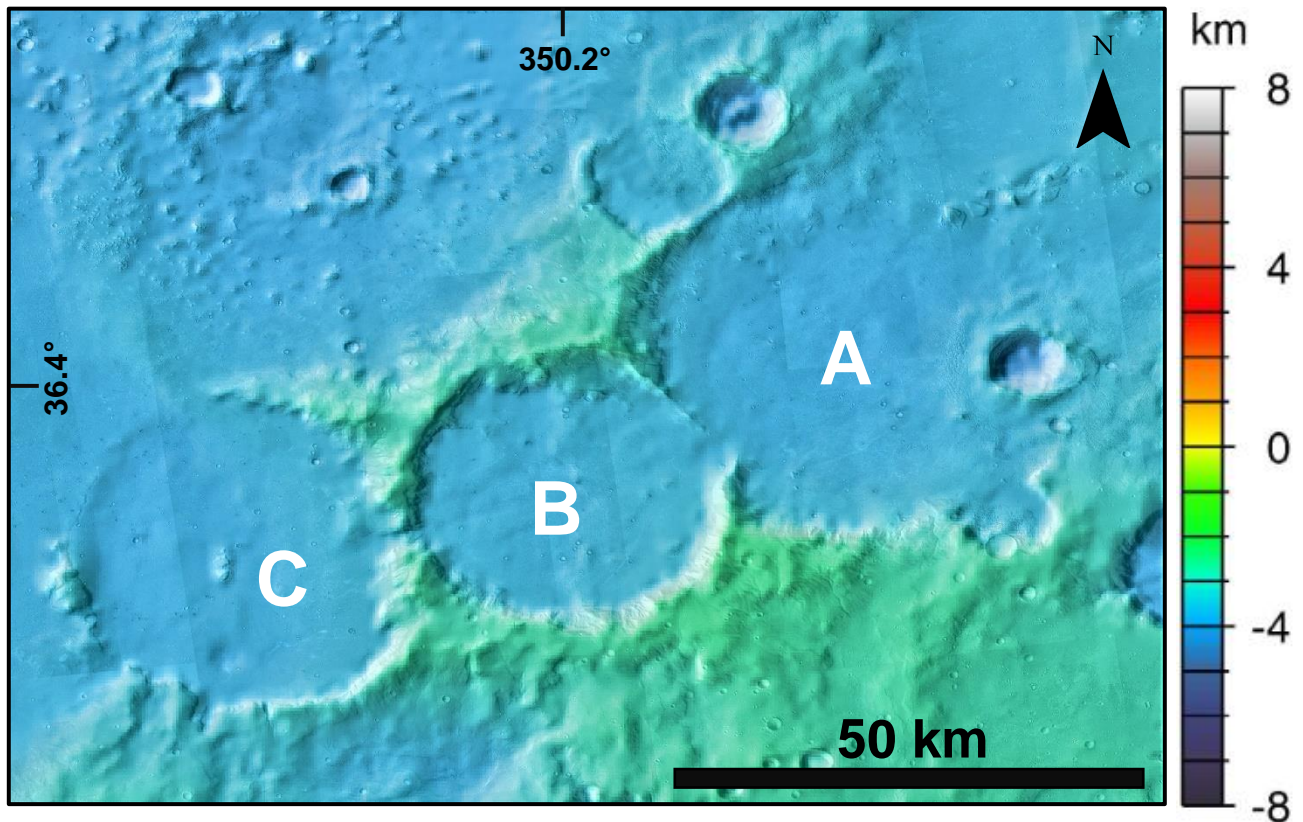


Figure B.1. CTX mosaic of the context region shown in Figure 4.1 with overlaid MOLA colorized elevations. Craters A-C are labeled.

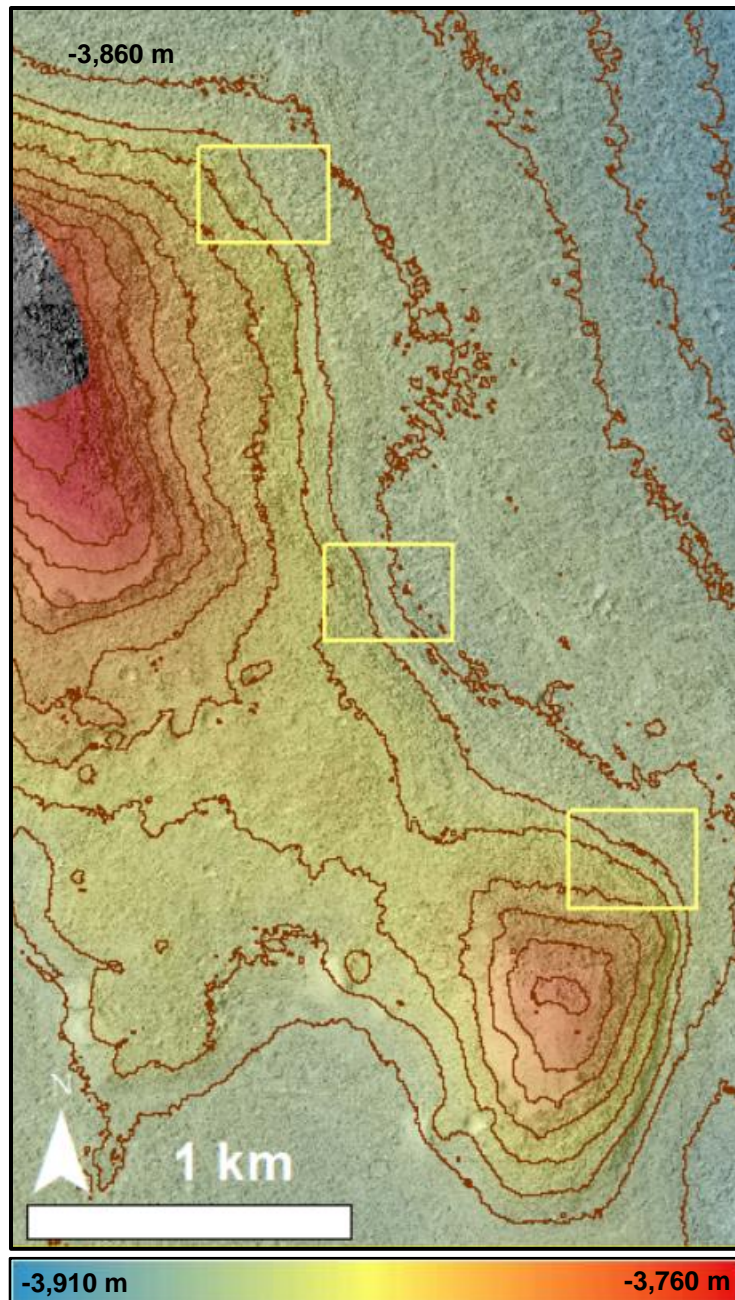


Figure B.2. Our colorized high-resolution DEM for the western site of Crater A (covering the area shown in Figure 4.3a) draped over the ASP-derived DRG (digital raster graphic). Contours (brown lines) are every 10 m. Yellow rectangles show the locations of zoomed in areas displayed in Figures 4.3b-d. Non-colored portion in the NW corner is a section that the ASP was unable to correlate and too large to patch through FocalStatistics; thus, it was cropped out (see main text for details).

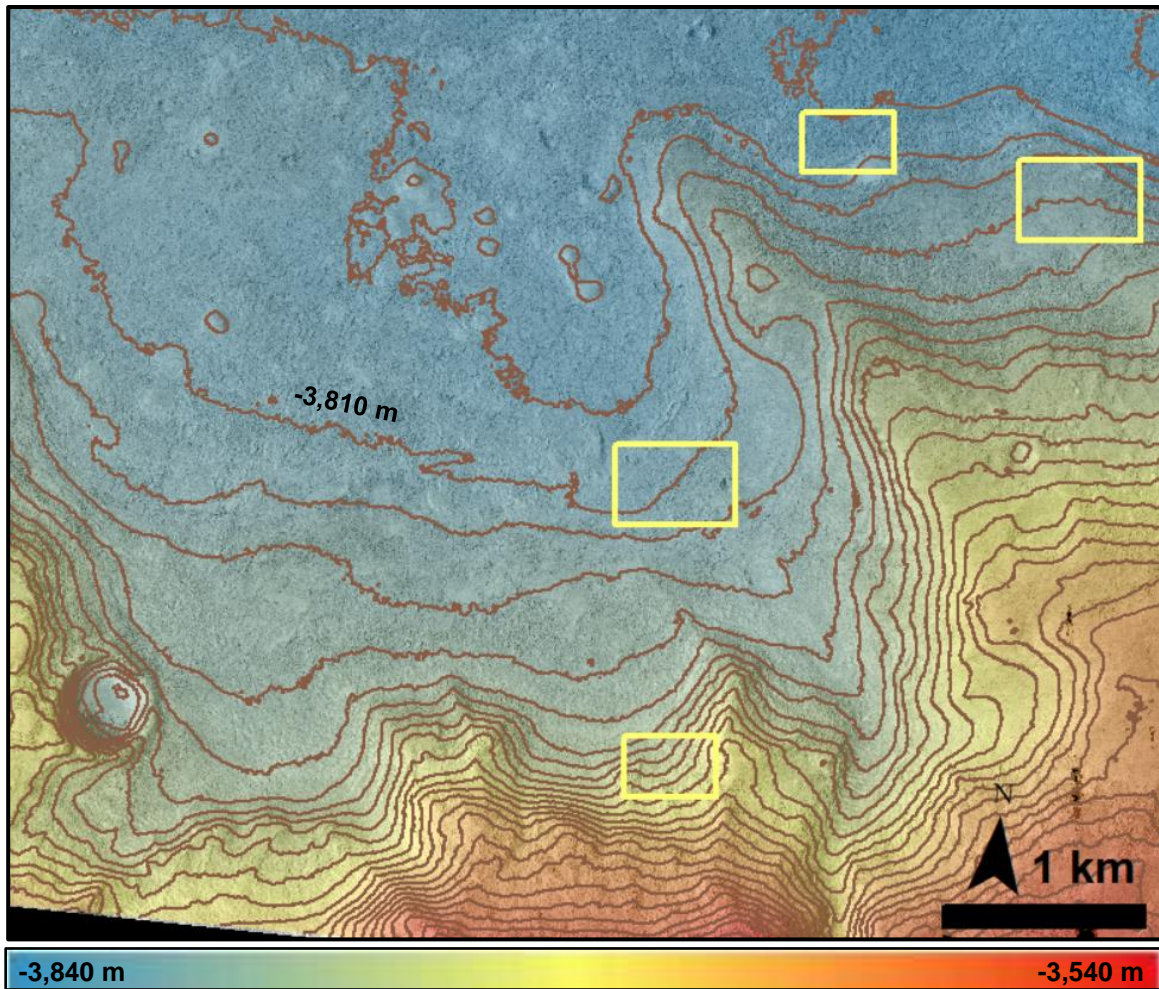


Figure B.3. Our colorized high-resolution DEM for the southern site of Crater A (covering the area shown in Figure 4.3a) draped over the ASP-derived DRG. Contours (brown lines) are every 10 m. Yellow rectangles show the locations of zoomed in areas displayed in Figures 4.4b-

e.

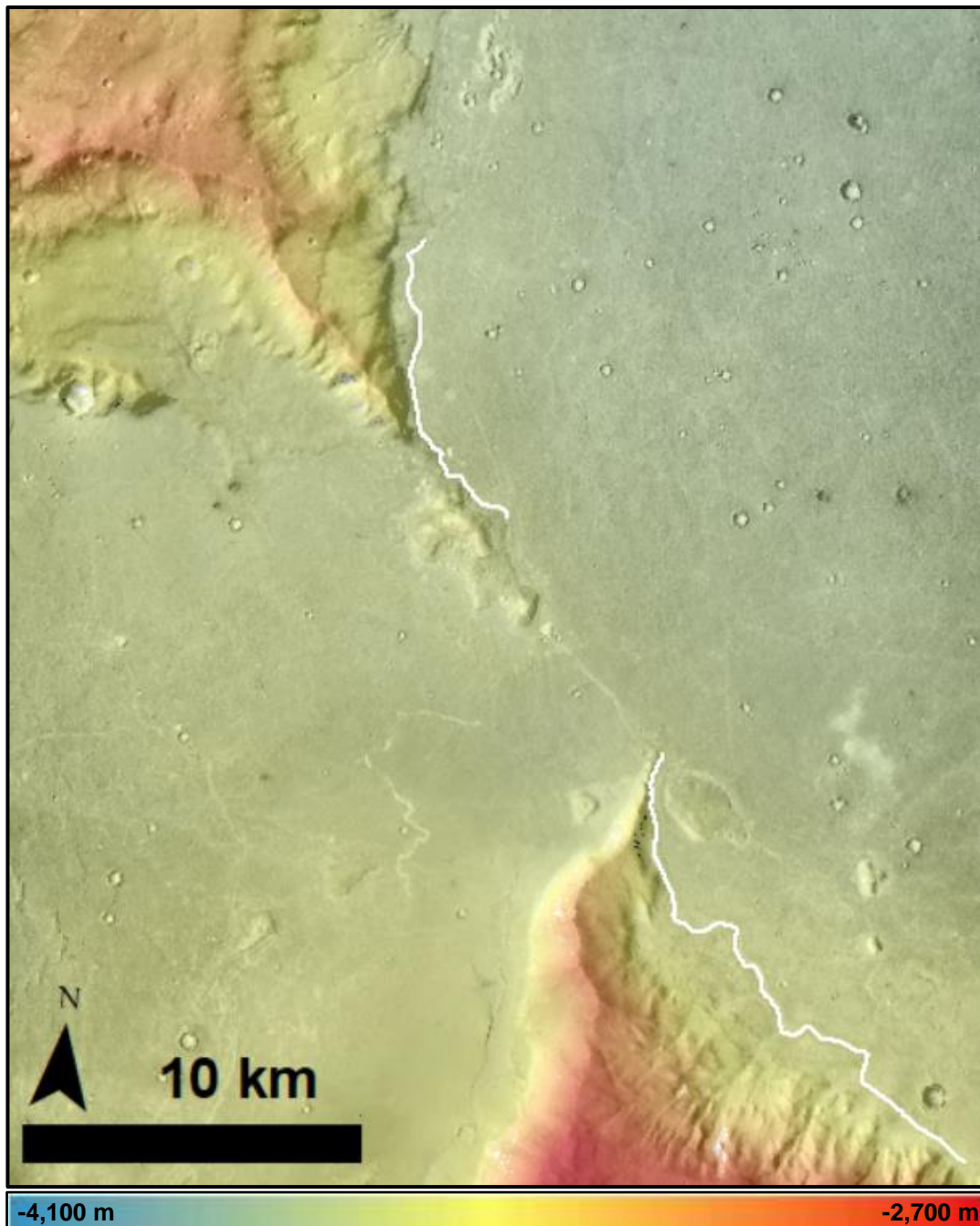


Figure B.4. Regional stereo-derived CTX DEM colored over CTX image G18_025360_2168. White lines show the most prominent mapped lineaments along the crater wall. The northern lineament continues from the northernmost-mapped lineament in Figure 4.3a. The southern lineament is directly west of the southern site and logically extends from the lineaments found there (the southern site is not within the CTX DEM footprint). Both lineaments dip northward $\sim 10 \text{ m km}^{-1}$.

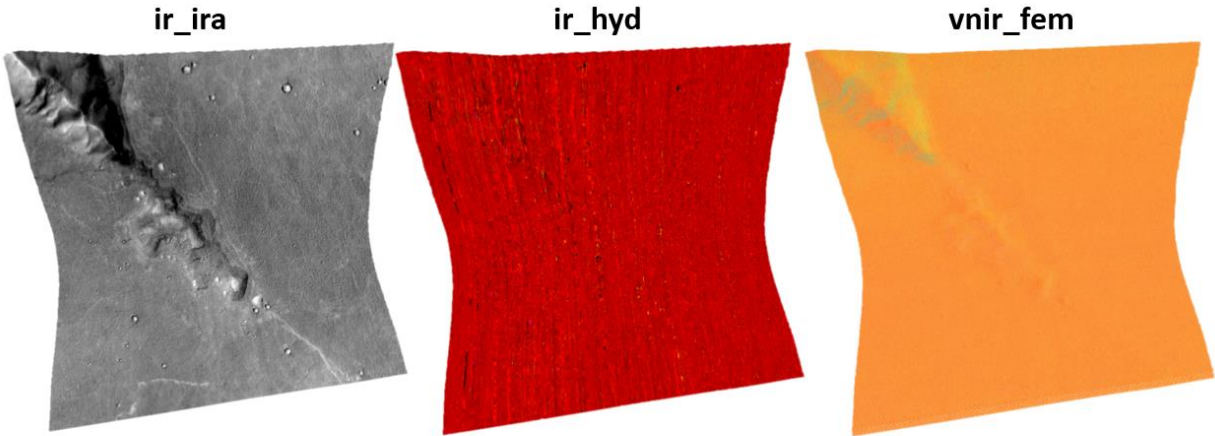


Figure B.5. Standard CRISM data products for the western site (from NASA/Johns Hopkins University Applied Physics Laboratory; FRT_0002204A_07_IF167S_TRR3). *ir_ira*: shows surface brightness in the infrared. *ir_hyd*: shows information related to bound water in minerals. *vnir_fem*: shows information related to oxidized iron minerals. Information regarding the data product and spectral index definitions, descriptions, and color band assignments can be found in Viviano-Beck et al. (2014).

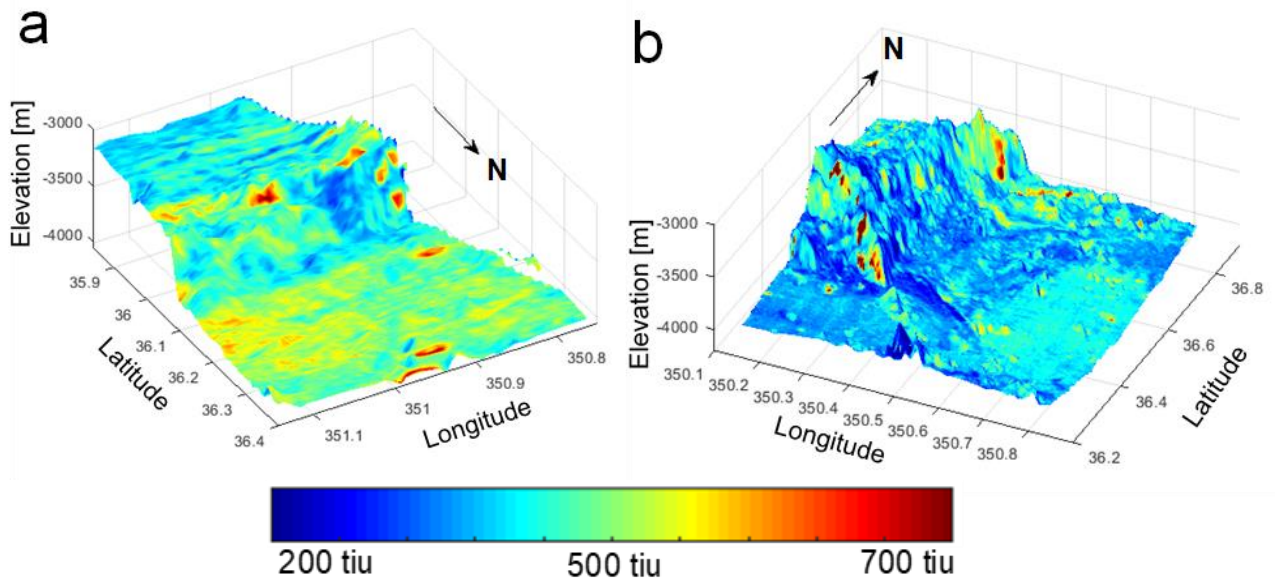


Figure B.6. Thermal inertia maps for the southern site (a) and the western site (b). 30x vertical exaggeration. See Sec. 4.2.3 of the main text for details on processing the radiative data and Sec. 4.3.3 for interpretation of these results.

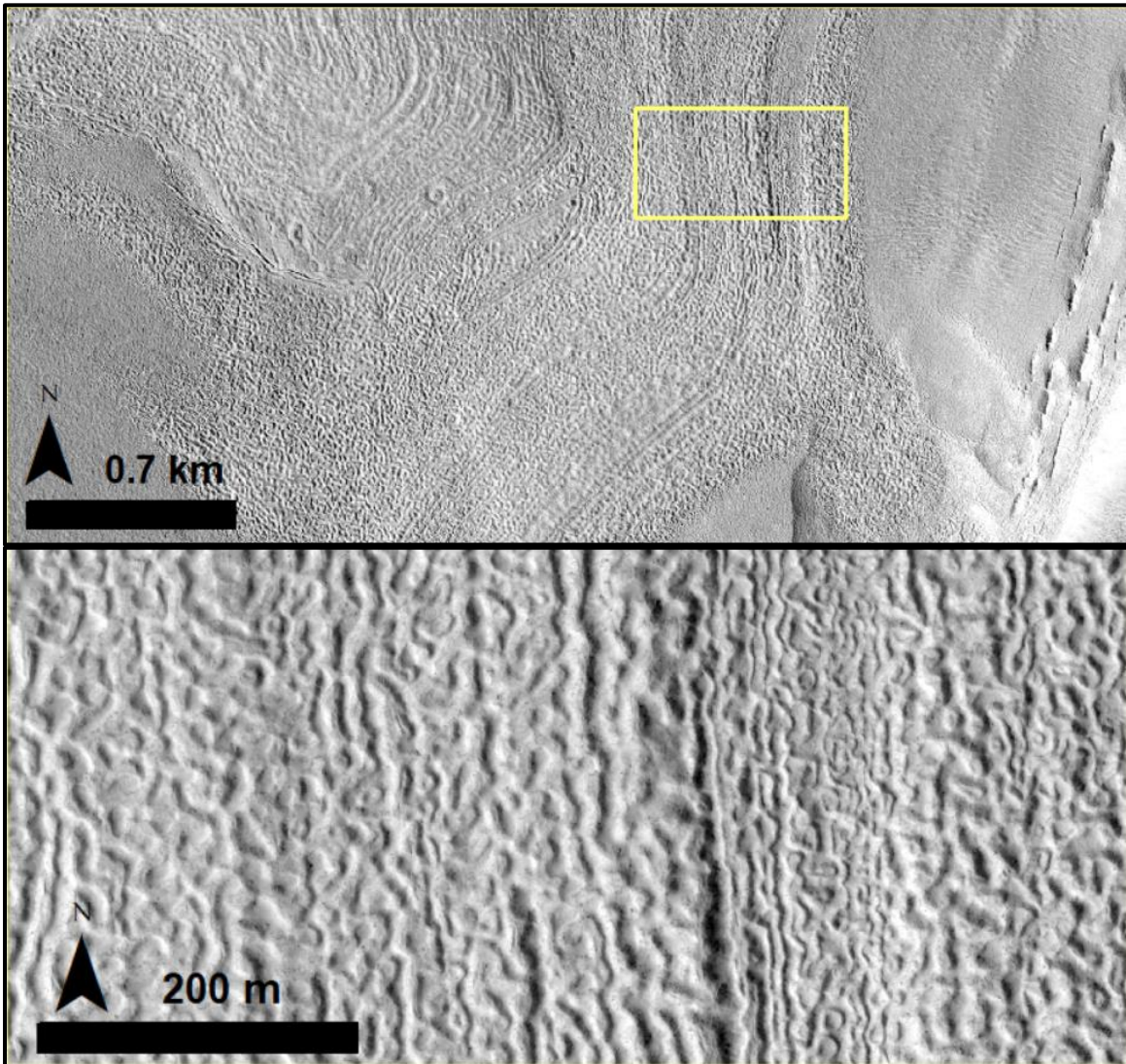


Figure B.7. Examples of the “brain terrain” from Levy et al. (2009, 2010) as discussed in Sec. 4.4.2). a) Examples of the concentric crater fill (CCF) in HiRISE image PSP_002175_2210. At these broader scales they appear as arcuate continuous lineaments. b) Zoom-in of the lineaments covered in the yellow box of a. At these fine scales the lineament morphologies show as discontinuous sinuous ridges with bifurcations and “cells.”

APPENDIX C: SUPPLEMENTAL MATERIAL TO CHAPTER 5

Here we provide additional figures and summaries of our findings for all of the putative paleoshoreline sites investigated in Chapter 5. Unless otherwise noted, figure insets are of MOLA colored elevation with black boxes/stars indicating figure location.

C.1 CONTEXT FIGURES

Many of the sites are located close to one another within northern Arabia Terra, so we present here Figures C.1 (Mamers Valles), C.2 (western Isidis Planitia), and C.3 (western Deuteronilus Mensae).

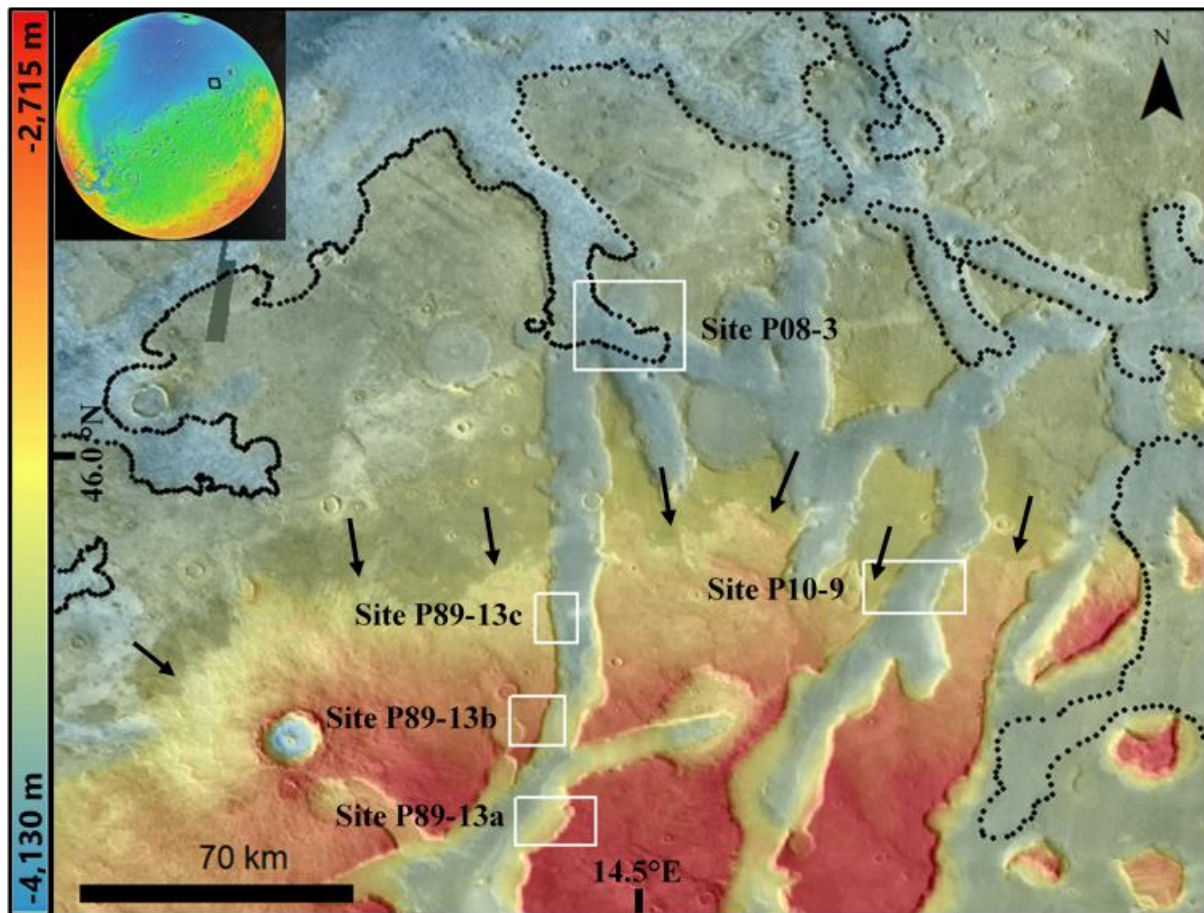


Figure C.1. Context for sites located around Mamers Valles with THEMIS-IR day mosaic with MOLA MEDGR topographic data. Black dots indicate the mapped Deuteronilus Level by Ivanov et al. (2017). Black arrows locate the tonal boundary used to define the Arabia Level locally by Parker et al. (1989)

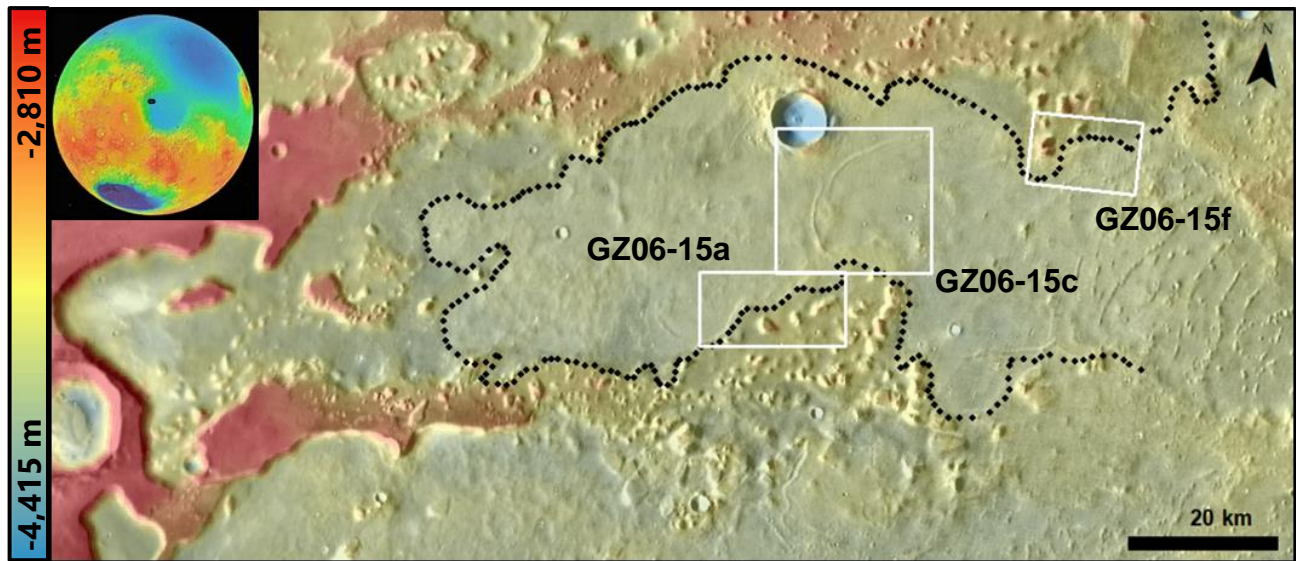


Figure C.2. Context figure for sites located in western Isidis Planitia. Dotted line indicates mapped Deuteronilus Level by Ivanov et al. (2017). THEMIS-IR day mosaic with MOLA MEDGR topography overlain.

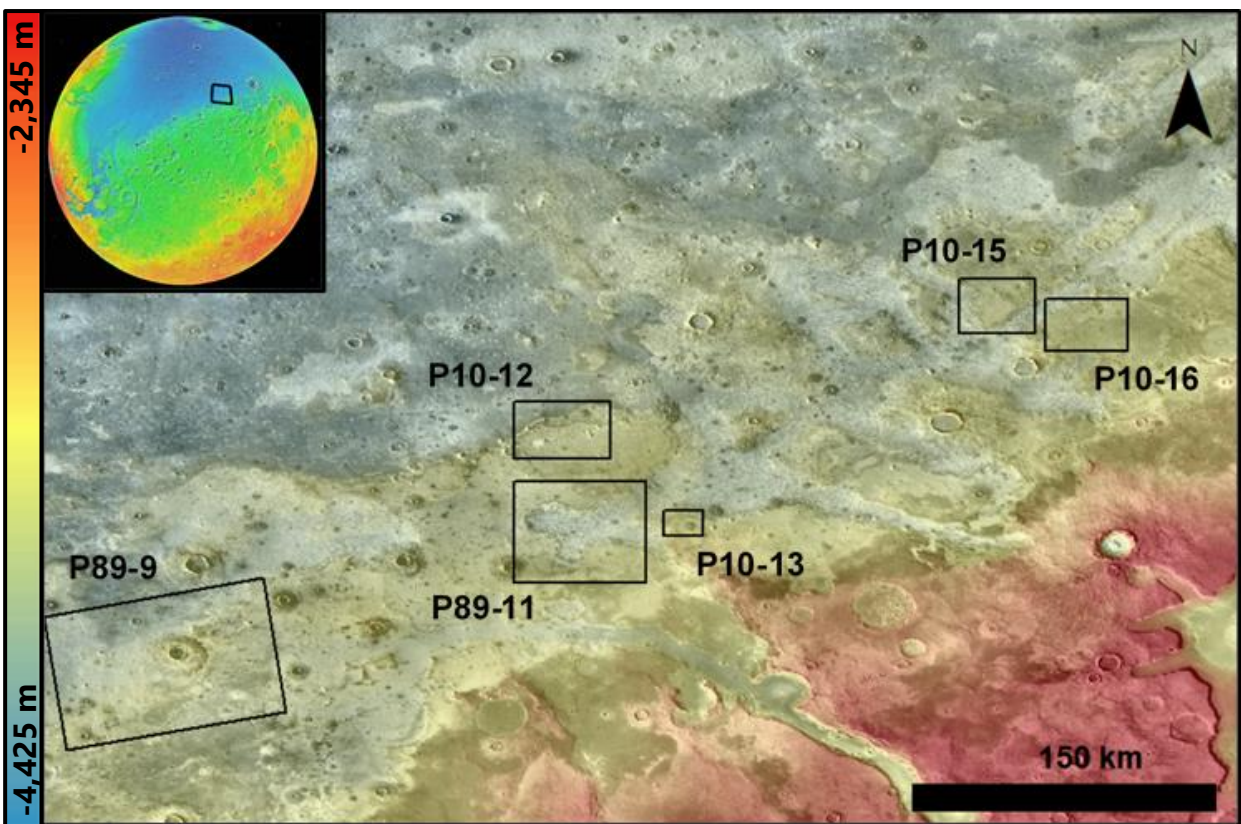


Figure C.3. Context figure for sites located in western Deuteronilus Mensae with THEMIS-IR day mosaic with MOLA MEDGR topography.

C.2 SITE DETAILS

C.2.1 *Site P89-13a*

Figure C.4a shows the approximate location of Figure 13a from Parker et al. (1989). The sectioned profile with labels A-E correspond to the different sections of the fret canyon wall. These are the highlands (A), canyon wall (B), “intermediate slope” (C), “debris apron” (D), and canyon floor material (E). The debris pile appears to be remnant material from Amazonian glaciation (e.g. A. Kress et al., 2006). The putative paleoshoreline features are the “ridge and swale” landforms along the intermediate slope unit. Figure C.4b provides a HiRISE zoom of these features which show that they are discontinuous, bifurcate (example shown with black arrow), and are escarpments that face towards the canyon wall. This suggests that the features are parts of the canyon wall that have undergone mass wasting, forming the intermediate slope against the glaciation remnants. These do not appear to be consistent with a migrating beach environment. Figure C.3c provides a zoom in of the curvilinear features on the debris pile itself showing that they are also inconsistent with a coastal origin.

C.2.2 *Site P89-13b*

Figure C.5 shows the approximate location of Figure 13c in Parker et al. (1989). Just as for Site P89-13a (Sec. C.2.1), the ridges along the intermediate slope are discontinuous and are at irregular orientations with the slope (e.g. the white arrow in Fig. C.5, which appears to dip unlike the other lineaments further south along the canyon wall). In some places (black arrows) the ridges shift direction and are angled towards the canyon floor. These features also appear to be from mass wasting of the canyon wall onto the lobate debris aprons associated with Amazonian glaciation.

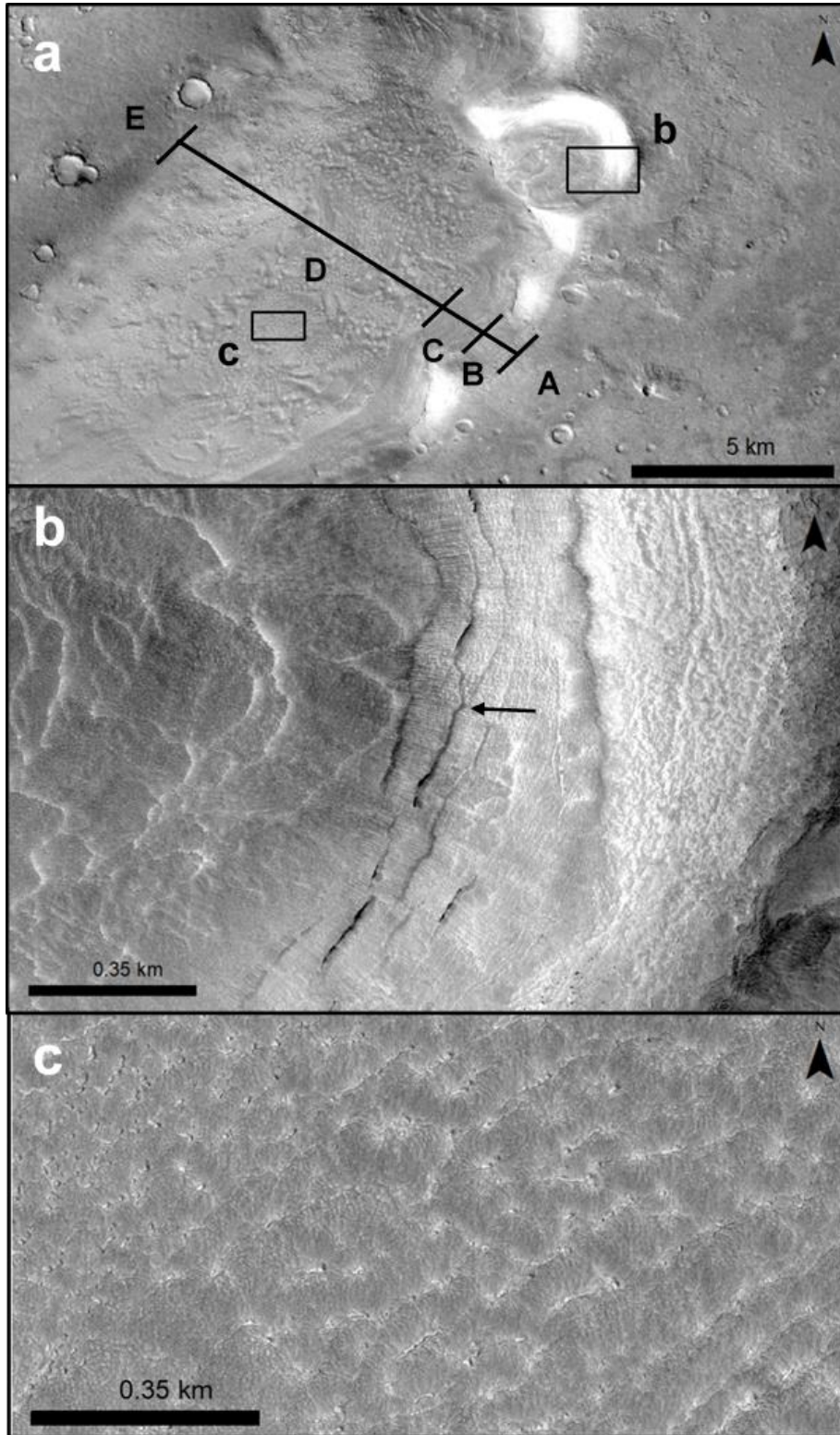


Figure C.4. Location of site P89-13a (see Figure C.1 for context). a) Location of image showing the different units (see Sec. C.2.1). CTX image P13_006200_2228_XN_42N345W. b) Zoom in of the “ridge-and-swale” pattern along the intermediate slope unit (C in a). HiRISE image ESP_044506_2245. c) Zoom in of the curvilinear lineaments found on the debris apron unit. HiRISE image PSP_006556_2245.

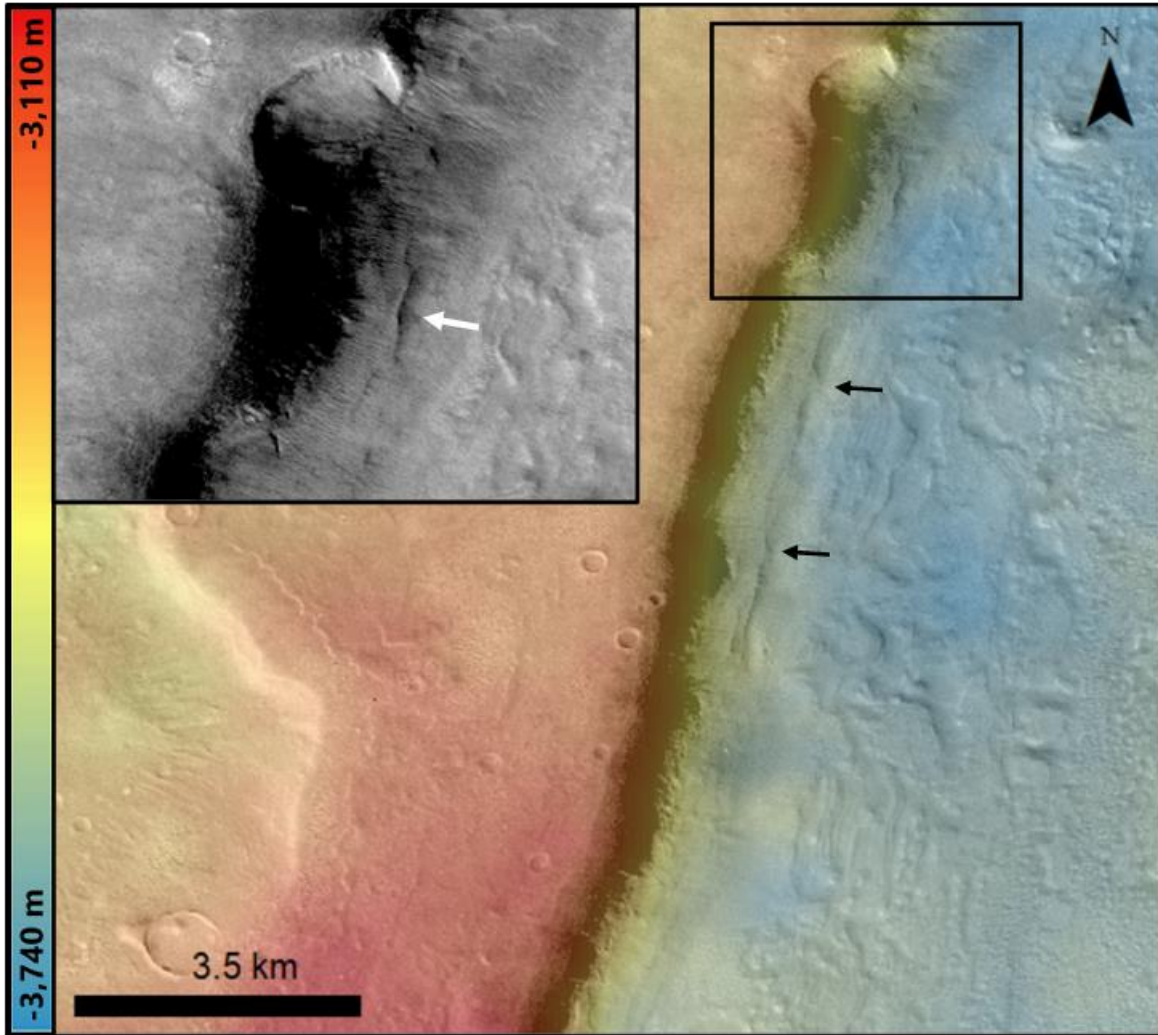


Figure C.5. Location of Site P89-13b (See Figure C.1 for context). CTX image P13_006200_2228_XN_42N345W with HRSC elevation data (H1289_0000_dt4). *Inset:* Zoom in of the black box. See Sec. C.2.2 for details.

C.2.3 Site P89-13c

Figure C.6 shows the approximate location of Figure 13c in Parker et al. (1989). Here, the authors examined a possible bench feature between the intermediate slope and the western wall of the canyon. In our CTX image stereo-derived DEM, we find no apparent bench nor other features that resemble coastal ridges or terraces. Here, TEA is unable to provide adequate information because 1) the resolution of the DEM is too coarse for such a narrow putative terrace; and 2) due to the Sun-synchronous orbit for the *Mars Reconnaissance Orbiter* (with CTX), the western

canyon wall is always obscured by shadow which can negatively affect the accuracy of the DEM process along this narrow strip where parts of the putative bench lie. As with the sister sites along Mamers Valles (P89-13a and P89-13b), any lineaments appear to be just mass-wasting of the canyon wall.

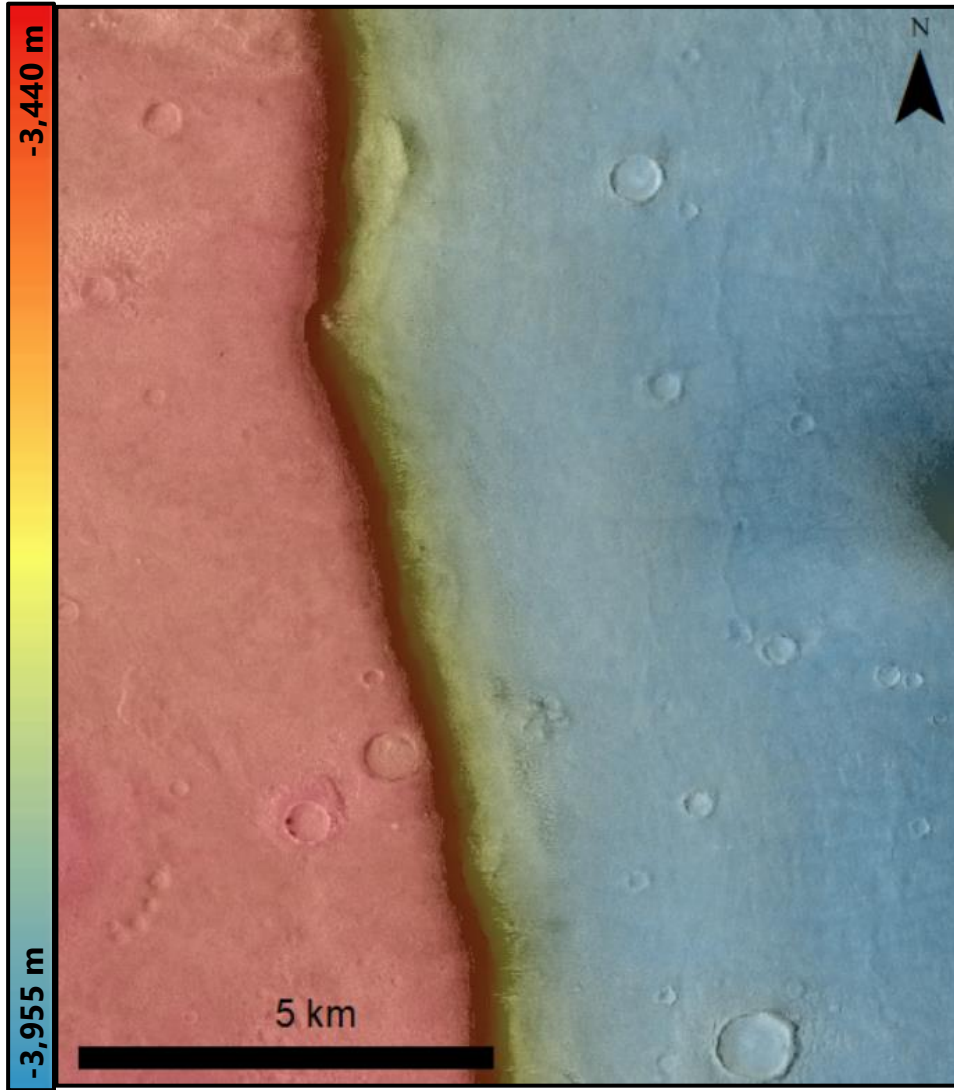


Figure C.6. Location of Site P89-13c (See Fig. C.1 for context image). Putative coastal bench lies between the intermediate bench (extent approximated by the yellow color) and the canyon wall (covered in shadow). CTX image B18_016643_2264_XI_46N345W with our stereo-derived CTX DEM overlaid.

C.2.4 Site GZ06-17a

Figure C.7 shows the location of Figure 17a from Ghatan and Zimbelman (2006). Site appears as stacked lineaments on the plainsward side of a pair of degraded craters. However, with HiRISE imagery, these lineaments are observed to be discontinuous, bifurcate and merge along track, and are highly degraded. Figure 5.3a in the main text shows a high-resolution zoom in of the site, these images provide context. These features more closely resemble the lineaments observed by Sholes et al. (2019b), which were interpreted as mass-wasting features, possibly mediated by ice, from different lithological units rather than coastal landforms.

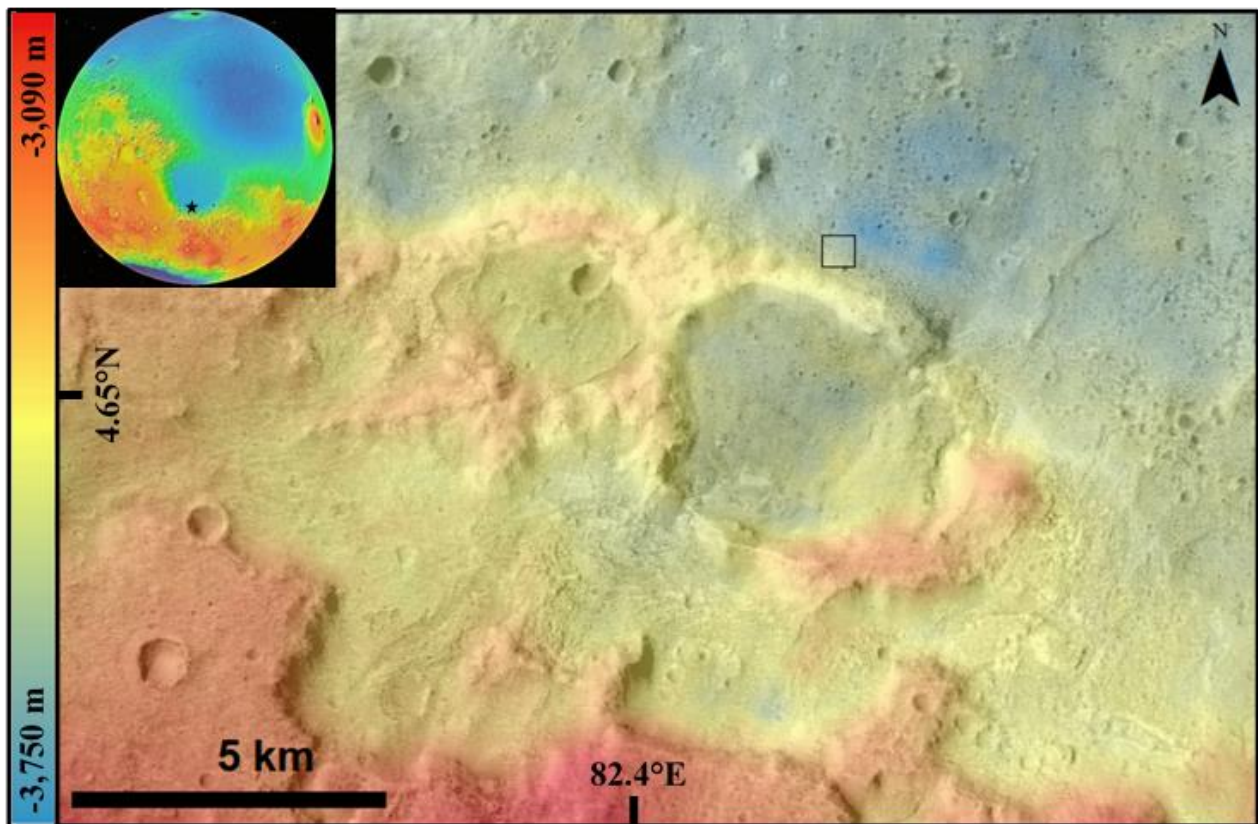


Figure C.7. Context location for Site GZ06-17a with CTX image

F16_042051_1838_XI_03N277W and HRSC elevation data (H2206_0002_DT4). Small black box shows the extent of Figure 5.3a in the main text. These lineaments are limited in extent to <1.5 km on either side of the black box.

C.2.5 *Site GZ06-17b*

Figure C.8 shows the context location of Figure 17b in Ghatan and Zimbelman (2006) and a zoom in of the lineaments investigated as possible coastal ridges (black arrows in top image). A series of ridges along the boundary between the Isidis Interior Plains and the dissected Libya Montes highlands to the south. Exposed layering can be seen in the ridges at HiRISE resolutions with different dips (black arrows in bottom image) that we interpret to be an unconformity between inclined bedding as the lowest unit with less-inclined beds above. Weathering appears to have eroded back some of the units which has manifested itself as a ridge at the base of the slope (with Libya Montes highlands). Additional mass wasting of the beds along the slope have piled up on top of the plains unit, creating softened additional lineaments (blue arrows).

C.2.6 *Site CP01-4*

Additional supplementary and context locations for the site described in Figure 4 of Clifford and Parker (2001) can be found in Appendix B.

C.2.7 *Site PC01-11*

Figure C.9 shows the location of Figure 11 in Parker and Currey (2001). The authors used photogrammetry of relatively low-resolution *Viking* images and claimed there were stepped aprons surrounding this massif. However, we find both in the HiRISE image and HiRISE-derived topography that there is no continuous bench. This appears to be a massif located on fractured terrain within a localized depression along the topographic dichotomy. There is a slight change in slope at the base of the dominant colluvium piles (roughly the yellow in the figure), but nothing suggests that this is a wave-cut platform. Thus, we lump this in with the other stepped massifs and likely caused by the collapse of the martian highlands along the dichotomy and subsequent mass wasting of the massifs.

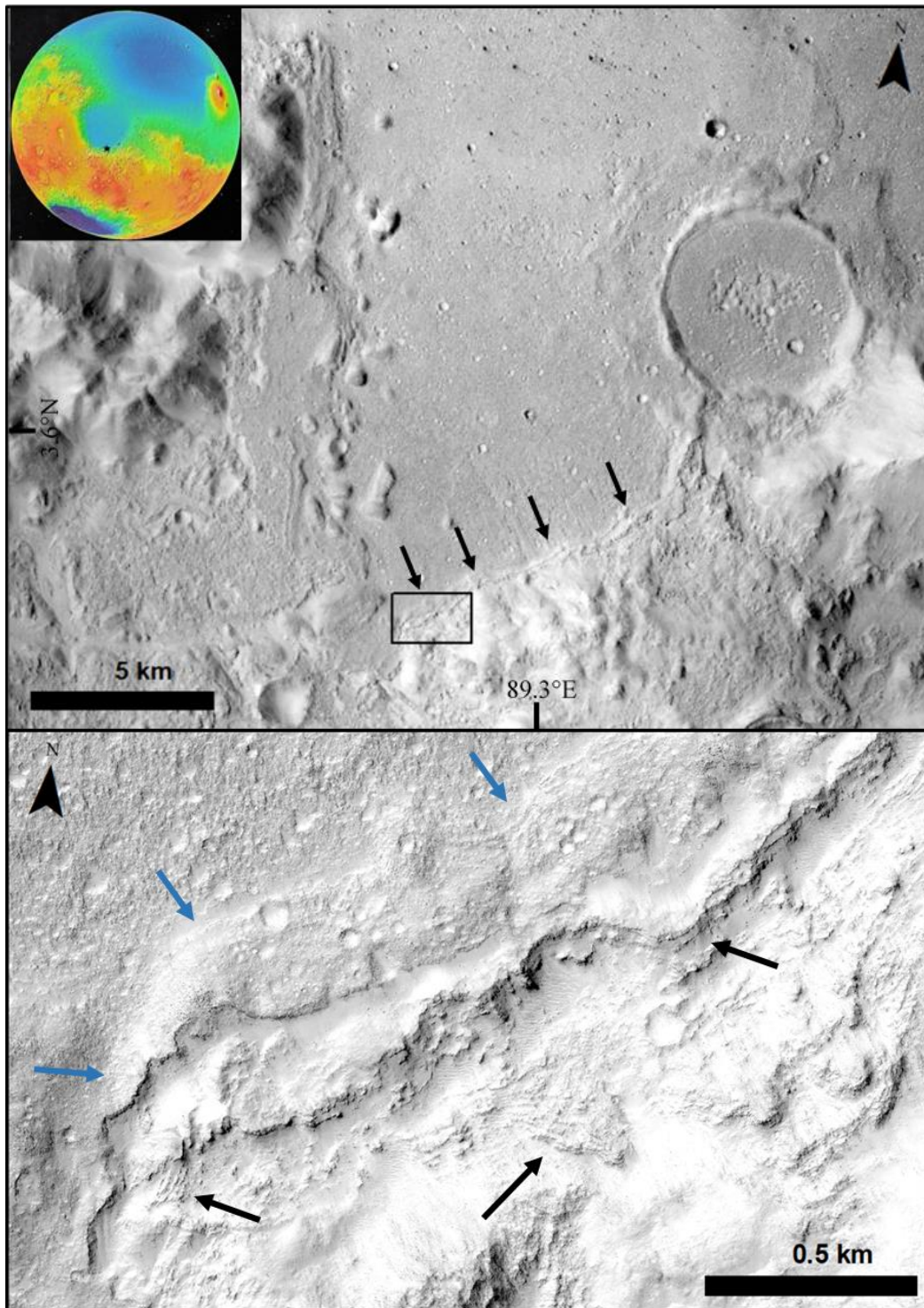


Figure C.8. Location of Site GZ06-17b. *Top*: CTX image P14_006593_1827_XN_02N270W showing the putative coastal ridges with black arrows. Black box marks location of bottom image. *Bottom*: Zoom in with HiRISE image PSP_009032_1835 showing layering with black arrows.

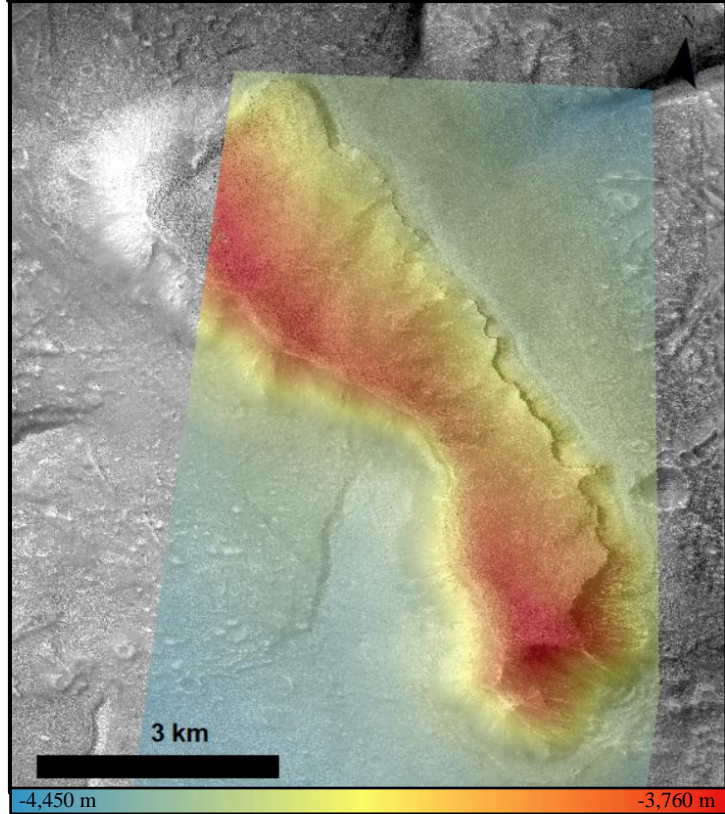
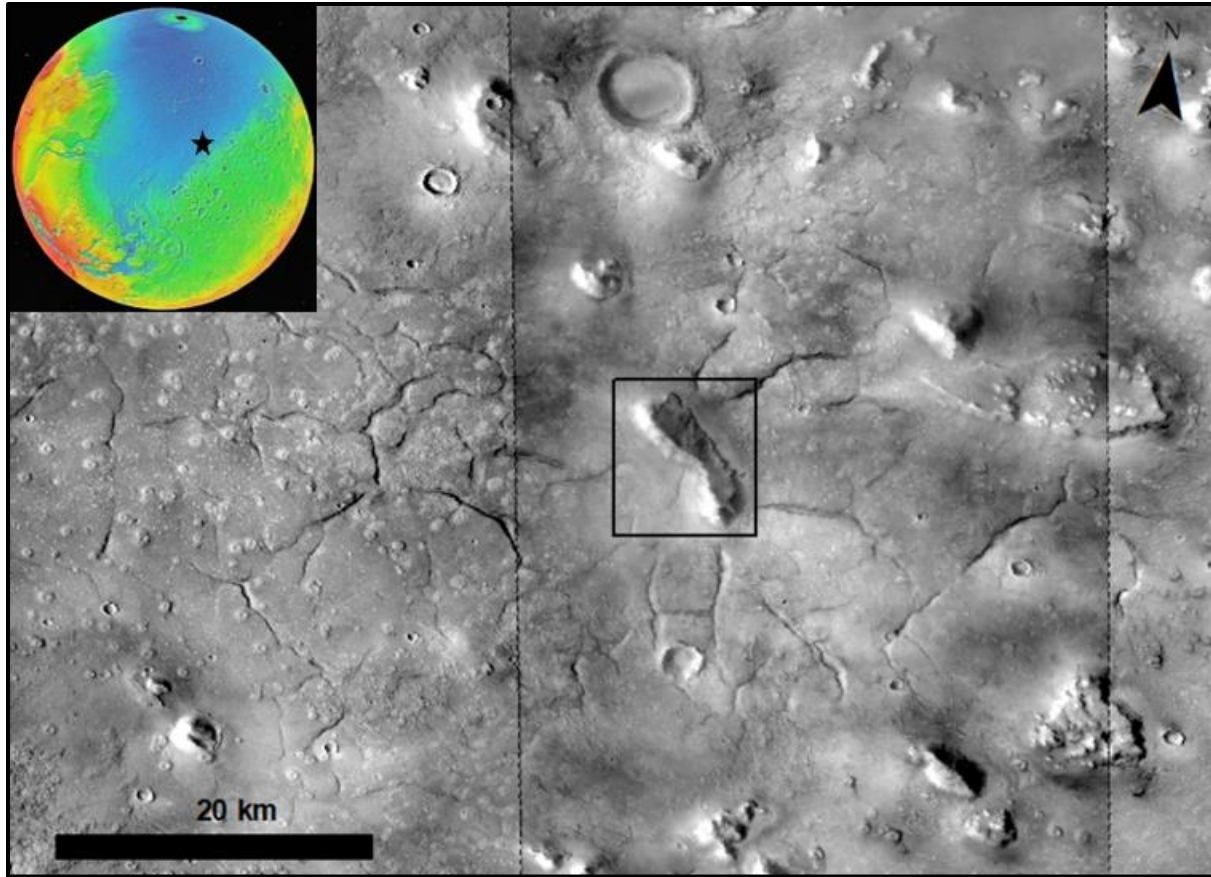


Figure C.9. *Top*: Context location for Site CP01-11. Zoom in of black box is shown to the left. CTX mosaic. *Left*: Zoom in of massif with HiRISE image ESP_016011_2185. HiRISE stereo DEM overlaid. The site appears to be mass wasting of material with a slight change in slope at the base.

C.2.8 Site PC01-12

Figure C.10 shows the context region for the site originally described in Figure 12 of Parker and Currey (2001) while Figure C.11 shows the approximate extent of the cited site. High-resolution imagery show that the massifs platforms are uneven and degrading (particularly the western massif). MOLA shotpoints that overlap the platforms are isolated from those that cover the massif peaks and surrounding plains material and planes are fit to the points using Trend tool in ArcGIS. The western massif appears to be dipping towards the south while the eastern massif platform is dipping to the north. Additionally, the average elevations of each platform are nearly 100 m apart, showing that they do not form an equipotential even locally and are likely the eroded features associated with the collapse of the highlands and subsequent uneven mass-wasting of the massif peaks from different lithological units. The surrounding plains material has some light-toned pitted mounds which have previously been interpreted to be mud volcanoes, however, these appear within the immediate plains material that onlaps the surrounding fractures and thus not likely directly connected to the formation of the massifs or their platforms.

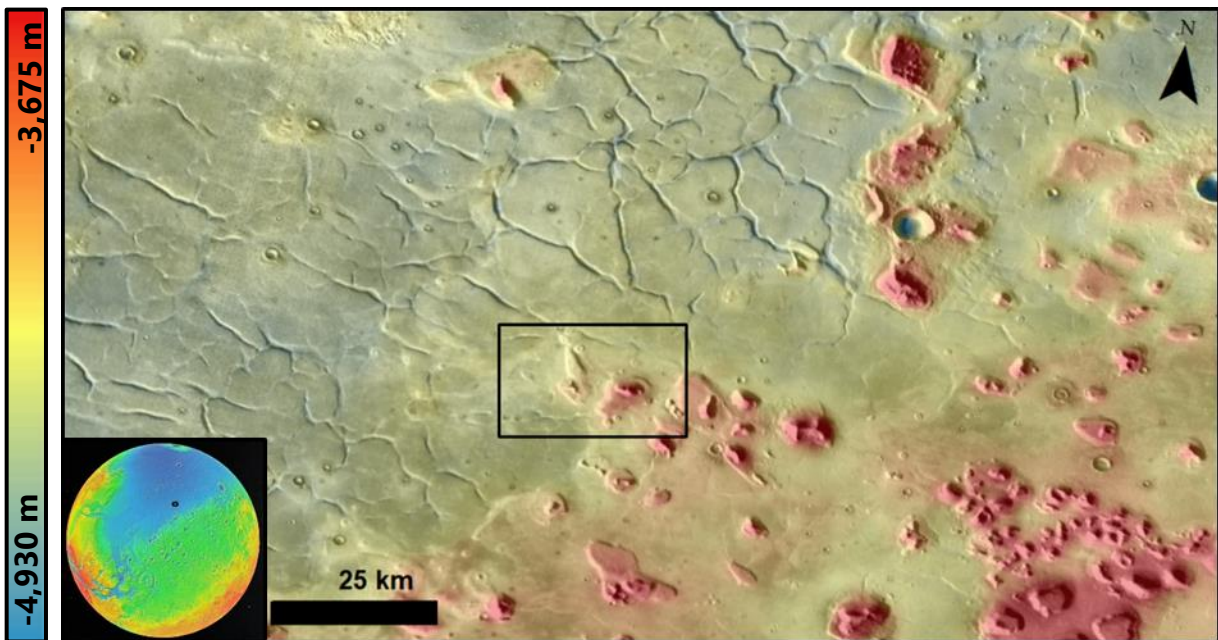


Figure C.10. Context location for Site PC01-12. THEMIS-IR day mosaic with MOLA MEGDR elevation data overlaid. Black box shows the location of Figure C.11.

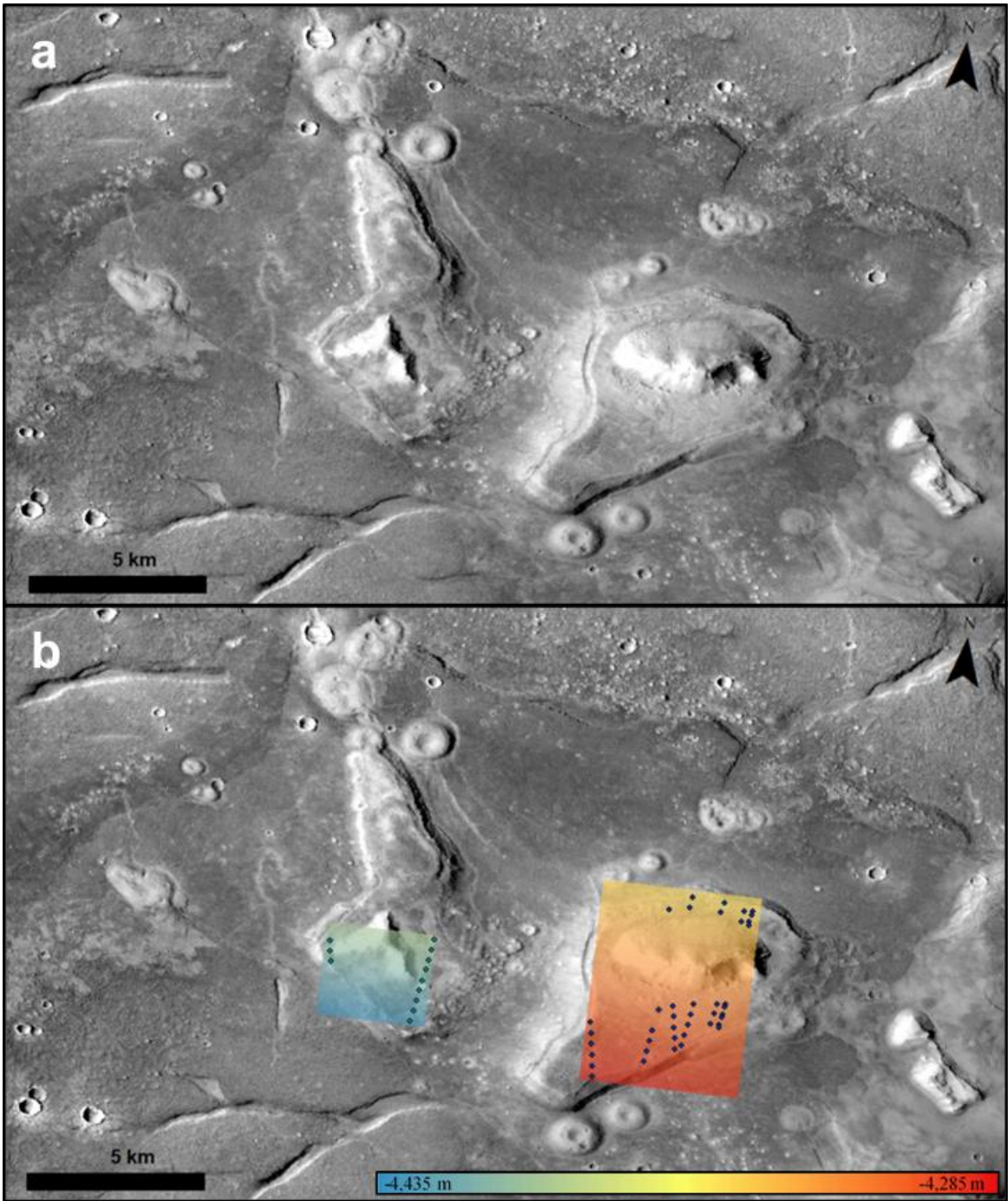


Figure C.11. Approximate extent of Site PC01-12 (See Figure C.10 for context location). CTX image G04_019756_2204_XI_40N011W. *a*) Two stepped massifs with putative wave-cut platforms. *b*) MOLA shotpoints (points) with trend-fitted planar surfaces for the western and eastern massifs.

C.2.9 Site GZ06-12b

Figure C.12a shows the location of Figure 12b in Ghatan and Zimelman (2006). Context image shows that the massif aprons in question have a more softened topography around the margin, with a sharper slope on the southern side. HiRISE image however shows that the apron platforms overlap with more irregular margins (Figure C.12b). The surrounding plains floor unit has many escarpments as well, which also tends to suggest a possible collapse mechanism in forming the platforms aided by mass wasting of the massifs.

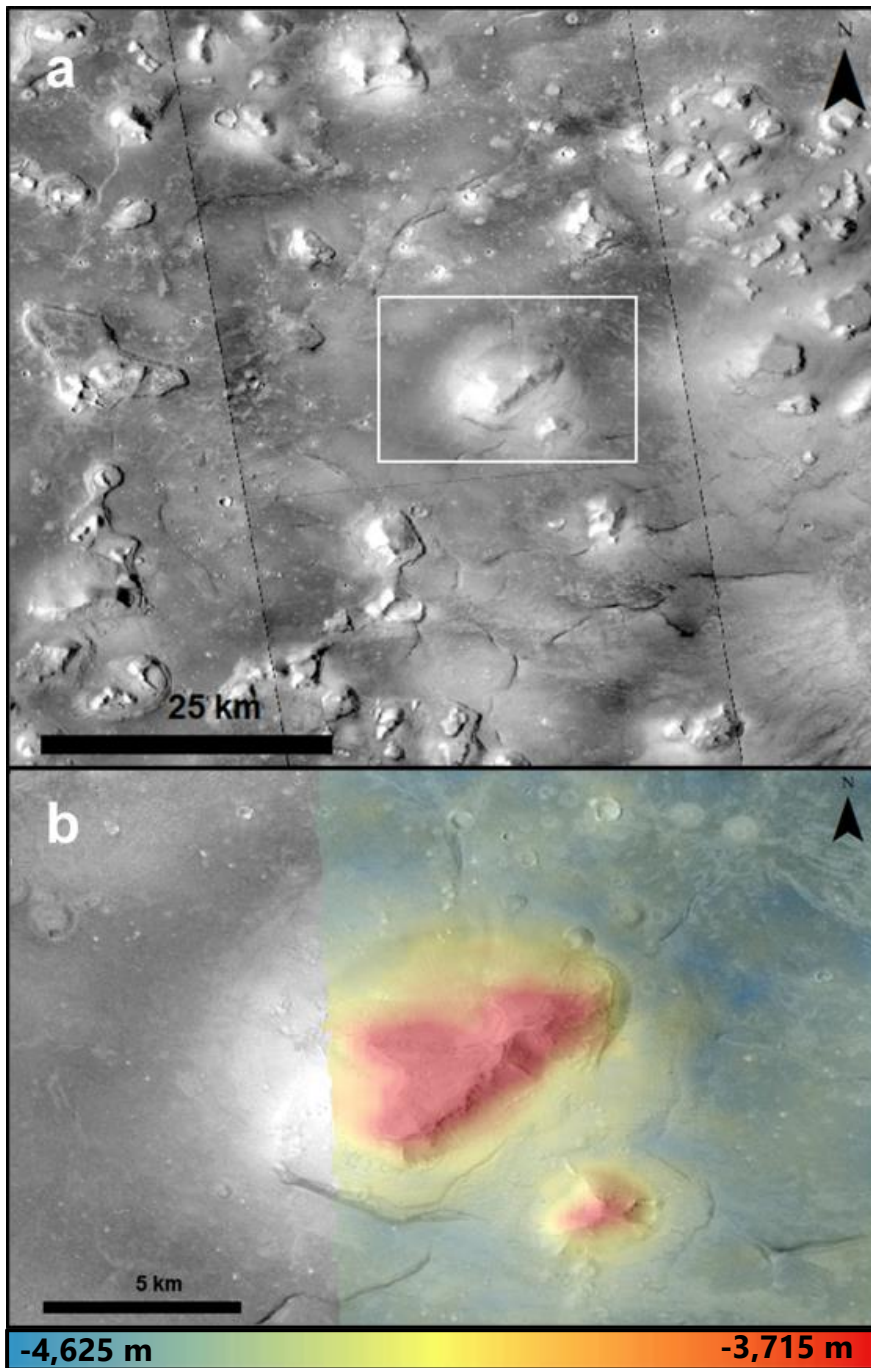


Figure C.12. Location of Site GZ06-12b. a) CTX mosaic providing context for the site, a pair of massifs within the white box. b) Enlargement of white box in a) with CTX image P17_007704_2223_XI_42N011W and HRSC elevation data (H1238_0000_DT4). Here, the aprons appear to overlap one another and are angled relative to the floor material.

C.2.10 Site GZ06-12d

Figure C.13 shows Oxus Patera with white arrows indicating the ridges examined in Figure 12d of Ghatan and Zimelman (2006). These ridges appear to be fractures along the patera floor while the curvilinear features along the patera rim appear to be the result of collapse of the wall. Additionally, while Oxus Patera is located along the topographic dichotomy, it is not immediately open to the northern plains. Work by Michalski and Bleacher (2013) suggests that a possible formational mechanism for this patera is either as a volcano or supervolcano. Other possible scenarios include impact and erosion or removal of subsurface volatiles. No coastal landforms are identified.

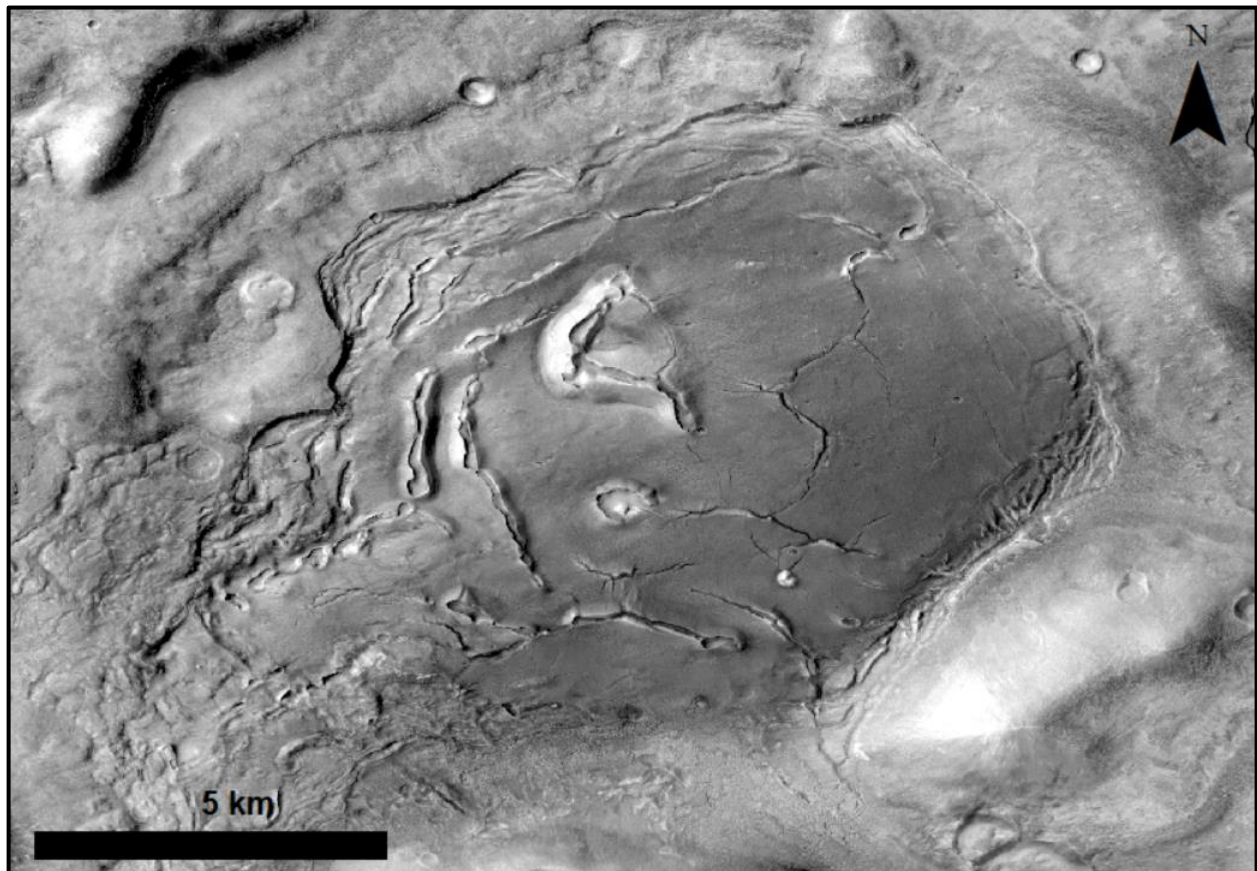


Figure C.13. Location of Site GZ06-12d showing Oxus Patera. CTX image D19_034656_2193_XN_39N000W. Black arrows indicate ridges investigated by original authors. No coastal landforms are observed.

C.2.11 *Site GZ06-12f*

Figure C.14 show the location of Figure 12f in Ghatan and Zimbelman (2006). While we classify this site in the general “Collapse” category, the site is a combination of collapse of the knobby/massif unit, onlap of the lobate flows associated with the Deuteronilus Level, and some sinuous massif ridges. It is unclear with the available CTX imagery whether the ridges present (black arrows in Figure C.14) are the result of degradation of knobby unit along its margin, or associated arcuate ridges along the margin of the VBF. In either case, these ridges do not appear to be of coastal origin as many of the massif platforms (when present) overlap each other within the knobby unit. The massif ridges are also highly sinuous suggesting they are wrinkle ridges and not coastal depositional features.

C.2.12 *Site P93-3*

Figure C.15 shows the extent of Figure 3 in Parker et al. (1993). Here there are three prominent types of ridges that were investigated as possible coastal landforms (e.g. spits/tombolos) with Figure C.16 providing zoomed in versions. The ridge in Figure C.16a bifurcates into two different morphological expressions with the southern fork appearing as more of a north-facing escarpment and the northern fork much more heavily subdued with segments of the ridge having little to no topographic expressions. The ridge in Figure C.16b has a relatively wide and flat crest and connects two adjacent massifs. HRSC elevation data is too coarse to identify and characterize the ridge, but does show that the plains material to the north is topographically lower in elevation than the plains material south of the ridge. The western segment of the ridge in Figure C.16c is morphologically similar to the ridge in Figure C.16b but becomes much more sinuous and narrower moving east along track. Here, the ridge (shown with white arrows) crosscuts the darker-toned debris apron (shown with black arrows) coming from the highland plateau. All of these detailed morphologies suggest that none of these ridges are coastal in origin.

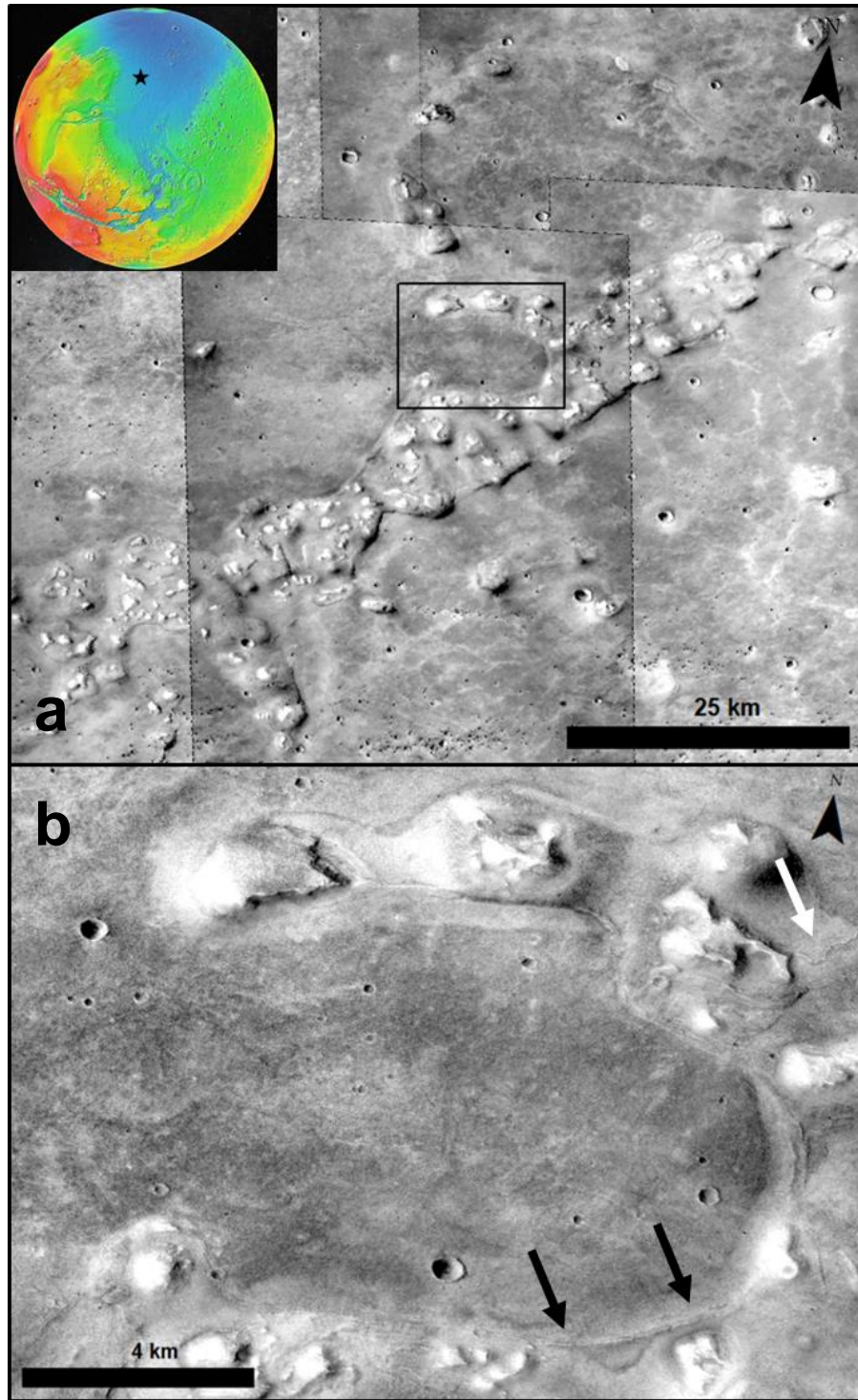


Figure C.14. *a)* Context location for Site GZ06-12f with CTX mosaic. *b)* Zoom in of the black box in *a)* with the extent of the investigated ridges marked with black arrows. White arrow shows a sinuous wrinkle ridge.

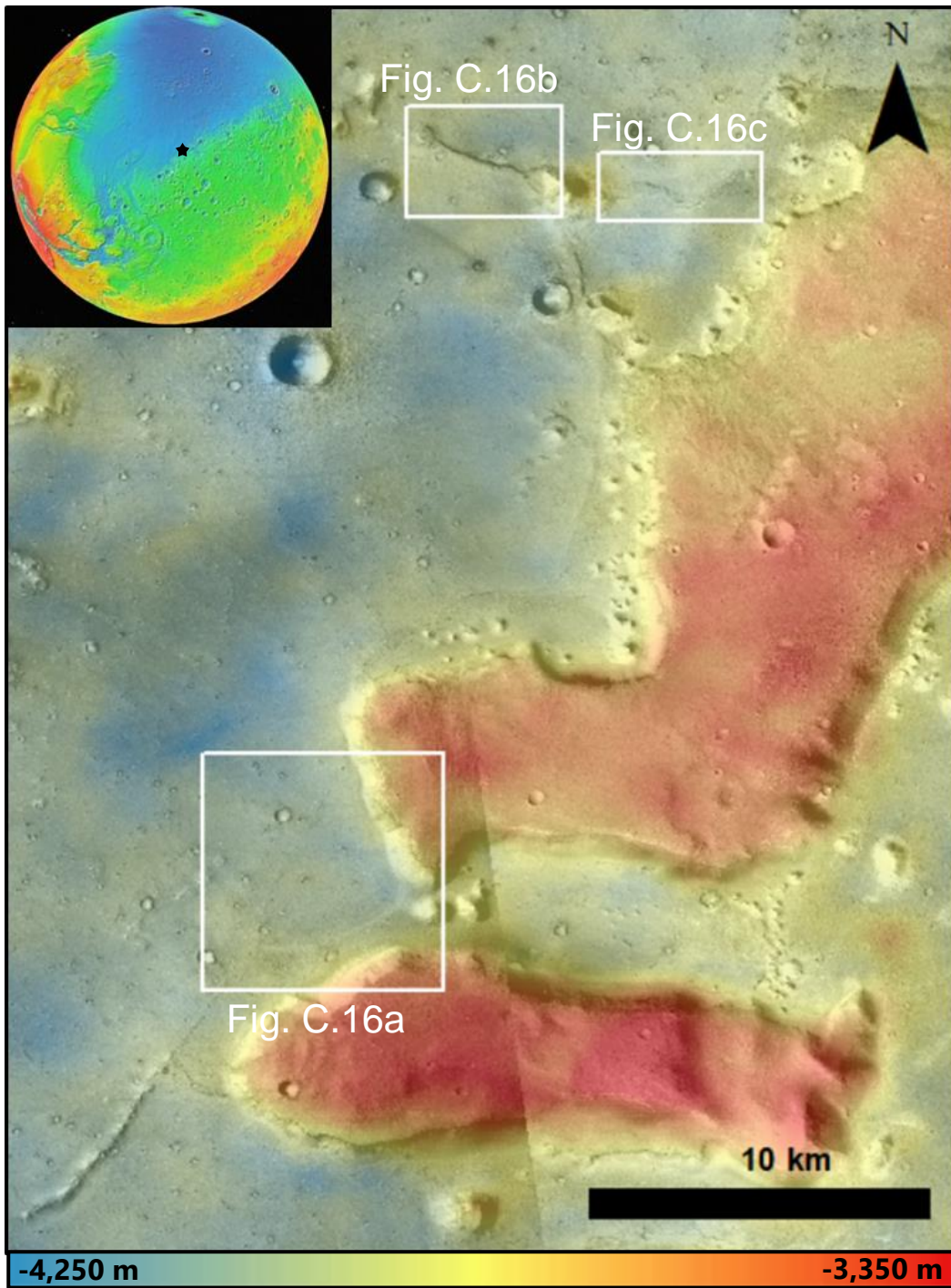


Figure C.15. Location of Site P93-3 with CTX mosaic and HRSC topography (H1542_0009_DT4) overlain.

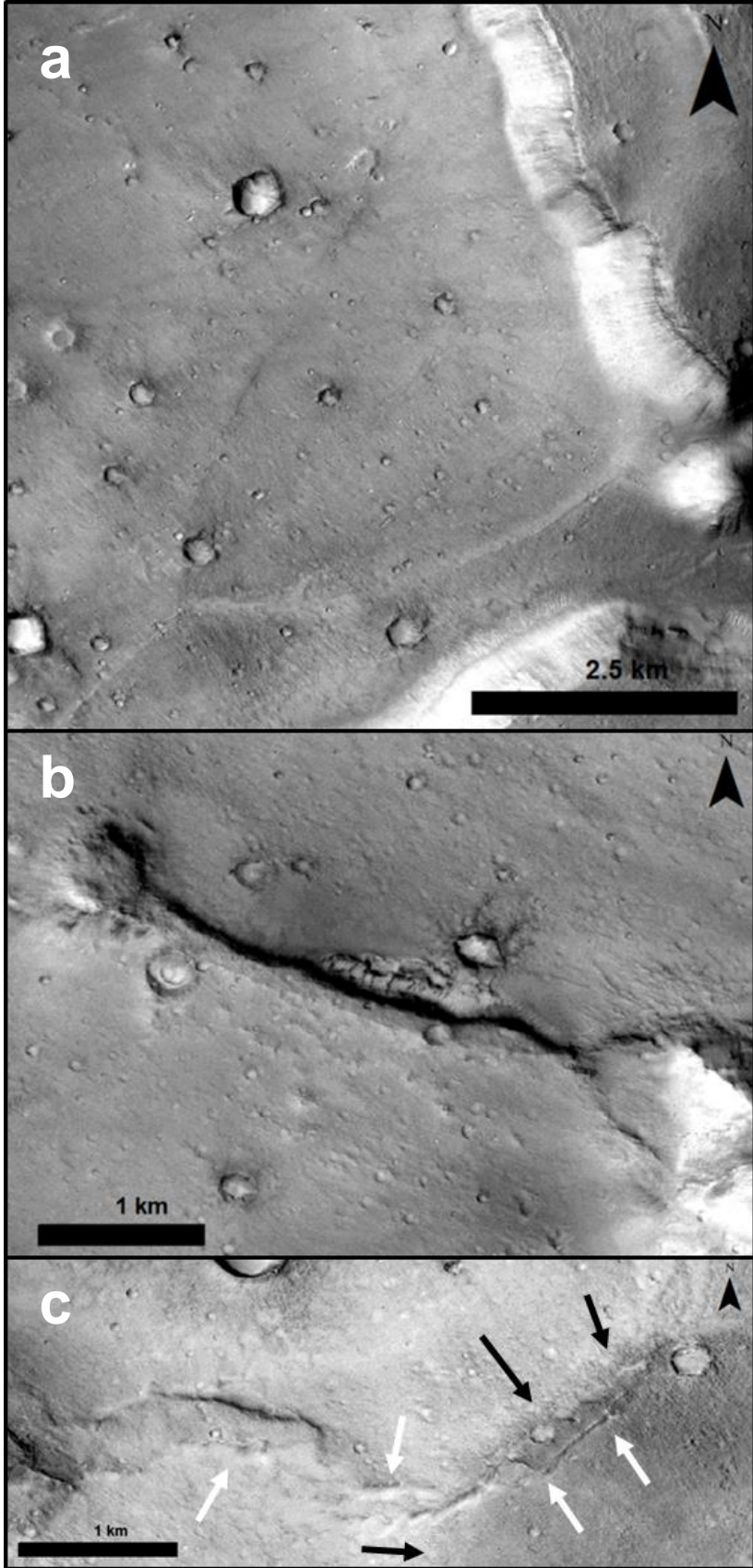


Figure C.16. Zoom in of ridges from Site P93-3 (See Figure C.145 for context) with CTX image P22_009761_2113_XN_31N016W. *a*) Wide flat-crested ridge between two small massifs. *c*) Sinuous ridge (white arrows) that crosscuts a dark-toned debris pile (black arrows).

C.2.13 Site GZ06-8b

Figure C.17 shows the location of Figure 8b from Ghatan and Zimbelman (2006). The ridge in question attaches sharply to the highland plateau (blue arrow). However, the surrounding region has many sinuous wrinkle ridges (black arrows), some of which also terminate at the base of the highlands. This ridge does not appear to be of coastal origin.

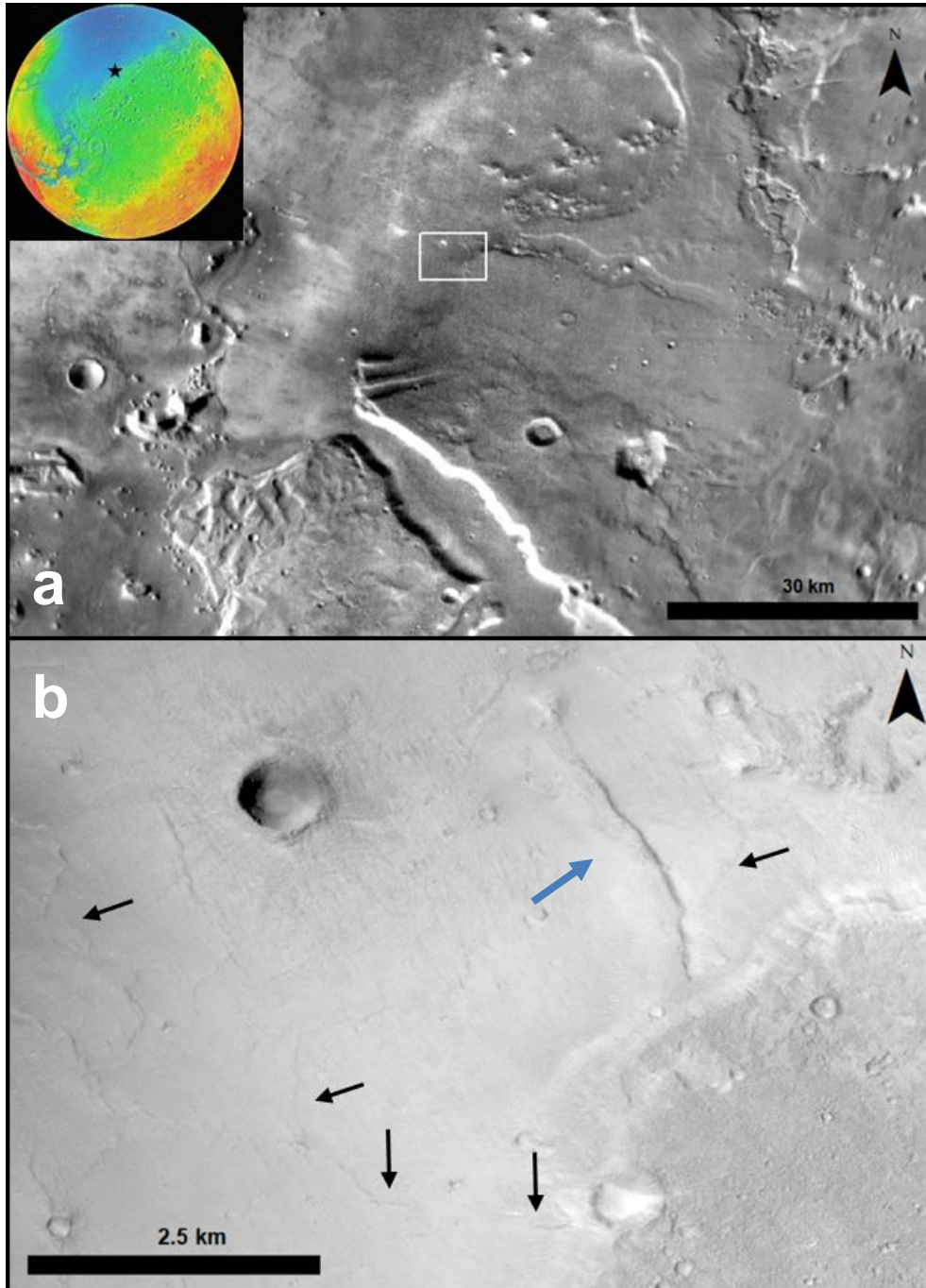


Figure C.17. Location of Site GZ06-8b. a) THEMIS-IR day mosaic providing context. b) Zoom in of white box in a with CTX image D01_027536_2083_XN_28N013W. Blue arrow shows ridge in question and black arrows show wrinkle ridges.

C.2.14 Site GZ06-8c

Figure C.18 shows the location of Figure 8c in Ghatan and Zimbelman (2006) with zoomed in figures of specific ridges shown in Figure C.19. Here, there is a massif unit that is completely surrounded by the VBF (white arrows in Figure C.18 indicate the boundary) with ridges extending into the VBF. The ridge shown in Figure C.19a appears to crosscut the massifs (white arrows) suggesting they are younger than the massifs and not coastal in origin. The ridge in Figure C.19b is somewhat discontinuous with pits along the crest and some oblong pits along the southern side. These are reminiscent of other such pit chain ridges found elsewhere in the northern plains which are suspected to have been caused by volatile eruptions (Orgel et al., 2019), though image resolution is inadequate to examine for boulder distributions at this site. These features do not appear to be consistent with coastal origins and are likely weathered remnants of the previous terrain prior to the deposition of the VBF (and thus associated with the collapse of the highlands).

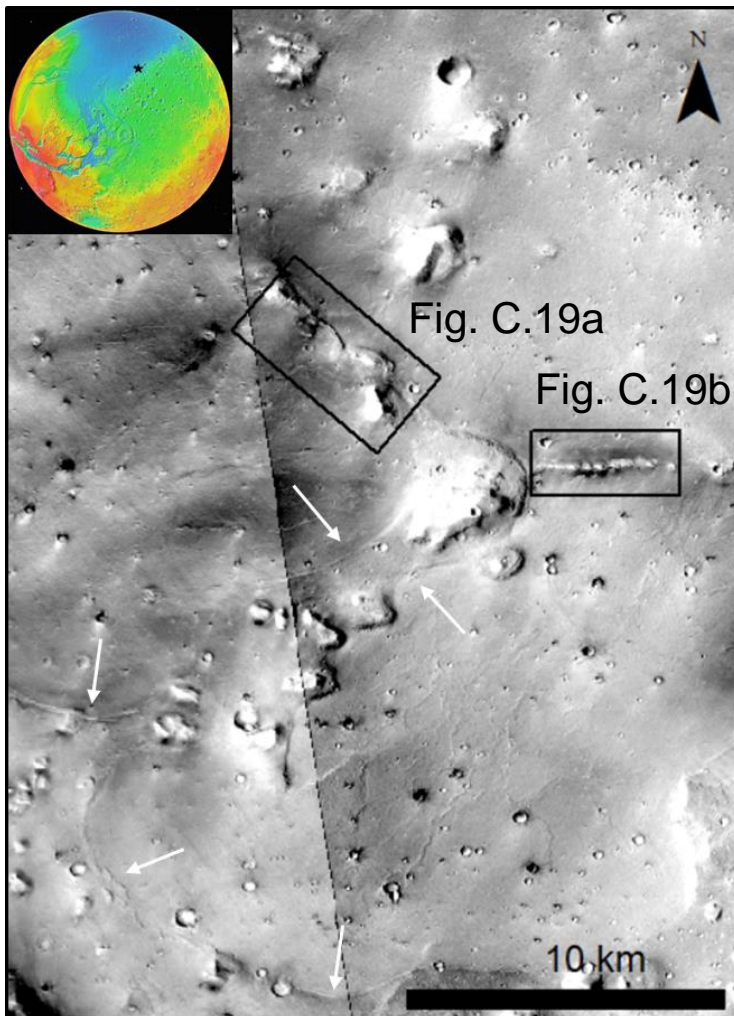


Figure C.18. Location of Site GZ06-8c with a CTX mosaic. White lines indicate boundary between the VBF and knobby massif unit. Black boxes show extents for Figure C.19.

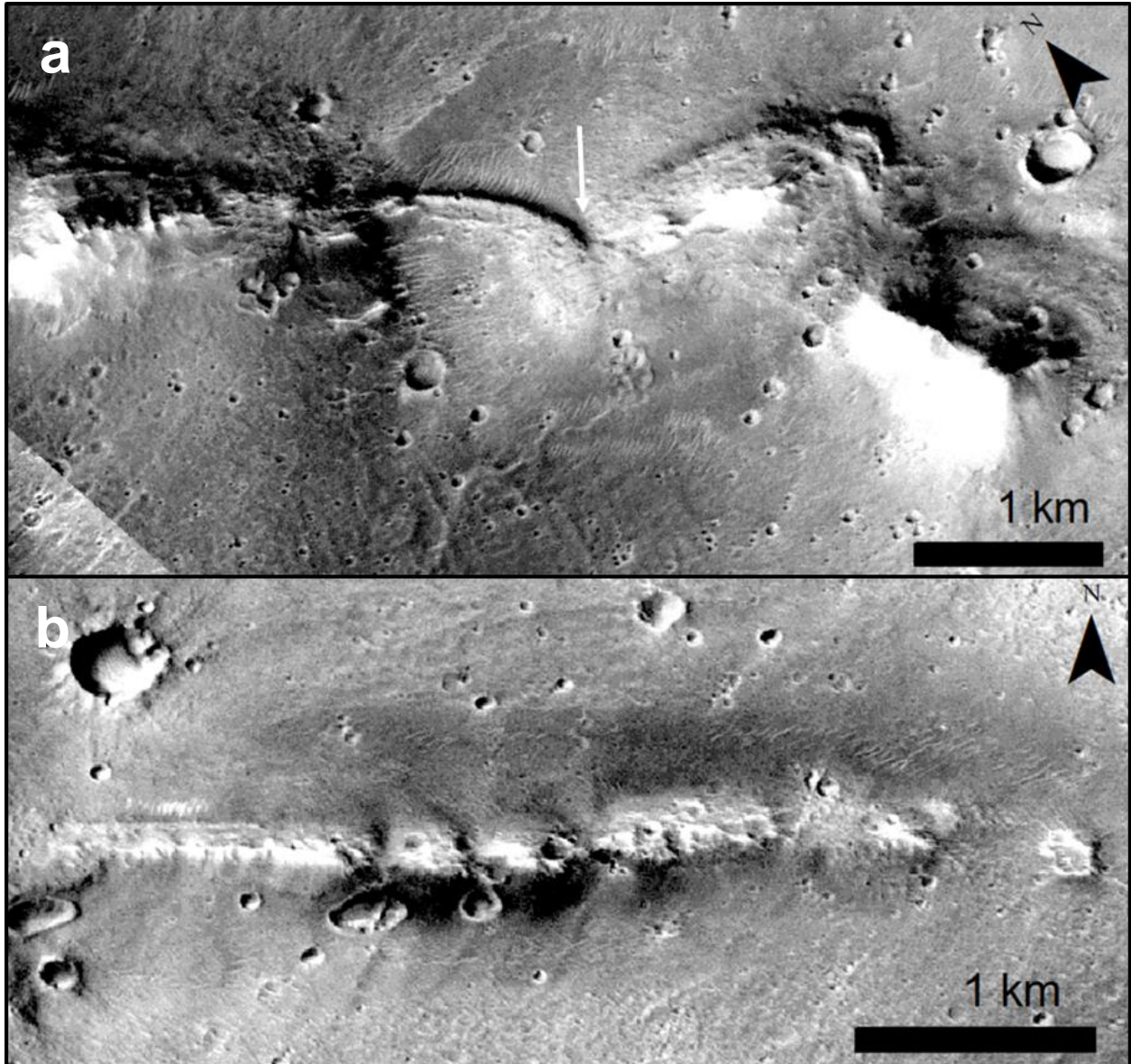


Figure C.19. *a*) Curvilinear ridge between massifs. White arrow indicates where the ridge crosscuts a massif and its debris apron. *b*) Discontinuous ridge with a pitted crest. Both figures are from CTX image B03_010684_2117_XN_31N016W.

C.2.15 Site GZ06-9a

Figure C.20 shows the location of Figure 9a from Ghatan and Zimbelman (2006). The context image (Figure C.20a) shows that the massif ridges are located with a dense massif unit in the Cydonia Mensae region, however the region has extensive tectonic landforms such as the large escarpment and wrinkle ridges to the west of the massif unit. The debris apron platforms are much

more subdued here than in other massif units, though in many places they do appear to be at different elevations. Figure C.20b is a reproduction of Figure 5.3c in the main text with white arrows indicating where the sinuous ridges crosscut the massifs. This is inconsistent with a coastal origin for these massif ridges.

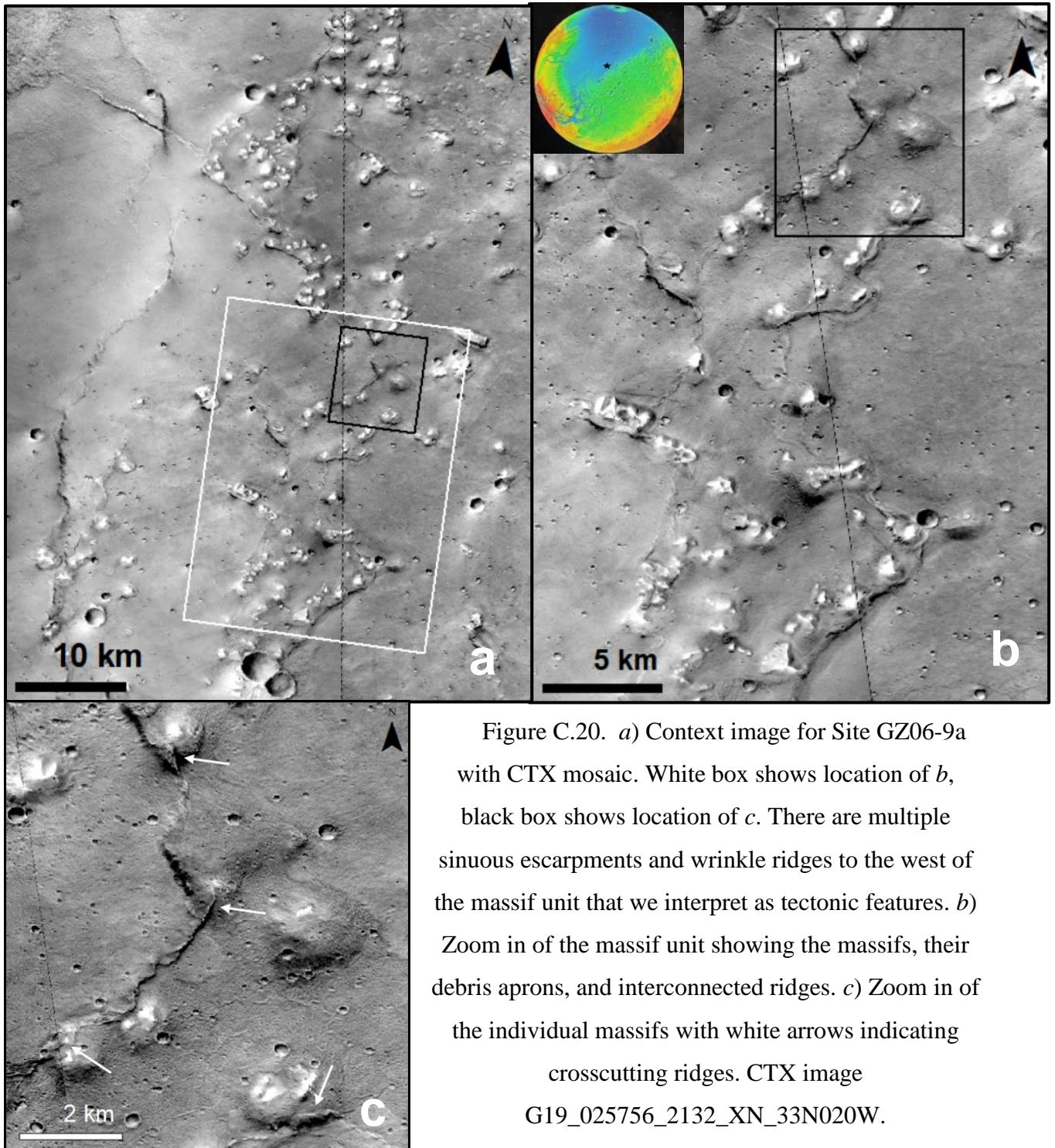


Figure C.20. *a*) Context image for Site GZ06-9a with CTX mosaic. White box shows location of *b*, black box shows location of *c*. There are multiple sinuous escarpments and wrinkle ridges to the west of the massif unit that we interpret as tectonic features. *b*) Zoom in of the massif unit showing the massifs, their debris aprons, and interconnected ridges. *c*) Zoom in of the individual massifs with white arrows indicating crosscutting ridges. CTX image G19_025756_2132_XN_33N020W.

C.2.16 *Site GZ06-12c*

Figure C.21a shows the locations of Figure 12c and portions of Figure 9b in Ghatan and Zimbelman (2006). The curvilinear ridge in Figure C.21b was suggested by the authors to be the remnants of a degraded crater rim, however the orientation of the ridge in relation to the massifs would imply that the massifs post-date the ridge if it were of impact origin, which seems unlikely. Morphologically it resembles the ridge found in Site GZ06-8b, just more arcuate in form; it may be the result of degradation of the massif unit or possibly a curvilinear (non-sinuuous) wrinkle ridge. Figure C.21c shows the actual feature examined for Site GZ06-12c, which is a highly-sinuuous ridge connecting two massifs, undoubtedly a wrinkle ridge and not coastal. A variety of other curvilinear ridges, which have not been previously investigated, are found south of these sites (Figure C.21d) which crosscut each other and are morphologically similar to other massif ridges investigated in this Appendix.

C.2.17 *Site GZ06-15c*

Figure C.22 shows the location of Figure 15c in Ghatan and Zimbelman (2006). The site is characterized by a pair of curvilinear ridges within the VBF-like unit within the Isidis Basin (see Ivanov et al. (2017) for detailed crater counting on why this is not the VBF unit of the northern plains). The southern end of the N-S oriented ridge transitions into a massif unit while the NE-SW oriented ridge is isolated within the VBF-like unit. The two ridges end up paralleling each other in the middle and curve away from each other at their ends. Due to their orientations and location within the VBF-like unit, these are unlikely to be coastal ridges and are probably associated with the depositional process that formed the VBF-like unit. As seen in Figure C.2, there are arcuate thumbprint terrain landforms with similar orientations to the east of this site, which further supports that these may be related to the viscous flow behavior seen elsewhere along the Isidis VBF-like unit.

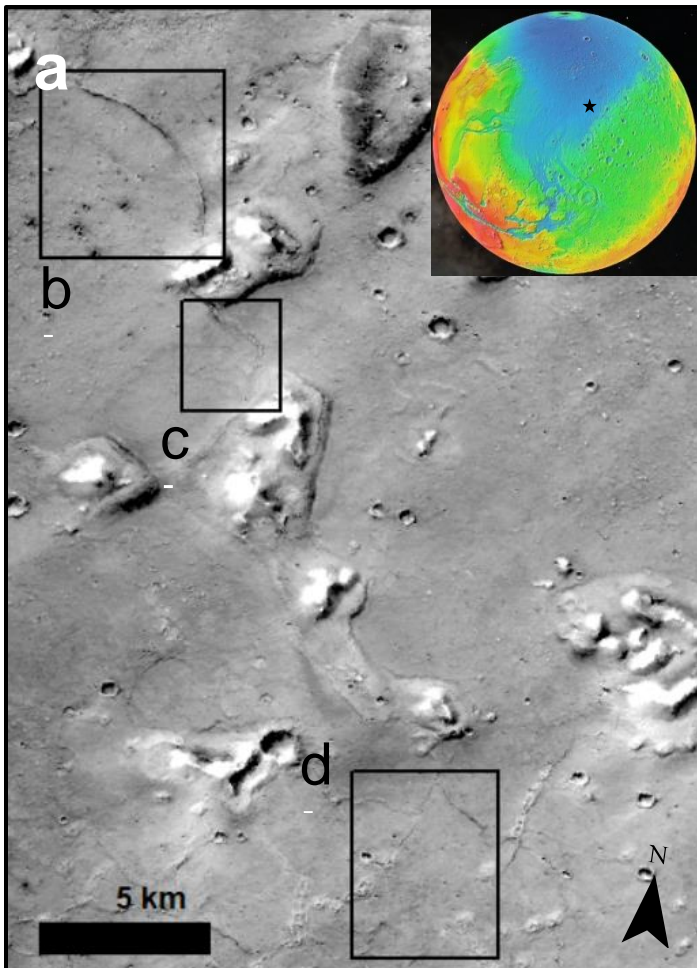
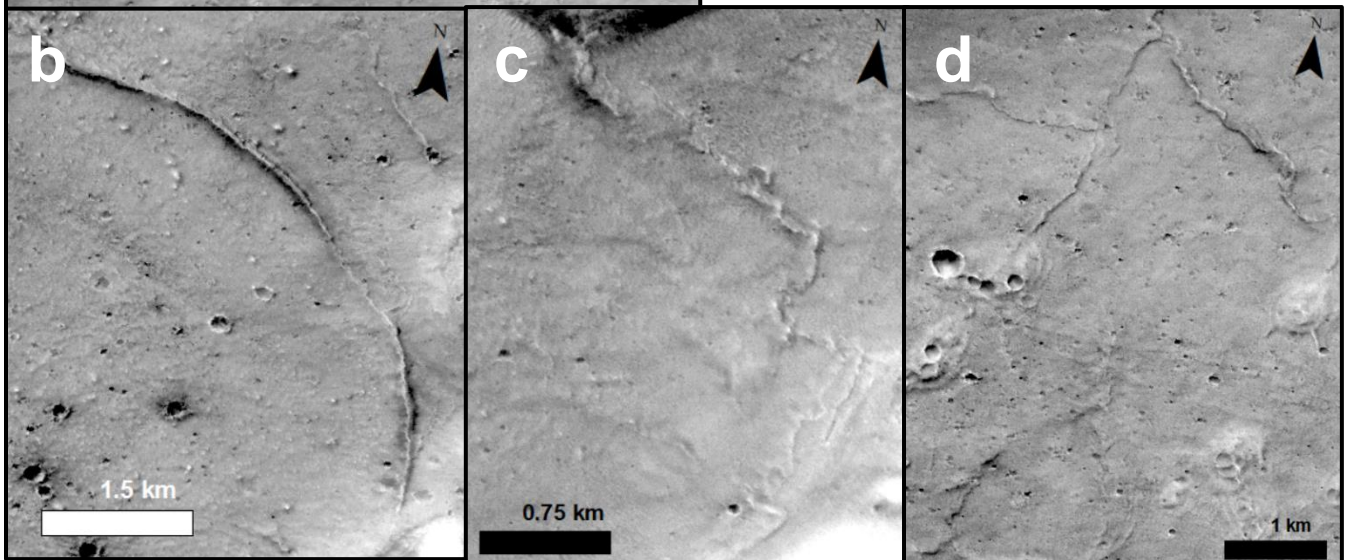


Figure C.21. Location of Site GZ06-12c. *a)* Context of the site with CTX image D22_035672_2152_XN_35N019W. *b)* Arcuate ridge connecting two massifs. *c)* Highly sinuous ridge connecting the gap between two massifs. *d)* Additional ridges that crosscut each other and are morphologically similar to ridges examined in this study (and appear inconsistent with a coastal origin).



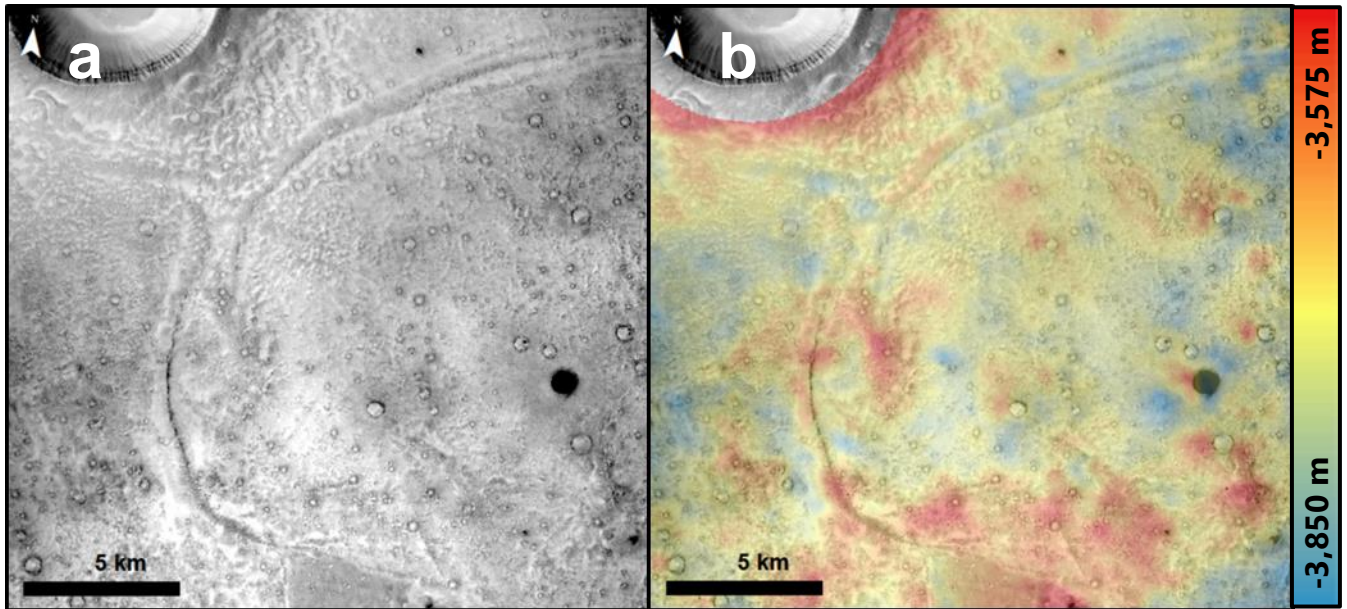


Figure C.22. Location of Site GZ06-15c (see Figure C.2 for context). Two ridges parallel one another in the middle. a) CTX image G14_023814_1955_XN_19N279W. b) HRSC topography (H5234_0000_DT4) overlain.

C.2.18 Sites GZ06-17c and GZ06-17e

Figure C.23a shows the locations for Figures 17c, 17e, and 17f in Ghatan and Zimbelman (2006) (Figures 17c and 17f of Ghatan and Zimbelman (2006) are different segments of the same ridge). These two sites are grouped together because they have near identical morphologies and are relatively spatially adjacent within the Isidis Basin VBF-like unit. Site GZ06-17c in Figure C.23b shows a spline-like arcuate ridge with linear depressions paralleling both sides of the ridge. The southern end of the ridge has an odd triangle-shaped geometry where the through ridge forks and meets an orthogonal trough ridge. Site GZ06-17e in Figure C.23c shows a linear ridge with troughs paralleling either side of the ridge. Here, though there are some lateral offsets of the ridge. Both sites are also oriented orthogonal to the local expression of the Deuteronilus Level. Overall, these features do not appear to be coastal landforms due to their geometries, morphologies, orientation, and location within the VBF-like unit. As mentioned in the main text, it has been suggested that these are glacially-formed eskers within tunnel-valleys.

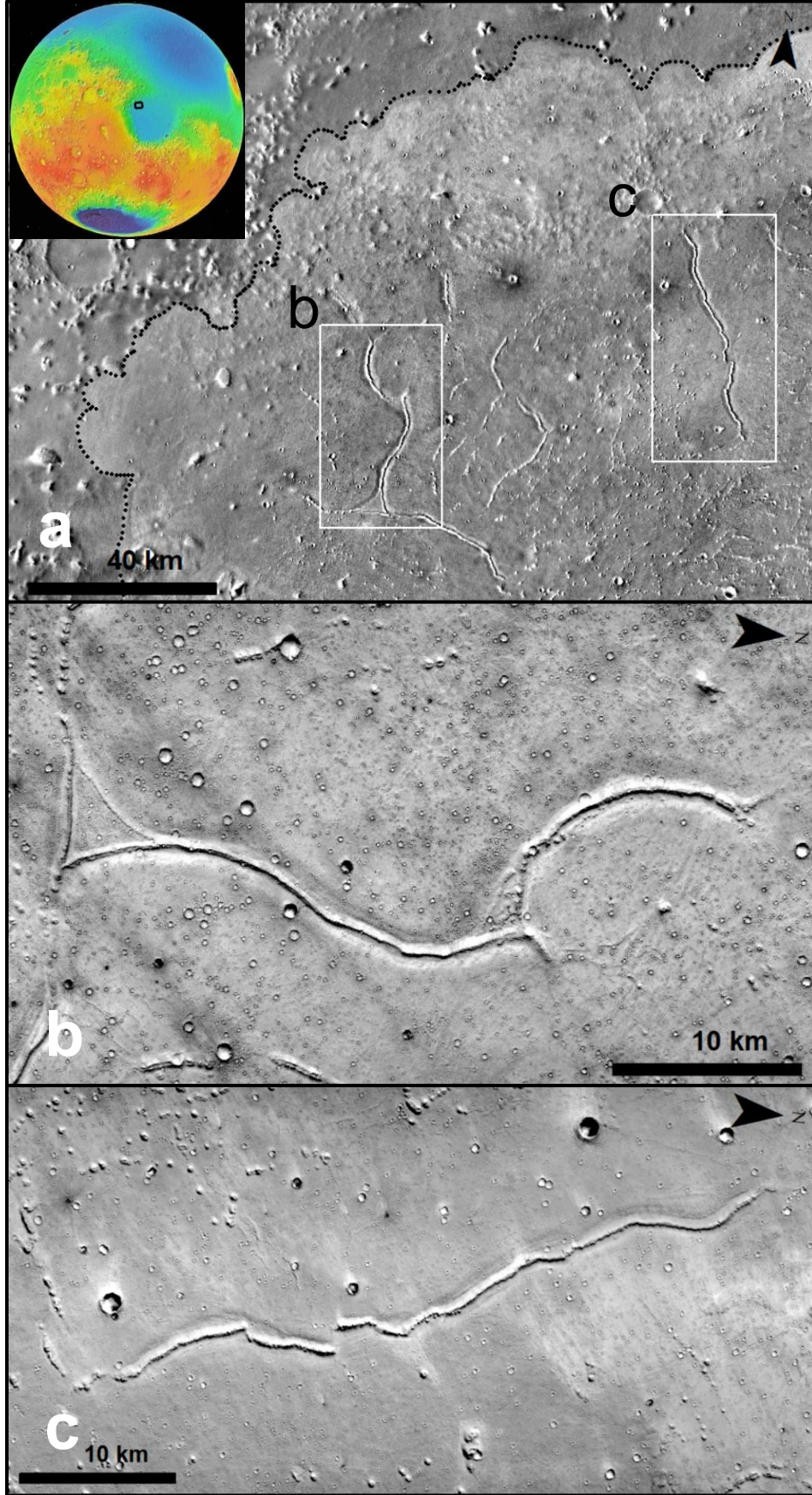


Figure C.23. Location of Sites GZ06-17c and GZ06-17e. a) Context image showing the locations of the candidate ridges in Isidis Basin, THEMIS-IR day mosaic. Black dots indicate mapped Deuteronilus Level by Ivanov et al. (2017). b) Isolated trough ridge of GZ06-17c with CTX image F05_037620_1978_XN_17N278W. c) Isolated trough ridge of GZ06-17e with CTX image P18_008228_1981_XI_18N277W.

C.2.19 Site GZ06-17d

Figure C.24 shows the location of Figure 17d in Ghatan and Zimelman (2006). This is a generally-linear ridge in northern Isidis Planitia within the Isidis Basin VBF-like unit and oriented orthogonal to the local expression of the Deuteronilus Level. A topographically-softened trough can be observed paralleling both sides of the ridge, though it appears to have been filled in with transverse aeolian ridges. The northern segment of the ridge is wider with a short bifurcation, trending into a more sinuous and subtly-expressed ridge transitioning into a small massif. Locally, there are other similar and shorter ridges that have various opposing orientations with some thumbprint-terrain like morphologies. These do not appear to be coastal landforms, and may be glacial in origin (like Sites GZ06-17c and GZ06-17e).

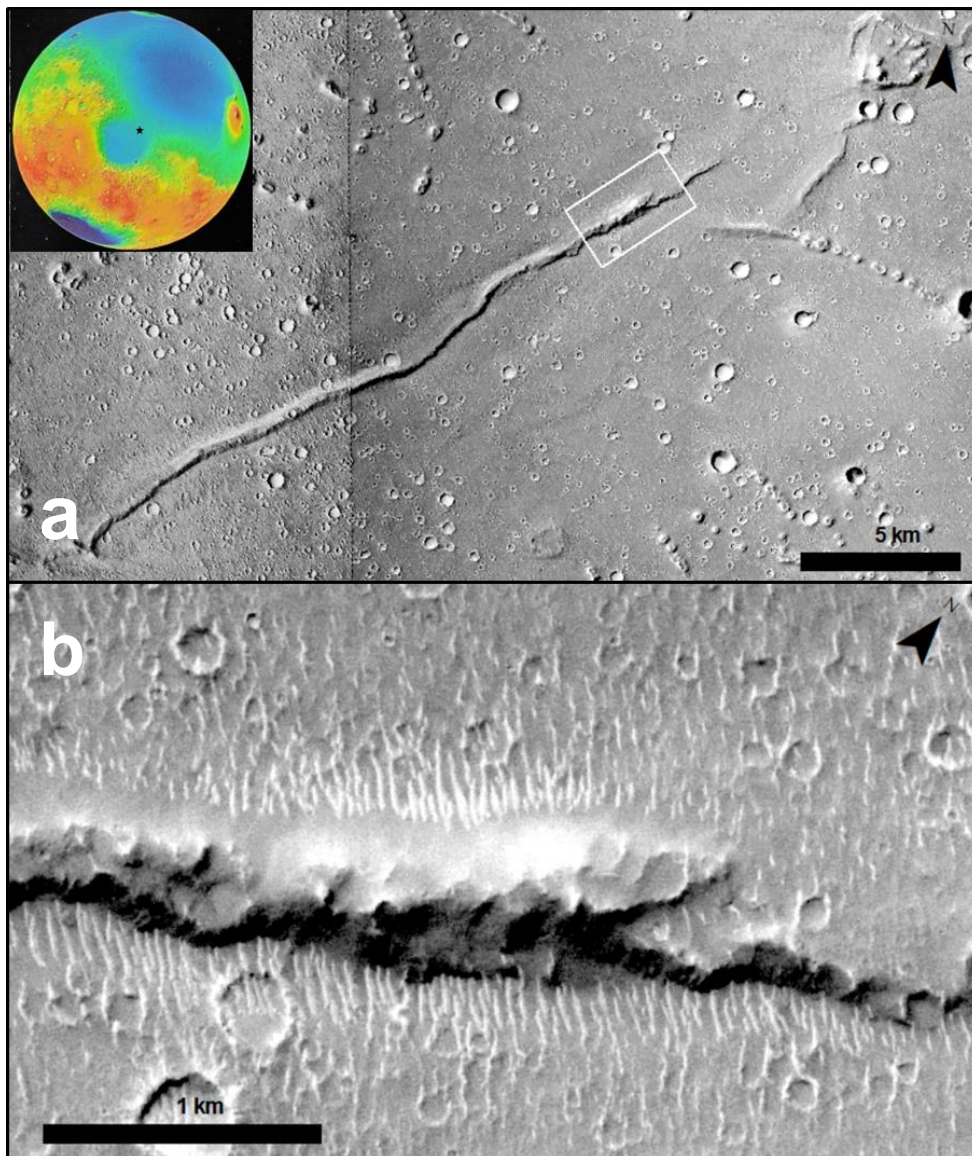


Figure C.24. Location of Site GZ06-12d. a) CTX mosaic showing the linear ridge which is orthogonal to and ~30 km to the southwest of the Deuteronilus Level locally. b) Zoom in of the widened and possibly bifurcated portion of the ridge. CTX image B20_017471_1977_XN_17N266W.

C.2.20 *Site GZ06-12e*

Figure C.25 shows the location of Figure 12e in Ghatan and Zimbelman (2006). The site is a series of arcuate ridges between some streamlined islands and the boundary of the VBF near the terminus of Ares Valles. Some of the ridge have linear depressions that parallel their sides, others appear to branch off from small massifs within the channel, and parts of the lobate flow fronts of the Deuteronilus Level have associated ridges that parallel their margins. However, the ridges do not have any coherent orientation that would be reasonable for such a coastal environment locally. It is likely that there are different processes creating spatially adjacent yet genetically dissimilar ridges, such as the proposed esker/tunnel valley hypothesis for the through ridges, exposed dikes or inverted cracks for the massif ridges (Ghatan and Zimbelman, 2006). None of these ridges appear to be likely candidate for coastal landforms.

C.2.21 *Site P08-4*

Figure C.26 shows the location of Figure 4 in Parker (2008), which highlighted only a portion of the northwestern lobate ridge. Zooming out from the original site reveals multiple overlapping, crosscutting, and bifurcating (black arrows) ridges with curvilinear depressions paralleling their sides. These lobate ridges also have no obvious dominant orientation or curvature, with some convex and concave with respect to the direction of the northern plains (Figure C.26b). The morphologies of the ridges also change along track, with some becoming more sinuous towards their ends, and even one cross-cutting a small knob (white arrow). Parker (2008) interpreted these ridges as the result of shoving of debris from an ice-and-debris covered ocean during a short transgressive period. Yet the regional morphologies of similar ridges (in Figure C.26a) indicate that these are unlikely to be from lobate flow fronts (as many of these trough ridges run N-S). One ridge (yellow arrow) terminates at the margin of the Deuteronilus Level. These ridges are unlikely candidate for shorelines, and morphologically closely resemble the isolated trough ridges of Sites GZ06-17c and GZ06-17e, which we interpret as glacial in origin.

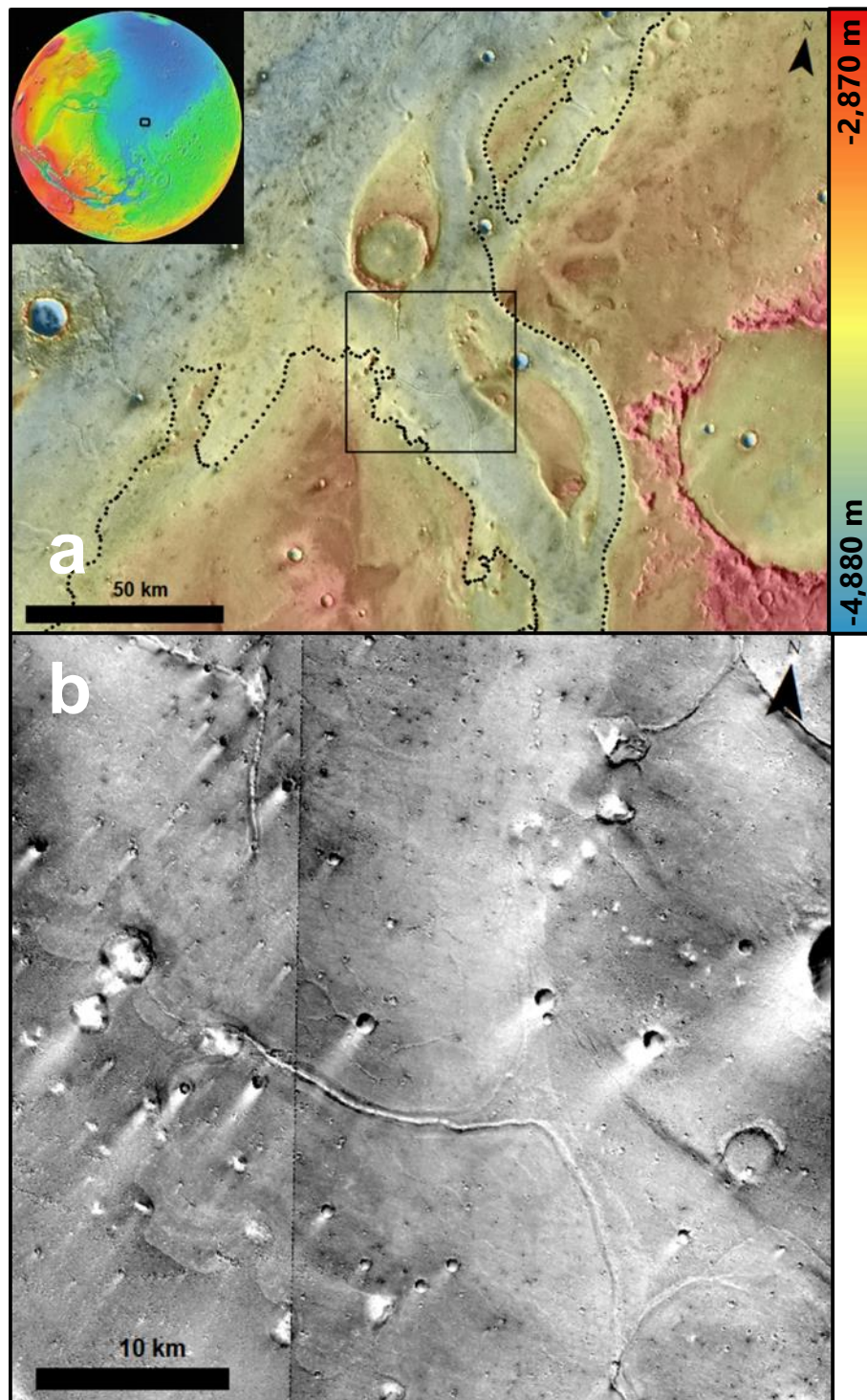


Figure C.25. Location of Site GZ06-12e. *a)* THEMIS-IR day mosaic with MOLA MEDGR elevation overlain. Black dots show mapped Deuteronilus Level by Ivanov et al. (2017). *b)* CTX mosaic showing the prominent ridges within the outflow channel.

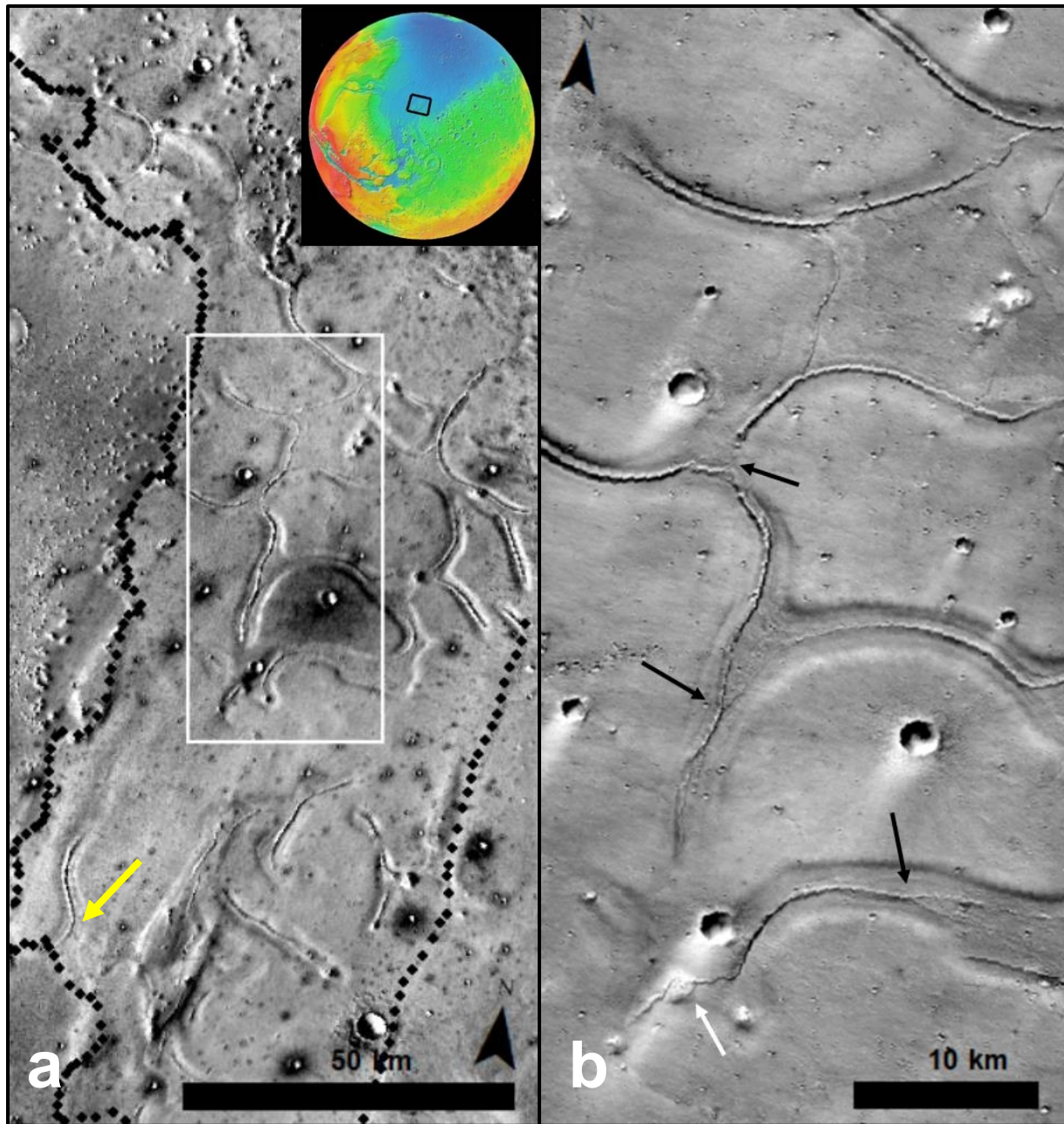


Figure C.26. Location of Site P08-4. a) Context of the terminus of Tiu Valles. Black points indicate mapped Deuteronilus Level by Ivanov et al. (2017). THEMIS-IR day mosaic. Yellow arrow identifies a sinuous ridge that terminates at the Deuteronilus Level margin. b) Zoom in (white box in a) of the ridges with CTX image P21_009089_XN_28N029W. Black arrows indicate bifurcations. White arrow indicates ridge that crosscuts a massif.

C.2.22 Site GZ06-16b

Figure C.27 shows the location of Figure 16b in Ghatan and Zimbelman (2006). This site is characterized by different ridges within the Isidis Interior Plains unit with varying morphologies. A indicates ridges that branch off from a massif and form arcuate paths in opposing directions. B shows relatively short discontinuous ridges trending in a general N-S orientation. C Shows a long and sinuous NE-SW oriented ridge also connected with a massif. An underlying sinuous topographic ridge can also be observed running N-S over the entirety of Figure C.27a. The orientation of ridges at A seem inconsistent with a coastal origin. The ridge at C appears to be a large wrinkle ridge given its sinuosity and presence of similar features in the region. Figure C.27b shows a zoom in of the ridges denoted by B, and at HiRISE scales, they are highly discontinuous and cross cut each other. These features are also found roughly orthogonal to the local Deuteronilus Level and overall are unlikely to be coastal in origin.

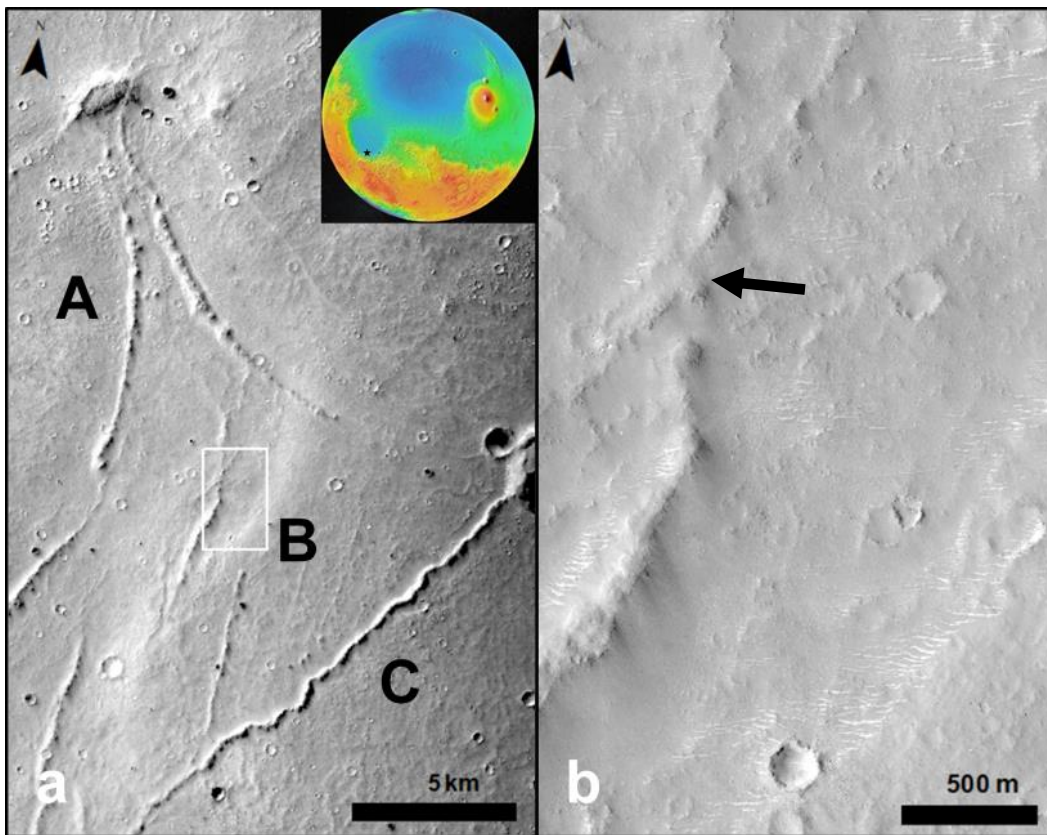


Figure C.27. Location of Site GZ06-16b. Labels A-C indicate different ridge morphologies observed. a) CTX context image B20_017379_1871_XN_07N273W. b) Zoom in of white box in a with HiRISE image ESP_055237_1845. Here the ridges in question are discontinuous and cross cut each other (black arrow).

C.2.23 Site ME99-1c

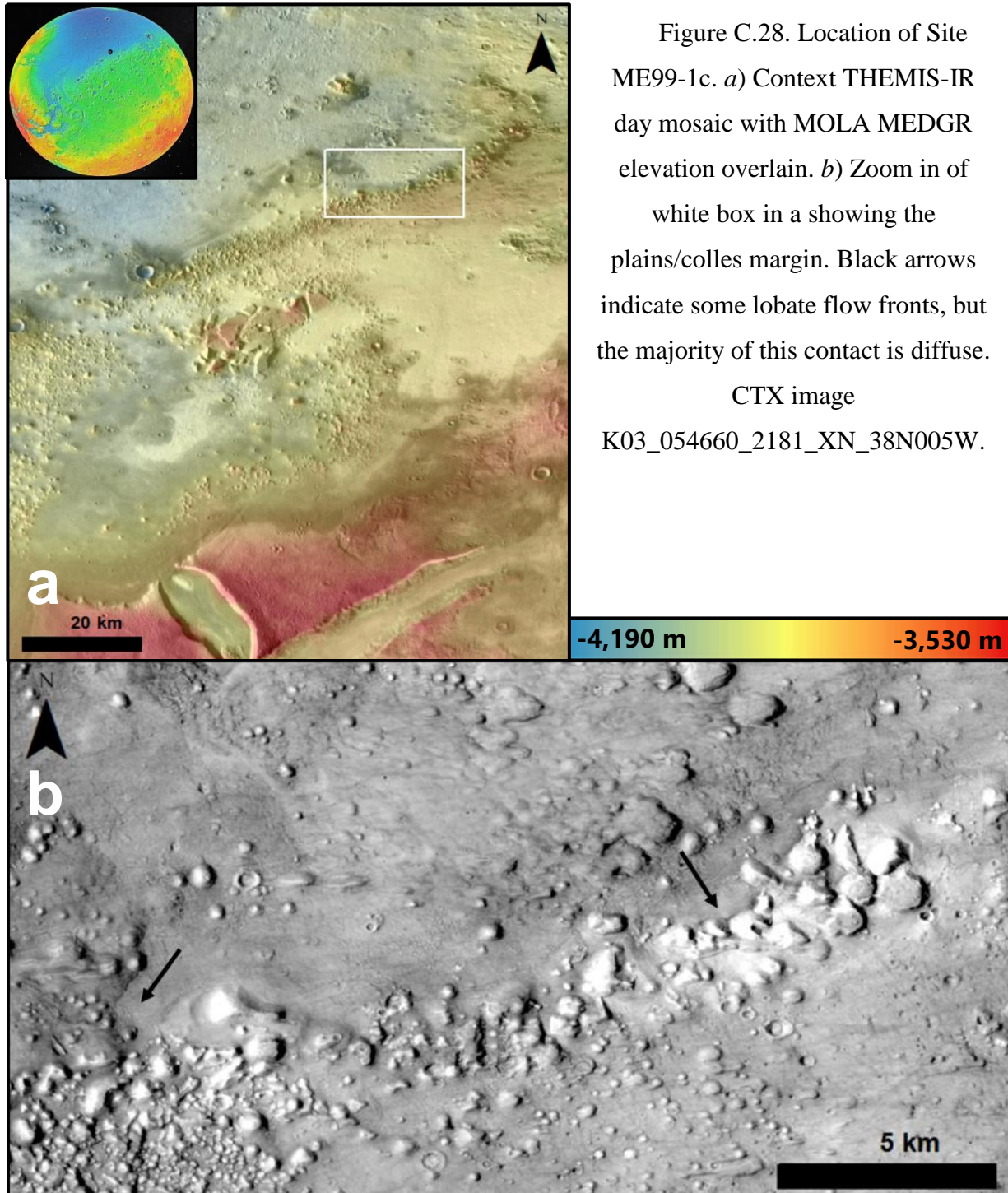
Figure C.28 shows the location of Figure 1c in Malin and Edgett (1999). As opposed to the “classic” lobate flow-front style of the Deuteronilus Level, this site is characterized by a softened gradational transition from the relatively smooth plains unit onlapping a knobby unit. There are a few small lobate flow fronts visible (black arrows) and several partially buried knobs are visible within the plains material suggesting that the deposits are relatively thin along this margin. Malin and Edgett (1999) concluded that due to the south-facing orientation of the lobate flows (opposite what would be expected for a shoreline), this could not be a shoreline. However, this received backlash from Clifford and Parker (2001) and Parker et al. (2010), as the defining characteristic of the Deuteronilus Level are these lobate south-facing flow fronts which could possibly represent more exotic shoreline features (see main text). Yet, we find no convincing evidence of this being an ancient coastline, with this being a contact between the plains-filling unit and a knobby highland unit.

C.2.24 Site ME99-1e

Figure C.29 shows the location of Figure 1e in Malin and Edgett (1999). This site is a mesa within the northern plains that has been interpreted to be an “island” within the ocean. The characteristic features here are the dark-toned lobate flow fronts that onlap the top of the mesae around the entire margin. These features are near identical to the margins of the Deuteronilus Level elsewhere (e.g., Sites P10-12 and P10-15), yet are located ~200 m above the surrounding plains. The mesa is flat-topped with a mean elevation of $-4,200 \pm 10$ m (1σ) and approximates a local equipotential surface. However, compared to the rest of the mapped Deuteronilus Level, the site is ~200 m lower in elevation than the 10% decile range of the Deuteronilus Contact within the Tempe-Chryse-Acidalia-Cydonia-Deuteronilus-Phlegra region (Ivanov et al., 2017).

High-resolution images of the contact itself are provided in Figure C.30. Here, we observe light-toned pitted mounds emanating along fractures from a graben on the southern side of the mesa (white arrows in Figure C.30a). These have been suggested to be mud volcanoes (e.g. Oehler & Allen, 2010; Skinner Jr & Mazzini, 2009) where material have erupted out of the fractures caused by structural collapse of the mesa along its margins. No obvious erosional shoreline features were observed, though we examined the curvilinear ridges on the eastern flank of the mesa for possible terraces (Figure C.30b). TEA was performed but found no evidence of continuous

terraces (either spatially or topographically). Rather, it appears as though these are additional collapse structures associated with the degradation of the mesa. However, none of these features are inherently unique to this location, as elsewhere along the dichotomy the Deuteronilus Level is shown flowing upslope (e.g. Site P08-3) and the putative mud volcanoes are found throughout the northern plains.



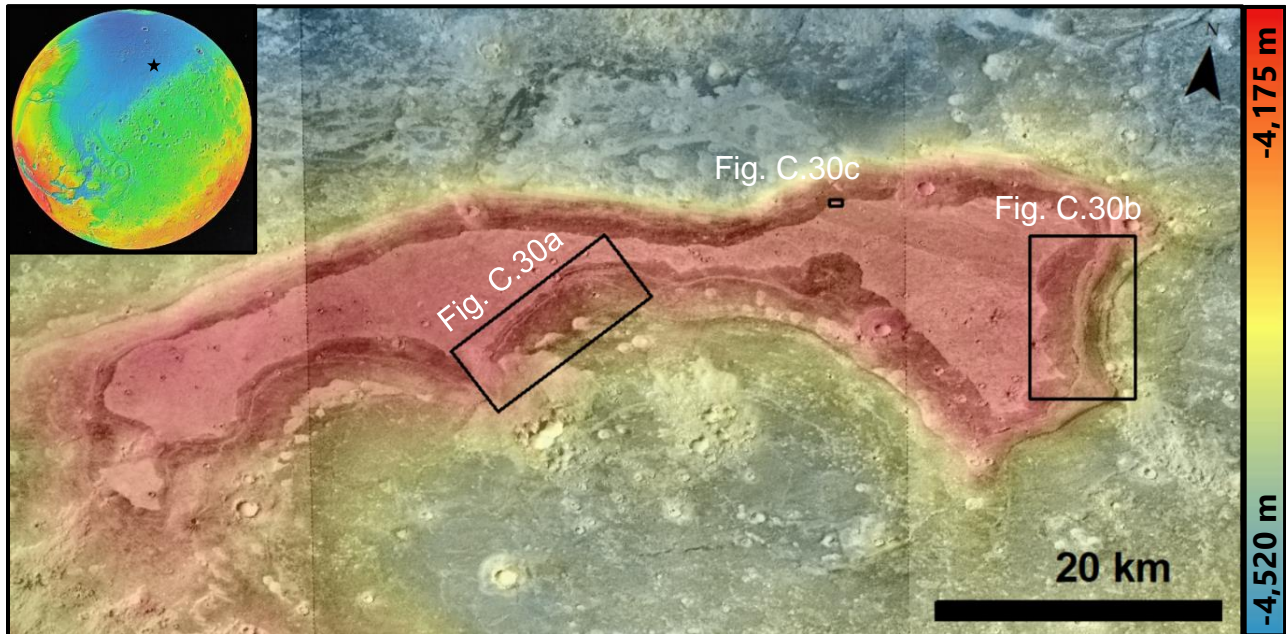


Figure C.29. Location of Site ME99-1e. CTX mosaic with MOLA MEDGR topography overlain. The Deuteronilus Contact is characterized by the dark-toned lobate flows around the top margin of the mesa. Black boxes indicate locations of high-resolution images in Figure C.30.

C.2.25 Site P89-9

Figure C.31 shows the location of Figure 9 in Parker et al. (1989), a typical example of the lobate flows that define the Deuteronilus Level. Here, it appears that there are multiple different flow events that have occurred and overlapped each other. Parker et al. (1989) examined the southern dark-toned lobate flow and later Ivanov et al. (2017) mapped the Deuteronilus Level here using the THEMIS-IR day mosaic (Figure C.31a). However, when we examine the visible CTX images (Figure C.31b), we find that there are different lowland units with varying thermophysical properties and textures which we map (Figure C.31c). The lower unit appears to be a smooth dark-toned flow coming from the north (Unit A) with a lighter-toned thumbprint terrain unit overlapping it and coming from the east (Unit B). Ivanov et al. (2017) generally used the southern boundary of these units as the location of the VBF/Deuteronilus Level, but this omits small underlying flows of Unit A in the northeast. CTX also reveals that the lowland unit to the west of Unit B (Unit C) is lighter-toned in THEMIS-IR day images but has near-identical tone and texture to the adjacent Unit B, which has caused local misidentification of the exact boundaries of the VBF. Due to the

high-density of small impact ejecta in the southwest we are unable to identify whether Unit C? belongs to Units B or C, but the lobate flow fronts at the southern boundary suggest it is part of the VBF.

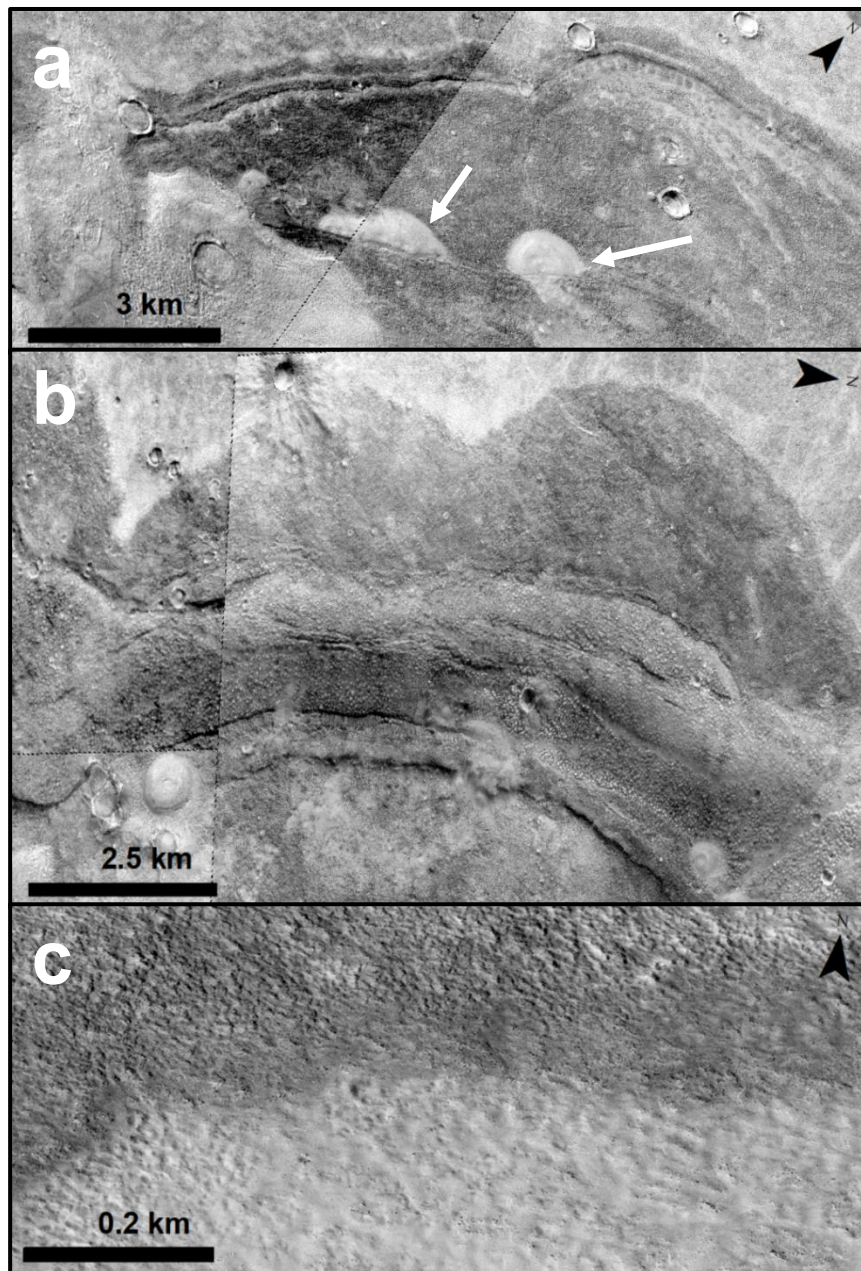


Figure C.30. Zoom in of features located at Site ME99-1e (see Figure C.29 for context). *a*) White arrows indicate pitted light-toned mound found along a graben fracture. There is also a ridge that follows the margin of the dark-toned lobate flows. CTX mosaic. *b*) Curvilinear ridges along the eastern flank of the mesa that appear to be from structural collapse. CTX mosaic. *c*) Zoom in of the contact where the dark-toned deposit onlaps the light-toned mesa top. HiRISE image ESP_046498_2250.

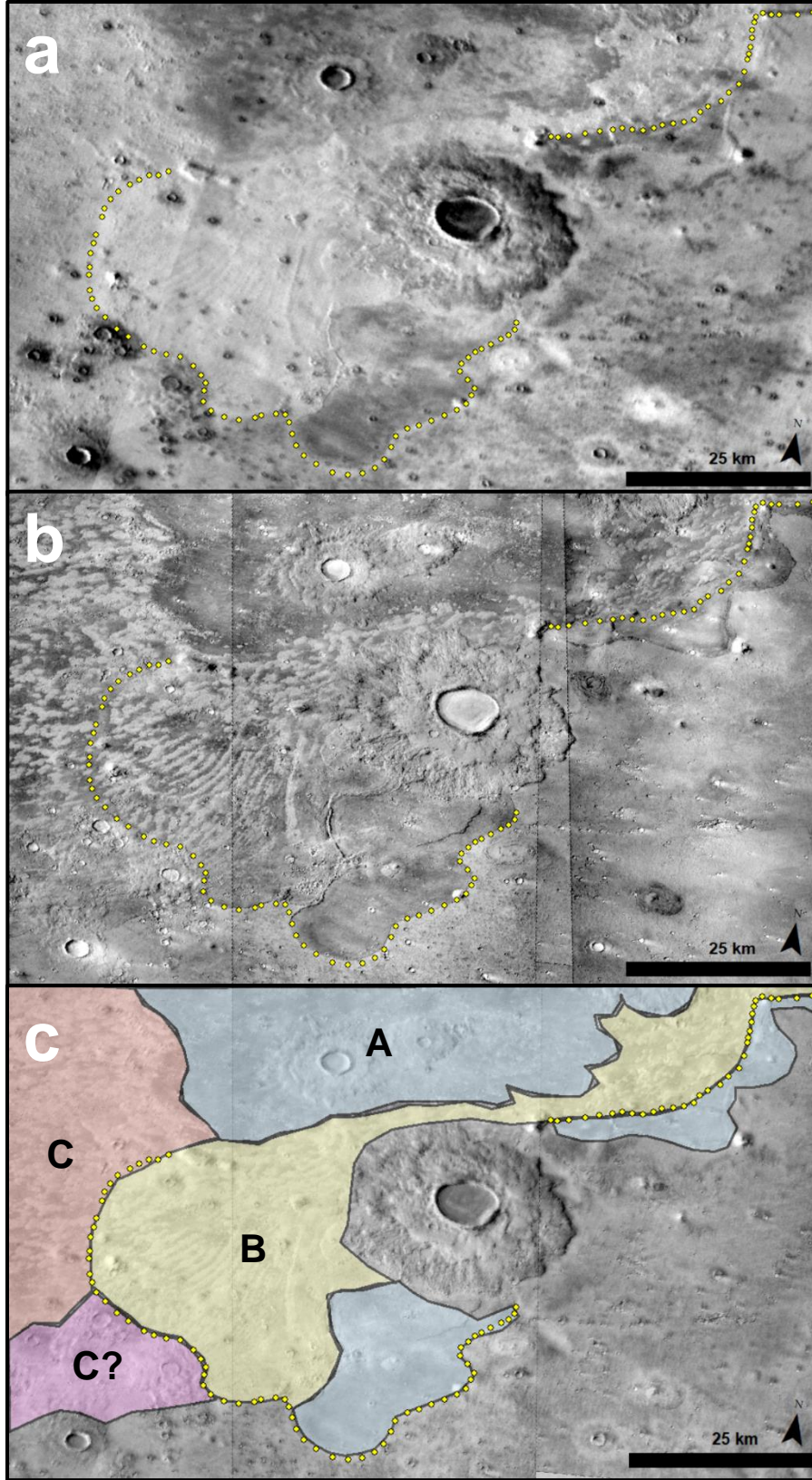


Figure C.31. Location of Site P89-9 (see Figure C.3 for context). *a*) THEMIS-IR day mosaic used by Ivanov et al. (2017) to map the Deuteronilus Level (yellow points). *b*) CTX mosaic. *c*) Our mapped units of the different lobate flows over the CTX mosaic. Unit A: a dark-toned smooth unit. Unit B: thumbprint terrain unit. Unit C: thumbprint terrain unit that is near-identical to Unit B in visible CTX, but appears light-toned in THEMIS-IR day mosaic (not mapped by Ivanov et al., 2017). Unit C?: likely the southern edge of Unit C, but crater ejecta obscure the boundary between Units C and B.

C.2.26 Site P89-11

Figure C.32 shows the location of Figure 11 from Parker et al. (1989). Here, the VBF has flowed into a topographic depression associated with the fretted terrain around Deuteronilus Mensae. The margins of the flow onlap the surrounding highlands and are nearly identical to those seen in Site ME99-1e. Similarly, the VBF has undergone shrinkage and/or topographic lowering equating to ~100-150 m (between the floor of the VBF and the onlapped margins). This is similar to that seen in Site ME99-1e where the margins were ~200 m above the surrounding plains material. Parker et al. (1993) suggested, in reference to the stepped massifs, that loss of volatiles or draining of magma could create the topographic lowering for volcanic features (e.g. steptoes) and that a sedimentary analog could be the desiccation of thick sedimentary layer.

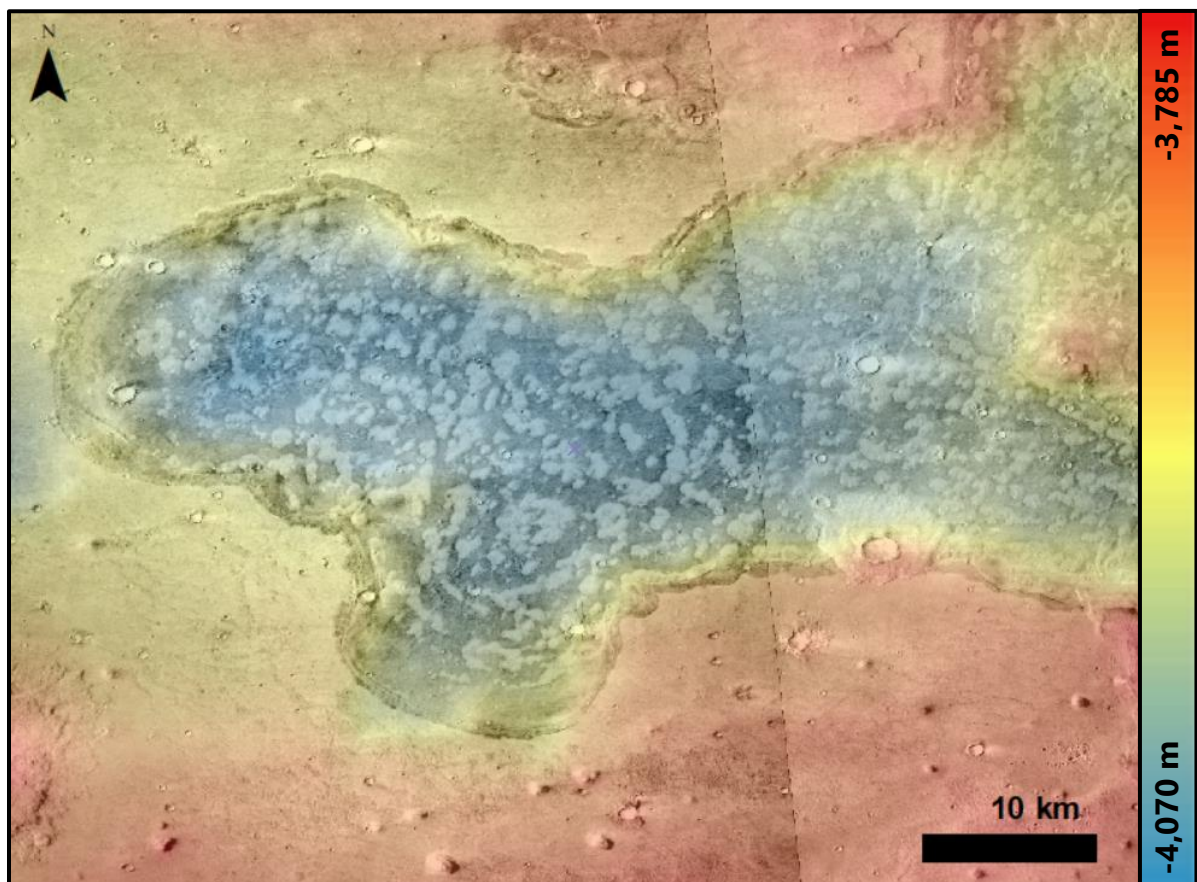


Figure C.32. Location of Site P89-11 (see Figure C.3 for context). Here, the VBF flows into a small fret canyon. CTX images F22_044480_2251_XI_45N352W and P18_007901_2250_XN_45N351W with MOLA MEDGR elevation data overlain.

C.2.27 Site GZ06-15a

Figure C.33a shows the location of Figure 15a in Ghatan and Zimbelman (2006). Here, the VBF-like unit of the Isidis Basin onlaps onto a knobby unit with curvilinear features (white arrows) paralleling the margin of the Deuteronilus Level (black arrows). However, when zoomed in, the features dissolve into the terrain, and no longer identifiable (Figure C.33b). These are likely tonal variations on the surface of the unit.

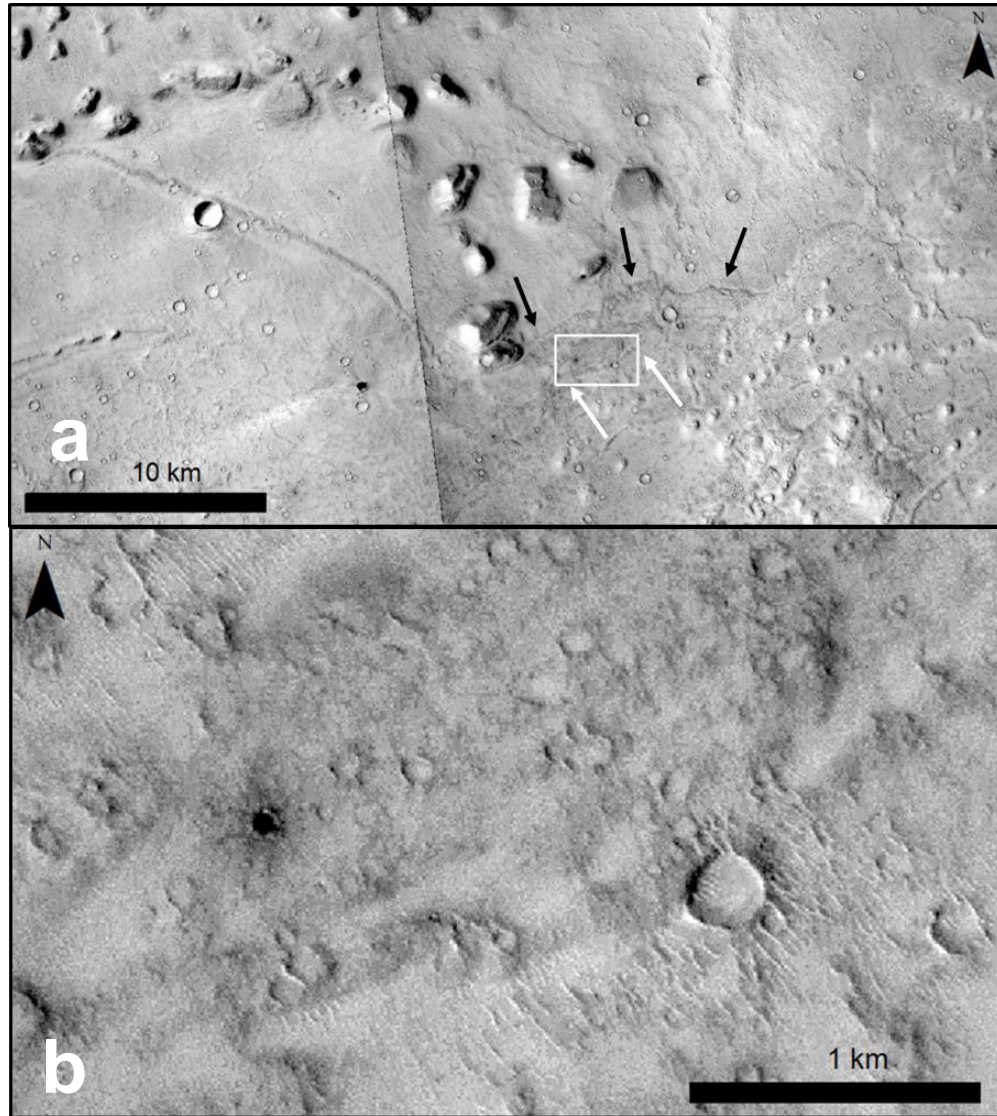


Figure C.33. Location of Site GZ06-15a (see Figure C.2 for context). Here the Isidis Basin VBF-like unit (Ivanov et al. 2017) onlaps the surrounding knobby highlands. *a*) Black arrows show the mapped Deuteronilus Level, white arrows show the candidate coastal ridge features. CTX mosaic. *b*) Zoom in of white box in *a*. CTX image P06_003244_1975_XN_17N279W.

C.2.28 Site GZ06-15f

Figure C.34 shows the location of Figure 15f from Ghatan and Zimelman (2006). This is a typical example of the lobate flow fronts of the VBF and Deuteronilus Level. The margins of the flows often have arcuate ridges that parallel the sides.

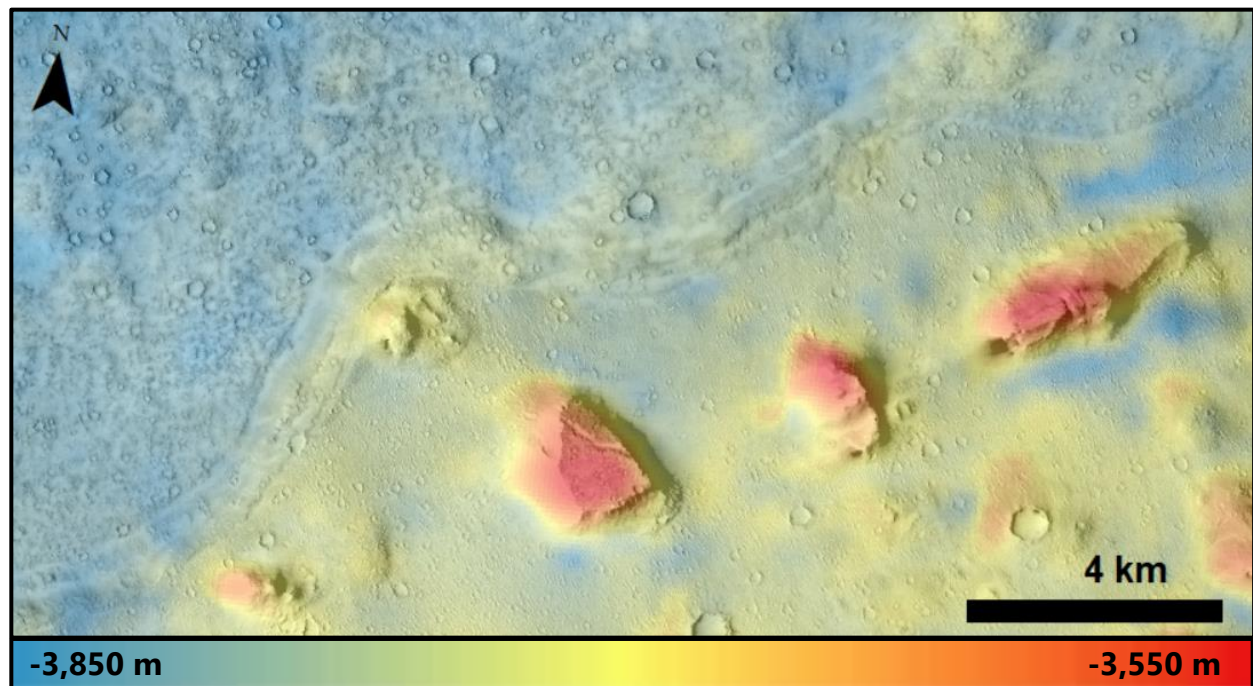


Figure C.34. Location of Site GZ06-15f (see Figure C.3 for context). This is a typical example of the lobate flow fronts that define the Deuteronilus Level. CTX image G06_020412_1953_XN_15N279W with HRSC topography (H5234_0000_DT4) overlain.

C.2.29 Site P08-3

Figure C.35 shows the location of Figure 3 in Parker (2008). Here, the VBF flows upslope through Mamers Valles in Deuteronilus Mensae and resembles a viscous lava or debris flow. Interior of the Deuteronilus Level here is the thumbprint terrain. A ridge parallels the margin of the flow, and HiRISE imagery shows that the ridge is dense with boulders (Figure C.35b).

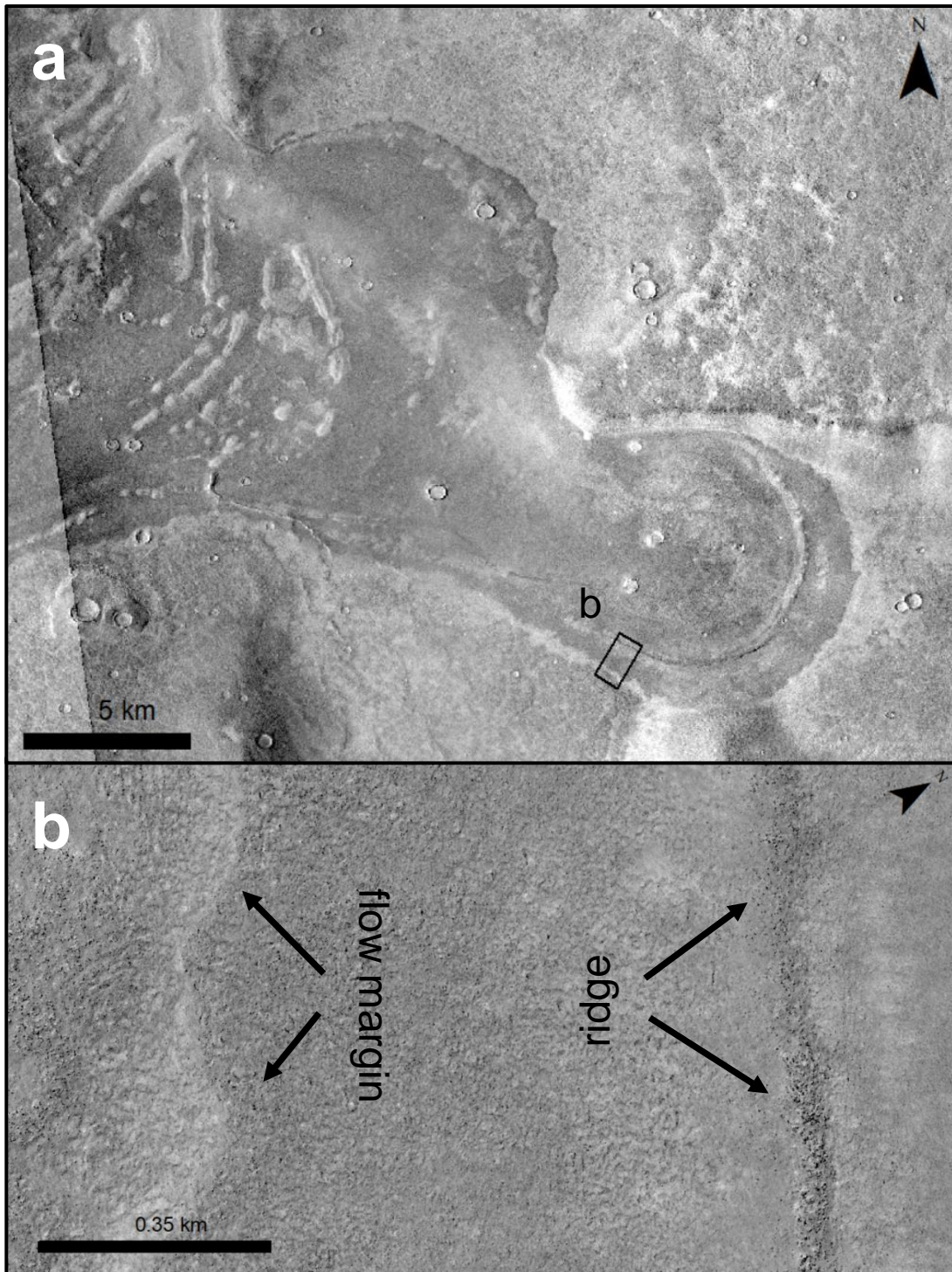


Figure C.35. Location of Site P08-3 (see Figure C.1 for context). *a*) CTX image B18_016498_2264_XI_46N345W showing the lobate flows of the Deuteronilus Level (upslope is to the south). *b*) HiRISE image ESP_016498_2265 showing the details of the flow margin and the boulder-dense ridge.

C.2.30 Site P10-12

Figure C.36 shows the location of Figure 12 in Parker et al. (2010). Here, there are two different lowland units, a smooth dark toned unit (blue here) similar to Unit A mapped in Site P89-9, and a narrow unit that onlaps the highlands with characteristic thumbprint terrain (yellow here) similar to Units B and C in Site P89-9. Parker et al. (2010) describe these as two different levels: the Deuteronilus Level which follows the southern edge of the yellow-mapped unit here; and the Acidalia Level which follows the southern edge of the blue-mapped unit here. Fluid from the yellow unit also appears to have infilled a crack and topographic depression within the highlands.

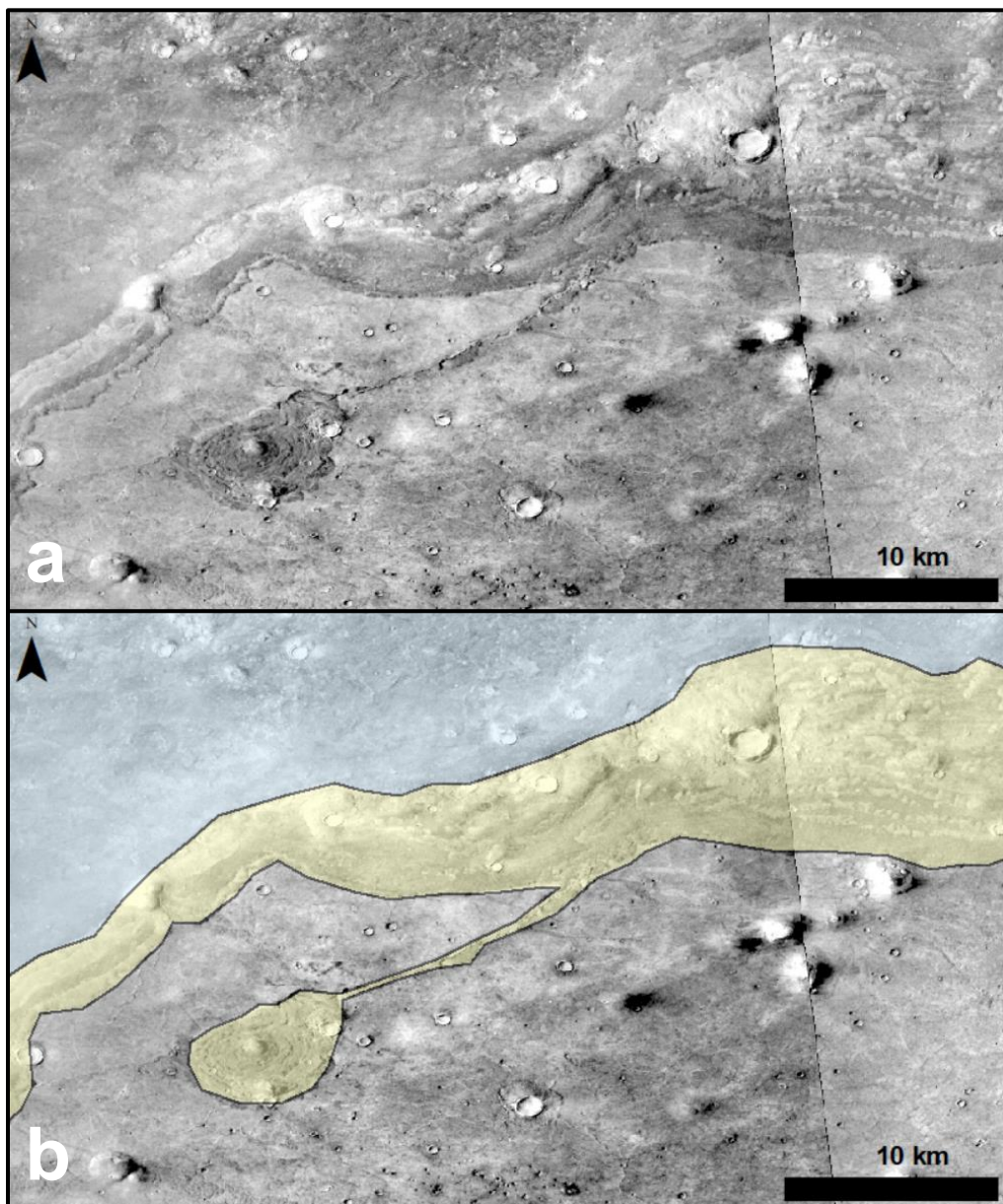


Figure C.36. Location of Site P10-12 (see Figure C.3 for context). *a*) CTX mosaic showing the different margins associated with flow events. *b*) Our mapped units that show the boundaries, which are distinct in both CTX and THEMIS-IR day.

C.2.31 Site P10-13

Figure C.37 shows the location of Figure 13 in Parker et al. (2010). This site is adjacent to Site P89-11 (see context image Figure C.3), but appears to have two different units (a smooth dark unit that onlaps the southern highlands and a thumbprint terrain unit that onlaps the smooth dark unit). However, the embayment relationships of these units appears to be opposite that of Site P10-12. This suggests that either there were multiple flows of each unit type (and thus >2 events for this region) or this dark-toned unit is an extension of the thumbprint terrain unit but does not produce the thumbprint terrain (possibly due to thickness of the unit along this margin). THEMIS-IR day images show that the dark-toned unit is also darker-toned in IR, suggesting two possible units, but due to the resolution and limited extent of this unit, it is unclear. Like Site P10-12, the fluid appears to have filled an irregular fracture along the margin.

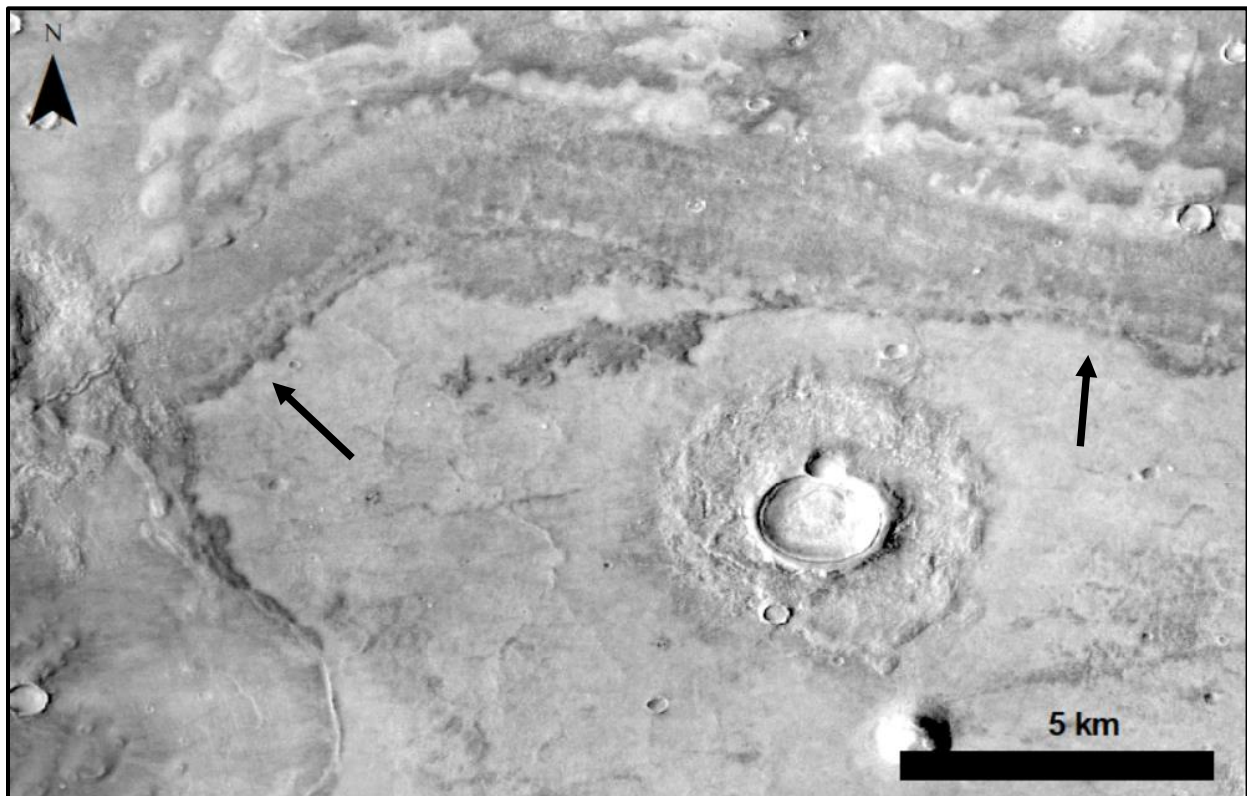


Figure C.37. Location of Site P10-13 (see Figure C.3 for context). CTX image P18_008046_2253_XN_45N350W. Arrows indicate the Deuteronilus Level mapped by Ivanov et al. (2017).

C.2.32 Sites P10-15 and P10-16

Figure C.38 shows the location of Figure 15 in Parker et al. (2010), which is also the location of Figure 10 in Parker et al. (1989). Here the Deuteronilus Level fills in topographic lows around a plateaued surface (white arrows). We mark with white arrows a depression that was filled with dark-toned material and appears to underly the dominant local thumbprint terrain unit (black arrows). This site was also investigated for dark-toned NW-SE streaks that begin at knobs and are cut off by the Deuteronilus Level. Parker et al. (2010) suggested that these features were formed by an ice-covered ocean where tears in the ice moved past immovable knobs and subsequent refreezing/sublimation of the water from the debris and ice cover preserved the streaks as pseudomorphs. However, when we zoom into the CTX image, the streaks are much more jagged, with some branches perpendicular to the overall orientation of the streaks (Figure C.38b). It is unclear how these streaks formed.

Figure C.39 shows the location of Figure 16 in Parker et al. (2010), which is on the opposite side of the Deuteronilus Level in Figure C.38 (i.e. to the southeast). Here are more streaks, some of which have kinks along track, and others crosscut the underlying dark-toned lobate flows (black arrow). This suggests that the streaks formed after the local dark-toned lobate flows.

C.2.33 Site ME99-1a

Figure C.40 shows the location of Figure 1a in Malin and Edgett (1999). This is a section of the northern extent of the Olympus Mons aureole with no coastal landforms present. Modern maps of the putative paleoshorelines generally no longer include the boundary between the aureole and northern plains (see main text), but we include it for completeness on the history of possible candidate coastal features.

C.2.34 Site GZ06-12a

Figure C.41 shows the location of Figure 12a in Ghatan and Zimbelman (2006). A pair of papers has recently provided a detailed analysis of these features located near the terminus of Hypanis Valles (Adler et al., 2019; Fawdon et al., 2018). They determined that these may be part of a delta or alluvial fan complex and the features here are exposed layers (as opposed to stacked ridges investigated by Ghatan and Zimbelman, 2006).

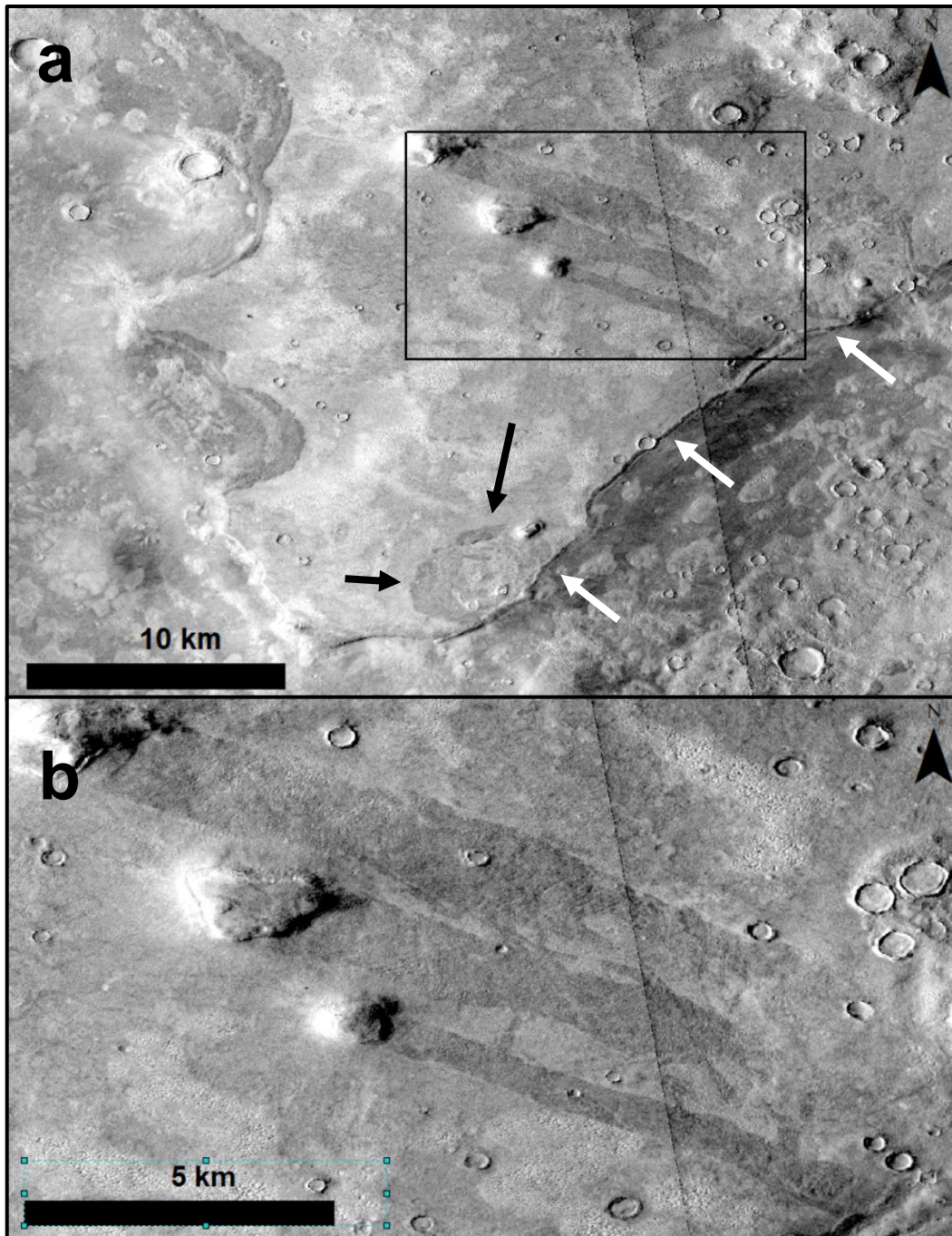


Figure C.38. Location of Site P10-15 (see Figure C.3 for context). CTX images P20_008916_2249_XN_44N348W and B01_010195_2277_XN_47N347W. *a*) White arrows indicate the Deuteronilus Level mapped by Ivanov et al. (2017). Black arrows show an underlying flow front. *b*) Zoom in of the knob streaks showing jagged and irregular expressions and different lengths.

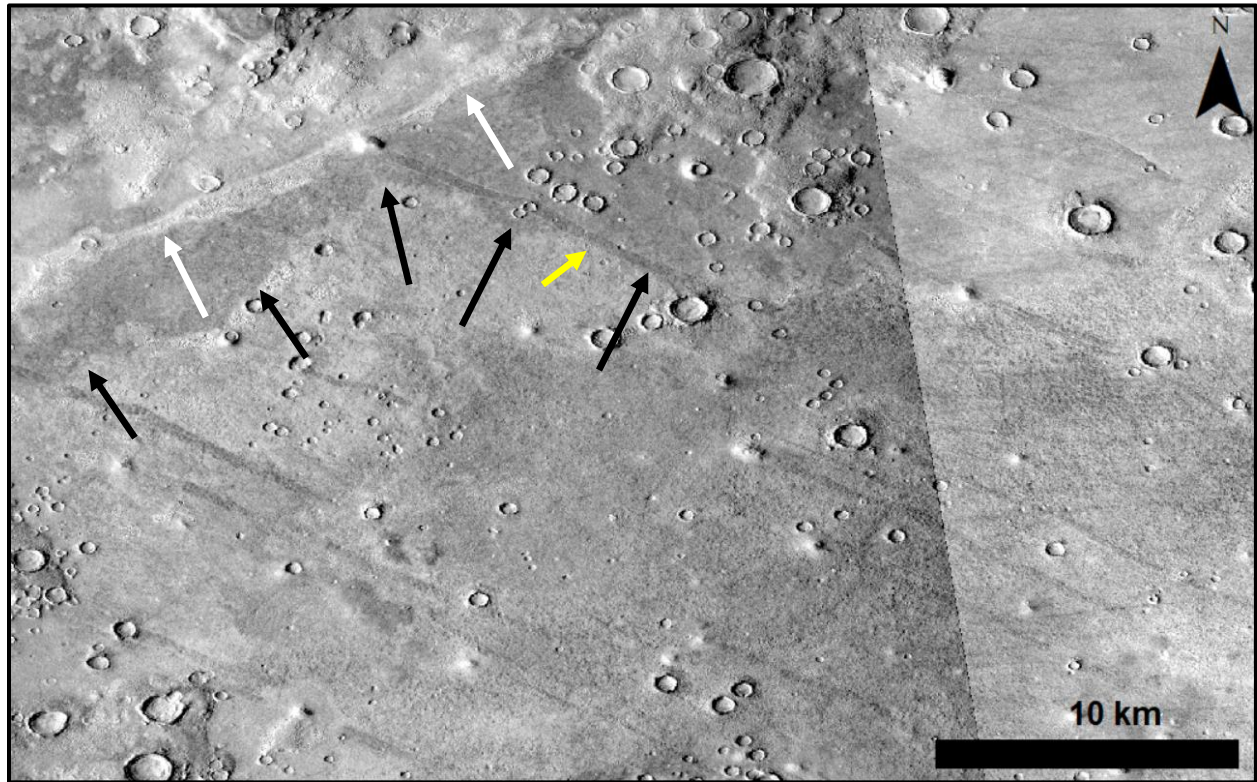


Figure C.39. Location of Site P10-16 (see Figure C.3 for context). CTX images B05_011685_2274_XI_47N347W and B01_010195_2277_XN_47N347W. Yellow arrow indicates a knob streak that crosscuts the dark-toned flow unit (black arrows as in Figure C.38) which is embayed by the thumbprint terrain unit (white arrows as in Figure C.38).

C.2.35 Site P89-6

Figure C.42 shows the location of Figure 6 in Parker et al. (1989). This site was one of the original areas used to define the Arabia Level, where a dark-toned unit embays the southern highlands near Semeykin Crater. However, this site has since been reexamined with high resolution data which suggests that this dark-toned unit are the deposits from outflow channels (sourced from much further inland to the south) (Mangold & Howard, 2013). Our analysis agrees with this assessment, especially given the terminal outflow channels. Additionally, Parker et al. (1989) observed that the Arabia Level unit flowed down into Semeykin Crater, but topographic data, MOLA and HRSC, show the opposite is true, further supporting the outflow channel ponding hypothesis. We find no morphologies to suggest the lowlands were occupied with liquid water when the deposits were laid down (e.g. deltas).

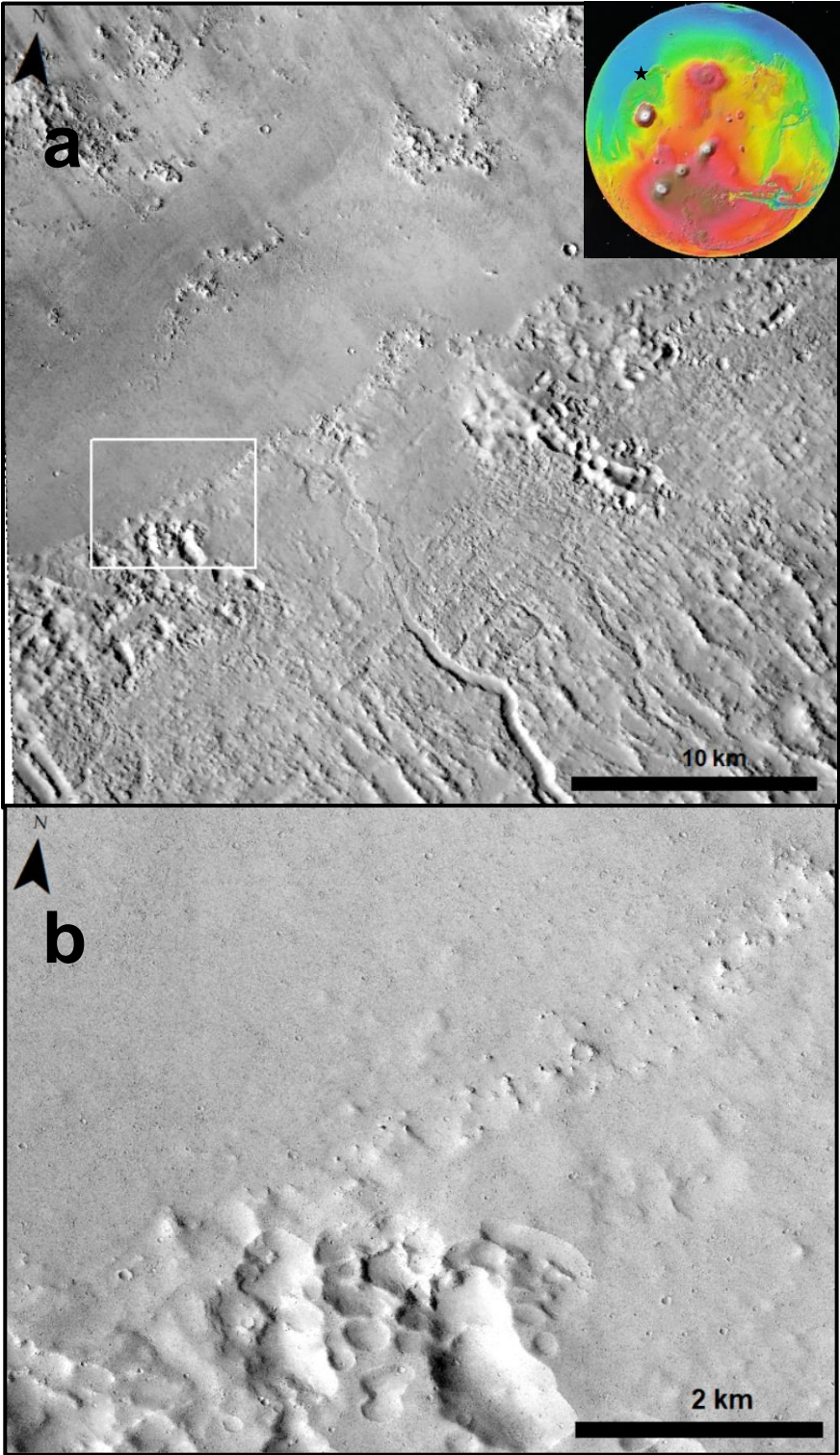


Figure C.40. Location of Site ME99-1a. a) CTX image F04_037470_2129_XI_32N145W showing the boundary between the Olympus Mons aureole and the northern plains. b) Zoom in of the boundary showing scalloped terrain. HiRISE image PSP_007498_2130. No coastal landforms present.

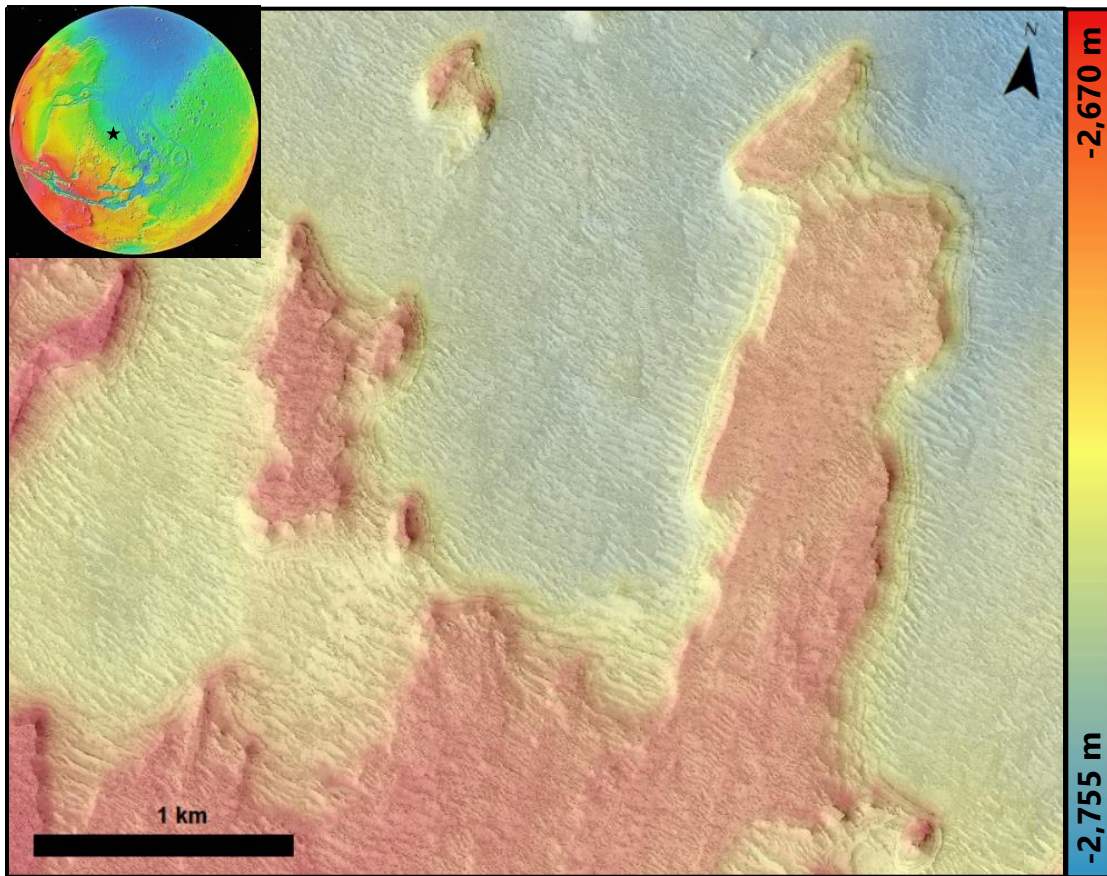


Figure C.41. Location of Site GZ06-12a. Multiple stacked lineaments surround the margins of the plateau; however these are revealed to be exposed layers of a possible delta or alluvial fan. Such a delta would have been deposited in the northern plains which would possibly support an ocean hypothesis, though the authors could not rule out that these may be alluvial fan deposits. Elevation data from DTEEC_022434_1920_021577_1920_L01.

C.2.36 Site P10-9

Figure C.43 shows the location of Figure 9 in Parker et al. (2010). This is where the putative Arabia Level meets a fret canyon near Mamers Valles. The Arabia Level here is defined by the stark tonal contrast observed in THEMIS-IR day imagery, but a diffuse boundary can be seen in visible CTX. Parker et al. (2010) suggested that the Arabia Level continues southward up the fret canyon and that the fret canyon wall is more rounded north of the level (topographically lower) compared to the sharper wall south of the level. We find no such distinction. Topographic data shows little to no slope along the Arabia Level.

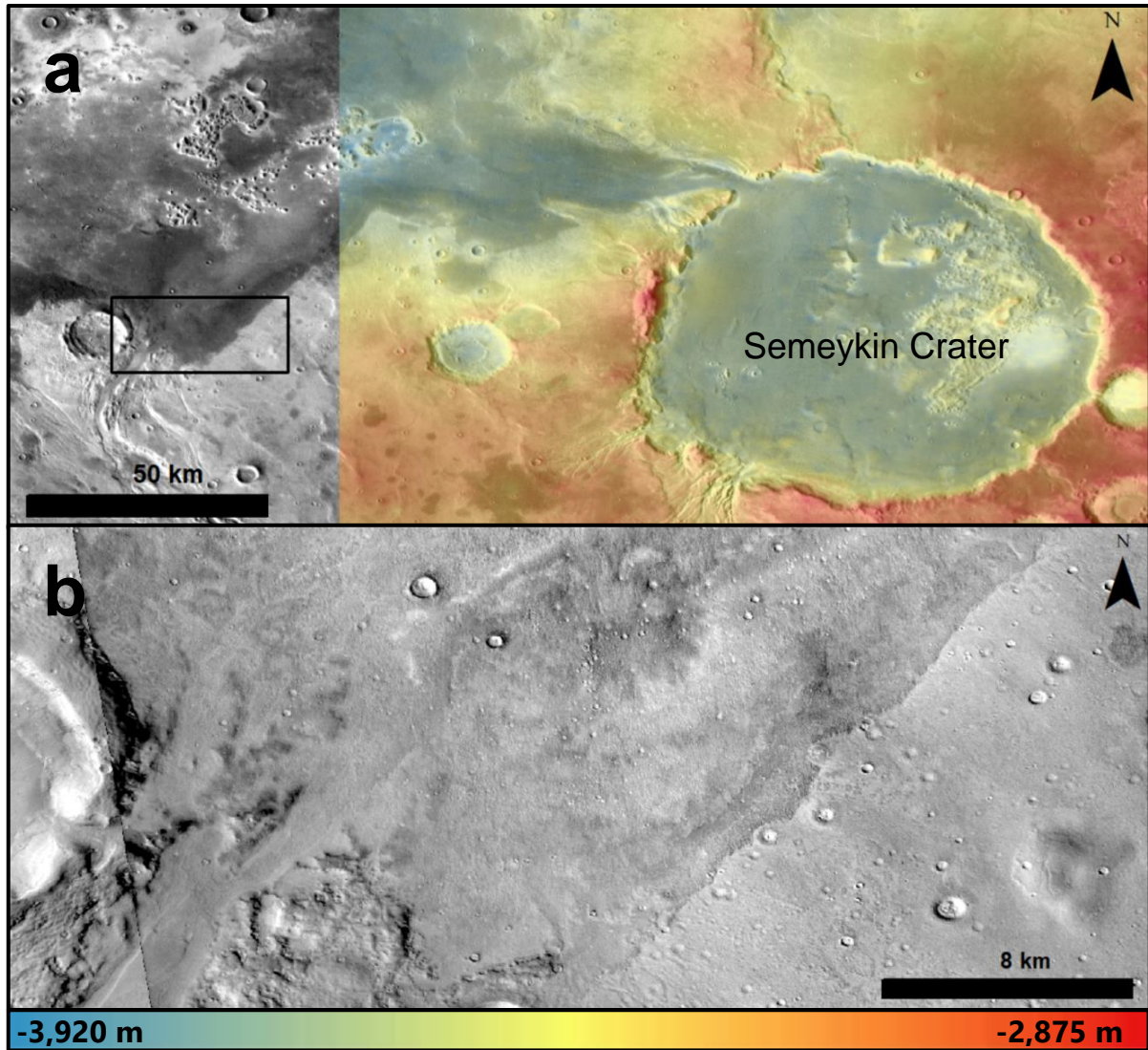


Figure C.42. Location of Site P89-6. Here the Arabia Level is characterized as a dark-toned deposit that onlaps the southern highlands (white arrows) near Semeykin Crater. *a*) THEMIS-IR day mosaic with HRSC topography (H1582_0000_DT4). These deposits have since been interpreted to be the end result of outflow channels and overland flow originating further south in Ismenius Lacus (Mangold & Howard, 2013). *b*) Zoom in of the contact by one of the outflow channels. No coastal landforms are observed.

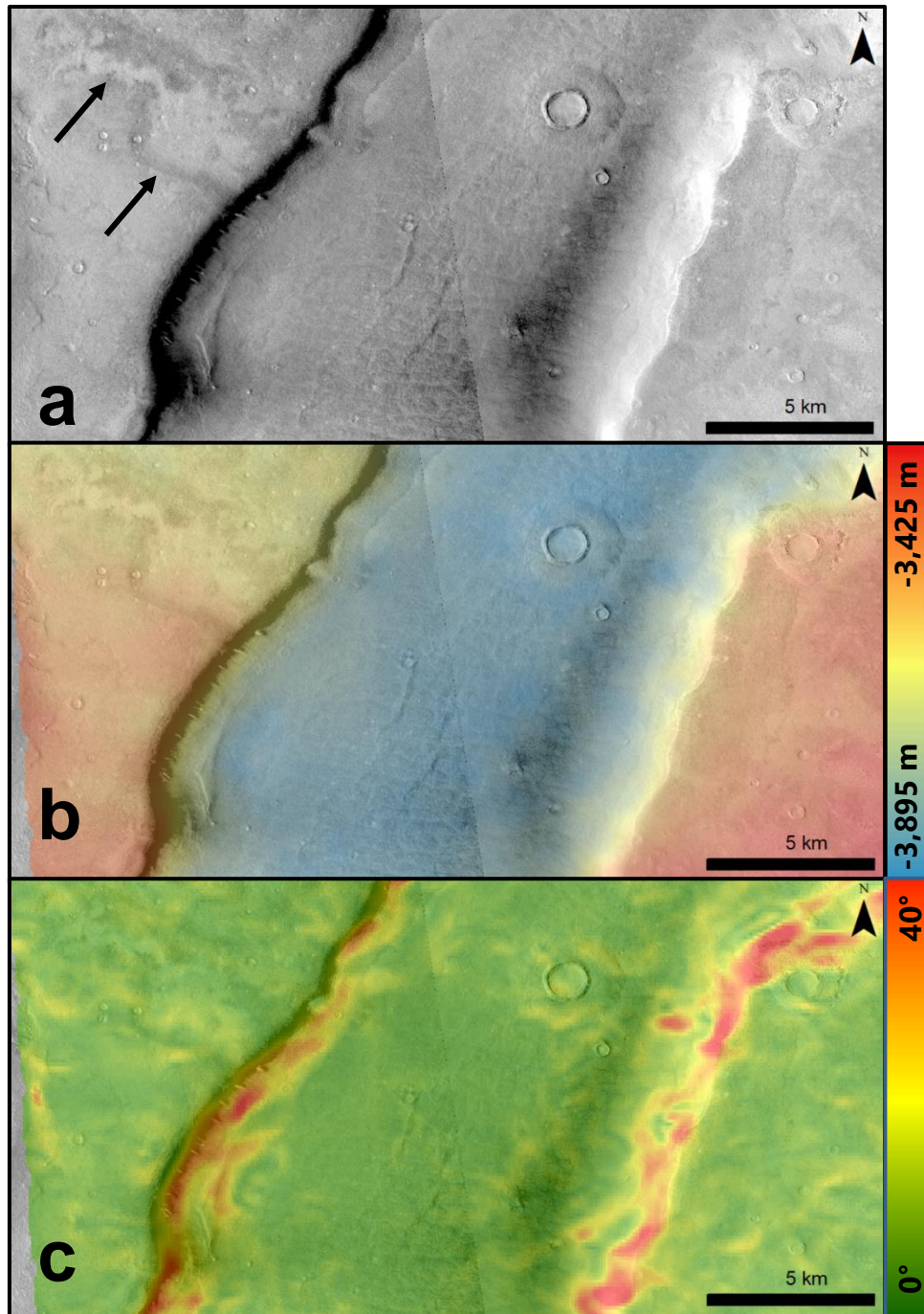


Figure C.43. Location of Site P10-9 (see Figure C.1 for context). CTX images B19_016999_2240_XN_44N343W and P17_007492_2261_XN_46N344W. *a*) CTX image with black arrows indicating the Arabia Level tonal contact. *b*) HRSC elevation data (H3304_0000_DT4). *c*) Slope map based off HRSC elevation data. The Arabia Level appears to simply be a tonal contact, possibly exposed lithological units exhumed during the breakup of the highlands and formation of fret canyons.

C.2.37 Site W04-9e

Figure C.44 shows the location of Figure 9e in Webb (2004). Ivanov et al. (2017) did not map the Deuteronilus Level here, but Webb (2004) misidentifies the contact, as the Deuteronilus Level is well mapped and identified as lobate flow fronts that onlap the surrounding terrain while this is a debris apron or platform extending from the massif unit (with the opposite escarpment direction of the Deuteronilus Level). The surface between the massifs have lineations which may be indicative of glacial processes. The Arabia Level is identified here as lineaments along the tops of the massifs, but in HiRISE imagery (Figure C.44c) these appear as diffuse tonal boundaries suggesting weathering of different lithologic units with varying physical properties. No coastal landforms are observed.

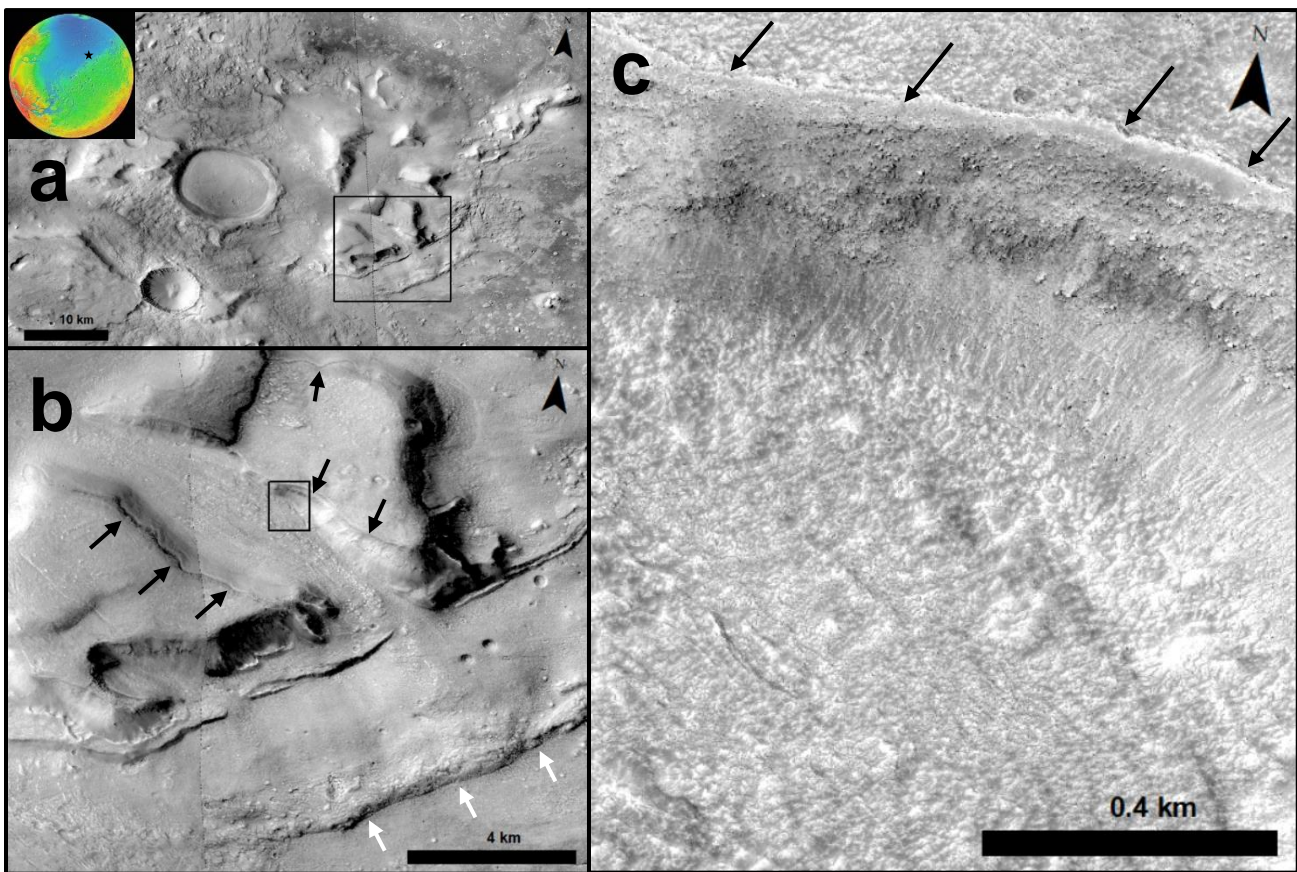


Figure C.44. Location of Site W04-9e. *a*) CTX mosaic showing the general region of the site, small massif unit. *b*) Zoom in of black box in *a* showing the Arabia Level (black arrows) and Deuteronilus Level (white arrows) as indicated by Webb (2004). *c*) Zoom in of the Arabia Level with HiRISE image ESP_017145_2200. Black arrows indicate the putative Arabia Level.

C.2.38 Site GZ06-15b

Figure C.45 shows the location of Figure 15b in Ghatan and Zimbelman (2006). In the main text this is listed as an “Uncertain” feature as there have been no resolution improvements since the 2001 MOC NA image analyzed by Ghatan and Zimbelman (2006). However, these features are unlikely to be marine coastal ridges. Elevation data shows that the features are ~200 m below the topographic divide between Isidis Basin and the northern plains indicating they are not from a hemispheric ocean (though they could possibly be from an Isidis Basin sea). Additional smaller ridges can be seen branching off the main ridge and subsequently forking in two (see black arrow in Figure C.45c). There are no obvious or unambiguous landforms here to suggest a coastal origin.

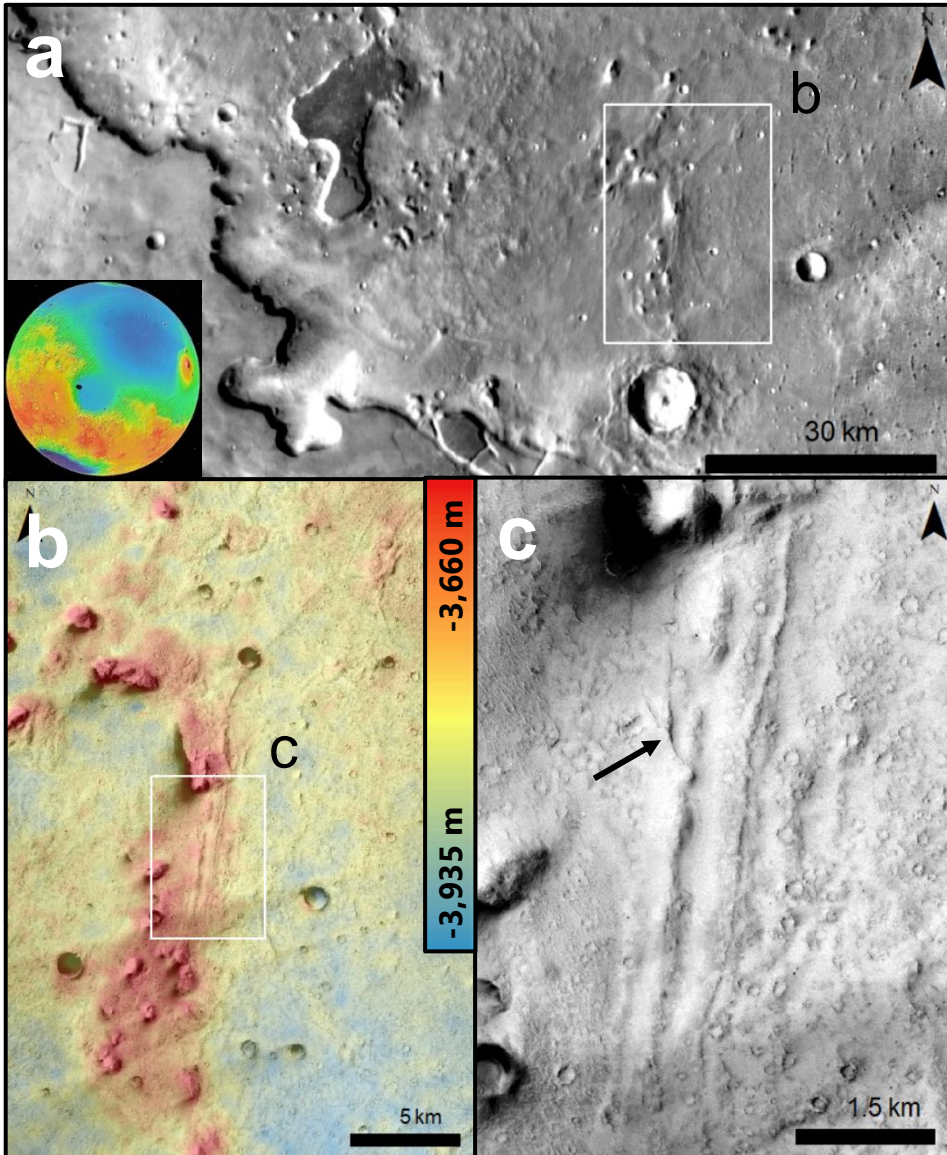


Figure C.45. Location of Site GZ06-15b. CTX image B21_017933_1943_XN_14N280W. a) THEMIS-IR day mosaic showing the context for the features in southwest Isidis Basin. b) HRSC topographic overlay (H5234_0000_DT4). c) Zoom in of the ridges. Black arrow indicates a forked branch of a smaller ridge.

BIBLIOGRAPHY

- Abelson, P. H. (1966). Chemical events on the primitive Earth. *Proceedings of the National Academy of Sciences*, 55, 1365. doi:10.1073/pnas.55.6.1365
- Adler, J. B., Bell III, J. F., Fawdon, P., Davis, J., Warner, N. H., Sefton-Nash, E., & Harrison, T. N. (2019). Hypotheses for the origin of the Hypanis fan-shaped deposit at the edge of the Chryse escarpment, Mars: Is it a delta? *Icarus*, 319, 885-908. doi:10.1016/j.icarus.2018.05.021
- Amador, E. S., & Bandfield, J. L. (2016). Elevated bulk-silica exposures and evidence for multiple aqueous alteration episodes in Nili Fossae, Mars. *Icarus*, 276, 39-51. doi:10.1016/j.icarus.2016.04.015
- Atkinson, R., Baulch, D., Cox, R., Crowley, J., Hampson, R., Hynes, R., et al. (2004). Evaluated kinetic and photochemical data for atmospheric chemistry: Volume I-gas phase reactions of O x, HO x, NO x and SO x species. *Atmospheric chemistry and physics*, 4(6), 1461-1738. doi:10.5194/acp-4-1461-2004
- Atwood, G. (2006). *Shoreline superelevation: evidence of coastal processes of Great Salt Lake, Utah*. (Thesis), Utah Geological Survey,
- Baker, D. M., & Head, J. W. (2015). Extensive Middle Amazonian mantling of debris aprons and plains in Deuteronilus Mensae, Mars: Implications for the record of mid-latitude glaciation. *Icarus*, 260, 269-288. doi:10.1016/j.icarus.2015.06.036
- Baker, D. M., Head, J. W., & Marchant, D. R. (2010). Flow patterns of lobate debris aprons and lineated valley fill north of Ismeniae Fossae, Mars: Evidence for extensive mid-latitude glaciation in the Late Amazonian. *Icarus*, 207(1), 186-209. doi:10.1016/j.icarus.2009.11.017
- Baker, V. R., Strom, R. G., Gulick, V. C., Kargel, J. S., Komatsu, G., & Kale, V. S. (1991). Ancient oceans, ice sheets and the hydrological cycle on Mars. *Nature*, 352(6336), 589-594. doi:10.1038/352589a0
- Bakken, L. R. (1985). Separation and purification of bacteria from soil. *Applied and Environmental Microbiology*, 49(6), 1482-1487.
- Bandfield, J. L., Amador, E. S., & Thomas, N. H. (2013). Extensive hydrated silica materials in western Hellas Basin, Mars. *Icarus*, 226(2), 1489-1498. doi:10.1016/j.icarus.2013.08.005
- Banfield, D., Donelan, M., & Cavaleri, L. (2015). Winds, waves and shorelines from ancient martian seas. *Icarus*, 250, 368-383. doi:10.1016/j.icarus.2014.12.001
- Bar-Nun, A., & Chang, S. (1983). Photochemical reactions of water and carbon monoxide in Earth's primitive atmosphere. *Journal of Geophysical Research*, 88, 6662-6672. doi:10.1029/JC088iC11p06662
- Bar-Nun, A., & Hartman, H. (1978). Synthesis of organic compounds from carbon monoxide and water by UV photolysis. *Origins of Life*, 9, 93-101. doi:10.1007/BF00931407
- Bar-On, Y. M., Phillips, R., & Milo, R. (2018). The biomass distribution on Earth. *Proceedings of the National Academy of Sciences*, 201711842. doi:10.1073/pnas.1711842115
- Basco, N., & Pearson, A. (1967). Reactions of sulphur atoms in presence of carbon disulphide, carbonyl sulphide and nitric oxide. *Transactions of the Faraday Society*, 63, 2684-2694. doi:10.1039/TF9676302684
- Batalha, N., Domagal-Goldman, S. D., Ramirez, R., & Kasting, J. F. (2015). Testing the early Mars H₂-CO₂ greenhouse hypothesis with a 1-D photochemical model. *Icarus*, 258, 337-349. doi:10.1016/j.icarus.2015.06.016
- Baulch, D. (1976). *Evaluated Kinetic Data for High Temperature Reactions. Vol. 3: Homogeneous Gas Phase Reactions of the CO-O₂-H₂ System and of Sulphur Containing Species*: Butterworths.
- Bear, A. N., & Cas, R. A. F. (2007). The complex facies architecture and emplacement sequence of a Miocene submarine mega-pillow lava flow system, Muriwai, North Island, New Zealand. *Journal of Volcanology and Geothermal Research*, 160(1), 1-22. doi:10.1016/j.jvolgeores.2006.09.002
- Beatty, D. W., Clifford, S. M., Borg, L. E., Catling, D. C., Craddock, R. A., Des Marais, D. J., et al. (2005). Key science questions from the second conference on early Mars: geologic, hydrologic, and climatic evolution and the implications for life. *Astrobiology*, 5(6), 663-689. doi:10.1089/ast.2005.5.663
- Becerra, P., Byrne, S., Sori, M. M., Sutton, S., & Herkenhoff, K. E. (2016). Stratigraphy of the north polar layered deposits of Mars from high-resolution topography. *Journal of Geophysical Research: Planets*, 121(8), 1445-1471. doi:10.1002/2015JE004992
- Bibring, J.-P., Langevin, Y., Gendrin, A., Gondet, B., Poulet, F., Berthe, M., et al. (2005). Mars surface diversity as revealed by the OMEGA/Mars Express observations. *Science*, 307(5715), 1576-1581. doi:10.1126/science.1108806

- Bibring, J.-P., Langevin, Y., Mustard, J. F., Poulet, F., Arvidson, R., Gendrin, A., et al. (2006). Global Mineralogical and Aqueous Mars History Derived from OMEGA/Mars Express Data. *Science*, 312(5772), 400-404. doi:10.1126/science.1122659
- Boisson, J., Heggy, E., Clifford, S. M., Yoshikawa, K., Anglade, A., & Lognonne, P. (2011). Radar sounding of temperate permafrost in Alaska: Analogy to the Martian midlatitude to high-latitude ice-rich terrains. *Journal of Geophysical Research: Planets*, 116(E11), E11003. doi:10.1029/2010JE003768
- Bottke, W. F., Nolan, M. C., Greenberg, R., & Kolvoord, R. A. (1994). Velocity distributions among colliding asteroids. *Icarus*, 107(2), 255-268. doi:10.1006/icar.1994.1021
- Bourgeois, J. (2009). Geologic effects and records of tsunamis. In A. R. Robinson & E. N. Bernard (Eds.), *The sea* (Vol. 15, pp. 53-91). Cambridge: Harvard University Press.
- Bradley, J. A., Amend, J. P., & LaRowe, D. E. (2018). Bioenergetic Controls on Microbial Ecophysiology in Marine Sediments. *Frontiers in microbiology*, 9, 180. doi:10.3389/fmicb.2018.00180
- Bratbak, G., & Dundas, I. (1984). Bacterial dry matter content and biomass estimations. *Applied and Environmental Microbiology*, 48(4), 755-757.
- Breuer, D., & Spohn, T. (2006). Viscosity of the Martian mantle and its initial temperature: Constraints from crust formation history and the evolution of the magnetic field. *Planetary and Space Science*, 54(2), 153-169. doi:10.1016/j.pss.2005.08.008
- Brown, K. A., & Bell, J. N. B. (1986). Vegetation—The missing sink in the global cycle of carbonyl sulphide (COS). *Atmospheric Environment* (1967), 20(3), 537-540. doi:10.1016/0004-6981(86)90094-6
- Brühl, C., Lelieveld, J., Crutzen, P., & Tost, H. (2012). The role of carbonyl sulphide as a source of stratospheric sulphate aerosol and its impact on climate. *Atmospheric chemistry and physics*, 12(3), 1239-1253. doi:10.5194/acp-12-1239-2012
- Burns, R. G., & Fisher, D. S. (1993). Rates of oxidative weathering on the surface of Mars. *Journal of Geophysical Research: Planets*, 98(E2), 3365-3372. doi:10.1029/92JE02055
- Byrne, B., & Goldblatt, C. (2014). Radiative forcings for 28 potential Archean greenhouse gases. *Climate of the Past*, 10(5), 1779-1801. doi:10.5194/cp-10-1779-2014
- Cabrol, N. A., & Grin, E. A. (1999). Distribution, classification, and ages of Martian impact crater lakes. *Icarus*, 142(1), 160-172. doi:10.1006/icar.1999.6191
- Carr, M. H. (1996). *Water on Mars*. New York: Oxford Univ. Press.
- Carr, M. H. (2006). *The Surface of Mars*. Cambridge: Cambridge Univ. Press.
- Carr, M. H., & Head, J. W. (2003). Oceans on Mars: An assessment of the observational evidence and possible fate. *Journal of Geophysical Research: Planets*, 108(E5), 5042. doi:10.1029/2002JE001963
- Carr, M. H., & Head, J. W. (2010). Geologic history of Mars. *Earth and Planetary Science Letters*, 294(3-4), 185-203. doi:10.1016/j.epsl.2009.06.042
- Carr, M. H., & Head, J. W. (2015). Martian surface/near-surface water inventory: Sources, sinks, and changes with time. *Geophysical Research Letters*, 42(3), 726-732. doi:10.1002/2014GL062464
- Carr, M. H., & Head, J. W. (2019). Mars: Formation and fate of a frozen Hesperian ocean. *Icarus*, 319, 433-443. doi:10.1016/j.icarus.2018.08.021
- Carter, J., Poulet, F., Bibring, J. P., Mangold, N., & Murchie, S. (2013). Hydrous minerals on Mars as seen by the CRISM and OMEGA imaging spectrometers: Updated global view. *Journal of Geophysical Research: Planets*, 118(4), 831-858. doi:10.1029/2012JE004145
- Castendyk, D., McKnight, D., Welch, K., Niebuhr, S., & Jaros, C. (2015). Pressure-driven, shoreline currents in a perennially ice-covered, pro-glacial lake in Antarctica, identified from a LiCl tracer injected into a pro-glacial stream. *Hydrological processes*, 29(9), 2212-2231. doi:10.1002/hyp.10352
- Catling, D. C. (1999). A chemical model for evaporites on early Mars: Possible sedimentary tracers of the early climate and implications for exploration. *Journal of Geophysical Research: Planets*, 104(E7), 16453-16469. doi:10.1029/1998JE001020
- Catling, D. C. (2009). Atmospheric Evolution, Mars. In V. Gornitz (Ed.), *Encyclopedia of Paleoclimatology and Ancient Environments* (pp. 66-75). Dordrecht, The Netherlands: Springer. doi:10.1007/978-1-4020-4411-3_17
- Catling, D. C. (2014). Mars Atmosphere: History and Surface Interactions. In T. Spohn, T. V. Johnson, & D. Breuer (Eds.), *Encyclopedia of the Solar System* (2nd Ed.) (pp. 343-357). New York: Academic Press. doi:10.1016/B978-0-12-415845-0.00016-5
- Catling, D. C., Claire, M. W., Zahnle, K. J., Quinn, R. C., Clark, B. C., Hecht, M. H., & Kounaves, S. (2010). Atmospheric origins of perchlorate on Mars and in the Atacama. *Journal of Geophysical Research: Planets*, 115(E1), E00E11. doi:10.1029/2009JE003425

- Catling, D. C., & Kasting, J. F. (2017). *Atmospheric Evolution on Inhabited and Lifeless Worlds*. In. doi:10.1017/9781139020558
- Catling, D. C., Krissansen-Totton, J., Kiang, N. Y., Crisp, D., Robinson, T. D., DasSarma, S., et al. (2018). Exoplanet Biosignatures: A Framework for Their Assessment. *Astrobiology*, 18, 709-738. doi:10.1089/ast.2017.1737
- Catling, D. C., Leovy, C. B., Wood, S. E., & Day, M. D. (2012). *Does the Vastitas Borealis Formation contain oceanic or volcanic deposits?* Paper presented at the Third Int. Conf. on Early Mars.
- Catling, D. C., & Moore, J. M. (2003). The nature of coarse-grained crystalline hematite and its implications for the early environment of Mars. *Icarus*, 165(2), 277-300. doi:10.1016/S0019-1035(03)00173-8
- Catling, D. C., Wood, S. E., Leovy, C., Montgomery, D. R., Greenberg, H. M., Glein, C. R., & Moore, J. M. (2006). Light-toned layered deposits in Juventae Chasma, Mars. *Icarus*, 181(1), 26-51. doi:10.1016/j.icarus.2005.10.020
- Chan, M. A., Jewell, P., Parker, T. J., Ormö, J., Okubo, C., & Komatsu, G. (2016). Pleistocene Lake Bonneville as an analog for extraterrestrial lakes and oceans. In C. G. Oviatt & J. F. Shroder (Eds.), *Developments in Earth Surface Processes* (Vol. 20, pp. 570-597): Elsevier. doi:10.1016/B978-0-444-63590-7.00021-4
- Chan, N. H., Perron, J. T., Mitrovica, J. X., & Gomez, N. A. (2018). New Evidence of an Ancient Martian Ocean from the Global Distribution of Valley Networks. *Journal of Geophysical Research: Planets*, 123(8), 2138-2150. doi:10.1029/2018JE005536
- Chemtob, S. M., Nickerson, R. D., Morris, R. V., Agresti, D. G., & Catalano, J. G. (2015). Synthesis and structural characterization of ferrous trioctahedral smectites: Implications for clay mineral genesis and detectability on Mars. *Journal of Geophysical Research: Planets*, 120(6), 1119-1140. doi:10.1002/2014JE004763
- Chevrier, V., Poulet, F., & Bibring, J. P. (2007). Early geochemical environment of Mars as determined from thermodynamics of phyllosilicates. *Nature*, 448(7149), 60-63. doi:10.1038/nature05961
- Christensen, P. R., Jakosky, B. M., Kieffer, H. H., Malin, M. C., McSween, H. Y., Jr., Nealon, K., et al. (2004). The Thermal Emission Imaging System (THEMIS) for the Mars 2001 Odyssey Mission. *Space Science Reviews*, 110(1-2), 85-130. doi:10.1023/B:SPAC.0000021008.16305.94
- Chung, K., Calvert, J. G., & Bottenheim, J. W. (1975). The photochemistry of sulfur dioxide excited within its first allowed band (3130 Å) and the "forbidden" band (3700-4000 Å). *International journal of chemical kinetics*, 7(2), 161-182. doi:10.1002/kin.550070202
- Citron, R. I., Manga, M., & Hemingway, D. J. (2018). Timing of oceans on Mars from shoreline deformation. *Nature*, 555(7698), 643-646. doi:10.1038/nature26144
- Claire, M. W., Kasting, J. F., Domagal-Goldman, S. D., Stüeken, E. E., Buick, R., & Meadows, V. S. (2014). Modeling the signature of sulfur mass-independent fractionation produced in the Archean atmosphere. *Geochimica et Cosmochimica Acta*, 141, 365-380. doi:10.1016/j.gca.2014.06.032
- Clark, B. C., Baird, A., Rose, H. J., Toulmin, P., Keil, K., Castro, A. J., et al. (1976). Inorganic analyses of Martian surface samples at the Viking landing sites. *Science*, 194(4271), 1283-1288. doi:10.1126/science.194.4271.1283
- Clifford, S. M. (1993). A model for the hydrologic and climatic behavior of water on Mars. *Journal of Geophysical Research: Planets*, 98(E6), 10973-11016. doi:10.1029/93JE00225
- Clifford, S. M., Lasue, J., Heggy, E., Boisson, J., McGovern, P., & Max, M. D. (2010). Depth of the Martian cryosphere: Revised estimates and implications for the existence and detection of subpermafrost groundwater. *Journal of Geophysical Research: Planets*, 115(E7001). doi:10.1029/2009JE003462
- Clifford, S. M., & Parker, T. J. (2001). The Evolution of the Martian Hydrosphere: Implications for the Fate of a Primordial Ocean and the Current State of the Northern Plains. *Icarus*, 154(1), 40-79. doi:10.1006/icar.2001.6671
- Cockell, C. S., Bush, T., Bryce, C., Direito, S., Fox-Powell, M., Harrison, J., et al. (2016). Habitability: a review. *Astrobiology*, 16(1), 89-117. doi:10.1089/ast.2015.1295
- Cockell, C. S., Catling, D. C., Davis, W. L., Snook, K., Kepner, R. L., Lee, P., & McKay, C. P. (2000). The ultraviolet environment of Mars: biological implications past, present, and future. *Icarus*, 146(2), 343-359. doi:10.1006/icar.2000.6393
- Colwell, J. E., & Jakosky, B. M. (2002). Effects of topography on thermal infrared spectra of planetary surfaces. *Journal of Geophysical Research: Planets*, 107(E11), 5106. doi:10.1029/2001JE001829
- Costard, F., Séjourné, A., Kelfoun, K., Clifford, S., Lavigne, F., Di Pietro, I., & Bouley, S. (2017). Modeling tsunami propagation and the emplacement of thumbprint terrain in an early Mars ocean. *Journal of Geophysical Research: Planets*, 122(3), 633-649. doi:10.1002/2016JE005230
- Currey, D. R. (1980). Coastal geomorphology of Great Salt Lake and vicinity. *Great Salt Lake: a scientific, historical and economic overview*. *Utah Geo. Miner. Sur. Bull.*, 116, 69-82.

- Dartnell, L. R., Desorgher, L., Ward, J., & Coates, A. (2007). Modelling the surface and subsurface martian radiation environment: implications for astrobiology. *Geophysical Research Letters*, 34(2). doi:10.1029/2006GL027494
- De Blasio, F. V. (2018). The pristine shape of Olympus Mons on Mars and the subaqueous origin of its aureole deposits. *Icarus*, 302, 44-61. doi:10.1016/j.icarus.2017.11.003
- Dehouck, E., Gaudin, A., Chevrier, V., & Mangold, N. (2016). Mineralogical record of the redox conditions on early Mars. *Icarus*, 271, 67-75. doi:10.1016/j.icarus.2016.01.030
- DeMore, W. B., Sander, S. P., Golden, D., Hampson, R. F., Kurylo, M. J., Howard, C., et al. (1997). Chemical Kinetics and Photochemical Data for Use in Stratospheric Modeling. Evaluation No. 12.
- Di Achille, G., & Hynek, B. M. (2010). Ancient ocean on Mars supported by global distribution of deltas and valleys. *Nature Geoscience*, 3(7), 459-463. doi:10.1038/ngeo891
- DiBiase, R. A., Limaye, A. B., Scheingross, J. S., Fischer, W. W., & Lamb, M. P. (2013). Deltaic deposits at Aeolis Dorsa: Sedimentary evidence for a standing body of water on the northern plains of Mars. *Journal of Geophysical Research: Planets*, 118(6), 1285-1302. doi:10.1002/jgre.20100
- Dickson, J. L., Head, J. W., & Marchant, D. R. (2008). Late Amazonian glaciation at the dichotomy boundary on Mars: Evidence for glacial thickness maxima and multiple glacial phases. *Geology*, 36(5), 411-414. doi:10.1130/G24382A.1
- Domagal-Goldman, S. D., Meadows, V. S., Claire, M. W., & Kasting, J. F. (2011). Using biogenic sulfur gases as remotely detectable biosignatures on anoxic planets. *Astrobiology*, 11(5), 419-441. doi:10.1089/ast.2010.0509
- Du, S., Francisco, J. S., Shepler, B. C., & Peterson, K. A. (2008). Determination of the rate constant for sulfur recombination by quasiclassical trajectory calculations. *The Journal of chemical physics*, 128(20), 204306. doi:10.1063/1.2919569
- Dundas, C. M., Byrne, S., McEwen, A. S., Mellon, M. T., Kennedy, M. R., Daubar, I. J., & Saper, L. (2014). HiRISE observations of new impact craters exposing Martian ground ice. *Journal of Geophysical Research: Planets*, 119(1), 109-127. doi:10.1002/2013JE004482
- Edgett, K. S., & Parker, T. J. (1997). Water on early Mars: Possible subaqueous sedimentary deposits covering ancient cratered terrain in western Arabia and Sinus Meridiani. *Geophysical Research Letters*, 24(22), 2897-2900. doi:10.1029/97GL02840
- Edwards, A. C. (2001). Grain size and sorting in modern beach sands. *Journal of Coastal Research*, 17(1), 38-52.
- Edwards, C. S., Bandfield, J., Christensen, P., & Fergason, R. (2009). Global distribution of bedrock exposures on Mars using THEMIS high-resolution thermal inertia. *Journal of Geophysical Research: Planets*, 114(E11001). doi:10.1029/2009JE003363
- Ehlmann, B. L., Berger, G., Mangold, N., Michalski, J. R., Catling, D. C., Ruff, S. W., et al. (2013). Geochemical consequences of widespread clay mineral formation in Mars' ancient crust. *Space Science Reviews*, 174(1-4), 329-364. doi:10.1007/s11214-012-9930-0
- Ehlmann, B. L., Mustard, J., & Murchie, S. (2010). Geologic setting of serpentine deposits on Mars. *Geophysical Research Letters*, 37(6). doi:10.1029/2010GL042596
- Ehlmann, B. L., Mustard, J. F., Murchie, S. L., Poulet, F., Bishop, J. L., Brown, A. J., et al. (2008). Orbital identification of carbonate-bearing rocks on Mars. *Science*, 322(5909), 1828-1832. doi:10.1126/science.1164759
- El Maarry, M. R., Markiewicz, W., Mellon, M., Goetz, W., Dohm, J., & Pack, A. (2010). Crater floor polygons: Desiccation patterns of ancient lakes on Mars? *Journal of Geophysical Research: Planets*, 115(E10006). doi:10.1029/2010JE003609
- Erkeling, G., Reiss, D., Hiesinger, H., Ivanov, M. A., Hauber, E., & Bernhardt, H. (2014). Landscape formation at the Deuteronilus contact in southern Isidis Planitia, Mars: Implications for an Isidis Sea? *Icarus*, 242, 329-351. doi:10.1016/j.icarus.2014.08.015
- Erkeling, G., Reiss, D., Hiesinger, H., Poulet, F., Carter, J., Ivanov, M. A., et al. (2012). Valleys, paleolakes and possible shorelines at the Libya Montes/Isidis boundary: Implications for the hydrologic evolution of Mars. *Icarus*, 219(1), 393-413. doi:10.1016/j.icarus.2012.03.012
- Fairen, A. G., Fernandez-Remolar, D., Dohm, J. M., Baker, V. R., & Amils, R. (2004). Inhibition of carbonate synthesis in acidic oceans on early Mars. *Nature*, 431(7007), 423-426. doi:10.1038/nature02911
- Falkowski, P. G., Fenchel, T., & Delong, E. F. (2008). The microbial engines that drive Earth's biogeochemical cycles. *Science*, 320(5879), 1034-1039. doi:10.1126/science.1153213
- Farquhar, J., Kim, S. T., & Masterson, A. (2007). Implications from sulfur isotopes of the Nakhla meteorite for the origin of sulfate on Mars. *Earth and Planetary Science Letters*, 264(1-2), 1-8. doi:10.1016/j.epsl.2007.08.006

- Farrand, W. H., Gaddis, L. R., & Keszthelyi, L. (2005). Pitted cones and domes on Mars: Observations in Acidalia Planitia and Cydonia Mensae using MOC, THEMIS, and TES data. *Journal of Geophysical Research: Planets*, 110(E05005). doi:10.1029/2004JE002297
- Fastook, J. L., & Head, J. W. (2014). Amazonian mid-to high-latitude glaciation on Mars: Supply-limited ice sources, ice accumulation patterns, and concentric crater fill glacial flow and ice sequestration. *Planetary and Space Science*, 91, 60-76. doi:10.1016/j.pss.2013.12.002
- Fawdon, P., Gupta, S., Davis, J. M., Warner, N. H., Adler, J. B., Balme, M. R., et al. (2018). The Hypanis Valles delta: The last highstand of a sea on early Mars? *Earth and Planetary Science Letters*, 500, 225-241. doi:10.1016/j.epsl.2018.07.040
- Feldman, W. C., Prettyman, T. H., Maurice, S., Plaut, J., Bish, D., Vaniman, D., et al. (2004). Global distribution of near-surface hydrogen on Mars. *Journal of Geophysical Research: Planets*, 109(E09), E09006. doi:10.1029/2003JE002160
- Ferry, J. G., & House, C. H. (2005). The stepwise evolution of early life driven by energy conservation. *Molecular biology and evolution*, 23(6), 1286-1292. doi:10.1093/molbev/msk014
- Fincham, C. J. B., & Richardson, F. D. (1954). The Behaviour of Sulphur in Silicate and Aluminate Melts. *Proceedings of the Royal Society of London A: Mathematical, Physical and Engineering Sciences*, 223(1152), 40-62. doi:10.1098/rspa.1954.0099
- Formisano, V., Atreya, S., Encrenaz, T., Ignatiev, N., & Giuranna, M. (2004). Detection of methane in the atmosphere of Mars. *Science*, 306(5702), 1758-1761. doi:10.1126/science.1101732
- Franz, H. B., Kim, S.-T., Farquhar, J., Day, J. M. D., Economos, R. C., McKeegan, K. D., et al. (2014). Isotopic links between atmospheric chemistry and the deep sulphur cycle on Mars. *Nature*, 508(7496), 364-368. doi:10.1038/nature13175
- Franz, H. B., Trainer, M. G., Malespin, C. A., Mahaffy, P. R., Atreya, S. K., Becker, R. H., et al. (2017). Initial SAM calibration gas experiments on Mars: Quadrupole mass spectrometer results and implications. *Planetary and Space Science*, 138, 44-54. doi:10.1016/j.pss.2017.01.014
- Franz, H. B., Trainer, M. G., Wong, M. H., Mahaffy, P. R., Atreya, S. K., Manning, H. L., & Stern, J. C. (2015). Reevaluated martian atmospheric mixing ratios from the mass spectrometer on the Curiosity rover. *Planetary and Space Science*, 109, 154-158. doi:10.1016/j.pss.2015.02.014
- Frey, H. V., Roark, J. H., Shockey, K. M., Frey, E. L., & Sakimoto, S. E. (2002). Ancient lowlands on Mars. *Geophysical Research Letters*, 29(10). doi:10.1029/2001GL013832
- Fuller, E. R., & Head, J. W. (2002). Amazonis Planitia: The role of geologically recent volcanism and sedimentation in the formation of the smoothest plains on Mars. *Journal of Geophysical Research: Planets*, 107(E10). doi:10.1029/2002JE001842
- Gaillard, F., Michalski, J., Berger, G., McLennan, S., & Scaillet, B. (2013). *Geochemical Reservoirs and Timing of Sulfur Cycling on Mars*. In Vol. 174. *Space Science Reviews* (pp. 251-300). doi:10.1007/s11214-012-9947-4
- Gaillard, F., & Scaillet, B. (2009). The sulfur content of volcanic gases on Mars. *Earth and Planetary Science Letters*, 279(1-2), 34-43. doi:10.1016/j.epsl.2008.12.028
- Gendrin, A., Mangold, N., Bibring, J.-P., Langevin, Y., Gondet, B., Poulet, F., et al. (2005). Sulfates in Martian layered terrains: the OMEGA/Mars Express view. *Science*, 307(5715), 1587-1591. doi:10.1126/science.1109087
- Ghatan, G. J., & Zimbelman, J. R. (2006). Paucity of candidate coastal constructional landforms along proposed shorelines on Mars: Implications for a northern lowlands-filling ocean. *Icarus*, 185(1), 171-196. doi:10.1016/j.icarus.2006.06.007
- Goudge, T. A., Aureli, K. L., Head, J. W., Fassett, C. I., & Mustard, J. F. (2015). Classification and analysis of candidate impact crater-hosted closed-basin lakes on Mars. *Icarus*, 260, 346-367. doi:10.1016/j.icarus.2015.07.026
- Goudge, T. A., Head, J. W., Mustard, J. F., & Fassett, C. I. (2012). An analysis of open-basin lake deposits on Mars: Evidence for the nature of associated lacustrine deposits and post-lacustrine modification processes. *Icarus*, 219(1), 211-229. doi:10.1016/j.icarus.2012.02.027
- Greeley, R., & Schneid, B. D. (1991). Magma Generation on Mars: Amounts, Rates, and Comparisons with Earth, Moon, and Venus. *Science*, 254(5034), 996-998. doi:10.1126/science.254.5034.996
- Greeley, R., & Spudis, P. D. (1981). Volcanism on Mars. *Reviews of Geophysics*, 19(1), 13-41. doi:10.1029/RG019i001p00013
- Grimm, R. E., Harrison, K. P., Stillman, D. E., & Kirchoff, M. R. (2017). On the secular retention of ground water and ice on Mars. *Journal of Geophysical Research: Planets*, 122(1), 94-109. doi:10.1002/2016JE005132

- Grimm, R. E., & Painter, S. L. (2009). On the secular evolution of groundwater on Mars. *Geophysical Research Letters*, 36(24). doi:10.1029/2009GL041018
- Grotzinger, J. P., Gupta, S., Malin, M. C., Rubin, D. M., Schieber, J., Siebach, K., et al. (2015). Deposition, exhumation, and paleoclimate of an ancient lake deposit, Gale crater, Mars. *Science*, 350(6257). doi:10.1126/science.aac7575
- Guidat, T., Pochat, S., Bourgeois, O., & Souček, O. (2015). Landform assemblage in Isidis Planitia, Mars: Evidence for a 3 Ga old polythermal ice sheet. *Earth and Planetary Science Letters*, 411, 253-267. doi:10.1016/j.epsl.2014.12.002
- Haberle, R. M. (2013). Estimating the power of Mars' greenhouse effect. *Icarus*, 223(1), 619-620. doi:10.1016/j.icarus.2012.12.022
- Haberle, R. M., Catling, D. C., Carr, M. H., & Zahnle, K. J. (2017). The early Mars climate system. In R. M. Haberle, R. T. Clancy, F. Forget, M. D. Smith, & R. W. Zurek (Eds.), *The Atmosphere and Climate of Mars* (pp. 526-568). Cambridge, MA: Cambridge University Press. doi:10.1017/9781139060172.017
- Haberle, R. M., Forget, F., Colaprete, A., Schaeffer, J., Boynton, W. V., Kelly, N. J., & Chamberlain, M. A. (2008). The effect of ground ice on the Martian seasonal CO₂ cycle. *Planet. Space Sci.*, 56(2), 251-255. doi:10.1016/j.pss.2007.08.006
- Haberle, R. M., Murphy, J. R., & Schaeffer, J. (2003). Orbital change experiments with a Mars general circulation model. *Icarus*, 161(1), 66-89. doi:10.1016/S0019-1035(02)00017-9
- Halevy, I., & Head, J. W. (2014). Episodic warming of early Mars by punctuated volcanism. *Nature Geoscience*, 7(12), 865-868. doi:10.1038/ngeo2293
- Halevy, I., Zuber, M. T., & Schrag, D. P. (2007). A sulfur dioxide climate feedback on early Mars. *Science*, 318(5858), 1903-1907. doi:10.1126/science.1147039
- Hanna, J. C., & Phillips, R. J. (2005). Hydrological modeling of the Martian crust with application to the pressurization of aquifers. *Journal of Geophysical Research: Planets*, 110(E1). doi:10.1029/2004JE002330
- Harder, H. (1978). Synthesis of iron layer silicate minerals under natural conditions. *Clays and Clay Minerals*, 26(1), 65-72. doi:10.1346/CCMN.1978.0260108
- Hare, J. L., Ferguson, J. F., Aiken, C. L., & Oldow, J. S. (2001). Quantitative characterization and elevation estimation of Lake Lahontan shoreline terraces from high-resolution digital elevation models. *Journal of Geophysical Research: Solid Earth*, 106(B11), 26761-26774. doi:10.1029/2001JB000344
- Harman, C. E., Schwieterman, E. W., Schottelkotte, J. C., & Kasting, J. F. (2015). Abiotic O₂ Levels on Planets around F, G, K, and M Stars: Possible False Positives for Life? *The Astrophysical Journal*, 812(2), 137. doi:10.1088/0004-637X/812/2/137
- Hartmann, W. K. (2005). Martian cratering 8: Isochron refinement and the chronology of Mars. *Icarus*, 174(2), 294-320. doi:10.1016/j.icarus.2004.11.023
- Hartmann, W. K., Anguita, J., de la Casa, M. A., Berman, D. C., & Ryan, E. V. (2001). Martian cratering 7. The role of impact gardening. *Icarus*, 149(1), 37-53. doi:10.1006/icar.2000.6532
- Hartmann, W. K., & Neukum, G. (2001). Cratering chronology and the evolution of Mars. In R. Kallenbach, J. Geiss, & W. K. Hartmann (Eds.), *Chronology and Evolution of Mars* (Vol. 12, pp. 165-194). Dordrecht: Springer. doi:10.1007/978-94-017-1035-0_6
- Hausrath, E. M., & Olsen, A. A. (2013). Using the chemical composition of carbonate rocks on Mars as a record of secondary interaction with liquid water. *American Mineralogist*, 98(5-6), 897-906. doi:10.2138/am.2013.4187
- Head, J. W., Forget, F., Wordsworth, R., Turbet, M., Cassanelli, J., & Palumbo, A. (2018). *Two Oceans on Mars?: History, Problems, and Prospects*. Paper presented at the 49th Lunar and Planetary Science Conference.
- Head, J. W., Hiesinger, H., Ivanov, M. A., Kreslavsky, M. A., Pratt, S., & Thomson, B. J. (1999). Possible ancient oceans on Mars: evidence from Mars Orbiter Laser Altimeter data. *Science*, 286(5447), 2134-2137. doi:10.1126/science.286.5447.2134
- Head, J. W., Kreslavsky, M., Hiesinger, H., Ivanov, M., Pratt, S., Seibert, N., et al. (1998). Oceans in the past history of Mars: Tests for their presence using Mars Orbiter Laser Altimeter (MOLA) data. *Geophysical Research Letters*, 25(24), 4401-4404. doi:10.1029/1998GL900116
- Head, J. W., Kreslavsky, M. A., & Pratt, S. (2002). Northern lowlands of Mars: Evidence for widespread volcanic flooding and tectonic deformation in the Hesperian Period. *Journal of Geophysical Research*, 107(E1), 5003. doi:10.1029/2000JE001445
- Head, J. W., Marchant, D., Agnew, M., Fassett, C., & Kreslavsky, M. (2006a). Extensive valley glacier deposits in the northern mid-latitudes of Mars: Evidence for Late Amazonian obliquity-driven climate change. *Earth and Planetary Science Letters*, 241(3-4), 663-671. doi:10.1016/j.epsl.2005.11.016

- Head, J. W., Nahm, A. L., Marchant, D. R., & Neukum, G. (2006b). Modification of the dichotomy boundary on Mars by Amazonian mid-latitude regional glaciation. *Geophysical Research Letters*, 33(8). doi:10.1029/2005GL024360
- Hecht, M. (2006). *CHRONOS: A journey through Martian history*. Paper presented at the Fourth International Conference on Mars Polar Science and Exploration.
- Herd, C. D. K., Borg, L. E., Jones, J. H., & Papike, J. J. (2002). Oxygen fugacity and geochemical variations in the martian basalts: implications for martian basalt petrogenesis and the oxidation state of the upper mantle of Mars. *Geochimica et Cosmochimica Acta*, 66(11), 2025-2036. doi:10.1016/S0016-7037(02)00828-1
- Hills, A. J., Cicerone, R. J., Calvert, J. G., & Birks, J. W. (1987). Kinetics of the reactions of diatomic sulfur with atomic oxygen, molecular oxygen, ozone, nitrous oxide, nitric oxide, and nitrogen dioxide. *Journal of Physical Chemistry*, 91(5), 1199-1204. doi:10.1021/j100289a033
- Hitchcock, D. R., & Lovelock, J. E. (1967). Life detection by atmospheric analysis. *Icarus*, 7(1-3), 149-159. doi:10.1016/0019-1035(67)90059-0
- Hoehler, T. M. (2004). Biological energy requirements as quantitative boundary conditions for life in the subsurface. *Geobiology*, 2(4), 205-215. doi:10.1111/j.1472-4677.2004.00033.x
- Hoehler, T. M., & Jorgensen, B. B. (2013). Microbial life under extreme energy limitation. *Nature Reviews: Microbiology*, 11(2), 83-94. doi:10.1038/nrmicro2939
- Hood, D. R., Karunatillake, S., Fassett, C., & Sholes, S. (2019). *Verification of Automatically Measured Boulder Populations in HiRISE Images*. Paper presented at the Lunar and Planetary Science Conference.
- Hu, R., Kass, D. M., Ehlmann, B. L., & Yung, Y. L. (2015). Tracing the fate of carbon and the atmospheric evolution of Mars. *Nature communications*, 6. doi:10.1038/ncomms10003
- Hubbard, J. S., Hardy, J. P., Voecks, G. E., & Golub, E. E. (1973). Photocatalytic synthesis of organic compounds from CO and water: Involvement of surfaces in the formation and stabilization of products. *Journal of Molecular Evolution*, 2(2-3), 149-166. doi:10.1007/BF01653995
- Huber, C., & Wächtershäuser, G. (1997). Activated acetic acid by carbon fixation on (Fe, Ni) S under primordial conditions. *Science*, 276(5310), 245-247. doi:10.1126/science.276.5310.245
- Huber, C., & Wächtershäuser, G. (1998). Peptides by activation of amino acids with CO on (Ni,Fe) surfaces: implications for the origin of life. *Science*, 281, 670-672. doi:10.1126/science.281.5377.670
- Hughes, C. M., Cardenas, B. T., Goudge, T. A., & Mohrig, D. (2019). Deltaic deposits indicative of a paleo-coastline at Aeolis Dorsa, Mars. *Icarus*, 317, 442-453. doi:10.1016/j.icarus.2018.08.009
- Hutchison, R. (2004). *Meteorites: A Petrologic, Chemical, and Isotopic Synthesis*. Cambridge, UK: Cambridge University Press.
- Hynek, B. M., Beach, M., & Hoke, M. R. (2010). Updated global map of Martian valley networks and implications for climate and hydrologic processes. *Journal of Geophysical Research: Planets*, 115(E9). doi:10.1029/2009JE003548
- Irwin, R. P., Howard, A. D., & Maxwell, T. A. (2004). Geomorphology of Ma'adim Vallis, Mars, and associated paleolake basins. *Journal of Geophysical Research: Planets*, 109(E12). doi:10.1029/2004JE002287
- Irwin, R. P., Maxwell, T. A., Howard, A. D., Craddock, R. A., & Leverington, D. W. (2002). A large paleolake basin at the head of Ma'adim Vallis, Mars. *Science*, 296(5576), 2209-2212. doi:10.1126/science.1071143
- Ivanov, M. A., Erkeling, G., Hiesinger, H., Bernhardt, H., & Reiss, D. (2017). Topography of the Deuteronilus contact on Mars: Evidence for an ancient water/mud ocean and long-wavelength topographic readjustments. *Planetary and Space Science*, 144, 49-70. doi:10.1016/j.pss.2017.05.012
- Ivanov, M. A., & Head, J. W. (2003). Syrtis Major and Isidis Basin contact: Morphological and topographic characteristics of Syrtis Major lava flows and material of the Vastitas Borealis Formation. *Journal of Geophysical Research: Planets*, 108(E6). doi:10.1029/2002JE001994
- Jakosky, B. M., Brain, D., Chaffin, M., Curry, S., Deighan, J., Grebowsky, J., et al. (2018). Loss of the Martian atmosphere to space: Present-day loss rates determined from MAVEN observations and integrated loss through time. *Icarus*. doi:10.1016/j.icarus.2018.05.030
- Jakosky, B. M., & Phillips, R. J. (2001). Mars' volatile and climate history. *Nature*, 412(6843), 237-244. doi:10.1038/35084184
- Jakosky, B. M., & Shock, E. L. (1998). The biological potential of Mars, the early Earth, and Europa. *Journal of Geophysical Research: Planets*, 103(E8), 19359-19364. doi:10.1029/98JE01892
- Jaumann, R., Neukum, G., Behnke, T., Duxbury, T. C., Eichertopf, K., Flohrer, J., et al. (2007). The high-resolution stereo camera (HRSC) experiment on Mars Express: Instrument aspects and experiment conduct from interplanetary cruise through the nominal mission. *Planetary and Space Science*, 55(7-8), 928-952. doi:10.1016/j.pss.2006.12.003

- Jeoung, J.-H., & Dobbek, H. (2007). Carbon dioxide activation at the Ni, Fe-cluster of anaerobic carbon monoxide dehydrogenase. *Science*, 318(5855), 1461-1464. doi:10.1126/science.1148481
- Jewell, P. W. (2016). Quantitative identification of erosional Lake Bonneville shorelines, Utah. *Geomorphology*, 253, 135-145. doi:10.1016/j.geomorph.2015.09.022
- Ji, M., Greening, C., Vanwonterghem, I., Carere, C. R., Bay, S. K., Steen, J. A., et al. (2017). Atmospheric trace gases support primary production in Antarctic desert surface soil. *Nature*, 552(7685), 400. doi:10.1038/nature25014
- Johnson, A. P., Cleaves, H. J., Dworkin, J. P., Glavin, D. P., Lazcano, A., & Bada, J. L. (2008). The Miller volcanic spark discharge experiment. *Science*, 322(5900), 404-404. doi:10.1126/science.1161527
- Johnson, S. S., Hebsgaard, M. B., Christensen, T. R., Mastepanov, M., Nielsen, R., Munch, K., et al. (2007). Ancient bacteria show evidence of DNA repair. *Proceedings of the National Academy of Sciences*, 104(36), 14401-14405. doi:10.1073/pnas.0706787104
- Johnson, S. S., Mischna, M. A., Grove, T. L., & Zuber, M. T. (2008). Sulfur-induced greenhouse warming on early Mars. *Journal of Geophysical Research: Planets*, 113(E8). doi:10.1029/2007JE002962
- Johnson, S. S., Pavlov, A. A., & Mischna, M. A. (2009). Fate of SO₂ in the ancient Martian atmosphere: Implications for transient greenhouse warming. *Journal of Geophysical Research: Planets*, 114(E11011).
- Jöns, H.-P. (1985). *Late sedimentation and late sediments in the northern lowlands on Mars*. Paper presented at the 16th Lunar Planetary Science Conference, 414-415.
- Kallmeyer, J., Pockalny, R., Adhikari, R. R., Smith, D. C., & D'Hondt, S. (2012). Global distribution of microbial abundance and biomass in subseafloor sediment. *Proceedings of the National Academy of Sciences*, 109(40), 16213-16216. doi:10.1073/pnas.1203849109
- Kargel, J. S., Baker, V. R., Begét, J. E., Lockwood, J. F., Péwé, T. L., Shaw, J. S., & Strom, R. G. (1995). Evidence of ancient continental glaciation in the Martian northern plains. *Journal of Geophysical Research: Planets*, 100(E3), 5351-5368. doi:10.1029/94JE02447
- Kasting, J. F. (1979). *Evolution of oxygen and ozone in the Earth's atmosphere*. University of Michigan,
- Kasting, J. F. (1990). Bolide impacts and the oxidation state of carbon in the Earth's early atmosphere. *Origins of life and evolution of the biosphere*, 20(3-4), 199-231. doi:10.1007/BF01808105
- Kasting, J. F. (1993). Earth's early atmosphere. *Science*, 259(5097), 920-926. doi:10.1126/science.11536547
- Kasting, J. F. (1997). Warming early Earth and Mars. *Science*, 276(5316), 1213-1213. doi:10.1126/science.276.5316.1213
- Kempes, C. P., van Bodegom, P. M., Wolpert, D., Libby, E., Amend, J., & Hoehler, T. (2017). Drivers of bacterial maintenance and minimal energy requirements. *Frontiers in microbiology*, 8. doi:10.3389/fmicb.2017.00031
- Kempes, C. P., Wang, L., Amend, J. P., Doyle, J., & Hoehler, T. (2016). Evolutionary tradeoffs in cellular composition across diverse bacteria. *The ISME journal*, 10(9), 2145. doi:10.1038/ismej.2016.21
- Kerr, J., & Trotman-Dickenson, A. (1957). The reactions of methyl radicals with thiols. *The Journal of the Chemical Society*, 79, 3322.
- Kesselmeier, J., Teusch, N., & Kuhn, U. (1999). Controlling variables for the uptake of atmospheric carbonyl sulfide by soil. *Journal of Geophysical Research: Atmospheres*, 104(D9), 11577-11584. doi:10.1029/1999JD900090
- Khalil, M. A. K., & Rasmussen, R. A. (1984). Global sources, lifetimes and mass balances of carbonyl sulfide (OCS) and carbon disulfide (CS₂) in the earth's atmosphere. *Atmospheric Environment*, 18(9), 1805-1813. doi:10.1016/0004-6981(84)90356-1
- Kharecha, P., Kasting, J. F., & Siefert, J. (2005). A coupled atmosphere-ecosystem model of the early Archean Earth. *Geobiology*, 3, 53-76. doi:10.1111/j.1472-4669.2005.00049.x
- King, P. L., & McLennan, S. M. (2010). Sulfur on Mars. *Elements*, 6(2), 107-112. doi:10.2113/gselements.6.2.107
- King, P. L., & McSween, H. (2005). Effects of H₂O, pH, and oxidation state on the stability of Fe minerals on Mars. *Journal of Geophysical Research: Planets*, 110(E12). doi:10.1029/2005JE002482
- Kirk, R. L., Howington-Kraus, E., Rosiek, M. R., Anderson, J. A., Archinal, B. A., Becker, K. J., et al. (2008). Ultrahigh resolution topographic mapping of Mars with MRO HiRISE stereo images: Meter-scale slopes of candidate Phoenix landing sites. *Journal of Geophysical Research: Planets*, 113(E3), E00A24. doi:10.1029/2007JE003000
- Kishi, K., & Roberts, M. W. (1975). Carbon monoxide adsorption on iron in the temperature range 85 to 350 K as revealed by X-ray and vacuum ultraviolet [He (II)] photoelectron spectroscopy. *Journal of the Chemical Society, Faraday Transactions 1: Physical Chemistry in Condensed Phases*, 71, 1715-1720. doi:10.1039/F19757101715
- Klein, H. P. (1978). The Viking biological experiments on Mars. *Icarus*, 34(3), 666-674. doi:10.1016/0019-1035(78)90053-2

- Klein, H. P. (1998). The search for life on Mars: What we learned from Viking. *Journal of Geophysical Research: Planets*, 103(E12), 28463-28466. doi:10.1029/98JE01722
- Komar, P. D. (1998). *Beach processes and sedimentation* (2nd ed. ed.). Upper Saddle River, N.J.: Prentice Hall.
- Kounaves, S. P., Hecht, M. H., Kapit, J., Quinn, R. C., Catling, D. C., Clark, B. C., et al. (2010). Soluble sulfate in the martian soil at the Phoenix landing site. *Geophysical Research Letters*, 37(9), L09201. doi:10.1029/2010GL042613
- Kraal, E. R., Asphaug, E., Moore, J. M., & Lorenz, R. D. (2006). Quantitative geomorphic modeling of Martian bedrock shorelines. *Journal of Geophysical Research: Planets*, 111(E3), E03001. doi:10.1029/2005JE002567
- Krasnopolsky, V. A. (1993). Photochemistry of the Martian atmosphere (mean conditions). *Icarus*, 101(2), 313-332. doi:10.1006/icar.1993.1027
- Krasnopolsky, V. A. (2005). A sensitive search for SO₂ in the martian atmosphere: Implications for seepage and origin of methane. *Icarus*, 178(2), 487-492. doi:10.1016/j.icarus.2005.05.006
- Krasnopolsky, V. A., & Feldman, P. D. (2001). Detection of molecular hydrogen in the atmosphere of Mars. *Science*, 294(5548), 1914-1917. doi:10.1126/science.1065569
- Krasnopolsky, V. A., & Lefevre, F. (2013). Chemistry of the atmospheres of Mars, Venus, and Titan. In S. J. Mackwell, A. A. Simon-Miller, J. W. Harder, & M. A. Bullock (Eds.), *Comparative Climatology of Terrestrial Planets* (pp. 231-275). Tucson: Univ. of Arizona Press.
- Krasnopolsky, V. A., Maillard, J. P., & Owen, T. C. (2004). Detection of methane in the martian atmosphere: evidence for life? *Icarus*, 172(2), 537-547. doi:10.1016/j.icarus.2004.07.004
- Kreslavsky, M. A., & Head, J. W. (2002). Fate of outflow channel effluents in the northern lowlands of Mars: The Vastitas Borealis Formation as a sublimation residue from frozen ponded bodies of water. *Journal of Geophysical Research*, 107, 5121. doi:10.1029/2001JE001831
- Kress, A., Head, J. W., & Marchant, D. R. (2006). *The nature of the transition from lobate debris aprons to lineated valley fill: Mamers Valles, northern Arabia Terra-Deuteronilus Mensae region on Mars*. Paper presented at the 37th Annual Lunar and Planetary Science Conference.
- Kress, M. E., & McKay, C. P. (2004). Formation of methane in comet impacts: implications for Earth, Mars, and Titan. *Icarus*, 168(2), 475-483. doi:10.1016/j.icarus.2003.10.013
- Krissansen-Totton, J., Bergsman, D. S., & Catling, D. C. (2016). On detecting biospheres from chemical thermodynamic disequilibrium in planetary atmospheres. *Astrobiology*, 16(1), 39-67. doi:10.1089/ast.2015.1327
- Kurbanov, M., & Mamedov, K. F. (1995). The role of the reaction of CO+ SH₂ → COS+ H₂ in hydrogen formation in the course of interaction between CO and H₂S. *Kinetics and catalysis*, 36(4), 455-457.
- Lammer, H., Lichtenegger, H., Kolb, C., Ribas, I., Guinan, E., Abart, R., & Bauer, S. (2003). Loss of water from Mars: Implications for the oxidation of the soil. *Icarus*, 165(1), 9-25. doi:10.1016/S0019-1035(03)00170-2
- Lammer, H., Zerkle, A. L., Gebauer, S., Tosi, N., Noack, L., Scherf, M., et al. (2018). Origin and evolution of the atmospheres of early Venus, Earth and Mars. *The Astronomy and Astrophysics Review*, 26(2), 1-72. doi:10.1007/s00159-018-0108-y
- LaRowe, D. E., & Amend, J. P. (2015). Power limits for microbial life. *Frontiers in microbiology*, 6, 718. doi:10.3389/fmicb.2015.00718
- Leavitt, S. (1982). Annual volcanic carbon dioxide emission: An estimate from eruption chronologies. *Environmental Geology*, 4(1), 15-21. doi:10.1007/BF02380495
- Lee, J., Stief, L., & Timmons, R. (1977). Absolute rate parameters for the reaction of atomic hydrogen with carbonyl sulfide and ethylene episulfide. *The Journal of chemical physics*, 67(4), 1705-1709. doi:10.1063/1.435005
- Leman, L., Orgel, L., & Ghadiri, M. R. (2004). Carbonyl sulfide-mediated prebiotic formation of peptides. *Science*, 306(5694), 283-286. doi:10.1126/science.1102722
- Lemoine, F. G., Smith, D. E., Rowlands, D. D., Zuber, M., Neumann, G., Chinn, D., & Pavlis, D. (2001). An improved solution of the gravity field of Mars (GMM-2B) from Mars Global Surveyor. *Journal of Geophysical Research: Planets*, 106(E10), 23359-23376. doi:10.1029/2000JE001426
- Lessner, D. J., Li, L., Li, Q., Rejtar, T., Andreev, V. P., Reichlen, M., et al. (2006). An unconventional pathway for reduction of CO₂ to methane in CO-grown Methanosarcina acetivorans revealed by proteomics. *Proceedings of the National Academy of Sciences*, 103(47), 17921-17926. doi:10.1073/pnas.0608833103
- Lever, M. A., Rogers, K. L., Lloyd, K. G., Overmann, J., Schink, B., Thauer, R. K., et al. (2015). Life under extreme energy limitation: a synthesis of laboratory-and field-based investigations. *FEMS microbiology reviews*, 39(5), 688-728. doi:10.1093/femsre/fuv020

- Levy, J. S., Head, J. W., & Marchant, D. R. (2007). Lineated valley fill and lobate debris apron stratigraphy in Nilosyrtis Mensae, Mars: Evidence for phases of glacial modification of the dichotomy boundary. *Journal of Geophysical Research: Planets*, 112(E8). doi:10.1029/2006JE002852
- Levy, J. S., Head, J. W., & Marchant, D. R. (2009). Concentric crater fill in Utopia Planitia: History and interaction between glacial “brain terrain” and periglacial mantle processes. *Icarus*, 202(2), 462-476. doi:10.1016/j.icarus.2009.02.018
- Levy, J. S., Head, J. W., & Marchant, D. R. (2010). Concentric crater fill in the northern mid-latitudes of Mars: Formation processes and relationships to similar landforms of glacial origin. *Icarus*, 209(2), 390-404. doi:10.1016/j.icarus.2010.03.036
- Li, J., & Agee, C. B. (1996). Geochemistry of mantle-core differentiation at high pressure. *Nature*, 381(6584), 686-689. doi:10.1038/381686a0
- Lillis, R. J., Deighan, J., Fox, J. L., Bougher, S. W., Lee, Y., Combi, M. R., et al. (2017). Photochemical escape of oxygen from Mars: First results from MAVEN in situ data. *Journal of Geophysical Research: Space Physics*, 122(3), 3815-3836. doi:10.1002/2016JA023525
- Lin, L.-H., Wang, P.-L., Rumble, D., Lippmann-Pipke, J., Boice, E., Pratt, L. M., et al. (2006). Long-term sustainability of a high-energy, low-diversity crustal biome. *Science*, 314(5798), 479-482. doi:10.1126/science.1127376
- Lloyd, A. C. (1974). Evaluated and estimated kinetic data for phase reactions of the hydroperoxyl radical. *International journal of chemical kinetics*, 6(2), 169-228. doi:10.1002/kin.550060202
- Lomstein, B. A., Langerhuus, A. T., D'hondt, S., Jørgensen, B. B., & Spivack, A. J. (2012). Endospore abundance, microbial growth and necromass turnover in deep sub-seafloor sediment. *Nature*, 484(7392), 101. doi:10.1038/nature10905
- Lovelock, J. E. (1965). A physical basis for life detection experiments. *Nature*, 207, 568-570. doi:10.1038/207568a0
- Lovelock, J. E. (1975). Thermodynamics and the recognition of alien biospheres. *Proceedings of the Royal Society of London B: Biological Sciences*, 189(1095), 167-181. doi:10.1098/rspb.1975.0051
- Lovelock, J. E. (1979). *Gaia: A New Look at Life on Earth*. Oxford: Oxford University Press.
- Lovelock, J. E. (1988). *The Ages of Gaia*. New York: W.W. Norton.
- Lu, Z., Chang, Y. C., Yin, Q.-Z., Ng, C., & Jackson, W. M. (2014). Evidence for direct molecular oxygen production in CO₂ photodissociation. *Science*, 346(6205), 61-64. doi:10.1126/science.1257156
- Lucchitta, B. K., Ferguson, H. M., & Summers, C. (1986). Sedimentary deposits in the northern lowland plains, Mars. *Journal of Geophysical Research: Solid Earth*, 91(B13), E166-E174. doi:10.1029/JB091iB13p0E166
- Mahaffy, P. R., Webster, C. R., Atreya, S. K., Franz, H., Wong, M., Conrad, P. G., et al. (2013). Abundance and Isotopic Composition of Gases in the Martian Atmosphere from the Curiosity Rover. *Science*, 341(6143), 263-266. doi:10.1126/science.1237966
- Malin, M. C., Bell, J. F., Cantor, B. A., Caplinger, M. A., Calvin, W. M., Clancy, R. T., et al. (2007). Context camera investigation on board the Mars Reconnaissance Orbiter. *Journal of Geophysical Research: Planets*, 112(E5), E05S04. doi:10.1029/2006JE002808
- Malin, M. C., Danielson, G., Ingersoll, A., Masursky, H., Veverka, J., Ravine, M., & Soulanille, T. (1992). Mars observer camera. *Journal of Geophysical Research: Planets*, 97(E5), 7699-7718. doi:10.1029/92JE00340
- Malin, M. C., & Edgett, K. S. (1999). Oceans or seas in the Martian northern lowlands: High resolution imaging tests of proposed coastlines. *Geophysical Research Letters*, 26(19), 3049-3052. doi:10.1029/1999GL002342
- Malin, M. C., & Edgett, K. S. (2001). Mars Global Surveyor Mars Orbiter Camera: Interplanetary cruise through primary mission. *Journal of Geophysical Research: Planets*, 106(E10), 23429-23570. doi:10.1029/2000JE001455
- Malm, J. (1999). Some properties of currents and mixing in a shallow ice-covered lake. *Water resources research*, 35(1), 221-232. doi:10.1029/98WR02609
- Mangold, N., & Howard, A. D. (2013). Outflow channels with deltaic deposits in Ismenius Lacus, Mars. *Icarus*, 226(1), 385-401. doi:10.1016/j.icarus.2013.05.040
- Marschall, E., Jogler, M., Henßge, U., & Overmann, J. (2010). Large-scale distribution and activity patterns of an extremely low-light-adapted population of green sulfur bacteria in the Black Sea. *Environmental microbiology*, 12(5), 1348-1362. doi:10.1111/j.1462-2920.2010.02178.x
- Martín-Torres, F. J., Zorzano, M.-P., Valentín-Serrano, P., Harri, A.-M., Genzer, M., Kemppinen, O., et al. (2015). Transient liquid water and water activity at Gale crater on Mars. *Nature Geoscience*, 8(5), 357-361. doi:10.1038/ngeo2412
- Martinez, R. I., & Herron, J. T. (1983). Methyl thiirane: Kinetic gas-phase titration of sulfur atoms in S_xO_y systems. *International journal of chemical kinetics*, 15(11), 1127-1132. doi:10.1002/kin.550151102

- McAdam, A. C., Franz, H. B., Sutter, B., Archer, P. D., Freissinet, C., Eigenbrode, J. L., et al. (2014). Sulfur-bearing phases detected by evolved gas analysis of the Rocknest aeolian deposit, Gale Crater, Mars. *Journal of Geophysical Research: Planets*, *119*(2), 373-393. doi:10.1002/2013JE004518
- McEwen, A. S., Eliason, E. M., Bergstrom, J. W., Bridges, N. T., Hansen, C. J., Delamere, W. A., et al. (2007). Mars Reconnaissance Orbiter's High Resolution Imaging Science Experiment (HiRISE). *Journal of Geophysical Research: Planets*, *112*(E5), E05S02. doi:10.1029/2005JE002605
- McGouldrick, K., Toon, O. B., & Grinspoon, D. H. (2011). Sulfuric acid aerosols in the atmospheres of the terrestrial planets. *Planetary and Space Science*, *59*(10), 934-941. doi:10.1016/j.pss.2010.05.020
- McGuire, P. C., Bishop, J. L., Brown, A. J., Fraeman, A. A., Marzo, G. A., Morgan, M. F., et al. (2009). An improvement to the volcano-scan algorithm for atmospheric correction of CRISM and OMEGA spectral data. *Planetary and Space Science*, *57*(7), 809-815. doi:10.1016/j.pss.2009.03.007
- McKay, C. P. (1997). The search for life on Mars. In *Planetary and Interstellar Processes Relevant to the Origins of Life* (pp. 263-289): Springer.
- McKay, C. P., & Nedell, S. S. (1988). Are there carbonate deposits in the Valles Marineris, Mars? *Icarus*, *73*(1), 142-148. doi:10.1016/0019-1035(88)90088-7
- McMahon, S., Parnell, J., & Blamey, N. J. (2016). Evidence for seismogenic hydrogen gas, a potential microbial energy source on Earth and Mars. *Astrobiology*, *16*(9), 690-702. doi:10.1089/ast.2015.1405
- McSween, H. Y. (1994). What we have learned about Mars from SNC meteorites. *Meteoritics*, *29*(6), 757-779. doi:10.1111/j.1945-5100.1994.tb01092.x
- McSween, H. Y., Grove, T. L., Lentz, R. C. F., Dann, J. C., Holzheid, A. H., Riciputi, L. R., & Ryan, J. G. (2001). Geochemical evidence for magmatic water within Mars from pyroxenes in the Shergotty meteorite. *Nature*, *409*(6819), 487-490. doi:10.1038/35054011
- Mellon, M. T., Jakosky, B. M., & Postawko, S. E. (1997). The persistence of equatorial ground ice on Mars. *Journal of Geophysical Research: Planets*, *102*(E8), 19357-19369. doi:10.1029/97JE01346
- Melosh, H. J. (1989). *Impact cratering: A geologic process* (Vol. 1). New York: Oxford University Press.
- MEPAG. (2018). Mars Scientific Goals, Objectives, Investigations, and Priorities: 2018. In D. Banfield (Ed.), white paper posted October, 2018 by the Mars Exploration Program Analysis Group (MEPAG) (pp. 81). Retrieved from <https://mepag.jpl.nasa.gov/reports.cfm>.
- Meyer, O., & Schlegel, H. G. (1983). Biology of aerobic carbon monoxide-oxidizing bacteria. *Annual Reviews in Microbiology*, *37*(1), 277-310. doi:10.1146/annurev.mi.37.100183.001425
- Michalski, J. R., & Bleacher, J. E. (2013). Supervolcanoes within an ancient volcanic province in Arabia Terra, Mars. *Nature*, *502*(7469), 47. doi:10.1038/nature12482
- Michalski, J. R., Cuadros, J., Niles, P. B., Parnell, J., Rogers, A. D., & Wright, S. P. (2013). Groundwater activity on Mars and implications for a deep biosphere. *Nature Geoscience*, *6*(2), 133. doi:10.1038/ngeo1706
- Michalski, J. R., & Niles, P. B. (2010). Deep crustal carbonate rocks exposed by meteor impact on Mars. *Nature Geoscience*, *3*(11), 751-755. doi:doi.org/10.1038/ngeo971
- Michalski, J. R., & Niles, P. B. (2012). Atmospheric origin of martian interior layered deposits: Links to climate change and global sulfur cycle. *Geology*, *40*, 419-422. doi:10.1130/G32971.1
- Mickol, R., & Kral, T. (2016). Low pressure tolerance by methanogens in an aqueous environment: implications for subsurface life on Mars. *Origins of Life and Evolution of Biospheres*, 1-22. doi:10.1007/s11084-016-9519-9
- Miller, S. L. (1953). A production of amino acids under possible primitive Earth conditions. *Science*, *117*, 528-529. doi:10.1126/science.117.3046.528
- Miller, S. L. (1955). Production of some organic compounds under possible primitive Earth conditions. *Journal of the American Chemical Society*, *77*, 2351-2361. doi:10.1021/ja01614a001
- Miller, S. L. (1986). Current status of the prebiotic synthesis of small molecules. *Chemica Scripta*, *26B*, 5-11.
- Miyakawa, S., Yamanashi, H., Kobayashi, K., Cleaves, H. J., & Miller, S. L. (2002). Prebiotic synthesis from CO atmospheres: Implications for the origins of life. *Proceedings of the National Academy of Sciences*, *99*(23), 14628-14631. doi:10.1073/pnas.192568299
- Moratto, Z. M., Broxton, M. J., Beyer, R. A., Lundy, M., & Husmann, K. (2010). *Ames Stereo Pipeline, NASA's Open Source Automated Stereogrammetry Software*. Paper presented at the 41st Lunar and Planetary Science Conference, 2364.
- Morgan, G. A., Head III, J. W., & Marchant, D. R. (2009). Lineated valley fill (LVF) and lobate debris aprons (LDA) in the Deuteronilus Mensae northern dichotomy boundary region, Mars: Constraints on the extent, age and episodicity of Amazonian glacial events. *Icarus*, *202*(1), 22-38. doi:10.1016/j.icarus.2009.02.017

- Morris, R. V., Ruff, S. W., Gellert, R., Ming, D. W., Arvidson, R. E., Clark, B. C., et al. (2010). Identification of Carbonate-Rich Outcrops on Mars by the Spirit Rover. *Science*, 329(5990), 421-424. doi:10.1126/science.1189667
- Moses, J. I., Allen, M., & Gladstone, G. R. (1995). Post-SL9 sulfur photochemistry on Jupiter. *Geophysical Research Letters*, 22(12), 1597-1600. doi:10.1029/95GL01200
- Moses, J. I., Fouchet, T., Bézard, B., Gladstone, G., Lellouch, E., & Feuchtgruber, H. (2005). Photochemistry and diffusion in Jupiter's stratosphere: constraints from ISO observations and comparisons with other giant planets. *Journal of Geophysical Research: Planets*, 110(E8). doi:10.1029/2005JE002411
- Moses, J. I., Zolotov, M. Y., & Fegley Jr, B. (2002). Photochemistry of a volcanically driven atmosphere on Io: Sulfur and oxygen species from a Pele-type eruption. *Icarus*, 156(1), 76-106. doi:10.1006/icar.2001.6758
- Mouginot, J., Pommerol, A., Beck, P., Kofman, W., & Clifford, S. M. (2012). Dielectric map of the martian northern hemisphere and the nature of the plain filling materials. *Geophysical Research Letters*, 39, L022022. doi:10.1029/2011GL050286
- Mumma, M. J., Villanueva, G. L., Novak, R. E., Hewagama, T., Bonev, B. P., DiSanti, M. A., et al. (2009). Strong release of methane on Mars in northern summer 2003. *Science*, 323(5917), 1041-1045. doi:10.1126/science.1165243
- Murchie, S. L., Arvidson, R., Bedini, P., Beisser, K., Bibring, J. P., Bishop, J., et al. (2007). Compact Reconnaissance Imaging Spectrometer for Mars (CRISM) on Mars Reconnaissance Orbiter (MRO). *Journal of Geophysical Research: Planets*, 112(E5), E05S03. doi:10.1029/2006JE002682
- Murchie, S. L., Mustard, J. F., Ehlmann, B. L., Milliken, R. E., Bishop, J. L., McKeown, N. K., et al. (2009). A synthesis of Martian aqueous mineralogy after 1 Mars year of observations from the Mars Reconnaissance Orbiter. *Journal of Geophysical Research: Planets*, 114(E2), E00D06. doi:10.1029/2009JE003342
- Myers, M. R., & King, G. M. (2017). Perchlorate-coupled carbon monoxide (CO) oxidation: evidence for a plausible microbe-mediated reaction in Martian brines. *Frontiers in microbiology*, 8, 2571. doi:10.3389/fmicb.2017.02571
- Nair, H., Allen, M., Anbar, A. D., Yung, Y. L., & Clancy, R. T. (1994). A photochemical model of the Martian atmosphere. *Icarus*, 111, 124-150. doi:10.1006/icar.1994.1137
- NASA Astrobiology Strategy 2015. (2016). Executive Summary. *Astrobiology*, 16(8), 654-656. doi:10.1089/ast.2016.78201.es
- Neumann, G. A., Rowlands, D. D., Lemoine, F. G., Smith, D. E., & Zuber, M. T. (2001). Crossover analysis of Mars orbiter laser altimeter data. *Journal of Geophysical Research: Planets*, 106(E10), 23753-23768. doi:10.1029/2000JE001381
- O'Neill, H., & Mavrogenes, J. A. (2002). The Sulfide Capacity and the Sulfur Content at Sulfide Saturation of Silicate Melts at 1400°C and 1 bar. *Journal of Petrology*, 43(6), 1049-1087. doi:10.1093/petrology/43.6.1049
- Oehler, D. Z., & Allen, C. C. (2010). Evidence for pervasive mud volcanism in Acidalia Planitia, Mars. *Icarus*, 208(2), 636-657. doi:10.1016/j.icarus.2010.03.031
- Öhman, T. (2013). A beginner's guide to stereo-derived DEM production and analysis using ISIS, ASP, and ArcMap. *Lunar and Planetary Institute, internal report*. doi:10.13140/RG.2.1.1743.7609
- Ojha, L., Wilhelm, M. B., Murchie, S. L., McEwen, A. S., Wray, J. J., Hanley, J., et al. (2015). Spectral evidence for hydrated salts in recurring slope lineae on Mars. *Nature Geoscience*, 8(11), 829-832. doi:10.1038/ngeo2546
- Onstott, T., Magnabosco, C., Aubrey, A., Burton, A., Dworkin, J., Elsila, J., et al. (2014). Does aspartic acid racemization constrain the depth limit of the subsurface biosphere? *Geobiology*, 12(1), 1-19. doi:10.1111/gbi.12069
- Onstott, T., McGown, D., Kessler, J., Lollar, B. S., Lehmann, K., & Clifford, S. (2006). Martian CH₄: sources, flux, and detection. *Astrobiology*, 6(2), 377-395. doi:10.1089/ast.2006.6.377
- Orgel, C., Hauber, E., van Gasselt, S., Reiss, D., Johnsson, A., Ramsdale, J. D., et al. (2019). Grid Mapping the Northern Plains of Mars: A New Overview of Recent Water-and Ice-Related Landforms in Acidalia Planitia. *Journal of Geophysical Research: Planets*, 124(2), 454-482. doi:10.1029/2018JE005664
- Orosei, R., Lauro, S., Pettinelli, E., Cicchetti, A., Coradini, M., Cosciotti, B., et al. (2018). Radar evidence of subglacial liquid water on Mars. *Science*, eaar7268. doi:10.1126/science.aar7268
- Parker, T. J. (2004). *A reassessment of the Mars ocean hypothesis*. Paper presented at the 2nd Conference on Early Mars: Geologic, Hydrologic, and Climatic Evolution and the Implications for Life, 8085.
- Parker, T. J. (2008). *Martian Outflow Channels and the Ocean Hypothesis*. Paper presented at the Lunar and Planetary Science Conference, 2496.
- Parker, T. J., & Calef, F. J. (2012). *Digital Global Map of Potential Ocean Paleoshorelines on Mars*. Paper presented at the Third Conference on Early Mars, 7085.

- Parker, T. J., & Currey, D. R. (2001). Extraterrestrial coastal geomorphology. *Geomorphology*, 37(3–4), 303-328. doi:10.1016/S0169-555X(00)00089-1
- Parker, T. J., Gorsline, D. S., Saunders, R. S., Pieri, D. C., & Schneeberger, D. M. (1993). Coastal geomorphology of the Martian northern plains. *Journal of Geophysical Research: Planets*, 98(E6), 11061-11078. doi:10.1029/93JE00618
- Parker, T. J., Grant, J., Anderson, F., & Franklin, B. (2002). *MOLA topographic evidence for a massive Noachian ocean on Mars*. Paper presented at the 33rd Lunar and Planetary Science Conference, 2027.
- Parker, T. J., Grant, J. A., & Franklin, B. J. (2010). The northern plains: A Martian oceanic basin? In N. A. Cabrol & E. A. Grin (Eds.), *Lakes on Mars* (pp. 249-273). Boston: Elsevier.
- Parker, T. J., Saunders, S. R., & Schneeberger, D. M. (1989). Transitional morphology in West Deuteronilus Mensae, Mars: Implications for modification of the lowland/upland boundary. *Icarus*, 82(1), 111-145. doi:10.1016/0019-1035(89)90027-4
- Pavlov, A., & Kasting, J. F. (2002). Mass-independent fractionation of sulfur isotopes in Archean sediments: strong evidence for an anoxic Archean atmosphere. *Astrobiology*, 2(1), 27. doi:10.1089/153110702753621321
- Pavlov, A., Vasilyev, G., Ostryakov, V., Pavlov, A., & Mahaffy, P. (2012). Degradation of the organic molecules in the shallow subsurface of Mars due to irradiation by cosmic rays. *Geophysical Research Letters*, 39(13). doi:10.1029/2012GL052166
- Pelkey, S. M., Mustard, J. F., Murchie, S., Clancy, R. T., Wolff, M., Smith, M., et al. (2007). CRISM multispectral summary products: Parameterizing mineral diversity on Mars from reflectance. *Journal of Geophysical Research: Planets*, 112(E8), E08S14. doi:10.1029/2006JE002831
- Peretyazhko, T., Sutter, B., Morris, R., Agresti, D., Le, L., & Ming, D. (2016). Fe/Mg smectite formation under acidic conditions on early Mars. *Geochimica et Cosmochimica Acta*, 173, 37-49. doi:10.1016/j.gca.2015.10.012
- Perrin, D., Richard, C., & Martin, R. (1988). Etude cinétique de la réaction thermique du pentène-2 cis vers 500°C. III: Influence de H₂S. *Journal de chimie physique*, 85(2), 185-192.
- Perron, J. T., Mitrovica, J. X., Manga, M., Matsuyama, I., & Richards, M. A. (2007). Evidence for an ancient martian ocean in the topography of deformed shorelines. *Nature*, 447(7146), 840-843. doi:10.1038/nature05873
- Pinto, J. P., Gladstone, C. R., & Yung, Y. L. (1980). Photochemical production of formaldehyde in the earth's primitive atmosphere. *Science*, 210, 183-185. doi:10.1126/science.210.4466.183
- Plaut, J. J., Safaeinili, A., Holt, J. W., Phillips, R. J., Head, J. W., Seu, R., et al. (2009). Radar evidence for ice in lobate debris aprons in the mid-northern latitudes of Mars. *Geophysical Research Letters*, 36(2). doi:10.1029/2008GL036379
- Postawko, S. E., & Kuhn, W. R. (1986). Effect of the greenhouse gases (CO₂, H₂O, SO₂) on Martian paleoclimate. *Journal of Geophysical Research: Solid Earth*, 91, D431-D438. doi:10.1029/JB091iB04p0D431
- Poulet, F., Bibring, J. P., Mustard, J. F., Gendrin, A., Mangold, N., Langevin, Y., et al. (2005). Phyllosilicates on Mars and implications for early martian climate. *Nature*, 438(7068), 623-627. doi:10.1038/nature04274
- Presley, M. A., & Christensen, P. R. (1997). Thermal conductivity measurements of particulate materials 1. A review. *Journal of Geophysical Research: Planets*, 102(E3), 6535-6549. doi:10.1029/96JE03302
- Putzig, N. E., & Mellon, M. T. (2007a). Apparent thermal inertia and the surface heterogeneity of Mars. *Icarus*, 191(1), 68-94. doi:10.1016/j.icarus.2007.05.013
- Putzig, N. E., & Mellon, M. T. (2007b). Thermal behavior of horizontally mixed surfaces on Mars. *Icarus*, 191(1), 52-67. doi:10.1016/j.icarus.2007.03.022
- Rabo, J., Risch, A., & Poutsma, M. (1978). Reactions of carbon monoxide and hydrogen on Co, Ni, Ru, and Pd metals. *Journal of Catalysis*, 53(3), 295-311. doi:10.1016/0021-9517(78)90102-1
- Ragsdale, S. W. (2004). Life with Carbon Monoxide. *Critical Reviews in Biochemistry and Molecular Biology*, 39(3), 165-195. doi:10.1080/10409230490496577
- Ramirez, R. M., & Craddock, R. A. (2018). The geological and climatological case for a warmer and wetter early Mars. *Nature Geoscience*, 11(4), 230. doi:10.1038/s41561-018-0093-9
- Ramirez, R. M., Koppapu, R., Zuger, M. E., Robinson, T. D., Freedman, R., & Kasting, J. F. (2014). Warming early Mars with CO₂ and H₂. *Nature Geoscience*, 7(1), 59-63. doi:10.1038/ngeo2000
- Rennó, N. O., Bos, B. J., Catling, D., Clark, B. C., Drube, L., Fisher, D., et al. (2009). Possible physical and thermodynamical evidence for liquid water at the Phoenix landing site. *Journal of Geophysical Research: Planets*, 114(E1). doi:10.1029/2009JE003362
- Rivera-Hernandez, F., & Palucis, M. (2018). *Deltas Along the Crustal Dichotomy of Mars Likely Record Large Lakes, Not a Global Ocean*. Paper presented at the AGU Fall Meeting Abstracts.
- Robbins, S. J., & Hynek, B. M. (2012). A new global database of Mars impact craters ≥ 1 km: 1. Database creation, properties, and parameters. *Journal of Geophysical Research: Planets*, 117(E5). doi:10.1029/2011JE003966

- Robbins, S. J., Hynek, B. M., Lillis, R. J., & Bottke, W. F. (2013). Large impact crater histories of Mars: The effect of different model crater age techniques. *Icarus*, 225(1), 173-184. doi:10.1016/j.icarus.2013.03.019
- Robock, A. (2000). Volcanic eruptions and climate. *Reviews of Geophysics*, 38(2), 191-219. doi:10.1029/1998RG000054
- Rodriguez, J. A. P., Fairén, A. G., Tanaka, K. L., Zarroca, M., Linares, R., Platz, T., et al. (2016). Tsunami waves extensively resurfaced the shorelines of an early Martian ocean. *Scientific Reports*, 6, 25106. doi:10.1038/srep25106
- Rother, M., & Metcalf, W. W. (2004). Anaerobic growth of *Methanosarcina acetivorans* C2A on carbon monoxide: an unusual way of life for a methanogenic archaeon. *Proceedings of the National Academy of Sciences of the United States of America*, 101(48), 16929-16934. doi:10.1073/pnas.0407486101
- Ruff, S. W., & Christensen, P. R. (2002). Bright and dark regions on Mars: Particle size and mineralogical characteristics based on Thermal Emission Spectrometer data. *Journal of Geophysical Research: Planets*, 107(E12), 5127. doi:10.1029/2001JE001580
- Ruff, S. W., Niles, P. B., Alfano, F., & Clarke, A. B. (2014). Evidence for a Noachian-aged ephemeral lake in Gusev crater, Mars. *Geology*, 42(4), 359-362. doi:10.1130/G35508.1
- Ruiz, J., Fairén, A. G., Dohm, J. M., & Tejero, R. (2004). Thermal isostasy and deformation of possible paleoshorelines on Mars. *Planetary and Space Science*, 52(14), 1297-1301. doi:10.1016/j.pss.2004.06.003
- Rummel, J. D., Beaty, D. W., Jones, M. A., Bakermans, C., Barlow, N. G., Boston, P. J., et al. (2014). A new analysis of Mars "special regions": findings of the second MEPAG Special Regions Science Analysis Group (SR-SAG2). *Astrobiology*, 14(11). doi:10.1089/ast.2014.1227
- Ryan, S., Dlugokencky, E. J., Tans, P. P., & Trudeau, M. E. (2006). Mauna Loa volcano is not a methane source: Implications for Mars. *Geophysical Research Letters*, 33(12), L12301. doi:10.1029/2006GL026223
- Sagan, C. (1977). Reducing greenhouses and the temperature history of Earth and Mars. *Nature*, 269(5625), 224-226. doi:10.1038/269224a0
- Salvatore, M. R., & Christensen, P. (2014). On the origin of the vastitas borealis formation in chryse and acidalia planitiae, mars. *Journal of Geophysical Research: Planets*, 119(12), 2437-2456. doi:10.1002/2014JE004682
- Salvatore, M. R., Mustard, J. F., Wyatt, M. B., & Murchie, S. L. (2010). Definitive evidence of Hesperian basalt in Acidalia and Chryse planitiae. *Journal of Geophysical Research: Planets*, 115(E7). doi:10.1029/2009JE003519
- Sander, S. P., Friedl, R., Golden, D., Kurylo, M., Moortgat, G., Wine, P., et al. (2006). Chemical kinetics and photochemical data for use in atmospheric studies evaluation number 15. *JPL Publication 06-02*.
- Sander, S. P., Friedl, R. R., Abbatt, J. P. D., Barker, J. R., Burkholder, J. B., Golden, D. M., et al. (2011). Chemical Kinetics and Photochemical Data for Use in Atmospheric Studies Evaluation Number 17. *JPL Publication 10-6*.
- Schide, K. H., Jewell, P. W., Oviatt, C. G., Jol, H. M., & Larsen, C. F. (2018). Transgressive-phase barriers as indicators of basin-wide lake-level changes in late Pleistocene Lake Bonneville, Utah, USA. *Geomorphology*, 318, 390-403. doi:10.1016/j.geomorph.2018.07.007
- Schofield, K. (1973). Evaluated chemical kinetic rate constants for various gas phase reactions. *Journal of Physical and Chemical Reference Data*, 2(1), 25-84. doi:10.1063/1.3253112
- Scholten, J. C., & Conrad, R. (2000). Energetics of syntrophic propionate oxidation in defined batch and chemostat cocultures. *Applied and Environmental Microbiology*, 66(7), 2934-2942. doi:10.1128/AEM.66.7.2934-2942.2000
- Schubert, G., Solomon, S. C., Turcotte, D. L., Drake, M. J., & Sleep, N. H. (1992). Origin and thermal evolution of Mars. In H. H. Kieffer, B. M. Jakosky, C. W. Snyder, & M. S. Matthews (Eds.), *Mars* (pp. 147-183).
- Schwieterman, E. W., Kiang, N. Y., Parenteau, M. N., Harman, C. E., DasSarma, S., Fisher, T. M., et al. (2017). Exoplanet Biosignatures: A Review of Remotely Detectable Signs of Life. *Astrobiology*, 18(6). doi:10.1089/ast.2017.1729
- Schwieterman, E. W., Reinhard, C. T., Olson, S. L., Ozaki, K., Harman, C. E., Hong, P. K., & Lyons, T. W. (2019). Rethinking CO Antibiosignatures in the Search for Life Beyond the Solar System. *The Astrophysical Journal*, 874(1), 9. doi:10.3847/1538-4357/ab05e1
- Scott, D. H., Chapman, M. G., Rice Jr, J. W., & Dohm, J. M. (1992). *New evidence of lacustrine basins on Mars-Amazonis and Utopia Planitiae*. Paper presented at the Lunar and Planetary Science Conference Proceedings.
- Seager, S., & Bains, W. (2015). The search for signs of life on exoplanets at the interface of chemistry and planetary science. *Science advances*, 1(2), e1500047. doi:10.1126/sciadv.1500047

- Sefton-Nash, E., Catling, D. C., Wood, S. E., Grindrod, P. M., & Teanby, N. A. (2012). Topographic, spectral and thermal inertia analysis of interior layered deposits in Iani Chaos, Mars. *Icarus*, 221(1), 20-42. doi:10.1016/j.icarus.2012.06.036
- Seinfeld, J. H., & Pandis, S. N. (2016). *Atmospheric chemistry and physics: from air pollution to climate change*: John Wiley & Sons.
- Sekine, Y., Sugita, S., Kadono, T., & Matsui, T. (2003). Methane production by large iron meteorite impacts on early Earth. *Journal of Geophysical Research: Planets*, 108(E7). doi:10.1029/2002JE002034
- Settle, M. (1979). Formation and deposition of volcanic sulfate aerosols on Mars. *Journal of Geophysical Research: Solid Earth*, 84(B14), 8343-8354. doi:10.1029/JB084iB14p08343
- Shean, D. E., Alexandrov, O., Moratto, Z. M., Smith, B. E., Joughin, I. R., Porter, C., & Morin, P. (2016). An automated, open-source pipeline for mass production of digital elevation models (DEMs) from very-high-resolution commercial stereo satellite imagery. *ISPRS Journal of Photogrammetry and Remote Sensing*, 116, 101-117. doi:10.1016/j.isprsjprs.2016.03.012
- Shiina, H., Oya, M., Yamashita, K., Miyoshi, A., & Matsui, H. (1996). Kinetic Studies on the Pyrolysis of H₂S. *The Journal of Physical Chemistry*, 100(6), 2136-2140. doi:10.1021/jp952472j
- Sholes, S. F., Catling, D. C., Pretlow, R., & Montgomery, D. R. (2014). *High-Resolution Examination of the Geomorphology of Proposed Ocean Shorelines on Mars*. Paper presented at the 8th International Conference on Mars, Pasadena, CA, 1014.
- Sholes, S. F., Krissansen-Totton, J., & Catling, D. C. (2019a). A Maximum Subsurface Biomass on Mars from Untapped Free Energy: CO and H₂ as Potential Antibiosignatures. *Astrobiology*, 19(5), 655-668. doi:10.1089/ast.2018.1835
- Sholes, S. F., Montgomery, D. R., & Catling, D. C. (2019b). Quantitative High-Resolution Reexamination of a Hypothesized Ocean Shoreline in Cydonia Mensae on Mars. *Journal of Geophysical Research: Planets*, 124(2), 316-336. doi:10.1029/2018JE005837
- Sholes, S. F., Mushkin, A., & Catling, D. C. (2017a). *Boulder-Size Distributions as Indicators for Depositional Processes on Earth and Mars*. Paper presented at the Geological Society of America Annual Meeting, Seattle, WA.
- Sholes, S. F., Smith, M. L., Claire, M. W., Zahnle, K. J., & Catling, D. C. (2017b). Anoxic atmospheres on Mars driven by volcanism: Implications for past environments and life. *Icarus*, 290, 46-62. doi:10.1016/j.icarus.2017.02.022
- Shum, L. G., & Benson, S. W. (1985). The pyrolysis of dimethyl sulfide, kinetics and mechanism. *International journal of chemical kinetics*, 17(7), 749-761. doi:10.1002/kin.550170705
- Singleton, D., & Cvetanović, R. J. (1988). Evaluated chemical kinetic data for the reactions of atomic oxygen O (3P) with sulfur containing compounds. *Journal of Physical and Chemical Reference Data*, 17(4), 1377-1437. doi:10.1063/1.555811
- Sizemore, H. G., & Mellon, M. T. (2008). Laboratory characterization of the structural properties controlling dynamical gas transport in Mars-analog soils. *Icarus*, 197(2), 606-620. doi:10.1016/j.icarus.2008.05.013
- Skinner Jr, J. A., & Mazzini, A. (2009). Martian mud volcanism: Terrestrial analogs and implications for formational scenarios. *Marine and Petroleum Geology*, 26(9), 1866-1878. doi:10.1016/j.marpetgeo.2009.02.006
- Smith, D. E., Zuber, M. T., Frey, H. V., Garvin, J. B., Head, J. W., Muhleman, D. O., et al. (2001). Mars Orbiter Laser Altimeter: Experiment summary after the first year of global mapping of Mars. *Journal of Geophysical Research: Planets*, 106(E10), 23689-23722. doi:10.1029/2000JE001364
- Smith, M. L., Claire, M. W., Catling, D. C., & Zahnle, K. J. (2014). The formation of sulfate, nitrate and perchlorate salts in the martian atmosphere. *Icarus*, 231(0), 51-64. doi:10.1016/j.icarus.2013.11.031
- Som, S. M., Buick, R., Hagadorn, J. W., Blake, T. S., Perreault, J. M., Harnmeijer, J. P., & Catling, D. C. (2016). Earth's air pressure 2.7 billion years ago constrained to less than half of modern levels. *Nature Geoscience*, 9(6), 448-451. doi:10.1038/ngeo2713
- Squyres, S. W. (1979). The distribution of lobate debris aprons and similar flows on Mars. *Journal of Geophysical Research: Solid Earth*, 84(B14), 8087-8096. doi:10.1029/JB084iB14p08087
- Squyres, S. W., & Carr, M. H. (1986). Geomorphic evidence for the distribution of ground ice on Mars. *Science*, 231(4735), 249-252. doi:10.1126/science.231.4735.249
- Squyres, S. W., Grotzinger, J. P., Arvidson, R. E., Bell, J. F., Calvin, W., Christensen, P. R., et al. (2004). In Situ Evidence for an Ancient Aqueous Environment at Meridiani Planum, Mars. *Science*, 306(5702), 1709-1714. doi:10.1126/science.1104559
- Stachnik, R., & Molina, M. (1987). Kinetics of the reactions of mercapto radicals with nitrogen dioxide and oxygen. *Journal of Physical Chemistry*, 91(17), 4603-4606. doi:10.1021/j100301a035

- Stevens, A. H., Patel, M. R., & Lewis, S. R. (2015). Numerical modelling of the transport of trace gases including methane in the subsurface of Mars. *Icarus*, 250, 587-594. doi:10.1016/j.icarus.2014.12.033
- Stevens, A. H., Patel, M. R., & Lewis, S. R. (2017). Modelled isotopic fractionation and transient diffusive release of methane from potential subsurface sources on Mars. *Icarus*, 281, 240-247. doi:10.1016/j.icarus.2016.08.023
- Stüeken, E. E., Anderson, R. E., Bowman, J. S., Brazelton, W. J., Colangelo-Lillis, J., Goldman, A. D., et al. (2013). Did life originate from a global chemical reactor? *Geobiology*, 11(2), 101-126. doi:10.1111/gbi.12025
- Świąder, A. (2014). Identification and visualisation of possible ancient ocean shoreline on Mars using submeter-resolution Digital Terrain Models. *Geologos*, 20(4), 289-301. doi:10.2478/logos-2014-0017
- Symonds, R. B., Rose, W. I., Bluth, G. J. S., & Gerlach, T. M. (1994). Volcanic-gas studies; methods, results, and applications. *Reviews in Mineralogy and Geochemistry*, 30(1), 1-66.
- Tanaka, K. L. (1997). Sedimentary history and mass flow structures of Chryse and Acidalia Planitiae, Mars. *Journal of Geophysical Research: Planets*, 102(E2), 4131-4149. doi:10.1029/96JE02862
- Tanaka, K. L., Banerdt, W. B., Kargel, J. S., & Hoffman, N. (2001). Huge, CO₂-charged debris-flow deposit and tectonic sagging in the northern plains of Mars. *Geology*, 29(5), 427-430. doi:10.1130/0091-7613(2001)029<0427:HCCDFD>2.0.CO;2
- Tanaka, K. L., Robbins, S. J., Fortezzo, C. M., Skinner, J. A., & Hare, T. M. (2014). The digital global geologic map of Mars: Chronostratigraphic ages, topographic and crater morphologic characteristics, and updated resurfacing history. *Planetary and Space Science*, 95, 11-24. doi:10.1016/j.pss.2013.03.006
- Tanaka, K. L., Skinner, J. A., Hare, T. M., Joyal, T., & Wenker, A. (2003). Resurfacing history of the northern plains of Mars based on geologic mapping of Mars Global Surveyor data. *Journal of Geophysical Research: Planets*, 108(E4). doi:10.1029/2002JE001908
- Tanaka, K. L., Skinner, J. A., Jr., & Hare, T. M. (Cartographer). (2005). Geologic map of the northern plains of Mars
- Tao, Y., Muller, J.-P., Sidiropoulos, P., Xiong, S.-T., Putri, A., Walter, S., et al. (2018). Massive stereo-based DTM production for Mars on cloud computers. *Planetary and Space Science*, 154, 30-58. doi:10.1016/j.pss.2018.02.012
- Techtmann, S. M., Colman, A. S., & Robb, F. T. (2009). 'That which does not kill us only makes us stronger': the role of carbon monoxide in thermophilic microbial consortia. *Environmental microbiology*, 11(5), 1027-1037. doi:10.1111/j.1462-2920.2009.01865.x
- Teodoro, L., Davila, A., Elphic, R. C., Hamilton, D., McKay, C., & Quinn, R. (2018). Habitability and Biomarker Preservation in the Martian Near-Surface Radiation Environment. In *From Habitability to Life on Mars* (pp. 211-231): Elsevier.
- Tian, F., Claire, M. W., Haqq-Misra, J. D., Smith, M., Crisp, D. C., Catling, D., et al. (2010). Photochemical and climate consequences of sulfur outgassing on early Mars. *Earth and Planetary Science Letters*, 295(3-4), 412-418. doi:10.1016/j.epsl.2010.04.016
- Tian, F., Toon, O. B., Pavlov, A. A., & De Sterck, H. (2005). A hydrogen-rich early Earth atmosphere. *Science*, 308(5724), 1014-1017. doi:10.1126/science.1106983
- Tijhuis, L., Van Loosdrecht, M. C., & Heijnen, J. (1993). A thermodynamically based correlation for maintenance Gibbs energy requirements in aerobic and anaerobic chemotrophic growth. *Biotechnology and bioengineering*, 42(4), 509-519. doi:10.1002/bit.260420415
- Toner, J. D., Catling, D. C., & Light, B. (2014). The formation of supercooled brines, viscous liquids, and low-temperature perchlorate glasses in aqueous solutions relevant to Mars. *Icarus*, 233, 36-47. doi:10.1016/j.icarus.2014.01.018
- Toon, O. B., Turco, R. P., & Pollack, J. B. (1982). The ultraviolet absorber on Venus: Amorphous sulfur. *Icarus*, 51(2), 358-373. doi:10.1016/0019-1035(82)90089-6
- Toulmin, P., Baird, A. K., Clark, B. C., Keil, K., Rose, H. J., Christian, R. P., et al. (1977). Geochemical and mineralogical interpretation of the Viking inorganic chemical results. *Journal of Geophysical Research*, 82(28), 4625-4634. doi:10.1029/JS082i028p04625
- Turbet, M., & Forget, F. (2019). The paradoxes of the Late Hesperian Mars ocean. *Scientific Reports*, 9(1), 5717. doi:10.1038/s41598-019-42030-2
- Ueno, Y., Johnson, M. S., Danielache, S. O., Eskebjerg, C., Pandey, A., & Yoshida, N. (2009). Geological sulfur isotopes indicate elevated OCS in the Archean atmosphere, solving faint young sun paradox. *Proceedings of the National Academy of Sciences*, 106(35), 14784-14789. doi:10.1073/pnas.0903518106
- Ueno, Y., Yamada, K., Yoshida, N., Maruyama, S., & Isozaki, Y. (2006). Evidence from fluid inclusions for microbial methanogenesis in the early Archaean era. *Nature*, 440(7083), 516. doi:10.1038/nature04584
- Urey, H. C. (1952). On the Early Chemical History of the Earth and the Origin of Life. *Proceedings of the National Academy of Sciences of the United States of America*, 38(4), 351-363. doi:10.1073/pnas.38.4.351

- Van Bodegom, P. (2007). Microbial maintenance: a critical review on its quantification. *Microbial ecology*, 53(4), 513-523. doi:10.1007/s00248-006-9049-5
- Van Gasselt, S., Hauber, E., & Neukum, G. (2010). Lineated valley fill at the Martian dichotomy boundary: nature and history of degradation. *Journal of Geophysical Research: Planets*, 115(E8). doi:10.1029/2009JE003336
- Velde, B. (1992). *Introduction to Clay Minerals: Chemistry, Origins, Uses and Environmental Significance*. London, UK: Chapman & Hall.
- Villanueva, G. L., Mumma, M. J., Novak, R. E., Käufel, H. U., Hartogh, P., Encrenaz, T., et al. (2015). Strong water isotopic anomalies in the martian atmosphere: Probing current and ancient reservoirs. *Science*, 348(6231), 218-221. doi:10.1126/science.aaa3630
- Viviano-Beck, C. E., Seelos, F. P., Murchie, S. L., Kahn, E. G., Seelos, K. D., Taylor, H. W., et al. (2014). Revised CRISM spectral parameters and summary products based on the currently detected mineral diversity on Mars. *Journal of Geophysical Research: Planets*, 119, 1403-1431. doi:10.1002/2014JE004627
- Wadsworth, J., & Cockell, C. S. (2017). Perchlorates on Mars enhance the bacteriocidal effects of UV light. *Scientific Reports*, 7. doi:10.1038/s41598-017-04910-3
- Walker, G. P. (1992). Morphometric study of pillow-size spectrum among pillow lavas. *Bulletin of Volcanology*, 54, 459-474. doi:10.1007/BF00301392
- Wang, Y., Tian, F., Li, T., & Hu, Y. (2016). On the detection of carbon monoxide as an anti-biosignature in exoplanetary atmospheres. *Icarus*, 266, 15-23. doi:10.1016/j.icarus.2015.11.010
- Wänke, H., & Dreibus, G. (1994). Chemistry and accretion history of Mars. *Philosophical Transactions of the Royal Society a-Mathematical Physical and Engineering Sciences*, 349, 285-293. doi:10.1098/rsta.1994.0132
- Webb, V. E. (2004). Putative shorelines in northern Arabia Terra, Mars. *Journal of Geophysical Research: Planets*, 109(E09010). doi:10.1029/2003JE002205
- Webster, C. R., Mahaffy, P. R., Atreya, S. K., Flesch, G. J., Mischna, M. A., Meslin, P.-Y., et al. (2015). Mars methane detection and variability at Gale crater. *Science*, 347(6220), 415-417. doi:10.1126/science.1261713
- Webster, C. R., Mahaffy, P. R., Atreya, S. K., Moores, J. E., Flesch, G. J., Malespin, C., et al. (2018). Background levels of methane in Mars' atmosphere show strong seasonal variations. *Science*, 360(6393), 1093-1096. doi:10.1126/science.aag0131
- Weight, W. D., & Sonderegger, J. L. (2001). *Manual of applied field hydrogeology*. New York: McGraw-Hill.
- Weiss, B. P., Yung, Y. L., & Neelson, K. H. (2000). Atmospheric energy for subsurface life on Mars? *Proceedings of the National Academy of Sciences*, 97(4), 1395-1399. doi:10.1073/pnas.030538097
- Weiss, M. C., Sousa, F. L., Mrnjavac, N., Neukirchen, S., Roettger, M., Nelson-Sathi, S., & Martin, W. F. (2016). The physiology and habitat of the last universal common ancestor. *Nature Microbiology*, 1, 16116. doi:10.1038/nmicrobiol.2016.116
- Werner, S. C. (2008). The early martian evolution—Constraints from basin formation ages. *Icarus*, 195(1), 45-60. doi:10.1016/j.icarus.2007.12.008
- Werner, S. C. (2009). The global martian volcanic evolutionary history. *Icarus*, 201(1), 44-68. doi:10.1016/j.icarus.2008.12.019
- Werner, S. C., & Tanaka, K. (2011). Redefinition of the crater-density and absolute-age boundaries for the chronostratigraphic system of Mars. *Icarus*, 215(2), 603-607. doi:10.1016/j.icarus.2011.07.024
- Wetzel, D. T., Rutherford, M. J., Jacobsen, S. D., Hauri, E. H., & Saal, A. E. (2013). Degassing of reduced carbon from planetary basalts. *Proceedings of the National Academy of Sciences*, 110(20), 8010-8013. doi:10.1073/pnas.1219266110
- Wharton, R. A., Crosby, J. M., McKay, C. P., & Rice, J. W. (1995). Paleolakes on Mars. *Journal of paleolimnology*, 13(3), 267-283. doi:10.1007/BF00682769
- Wignall, P. B. (2001). Large igneous provinces and mass extinctions. *Earth-Science Reviews*, 53(1-2), 1-33. doi:10.1016/S0012-8252(00)00037-4
- Wolfe, J. M., & Fournier, G. P. (2018). Horizontal gene transfer constrains the timing of methanogen evolution. *Nature ecology & evolution*, 2(5), 897. doi:10.1038/s41559-018-0513-7
- Wood, S. E. (2011). *A General Analytic Model for the Thermal Conductivity of Loose, Indurated or Icy Planetary Regolith*. Paper presented at the 42nd Lunar and Planetary Science Conference, 2795.
- Wordsworth, R. D., Forget, F., Millour, E., Head, J., Madeleine, J.-B., & Charnay, B. (2013). Global modelling of the early martian climate under a denser CO₂ atmosphere: Water cycle and ice evolution. *Icarus*, 222(1), 1-19. doi:10.1016/j.icarus.2012.09.036
- Wordsworth, R. D., Kerber, L., Pierrehumbert, R. T., Forget, F., & Head, J. W. (2015). Comparison of “warm and wet” and “cold and icy” scenarios for early Mars in a 3-D climate model. *Journal of Geophysical Research: Planets*, 120(6), 1201-1219. doi:10.1002/2015JE004787

- Xiao, L., Huang, J., Christensen, P. R., Greeley, R., Williams, D. A., Zhao, J., & He, Q. (2012). Ancient volcanism and its implication for thermal evolution of Mars. *Earth and Planetary Science Letters*, 323–324(0), 9-18. doi:10.1016/j.epsl.2012.01.027
- Yen, A. S., Gellert, R., Schröder, C., Morris, R. V., Bell, J. F., Knudson, A. T., et al. (2005). An integrated view of the chemistry and mineralogy of Martian soils. *Nature*, 436(7047), 49-54. doi:10.1038/nature03637
- Yen, A. S., Mittlefehldt, D. W., McLennan, S. M., Gellert, R., Bell, J., McSween, H. Y., et al. (2006). Nickel on Mars: Constraints on meteoritic material at the surface. *Journal of Geophysical Research: Planets*, 111(E12). doi:10.1029/2006JE002797
- Yung, Y. L., Chen, P., Nealson, K., Atreya, S., Beckett, P., Blank, J. G., et al. (2018). Methane on Mars and Habitability: Challenges and Responses. *Astrobiology*, 18(10). doi:10.1089/ast.2018.1917
- Yung, Y. L., & DeMore, W. (1982). Photochemistry of the stratosphere of Venus: Implications for atmospheric evolution. *Icarus*, 51(2), 199-247. doi:10.1016/0019-1035(82)90080-X
- Yung, Y. L., Liang, M., Jiang, X., Shia, R., Lee, C., Bézard, B., & Marcq, E. (2009). Evidence for carbonyl sulfide (OCS) conversion to CO in the lower atmosphere of Venus. *Journal of Geophysical Research: Planets*, 114(E5). doi:10.1029/2008JE003094
- Zahnle, K. J. (1986). Photochemistry of methane and the formation of hydrocyanic acid (HCN) in the Earth's early atmosphere. *Journal of Geophysical Research: Atmospheres*, 91, 2819-2834. doi:10.1029/JD091iD02p02819
- Zahnle, K. J. (1990). Atmospheric chemistry by large impacts. *Geological Society of America Special Papers*, 247, 271-288. doi:10.1130/SPE247-p271
- Zahnle, K. J. (1998). *Origins of atmospheres*. Paper presented at the Origins.
- Zahnle, K. J. (2015). Play it again, SAM. *Science*, 347(6220), 370-371. doi:10.1126/science.aaa3687
- Zahnle, K. J., Claire, M., & Catling, D. (2006). The loss of mass-independent fractionation in sulfur due to a Palaeoproterozoic collapse of atmospheric methane. *Geobiology*, 4(4), 271-283. doi:10.1111/j.1472-4669.2006.00085.x
- Zahnle, K. J., Freedman, R. S., & Catling, D. C. (2011). Is there methane on Mars? *Icarus*, 212(2), 493-503. doi:10.1016/j.icarus.2010.11.027
- Zahnle, K. J., Haberle, R. M., Catling, D. C., & Kasting, J. F. (2008). Photochemical instability of the ancient Martian atmosphere. *Journal of Geophysical Research: Planets*, 113(E11), E11004. doi:10.1029/2008JE003160
- Zahnle, K. J., Marley, M. S., Morley, C. V., & Moses, J. I. (2016). Photolytic Hazes in the Atmosphere of 51 Eri b. *The Astrophysical Journal*, 824(2), 137. doi:10.3847/0004-637X/824/2/137
- Zuber, M. T. (2018). Oceans on Mars formed early. *Nature*, 555, 590-591. doi:10.1038/d41586-018-03415-x

CURRICULUM VITAE

Steven F. Sholes

Planetary Scientist & Astrobiologist
sfsholes@uw.edu | www.sfsholes.xyz

Education

University of Washington	Seattle, WA
Ph.D. in Earth and Space Sciences & Astrobiology	2019
Cornell University	Ithaca, NY
B.A. in Astronomy, Minor in Mathematics, <i>cum laude</i>	2013

Professional Experience

University of Washington	Seattle, WA
Research Assistant, Advisor: David Catling	2013 – 2019
University of Arkansas	Fayetteville, AR
REU Intern, Advisor: Vincent Chevrier	2012
Cornell University	Ithaca, NY
Undergraduate Research Assistant, Advisor: Peter Thomas	2011 – 2012
Paleontological Research Institute	Ithaca, NY
Collections Assistant, Advisor: Judith Nagel-Myers	2009 – 2011

Publications (in preparation)

Sholes, S.F., K.J. Zahnle, and D.C. Catling. 2019. “Time-dependent Response of the Martian Atmosphere to Volcanic Inputs: Formation of Salts and Redox Evolution.” (to be submitted to *Icarus* in Sep. 2019).

Hood, D.R., S. Karunatilake, C. Fassett, and **S.F. Sholes**. 2019. “The Martian Boulder Automatic Recognition System: MBARS.” (to be submitted to *Computers and Geoscience* in Aug. 2019).

Sholes, S.F., D.R. Montgomery, and D.C. Catling. 2019. “Global Investigation of Hypothesized Ocean Shoreline Sites on Mars.” (to be submitted to in June 2019).

Publications

Sholes, S.F., D.R. Montgomery, and D.C. Catling. 2019. “Quantitative High-Resolution Re-examination of a Hypothesized Ocean Shoreline in Cydonia Mensae on Mars.” *Journal of Geophysical Research: Planets* 124: 316-336. [doi:10.1029/2018JE005837](https://doi.org/10.1029/2018JE005837)

Sholes, S.F., J. Krissansen-Totton, and D.C. Catling. 2019. “A Maximum Subsurface Biomass on Mars from Untapped Free Energy: CO and H₂ as Potential Antibiosignatures.” *Astrobiology* 19(5): 655-668. [doi:10.1089/ast.2018.1835](https://doi.org/10.1089/ast.2018.1835)

- Sholes, S.F.**, M.L. Smith, M.W. Claire, K.J. Zahnle, and D.C. Catling. 2017. "Anoxic atmospheres on early Mars driven by volcanism: Implications for the early environment and life." *Icarus* 290: 46-62. [doi:10.1016/j.icarus.2017.02.022](https://doi.org/10.1016/j.icarus.2017.02.022)
- Misra, A., J. Krissansen-Totton, M.C. Koehler, and **S. Sholes**. 2015. "Detecting Volcanism on Exoplanets using Transient Sulfate Aerosols." *Astrobiology* 15(6): 462-477. [doi:10.1089/ast.2014.1204](https://doi.org/10.1089/ast.2014.1204)
- Thomas, P.C., W. Calvin, P. Gierasch, R. Haberle, P.B. James, and **S. Sholes**. 2013. "Time Scales of Erosion and Deposition Recorded in the Residual South Polar Cap of Mars." *Icarus* 225(2): 923-932. [doi:10.1016/j.icarus.2012.08.038](https://doi.org/10.1016/j.icarus.2012.08.038)

Selected Conference Abstracts

- Sholes, S.F.**, D.R. Montgomery, and D.C. Catling. "Reassessing Mars' Global Ocean Shorelines." *9th International Conference on Mars*, Abstract #6282. 22 July 2019. (talk).
- Hood, D.R., S. Karantillake, C. Fassett, and **S.F. Sholes**. "Verification of Automatically Measured Boulder Populations in HiRISE Images." *50th Lunar and Planetary Science Conference*, Abstract #1893. 21 Mar 2019. (poster) [ads:2019LPI....50.1893H](https://ads2019lpi....50.1893H)
- Sholes, S.F.**, J. Krissansen-Totton, and D.C. Catling. "Biomass Limits on Subsurface Martian Life from Atmospheric Gases." *Mars Extant Life: What's Next?* Abstract #5019, Jan 2019. (invited talk, rescheduled).
- Hood, D.R., S. Karantillake, C. Fassett, and **S.F. Sholes**. "Automated Boulder Detection and Measuring in HiRISE Images." *49th Lunar and Planetary Science Conference*, Abstract #2437, 20 Mar 2018. (poster) [ads:2018LPI....49.2437H](https://ads2018lpi....49.2437H)
- Sholes, S.F.**, A. Mushkin, and D.C. Catling. "Boulder-size Distributions as Indicators for Depositional Process on Earth and Mars." *Geological Society of America Annual*, Abstract #304073, 25 Oct 2017. (talk). [doi:10.1130/abs/2017AM-304073](https://doi.org/10.1130/abs/2017AM-304073)
- Sholes, S.F.**, J. Krissansen-Totton, and D.C. Catling. "How Many Blue Whales on Mars? Obtaining a Maximum Extant Biomass Using CO Antibiosignatures." *Astrobiology Science Conference 2017*, Abstract #3189, 27 Apr 2017. (talk).
- Sholes, S.F.**, D.C. Catling, and D.R. Montgomery. "Quantified Identification of Paleo-Terraces Along a Proposed Martian Ocean Contact." *48th Lunar and Planetary Science Conference*, Abstract #1764, 23 Mar 2017. (talk). [ads:2017LPI....48.1764S](https://ads2017lpi....48.1764S)
- Sholes, S.F.**, M.L. Smith, M.W. Claire, K.J. Zahnle, and D.C. Catling. "An Anoxic Atmosphere on Early, Volcanically Active Mars and its Implications for Life." *Astrobiology Science Conference 2015*, Abstract #7455, 15 Jun 2015. (talk).
- Sholes, S.F.**, D.C. Catling, R. Pretlow, and D.R. Montgomery. "High-Resolution Examination of the Geomorphology of Proposed Ocean Shorelines on Mars." *8th International Conference on Mars*, Abstract #1014, 14 Jul 2014. (poster). [ads:2014LPICo1791.1014S](https://ads2014lpico1791.1014S)
- Sholes, S.F.**, V.F. Chevrier, and J.A. Tullis. "Object Based Image Analysis for Remote Sensing of Planetary Surfaces." *44th Lunar and Planetary Science Conference*, Abstract #1527, 17 Mar 2013. (poster). [ads:2013LPI....44.1527S](https://ads2013lpi....44.1527S)

Teaching Experience

University of Washington, Teaching Assistant	Seattle, WA
ESS 101: Introduction to Geology/Geology and Society	2018, 2015
ESS 102: Space and Space Travel	2017
ESS 106: Living with Volcanoes	2017
ASTBIO 115: Introduction to Astrobiology	2016
ESS 213: Evolution of the Earth	2018, 2016
ESS 310: Mathematical Methods in the Earth Sciences	2019
ESS 421: Introduction to Geological Remote Sensing	2017
ESS 454: Hydrogeology	2019
ESS 455: Stratigraphy	2016
Hannibal Central School District	Hannibal, NY
Substitute Teacher, Tutor, Proctor	2009 – 2011

Selected Honors & Awards

Mars Student Travel Grant (\$1,300)	2019
G.E. Goodspeed Geology and Peter Misch Fellowships (RA)	2018
R.G. and N.E. Bassett Endowment in ESS, H. and L. Coombs Endowed Fellowship in Geological Sciences and M. Ferrel Endowment (RA)	2017
“Why do We Care? Award” ESS Research Gala (\$150)	2017
UW College of the Environment Student Travel Grant (\$500)	2017
G.E. Goodspeed Geology and K.C. Robbins Fellowships (RA)	2016
Pacific Science Center Science Communication Fellowship (Tuition)	2015
Nordic-Hawaii Astrobiology Summer School Grant (Tuition)	2015
Best Space/Planetary Talk, ESS Research Gala (\$150)	2015
R.M. and J.J. Winglee Graduate Student Support Fund (Co-I, \$800)	2015
Mars Student Travel Grant (\$1,000)	2014

Workshops Attended

Pacific Science Center	Seattle, WA
Science Communications Workshop	2015
Nordic-Hawaii Summer School	Reykjavik, IS
Water, Ice and the Origin of Life in the Universe	2015
University of Washington Astrobiology Program	Seattle, WA
Pacific Ocean Research Cruise (oceanography/microbiology)	2014
Yellowstone National Park (geology/microbiology)	2015
Jet Propulsion Laboratory (astronomy/planetary)	2018

Field Trips Led/Co-Led

Eastern Washington (Evolution of the Cascades), <i>ESS 213</i>	2018, 2016
Kitsap Peninsula (Turbidites and Stratigraphy), <i>ESS 213</i>	2018, 2016
Eastern Washington (Columbia Plateau), <i>ESS 101</i>	2018
Eastern Washington (Frenchman Coulee), <i>CWU Mars Week</i>	2016
Mt. St. Helens (Blast Zone), <i>ESS 101</i>	2015
Eastern Washington (Missoula Floods), <i>Field Work/ESS 590</i>	2015

Invited Class Lectures

“ <i>Volcanism on Mars</i> ,” ESS 106: Living with Volcanoes	2017
“ <i>Water on Mars</i> ,” ESS 495: NASA Research Seminar	2017
“ <i>Planetary Stratigraphy</i> ,” ESS 455: Stratigraphy	2016

Undergraduate Research Mentees

William Keller, ESS major	2017
Caitlin Schaefer, EE and INFO majors	2017
Emily Johnson, ESS major	2017
Elizabeth McKinnie, CSE and AMATH majors, NASA WSG Intern	2017
Ken Aragon, AA major	2017 – 2018
Arielle Michelman, HS student	2017 – 2018

Professional Service

ESS Planetary Sciences Research Assistant Prof. Hiring Committee	2017
UW University Rover Challenge Science Advisor	2017
PSC Science Communications Fellow	2015 – 2018
Head of the ESS 594/Prelim Improvement Committee	2014 – 2019
Human Exploration Integration Team, Mars 8 Conference	2015

Selected Press

NewScientist:	Martian Life Must be Rare as Free Energy Source Remains Untapped
NewScientist:	If Mars has Life, its Total Mass is 10,000 Times Smaller Than Earth’s
Eos:	A New Way to Analyze Evidence of Martian Oceans
Seeker:	Volcanic Activity on Ancient Mars May Have Produced Organic Life
Astrobiology:	Volcanoes Light Up Atmospheres of Small Exoplanets
UW News:	Atmospheric Signs of Volcanic Activity Could Aid Search for Life
The Daily:	The Red Planet’s Blue Past

Education and Public Outreach

Pacific Science Center Fellow	
“Oceans on Mars,” Meet a Scientist, Seattle, WA	2017
“Challenges in Astrobiology,” Teen Science Café, Redmond, WA	2016
“Oceans on Mars,” Meet a Scientist, Seattle, WA	2016
“Oceans on Mars,” Meet a Scientist – AstronoMay, Seattle, WA	2016
Mars/Temperature Exhibit, Polar Science Weekend, Seattle, WA	2014
ESS Rockin’ Out	
Mars Rovers/Identifying Powders, Cougar Ridge ES, Bellevue, WA	2017
Design a Mission to Mars, Homeschool Group, Seattle, WA	2016
Design a Mission to Mars, Aki Kurose MS, Seattle, WA	2016
Design a Mission to Mars, Emerson ES, Seattle, WA	2016
Mars Rovers/Identifying Powders, Cougar Ridge ES, Bellevue, WA	2015
Dinosaurs Week, ESS 100 / Burke Museum, Seattle, WA	2015
Identifying Rocks, Open Window School, Bellevue, WA	2014
What is a Rock, Crystal Springs ES, Bothell, WA	2014
Mars/Temperature Exhibit, ESS Family Fun Day, Seattle, WA	2014

Rocks and Minerals, Key Peninsula MS, Lakebay, WA	2014
UW Astrobiology EPO	
“Hunting for Oceans on Mars,” Lakewood HS, Seattle, WA	2018
“Oceans on Mars,” Lakewood HS, Seattle, WA	2016
Intro. To Astrobiology, The Harbor School, Vashon, WA	2015
“What is Life?” Lister ES, Tacoma, WA	2014
Intro. To Astrobiology, The Harbor School, Vashon, WA	2014
Hometown Outreach	
Astronomy & Paleontology Q&A, M.W. Cuyler ES, Red Creek, NY	2013
Astronomy Q&A, M.W. Cuyler ES, Red Creek, NY	2009 – 2011
Inventive Minds Judge, M.W. Cuyler ES, Red Creek, NY	2011
Reach for the Stars Afterschool Program, Hannibal, NY	2008 – 2009
Div. B Science Olympiad Regional Judge, Syracuse, NY	2008 – 2009
The Sholesonian (www.sholesonian.com)	
Family Fun Day, Museum of the Earth, Ithaca, NY	2011
5th Annual Summer Symposium, PRI, Ithaca, NY	2011
Other EPO	
Carl Sagan’s <i>Cosmos</i> Mars Update, Astronomy on Tap, Seattle, WA	2016
Mars Week, Central Washington University, Ellensburg, WA	2016